AUGUST 2016 Ph.D. in MECHANICAL ENGINEERING ADNAN A. UGLA AL-OMAR

UNIVERSITY OF GAZIANTEP
GRADUATE SCHOOL OF
NATURAL & APPLIED SCIENCES

EXPERIMENTAL INVESTIGATION OF SHAPED METAL DEPOSITION PROCESS BY PULSED TIG-WIRE TECHNIQUE

Ph.D. THESIS
IN
MECHANICAL ENGINEERING

BY
ADNAN A. UGLA AL-OMAR
AUGUST 2016

Experimental Investigation of Shaped Metal Deposition Process by Pulsed TIG-Wire Technique

Ph.D. Thesis

in

Mechanical Engineering

University of Gaziantep

Supervisor

Assoc. Prof. Dr. Oğuzhan YILMAZ

By

Adnan A. Ugla AL-OMAR

August 2016

REPUBLIC OF TURKEY
UNIVERSITY OF GAZİANTEP
GRADUATE SCHOOL OF NATURAL & APPLIED SCIENCES
MECHANICAL ENGINEERING

Name of the thesis: Experimental Investigation of Shaped Metal Deposition Process by Pulsed TIG - Wire Technique
Name of the student: Adnan A. Ugla ALOMAR
Exam date: 03.08.2016

Approval of the Graduate School of Natural and Applied Sciences

Prof. Dr. Metin BEDİR
Director

I certify that this thesis satisfies all the requirements as a thesis for the degree of Doctor of Philosophy.

Prof. Dr. Mehmet Sait SÖYLEMEZ
Head of Department

This is to certify that we have read this thesis and that in our consensus/majority opinion it is fully adequate, in scope and quality, as a thesis for the degree of Doctor of Philosophy.

Assoc. Prof. Dr. Oğuzhan YILMAZ
Supervisor

Examining Committee Members:	Signature
Prof. Dr. Metin U. SALAMCI	....
Prof. Dr. Ömer EYERCIOĞLU	....
Prof. Dr. Rahmi ÜNAL	....
Assoc. Prof. Dr. Oğuzhan YILMAZ	....
Assoc. Prof. Dr. Necip F. YILMAZ	....

I hereby declare that all information in this document has been obtained and presented in accordance with academic rules and ethical conduct. I also declare that, as required by these rules and conduct, I have fully cited and referenced all material and results that are not original to this work.

Adnan A. Ugla AL-OMAR

ABSTRACT

EXPERIMENTAL INVESTIGATION OF SHAPED METAL DEPOSITION PROCESS BY PULSED TIG-WIRE TECHNIQUE

AL-OMAR, Adnan A. Ugla
Ph.D. in Mechanical Engineering
Supervisor: Assoc. Prof. Dr. Oğuzhan YILMAZ
August 2016, 222 page

Shaped metal deposition using tungsten inert gas arc welding heat source is a novel additive manufacturing technique which can be used for fabricating solid dense parts by melting a cold wire on a substrate in a layer by layer manner. This work presents an extensive investigation (designing, constructing, controlling, mechanical properties, micro and macro-structural analysis etc.) of the shaped metal deposition process. The aim of this work is to investigate the designed additive manufacturing system capabilities about the part modeling and slicing, deposition-path planning, and the part deposition processes, as well as reporting the limitations of the developed system. In the experimental investigations, continuous and pulsed TIG arc heat sources were used to be able to compare the resultant deposited part qualities. The results of this study have been used to form a shaped metal deposition process window for SS308LSi alloy. The developed system is capable of fabricating near-net-shaped metal components of maximum volume of 400 mm^3 directly from CAD data with minimum buy-to-fly ratio and higher saving in waste material. The resultant deposited parts that were produced with pulsed current arc technique with relatively high frequencies, were observed that they all have good metullurgical bonding, defect free depositions, and high mechanical properties.

Keywords: Shaped metal deposition, Additive Manufacturing, Tungsten Inert Gas Welding.

ÖZET

TEL BESLEMELİ DARBELİ TIG KAYNAK TEKNİĞİ KULLANILARAK ŞEKİLLİ METAL YIĞMA İŞLEMİNİN DENEYSEL İNCELENMESİ

AL-OMAR, Adnan A. Ugla
Doktora Tezi, Makine Mühendisliği Bölümü
Tez Yöneticisi: Doç. Dr. Oğuzhan YILMAZ
Ağustos 2016, 222 Sayfa

Tungsten asal gaz kaynak ark ısısı kullanılarak harici tel beslemeli şekilli metal yığma, yeni bir katmanlı üretim tekniği olarak adlandırılmakta ve soğuk metal telin ergitilerek bir zemin üzerine katman katman yağılması ile yoğun dolu metal parçaların üretiminde kullanılmaktadır. Bu çalışma, şekilli metal yığma işlemi üzerine çok geniş bir incelemeyi (tasarım, inşa, kontrol, mekanik özellikler, mikro ve makro yapı analizleri) içermektedir. Çalışmada kullanılan bütünleşik katmanlı üretim sistemi, metal yığma sürecinde teslim sürelerini azaltmak üzere geliştirilmiştir. Bu çalışmanın amacı, tasarlanan katmanlı üretim sisteminin, parça modelleme ve bölme, yığma yolu planlama ve parça yığma alanlarındaki kabiliyetlerini incelemekle beraber geliştirilen sistemin üretim limitlerini de raporlamaktır. Bu çalışmanın ayrıca diğer amacı östenitik paslanmaz çeliklerin tek katmanlı ve çok katmanlı yığma süreçlerinde temel mekanizmaları anlamaya çalışmaktır. Deneysel incelemelerde, sürekli ve darbeli TIG ark tipleri kullanılarak yığılmış parçaların kaliteleri karşılaştırılmıştır. Çalışmada elde edilen bulgular kullanılarak, SS308LSi alaşımının şekilli metal yığma işlemi için bir süreç penceresi oluşturulmuştur. Geliştirilen katmanlı üretim sistemi maksimum 400 mm^3 hacminde, doğrudan CAD verilerinden elde edilen net geometriye yakın metal parçaların üretilmesinde kullanılabilmektedir ve en az satın-al-uç oranı ile yüksek atık malzeme kazancı elde edilebilmektedir. Yüksek frekanslı darbeli ark ısısının kullanıldığı şekilli yığılmış metal parçalarda iyi derecede metalürjik bağlar, hatasız yığınlar ve yüksek mekanik özellikler elde edilmiştir.

Anahtar Kelimeler: Şekilli Metal Yığma, Katmanlı Üretim, Tungsten Asal Gaz Kaynağı

DEDICATION

.... To My Family

ACKNOWLEDGEMENTS

I would like to express my most sincere gratitude to my supervisor Assoc. Prof. Dr. Oğuzhan YILMAZ for the guidance and support showed throughout this research work. Without his help, this work would not have taken place.

I would also like to thank my dear friend Dr. Ahmed Rahman Almusawi for his friendly help and advice. My very special thanks go to the technical staff in the mechanical department/ division of manufacturing and construction, Mehmet TAȘDEMIR, Mehmet YILDIZ, Seyit BOSTANCIERI, and all other workers in the workshops

This dissertation was performed as a project by Advanced Manufacturing Technology Research Group (AMTRG) in Gaziantep University in the metallic additive manufacturing (MAM) technology using shaped metal deposition technique. I gratefully acknowledge the funding sources and those who made this doctoral thesis possible. I am indebted to the full financial support provide by Gaziantep University Scientific Research Project Unit under the Grant No. MF.14.29.

I would like to acknowledge my sponsor, the ministry of higher education/ Turkey, who gave me the opportunity to study a Ph.D. by granting me a scholarship. I would also like to thank the Ministry of Higher education/ Iraq for the complementary scholarship I received during my studies.

I would like to thank all my friend in Faculty of Engineering / Thi-Qar University for their encouragement. I would like to thank my dear friend Adnan Razaq for his support and friendly help.

I would like to specifically thank all my family. My sincere love to my wife and my beautiful children for their love and support.

Finally, and above all, my gratitude to God.

TABLE OF CONTENTS

Page

LIST OF TABLES

LIST OF FIGURE

Page

_Toc454885357

LIST OF SYMBOLS/ABBREVIATIONS

RMM	Rapid metal manufacturing
SMD	Shaped metal deposition
AM	Addtive manufacturing
CAD	Computer aided design
CAM	Computer aided manufacturing
TIG	Tungsten inert gas
TW-SMD	TIG plus wire shaped metal deposition
MW-SMD	MIG plus wire shaped metal deposition
MRM	Metal rapid manufacturing
MAM	Metal additive manufacturing
RMM	Rapid metal manufacturing
CAMDM	Computer aided metal deposition machine
CCSMD	Continuous current shaped metal deposition
PCSMD	Pulsed current shaped metal deposition
ASS	Austenitic stainless steel
3D	Three dimensions
SLA	Stereolithography
STL	Standard tessellation language
LENS	Laser engineered net shaping
LMD	Laser metal deposition
SLS	Selective laser sintering
SLM	Selective laser melting
Ar	Argon
WERC	welding engineering research centre
WAAM	Wire plus arc additive manufacturing
DMD	Direct metal deposition
BTF	Buy-to-fly
EBF^3	Electron beam free form fabrication

LENS	Laser Engineered Net Shaping
LMDS	Laser Metal Deposition Shaping
SLM	Selective Laser Melting
DMLS	Direct Metal Laser Sintering
IFF	Ion Fusion Formation
CMT	Cold Metal Transfer
LDF	Laser Direct Forming
LAM	Laser Additive Manufacturing
LMDS	Laser Metal Deposition Shaping
LMD	Laser Metal Deposition
SLAM	Sheet Lamination Additive Manufacturing
UC	Ultrasonic Consolidation
EBSM	Electron Beam Selective Melting
EBAM	Electron Beam Additive Manufacturing
PWD	Plasma plus Wire Deposition
RUAM	Ready to Use Additive Manufacturing
SW	Shape welding
MIG	Metal inert gas
WFS	Wire feed speed, m/min
TS	Travel Speed, mm/s
I	Welding current, A
OLP	Off-line programming
LOF	Lack of fusion
σ	Sigma phase
A	Austenite solidification
AF	Primary austenite solidification
FA	Primary ferrite solidification
F	Ferrite solidification
FN	Ferrite number
SMAW	shielded metal arc welding
δ	Delta ferrite
SMDM	Shaped metal deposition machine
DT	Deposition tool
GUIDE	graphical user interface development environment
DOE	Design of experiment

MLT	Machining layer thickness, mm
LF	Low-Frequency, Hz
HF	High-Frequency, Hz
CR	Current ratio, A/A
RHT	Stress relief heat treatment
UTS	Ultimate tensile strength, MPa
Hi	Heat input, J/mm
η	Welding efficiency
DV	Deposition volume, mm^3/mm
α°	Wire feeding angle
ANOVA	Analysis of variance

CHAPTER 1

INTRODUCTION

1.1. Background

In aerospace industry, there are various featured components having intricate shapes which produce from expensive alloys and metals. These parts are usually manufactured by traditional manufacturing methods, (forging, casting, machining etc.). The production of these components is accompanied by extensive machining and finishing operations as well as the cost of moulding and tooling. There is a need for developing an alternative technique to fabricate the important metal parts. One of the interesting alternatives is the shaped metal deposition technique which is considered as a rapid metal manufacturing (RMM) method. It is used for producing a new component, or to repair worn parts. It has the capability to manufacture parts with internal cavities and/or with geometric complexity, and ease of automatic planning, and smaller lot sizes than offered by traditional methods [1-3]. Shaped metal deposition (SMD) method allows complex solid parts to be produced, and it provides a rapid, flexible and cost-effective way compared to the traditional production method, especially in the ability to fabricate middle-sized and large near-net shaped fully dense parts [2-5]. In the welding-based SMD process, near net-shaped metallic components are manufacturing by depositing beads of weld metal in layer by layer and tool path generation for each layer. Figure 1.1 shows the main steps that were followed in the tungsten inert gas welding-based shaped metal deposition (TW-SMD) techniques. The first step is the computer aided design (CAD) software to draw and define the part geometry graphically. Computer-aided manufacturing (CAM) program slices the part model into layers and the layers are converted into lines. Lines are regarded as paths to be followed and these paths are simulated in the control software. The deposition control parameters are set on the welding machine and wire feeder. For the near net shaped metal testing, a special RMM system including hardware and software comprises the path planning steps of creating the part drawing, slicing that drawing, finally, the modeled part is built via defined paths on the substrate using SMD machine.

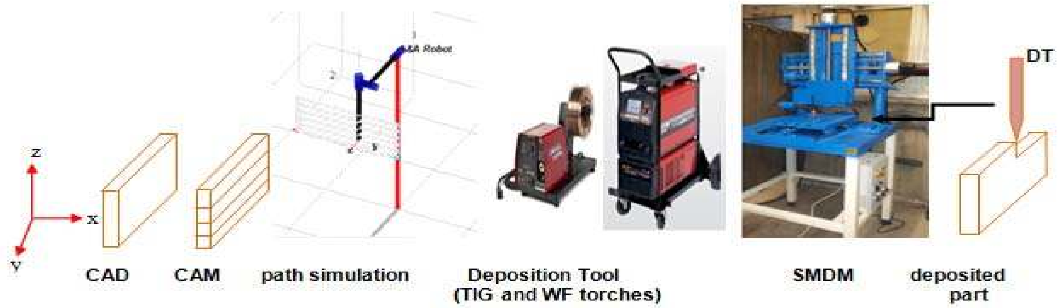

Figure 1.1 Part manufacturing steps in the TW-SMD manufacturing method.

1.2. Problem Statement

Nowadays, there has been a growing interest in the use of RMM for producing fully dense metallic near net shaped components for modern manufacturing industries, such as automotive and aerospace industries. The main advantages of the tungsten inert gas welding shaped metal deposition (TW-SMD) technique are a reduction of production cost by lowering the wasted material and shortening the tooling time. This need to develop basic understanding or process characteristics of TW-SMD, regarding deposition stability and formation of defects, through an experimental study, using a high grade of stainless steel. So that for making the high-quality deposition parts and raising the product efficiency it is necessary to optimize the welding operational parameters and this is being usually associated with the selection of the most suitable welding conditions and deposition consumable compositions. The optimality criterion requires possessing the deposited components high properties such as ultimate tensile strength, ductility, hardness, and soundness. The main challenges in this technology are the process stability, the effect of cumulative heat during adding the successive layers on the grain growth of the deposited parts, and also the effect of cumulative heat on phases formation and other carbides. Anisotropy phenomenon of mechanical properties as well as common weld defects such as lack of penetration (lack of fusion), poor profile, weld humping and internal cracks and porosities. Additionally, the effects of path patterns used on the outside part roughness and solid part filling quality

1.3. Research Aims and Objectives

1.3.1. Research Aims

The aim of this research study is to investigate the control of the developed SMD system, understanding the deposition process of the TW-SMD system by studying the conventional and pulsed TIG technology. So the main aim is to:

1. Design, construct, and control of a computer aided metal deposition machine (CAMDM). It is a workshop size machine which is integrated with TIG welding machine and wire feeding mechanism to be able to study the whole process parameters and to produce net or near-net-shaped components.
2. Develop an SMD system, which is flexible to alter and edit the operation program as well as it should let controlling and tuning the process parameters during the deposition process by using an open- source simple microcontroller board in the CAMDM system.
3. Develop a basic understanding or process characteristics of Pulsed and non-pulsed TIG welding–wire deposition, regarding deposition stability and formation of defects, through an experimental study using different materials such as high grade of stainless steel, and grades of steel,
4. Investigate the process characterization by analyzing the influence of the main parameters on the bead geometry and deposit quality.

1.3.2. Objectives of the Thesis

i. To study the deposition path pattern of the TW-SMD process and demonstrate the CAMDM system capabilities and limitations.

ii. To study the relationship between the process parameters and weld bead geometry in single and multilayer deposits.

iii. To establish the process window for the main parameters of the process.

iv. To investigate the benefit of PCSMD method compared to CCSMD technique.

V. To evaluate the process behavior and stability CCSMD and PCSMD methods for producing SS308LSi components.

VI. To characterize microstructures and determine mechanical properties of the deposited SS308LSi stainless steels components. This part consists of:

a. Macro- and Microstructural examinations of the samples prepared by both CCSMD and PCSMD processes.

b. Determination of components' hardness for both CCSMD and PCSMD processes.

c. Investigation the tensile properties of the specimens prepared by CCSMD and PCSMD processes.

1.4. Scope of the Thesis:

Based on the objectives the research scope is as follows:

- Area: this research work addresses the designing, constructing, and controlling of a new TW-SMD system. Using the developed setup to study the process characterization by analyzing the influence of the main parameters on the bead geometry. In this work, the TW-SMD process is investigated using a cold wire of austenitic stainless steel Type 308LSi as a deposition material and the process is modeled and research is carried out to determine stable parameter windows for deposition different austenitic stainless steel components and discover the mechanical and microstructural properties of the resulting parts. The research includes the conventional process using continuous current (CCSMD) and for the first time the pulsed current SMD (PCSMD).
- Literature survey: there is a concentration on SMD types and applications, control system used, path planning strategies, microstructure and mechanical properties of components manufacturing using CCSMD and PCSMD techniques, and grain refinement in SMD processes.
- The design of experiment: a suitable design of the experiment that proposed in this thesis is developed to study and analysis the effects of the main process parameters on bead geometries and process stability and to establish the process window.

- Experimental work: the experiments that carried out in this thesis are undertaken on a cold metal wire machine integrated with TIG welding machine and the computer aided metal deposition machine.
- The experimental work is involved also the description in detail about the effects of the pulse frequency on the microstructure, morphology, and mechanical properties of TW-SMD manufacturing using AISI 308LSi ASS. Anisotropy of the manufactured components is also investigated.
- Case Study: A case study that performed in this thesis is involved a 3D-part designing, modeling, depositing, and machining to final shape. Calculation of the buy-to-fly ratio and time of production is calculated in a comparative study.
- The workpiece sizes: the system that developed in this thesis does not use for manufacturing of large components since the designed work envelope is about 400 mm^3

1.5. Research Structure

The study was through planned to follow the workflow detailed in Figure 1.2, which was prepared according to the research aims and objectives presented in this chapter.

1.6. Overview of Thesis

The overall structure of this thesis is comprised of seven main chapters. This overview describes a brief idea of each chapter of this thesis.

Chapter 1

This chapter gives insight into the general research introductory, overviews the aim and objectives of the thesis, research scope and study structure

Chapter 2

This chapter summarizes the state of the art of the related area of this research where particular attention is given to the following subjects:

- Additive manufacturing classification and applications
- SMD description and classification.
- SMD Control processes and path planning strategies.
- Microstructure and mechanical properties of components manufacturing using CCSMD and PCSMD techniques.

- Grain refinement in SMD processes.
- Bead geometries in SMD process.
- Weld bead imperfection and defects.

Chapter 3

This chapter describes with details the experimental setup design and constructing. It is also including the materials used and procedures for measurements and testing.

Chapter 4

This chapter presents the findings of the process control model development of single and multilayer deposits in austenitic stainless steel for both CCSMD and PCSMD processes. These results include also the process window, path planning strategies, and testing results.

Chapter 5

This chapter summarizes the overall discussion of the results presented in chapter 4, focusing on the effects of the main parameters on the process stability, bead geometry, and surface quality. Additionally, this chapter discusses the mechanical and metallographic results.

Chapter 6

This chapter gives a brief summary of the papers appended in this thesis.

Chapter 7

This chapter summarizes the important findings and conclusions of this thesis and identifies some recommendations for the future work that can be undertaken.

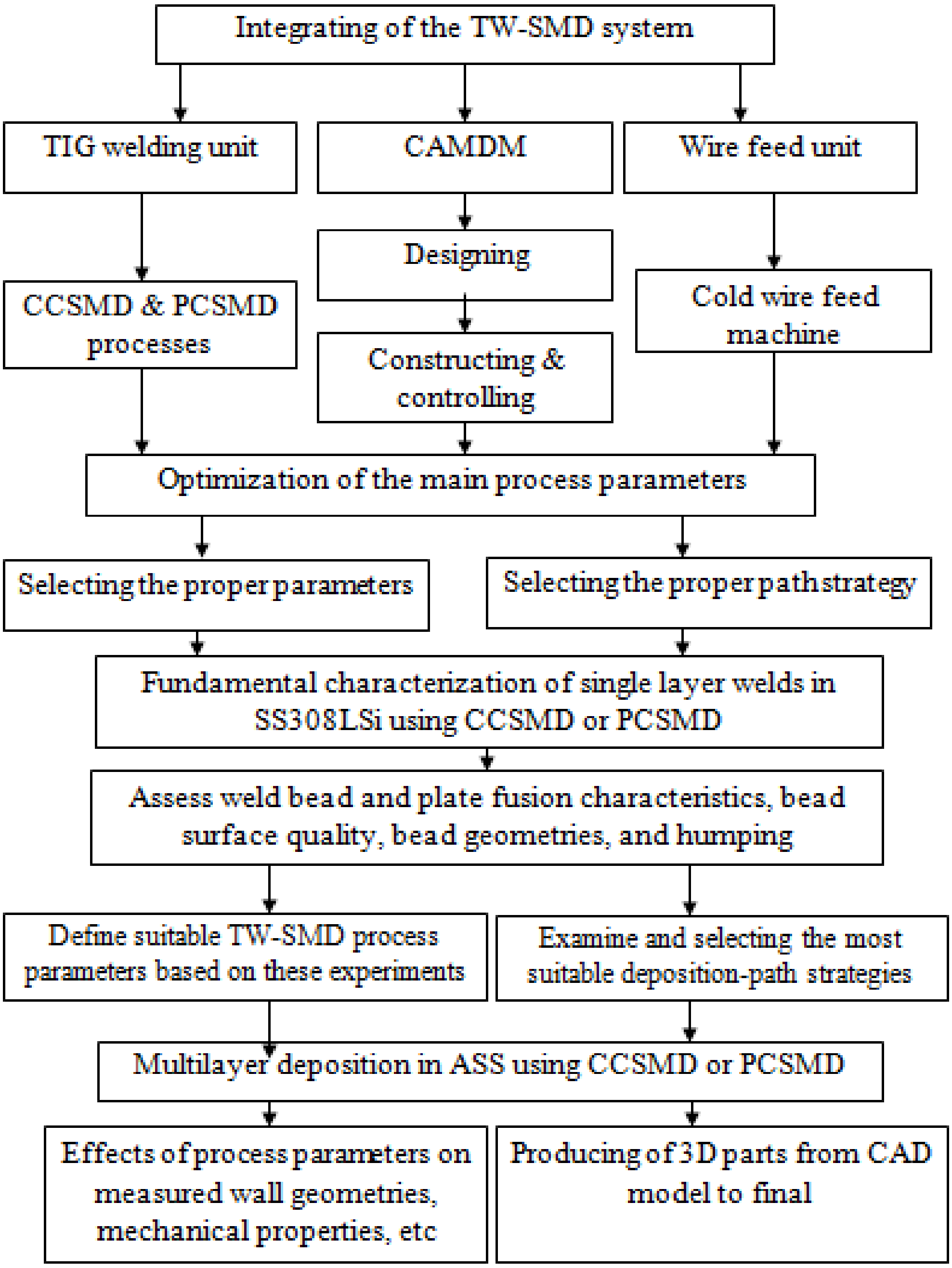

Figure 1.2. Research workflow

CHAPTER 2

LITERATURE REVIEW

2.1 Additive Layered Manufacturing

Additive manufacturing (AM) is an innovative net or near-net-shape manufacturing technology used to produce final solid objects by depositing successive layers of material (powder or wires) by melting the musing a focused heat source resulted from an electron beam, laser beam, plasma or electric arc welding [1, 2, 3]. AM is a novel manufacturing technology, which was developed in 1987 by 3D systems company in the US using stereolithography (SLA) technology [4]. It is well known that there are many difficulties in machining of some materials such as titanium, nickel alloys etc. through traditional manufacturing methods. Therefore, there is a need for alternative manufacturing technique that will offset most of these difficulties. Candidate manufacturing method is the AM technology where there is no individual tooling required. Thus, AM is an ideal technology for rapid manufacturing [5, 6].

In 1990, this technology emerged in Europe and now it is pioneered in the same continent [4]. Several new AM technologies were established and more new commercial systems introduced to the market after 1991 [7]. AM technology basically offers a significant reduction in lead time, cost, and waste material in the form of machining chips and less toxic waste from cutting fluid [2, 4]. As AM is a comparably young Testing and Materials (ASTM) in cooperation with the American Society of Mechanical Engineering (ASME) started the development of AM standardization procedure [1]. According to the ASTM F2792.429494-1 standard, AM is a process of joining materials to make objects from 3D model data usually layer upon layer, as opposed to subtractive manufacturing methodologies, such traditional machining [8]. Similarly, VDI 3404 standard, AM is the manufacturing process in which the workpiece is built up in successive units or layers [9]. Additive manufacturing technologies are used in different of industries such medical, automotive, aerospace, construction and tooling industry [10].

The related industries benefit from applying this technology by shortening the production time, manufacturing complex geometries with internal features, producing of consolidated parts instead of several sub-parts, reducing material consumption and manufacturing costs. AM involves a number of steps that move from the virtual CAD description to the physical resultant part. The generic AM processes involves the following steps [10]:

- A computer-aided design (CAD)
- Conversion to standard tessellation language (STL)
- File transfer and manipulation
- Machine setup and job preparation
- Build
- Removal and clean-up
- Post-processing

AM processes can be grouped into three categories according to feedstock material types: (I) powder bed processes, (II) powder fed processes, and (III) wire feed processes [11]. Table 2.1 shows metal additive manufacturing classification based on the heat source and material additive method, and also shows a comparison of the characteristics of these processes [2, 12-20]. But the most suitable classification of AM techniques can be done according to the type of the heat sources and additive materials. Figure 2.1 depicts the classification of various AM processes with the combination of different heat sources with different material feeding methods.

There are more than twenty different AM techniques have been developed until now and they emerged to the industry to produce prototypes and net shaped products. The most attractive feature of AM is thus flexibilities in designing of products [21]. AM gives an ability to the designers to adopt more nature based inspiration to their design since AM gives ease of manufacture capability [21]. In metal industry, AM processes can easily be used to fabricate large parts with relatively high complexities. In fact, manufacturing of some complex shapes and geometric features is extremely difficult using traditional methods (milling, turning, forging etc.).

Table 2. 1. Classification and comparison of additive manufacturing processes.

		Method of layering	Examples	Characteristics				
				Resolution	Deposition rate	Surface finish	Power efficiency	Cost
Fusion	Laser Beam	Powder-bed	DMLS, SLS, SLM	++	-	+++	-	-
		Powder-blown	LENS, LAM, DLD, LMDS, LMD	+	++	+	-	0
		Wire-feed	SMD- DMD	0	++	0	-	-
	Electron Beam	Powder-bed	EBSM, EBM, EBAM	0	+	+	++	-
		Wire-feed	SMD-EBF³	-	++	0	++	+
	Arc Beam	Wire-feed	SMD-WAAM	-	+++	-	++	+++
Solid -State	High frequency vibration	Metallic foils	UC					
	Laser		Cold consolidation					
	Impact (explosive) energy	Plates, strips, sheets	SLAM					

++ = excellent; + = good; 0 = neutral; - = negative

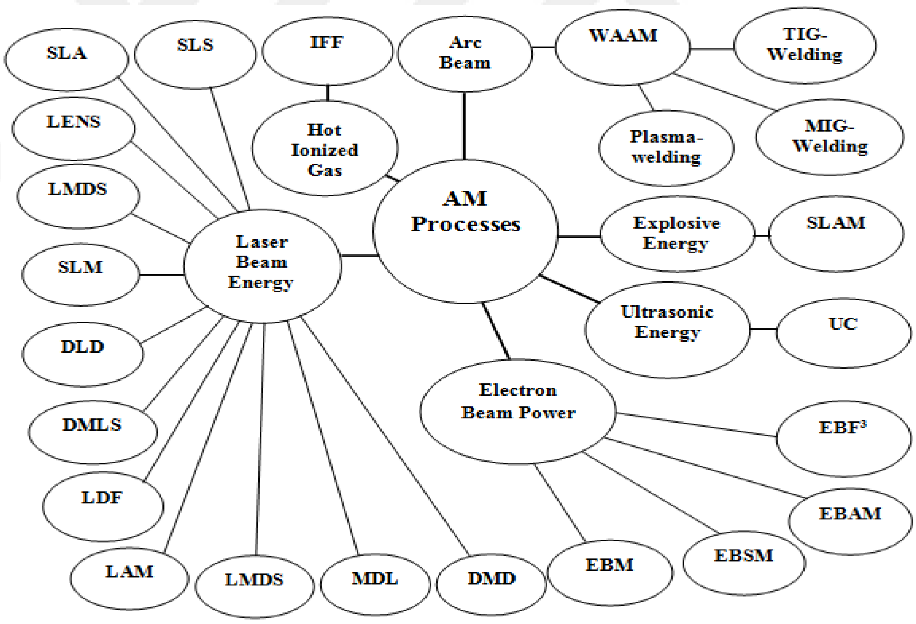

Figure 2. 1. Classification of metallic AM processes

AM makes it possible to produce parts or batch of parts with high complexities without tooling. Therefore, AM techniques have been preferred in many areas. Figure 2.2 highlights the current AM applications in different fields.

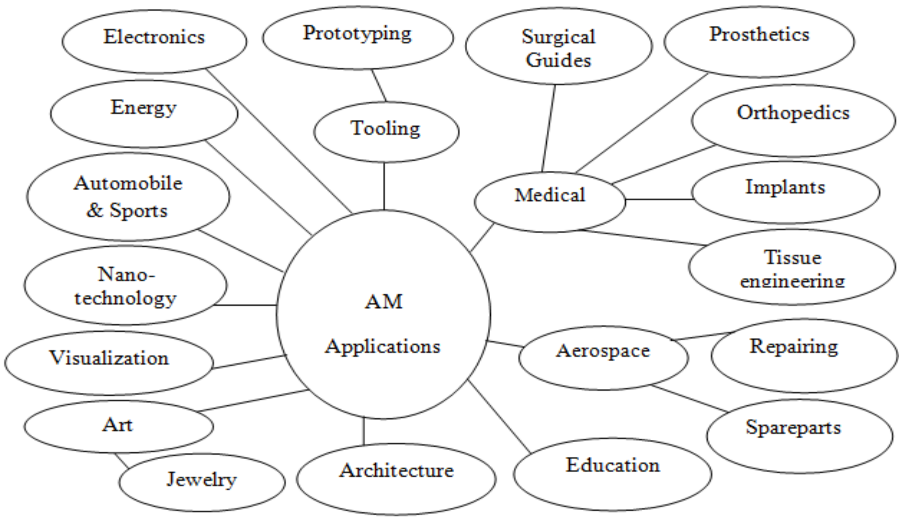

Figure 2. 2 AM applications in different industrial areas

In more recent years, the capability of producing fully functional metal parts was interested using rapid manufacturing in order to fabricate complex metal components with the required accuracy. This was done through converting traditional rapid prototyping equipment into robust freeform fabrication systems to produce the metal parts from powders or metal wires. This concept is currently named as additive manufacturing [22]. The metal additive manufacturing (MAM) can be mainly classified in tow main categories according to the physical state of the raw materials utilized in processing: powders (using blown powder or powder-bed) based and wire-feed based techniques [11]. The main heating sources in powder based MAM machines are electron beam and laser beam. Extremely small and highly complex parts can be produced or remanufactured using fine metal powders enabling manufacturing or adding functionality to existing components [22].

Laser engineered net shaping (LENS) technique was applied by Griffith [13, 23] to fabricate fully dense components with material properties that are similar to that of wrought materials [24-26]. Laser metal deposition (LMD) is another technique using powder metal to fabricate parts in layer-wise fashion. [14, 16, 27-30].

The selective laser sintering (SLS) technique was used by some of the researchers to fabricate metal solid parts in ALM technology [31-34]. Rieder et al. [35] used selective laser melting (SLM) to build components of metal powder. These systems need special attention during the processing, they require environmental chamber with high temperature and at controlled atmosphere such as argon (Ar) gas, to prevent contamination. Furthermore, they need to pre-heat the powder-bed to reduce the thermal distortion and to improve the consolidation of the layers. The main difficulties and drawbacks in powder base systems are summarized as follows [22, 36]:

- Deposition rates are relatively low with limited sizes.
- High susceptibility to contamination by gasses, affect the corrosion and mechanical properties.
- The powder specifications such as particle shape, particle size distribution, powder flow, and alloy capability.
- Recycling of the metal powders is difficult, especially when different powders are mixed during the process.
- Gas porosities and lack of fusion in these systems lead to the integrity of the manufacturing parts.
- Post-processing is required to improve the component properties.
- High investment is required for these systems.
- Energy efficiency is relatively low for laser systems, because of high beam reflection.

In recent years more efforts were put into the possibility of using wire feed and powder together for reducing the main problems and difficulties in the powder systems.

Syed et al. [37, 38] studied a combined process, wire and powder were delivered to the melt pool simultaneously using laser energy. They showed that the overall mass deposition rate and efficiency could be increased and less porosity obtained.

More recently, Brandl et al. [39] carried out a comparative study using wire-feed and powder-bed Ti6Al4V. They proved that the wire-feed samples conducted high mechanical properties and low porosities and contaminations than the powder-bed samples.

In more recent years much of studies were carried out in the AM field, which focused on using metallic wire feedstock as a deposition material and using a laser beam, electron beam, or arc beam as a heating source for melting the metal wires and depositing the shaped metal parts. In the mid-1990s further progress was made at welding engineering research center (WERC) in Sheffield University is the shaped metal deposition (SMD) technique, which was patented by Roll-Royce [40].

Nowadays, the term SMD refers to all the processes which use metal wire-feed as a deposition material associated with one of the main energy sources such as laser beam, electron beam, and electric arc beam.

2.2. SMD Process Description, Challenges, and Applications

SMD process is performed by externally feeding a cold wire of metallic material into weld pool layer by layer in order to obtain a designed component shape [40, 41]. SMD can be considered as a net or near net shaped part production technique compared to the modern additive layer manufacturing techniques. This process can be used especially for rapid manufacturing of metal components where no additional tooling is available. SMD method could be most beneficial for the components produced from expensive alloys such as Ti-6Al-4V, Inconel 718, TiAl, high grade of stainless steels, etc. [42-45]. SMD technology produces fully dense parts and promises great advantages of using any material which can be welded particularly difficult-to-machine and formed alloys. However, it should be clear that the microstructure of the SMD components differs from those prepared with conventional techniques since SMD process repeatedly subjects high temperatures and high cooling rates to the deposited components and this may lead to anisotropic phenomenon [46-48]. SMD components may have some superior properties compared to the casting components with the same design. In fact castings have a weight penalty due to their less consistent mechanical properties while SMD components have internal potentials to outperform polycrystalline castings of the same chemistry due to the more consistent solidification conditions made possible by the deposition process as comparing to the solidification conditions of the casting processes which results in the ultimate strength and strain values of SMD components are slightly higher than that of the as-cast material [49, 50].

Mechanical properties of a component produced via an SMD process (WAAM or DMD) vary greatly depending on the deposition parameters, such as arc plasma energy, speed, wire feeding etc. Generally, mechanical properties of the deposited parts are competitive to cast and even wrought material properties and they may possess some desirable properties appropriate for aerospace industries [51].

In general, SMD group of AM processes offer high flexibilities and cost effective alternatives to conventional manufacturing methods for both large production runs and one-off prototype creations [52, 53]. It is expected that the SMD process has a major impact on design changes and production of large dense parts and it can also be considered as a repair method to be used for high-performance alloy components such as metal dies across a wide market base [54]. In addition, this process promises to produce large-scale and high-quality parts with very high deposition rates [55, 56]. SMD techniques have been presented to the aerospace manufacturing industry as a unique low-cost solution for large structural component manufacture due to their high deposition rate and efficiency. These techniques can significantly improve product development time, capital investment, and BTF ratios [22]. The main advantages and limitations of SMD methods would be summarized as:

- Deposition process using WAAM techniques can be done using chamber or outside chamber and there is no need for vacuum environment such as in EBM process [57, 58].
- It is suitable for full automation [41-43, 55, 59-61].
- High deposition rates, low-cost parts, and less time of production due to less cooling time [22-41]
- It is able to manufacture large structural components, especially for aerospace and defense industry components [22, 45].
- It has been gaining considerable interest in the recent years due to its high deposition rate and higher efficiency [22, 62].
- It always needs further machining processes to get a better surface finish [7].
- It is limited to mass production [63].
- The WAAM techniques cannot be used to produce small components and very intricate part geometries [2].

2.3. Classification of SMD Methods

AM processes are generally categorized based on the type of heat sources and the material supply. A typical SMD system integrates four basic units: (1) deposition path motion unit, (2) melting source unit, (3) material supply unit, and (4) control system and software unit which enables depositing materials according to the defined path. Figure 2.3 shows the main units in the SMD system, and also show a new classification for the SMD methods according to the heat source used for melting the metal wire which is separately fed into the melting pool in either hot or cold state. Such systems are controlled via either robot, CNC machines, manipulator arms as well as gantry type routers. Currently, two typical heat sources have been used in SMD systems, i.e. electric arc and power beam obtained by laser and electron beam. These heat sources are used for melting the supplied material in the form of wire. Although powder material supply type of AM techniques is popular, wire-based SMD processes are gaining more favor because of their higher deposition rates and higher efficiencies compared to others [22]. In the following sections, the most used SMD techniques are briefly introduced: (1) SMD using an electron beam heat source (EBF^3), (2) Laser Beam heat source (DMD-Laser wire feed), and (3) In more detailed the SMD using a Wire and Arc Additive Manufacturing (WAAM).

2.3.1 SMD Using Electron Beam Heat Source (EBF^3)

Electron beam freeform fabrication (EBF^3) process was firstly introduced by NASA Langley research center [64, 65]. This process uses electron beam as a melting source and a wire feedstock which is fed into the melt pool in a vacuum environment. It uses engineering alloys such as Ti-6Al-4V and Al-2219 in standard wire form. Figure 2.4 (a) shows the shapes of the components produced at NASA Langley [2, 64]. The EBF^3 system consists of an electron-beam gun, wire feeder, and positioning system enclosed in and vacuum chamber as shown in Figure 2.4(b). This process uses a wire-feed system to deposit good quality parts that are better than cast and similar to wrought materials [22, 64]. The work [66] introduces an acoustic emission (AE) technique as a non-destructive testing method that can be used as an online monitoring tool for finding place and characterization of different types of active defects during any process especially for electron beam welding defects during EBW of titanium alloys to get the information about nature and location of the defect formed. Taminger et al. [67] used EBF^3 for feasible solutions to the problems on deposition rate, process efficiency, and material compatibility for insertion into the production environment.

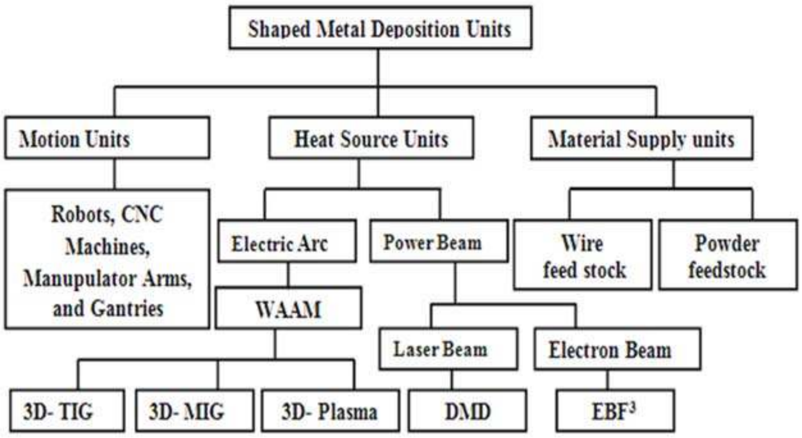

Figure 2. 3. Shaped Metal Deposition Units

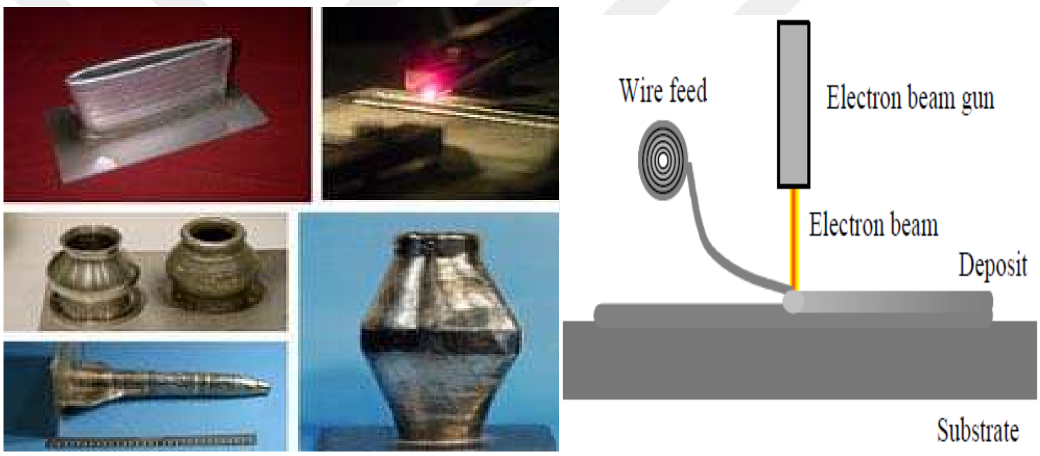

(a) (b)

Figure 2. 4 (a) Some typical components produced using EBF3 and, (b) schematic of EBF3 system components [2, 64, 67]

2.3.2. SMD Using a Laser Beam Heat Source (DMD –Laser Wire Feed)

Lasers can be categorized according to different criteria such as the pumping method or operation mode, but the most common classification is based on the type of active medium used to active the lasing action. So the lasers are classified as Gas, solid-state, semiconductor or diode, liquid, fibre and Free-electron X-ray [68].

The gas laser provides various practical advantages such as gasses are relatively inexpensive and there is no practical limit in the volume of the gas that is required and there is no risk of damaging the gain medium due to thermally induced deformation [69]. Laser metal deposition can be defined as a process in which a metal is overlaid on another using a laser beam. A high-power laser beam is focused on the surface of a substrate, where the intense energy is absorbed and a melt pool is generated. An external material, commonly in the form of powder or wire is then fed to the melt pool, where it melts and adds to the volume of the pool [70]. Four different methods can be used for material delivery in laser metal deposition (LMD) [70]: (1) Pre-placed powder (powder-bed), (2) Paste (powder-binder mixture paste feed), (3) Blown powder (injection powder), (4) Wire feeding method.

DMD technique works by introducing wire feedstock into the melt pool zone, which results from the heat generated by the focused laser beam [2, 51]. Figure 2.5 shows a schematic drawing of the process, top and side view images of the real process, and some of the parts fabricated using this technique. Some of the processes such as SLDM, SLS, and DLD, which use the laser beam as a heat source and powders as filler materials face major practical difficulties during depositing parts. Some of the drawbacks are [2, 18, 22, 37, 71, 72]:

- The lower capture efficiency of the metal powders.
- Some of the gases (e.g. O_2, H_2, N_2, CO) and other impurities may contaminate the metal powder feedstock. This leads to poor quality of the deposited parts (poor overhung surfaces).
- Existing of porosities and lack of fusion problems.
- Low laser energy efficiency, since less than 10% of the plug input energy is converted to beam energy.
- Lower deposition rates and builds volumes of limited size.

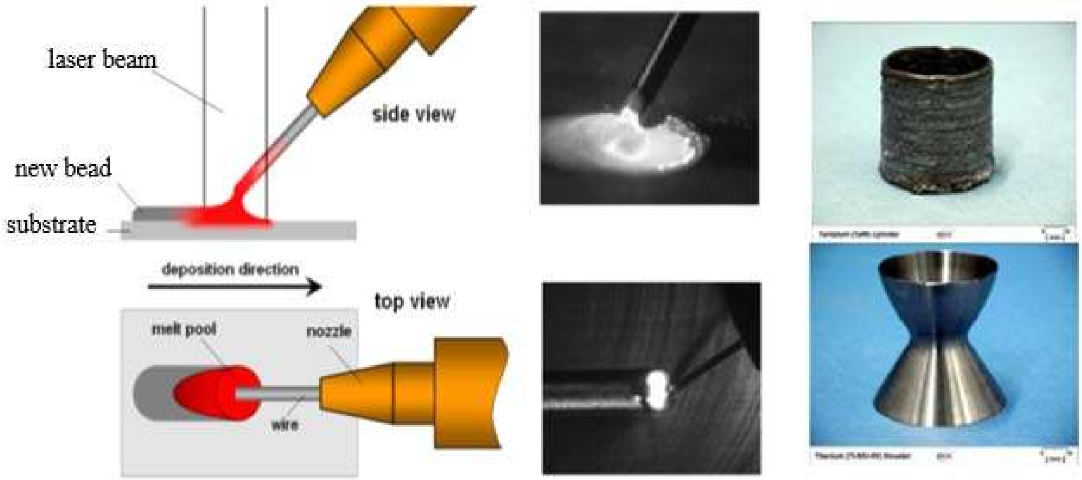

(a) (b) (c)

Figure 2.5 (a) Schematic drawing of the process; (b) top and side view images of real process; and (c) Exemplary components: Ta-20W cylinder (as-built surface) [55].

In the last decade, a considerable amount of attempts has been conducted of using laser-wire feedstock combination in order to overcome the mentioned drawbacks [55]. Advantages of this process are higher deposition rates in depositing large components, more stable melt pool results with better control of the weld pool shape, no porosity problems, and metal wires are always cheaper than metal powders [37, 55, 62] Laser additive manufacturing technology is mainly preferred in the manufacturing of complex geometry parts where the productivity and the amount of the parts are of concern [73].

An experimental study of laser and wire feedstock system through the studying of hardness and dimensions of single beads of Ti-6Al-4V filler wire was conducted by the work of Brandl et al. [74]. It was shown that the mechanical properties of SMD components are greatly dependent on the microstructure, which is in turn greatly dependent on the thermal history and certainly process parameters. Syed et al. [75] presented a study that compared the wire and powder feed system indirect laser deposition process. The authors showed that the wire based laser process is gaining more acceptances due to higher efficiency and higher deposition rates compared to the powder feed system. Brandl et al. [51] used two different SMD methods: DMD using Nd:YAG laser beam + wire feedstock system and the other is WAAM using 3D-TIG welding + wire feedstock system. They aimed to increase the knowledge regarding material properties in one system Ti-6Al-4V alloy as a deposition material with respect to aerospace material specifications. Mechanical properties, such as static tension and high cycle fatigue with heat treatment were investigated. The results showed that the specimens fabricated by the SMD techniques could achieve static tensile properties similar to the material specifications AMS 4928 of wrought material and/or ASTM F1108 of the cast material. On the other hand Gong et al. [76] investigated the effect of existing defects in fatigue performance of Ti-6Al-4V samples in an as-built surface finish condition. They also showed that the defects play a serious role in reducing fatigue properties and fatigue life of specimens.

More recently, some of the studies focused on the investigation of microstructure and mechanical properties of single wall multi-layer Ti-6Al-4V structures deposited with DMD techniques. The microstructure examinations denoted that long columnar grains were found growing parallel to the build direction across the multiple layers. The solid areas can be hardened by dislocation or boundary hardening [74, 77, 78]. Flexible techniques were used, which allow cladding consumables deposited in either wire or powder form fed into the molten pool using DMD techniques. These techniques can be used on new or worn components and are typically used to rebuild worn or damaged surfaces and to hard-face wear, corrosion, oxidation susceptible materials, or depositing super alloys on turbine blades and valve seats [79, 80].

In the study of Strano et al. [81] the authors submitted an experimental work consists of developing a model for part surface quality prediction and model for simultaneously energy consumption prediction. Pareto set was used to represent the best compromises between the surface roughness and energy saving objectives. In the study of Bakhadyrov et al. [82], a machine vision setup for surface voids detection, was shown. It can be used for surface quality inspection of parts built with layered manufacturing (LM) techniques. The work of Jin et al.[83] used an adaptive process to deal with different intricate product models by introducing NURBS to represent the contours of the sliced layers instead of STL files. The authors studied a series of optimization algorithms and strategies to optimize the toolpath generation. A number of case studies have been tested for example an ear model and a bone model. They showed that by using this optimal strategy, the average reduction of the building time is 16 seconds for a single layer in the ear model and 46 seconds for a single layer in the bone model.

A temperature measurement system was developed by Hua et al. [84] since the molten pool temperature is an important controlling parameter during a laser rapid forming process which immediately governs metallurgical quality and forming accuracy of the part. The thermal monitoring techniques were described and the influences of the processing parameters on the thermal behavior of the molten pool were also investigated [23, 84].

2.3.3 SMD Using Wire and Arc Additive Manufacturing (WAAM)

Wire and arc additive manufacturing (WAAM) represents a turning point in the metal AM technologies since it combines the electric arc heating sources with a metallic wire feeding system to create a 3D metallic parts by depositing beads of weld metal in a layer by layer fashion. WAAM technique can be sub-grouped into three major processes based on the type of electric arc torch used to melt the filler wire as aforementioned in Figure 2.3: (i) 3D-TIG welding (TIG or GTAW + wire feedstock) as shown in Figure 2.6, (ii) 3D-MIG welding (MIG or GMAW + wire feedstock) and (iii) 3D-Plasma Welding (Plasma + wire feedstock).

The roots of wire added AM processes went back to 1920s patented by Baker [85], which stated a new method for producing 3D metallic parts in successive layers using manual arc welding. In the work of Shockey [86], a WAAM technique was investigated in facing and cladding applications for improving the lifetime of components subjected to abrasive wear. White [87] used wire + arc welding method to repair worn surfaces of large metal pressure rollers. The development of shape welding (SW) technology was performed later in many experimental works. In the beginning of the 1980s, some of the shape welded products (rotors and cylindrical courses) were conducted [88]. In the study of Schmidt et al. [89], the authors used SW process to build large reactor coolant components for up to 10.5 m in length and 5.8 m in diameter which showed the capabilities and successful applications of WAAM process. At the beginning of the1990s WAAM technology gained a significant importance in the Welding Engineering Research Centre of Cranfield University. The works of Ribeiro and Norish et al. [90, 91] introduced a new fabrication approach by developing a manufacturing system for Rolls-Royce plc. Their system was capable of creating solid metal parts directly from the CAD models.

Spencer et al. [92] studied the surface roughness, microstructural effects, and bead geometries for samples produced by the MIG-SMD system and the effect of heat built-

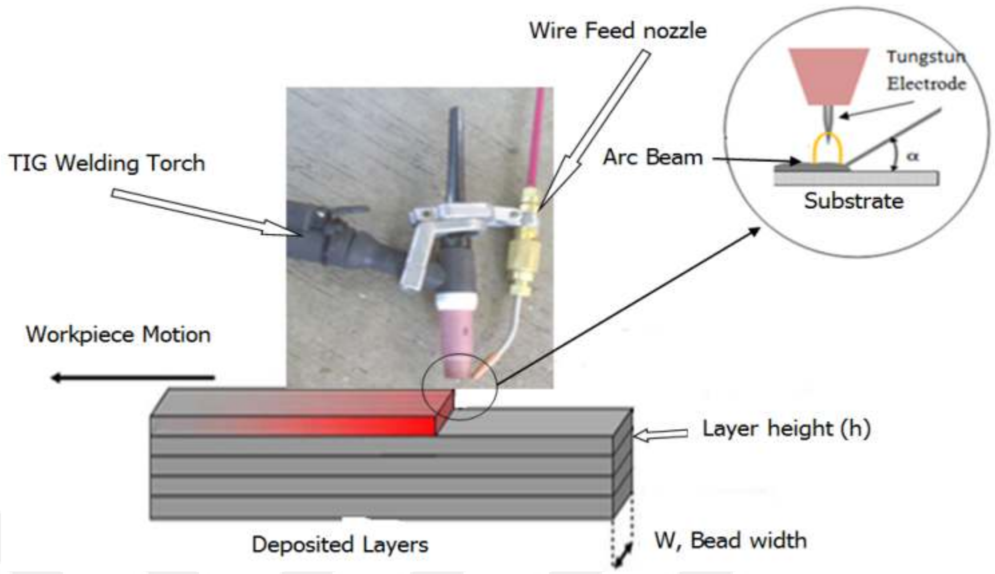

Figure 2. 6 Deposition process using the 3D-TIG method.

up during deposition. In more recent years, TIG and wire SMD (TW-SMD) process was further developed by investigating the additive shaped metal deposition process and it was practically developed in a European project entitled as Rapid Production of Large Aerospace Components (RAPOLAC) [40]. RAPOLAC was initiated in 2005 by Advanced Manufacturing Research Centre (AMRC) at The University of Sheffield in collaboration with seven partners from across Europe. Main aims of the project were to develop the SMD process based on cold wire fed GTAW, build large parts with a variety of aerospace materials, material properties control, and process parameters optimization [40]. The further developments that were made within RAPOLAC project have been recently presented by the work of Escobar-Palafox et al. [93]. They supposed that deposition condition is attained faster with closed-loop control than in manually deposited parts, and the surface conditions of the produced parts can also be considerably improved in quality. Martina et al. [94] investigated the feasibility of using Plasma Wire Deposition (PWD) in AM technology. They used 1.2 mm Ti-6Al-4V material to deposit and measure walls of 140 mm long. Superalloys such as Inconel 718 was used as a deposition material to fabricate components using welding based-SMD technique [49, 50]. They investigated the mechanical properties of the manufactured parts and demonstrated that the ultimate strength is compared to the wrought material and slightly higher than of as-cast one. Skiba et al. [45] reported for the first time use filler wire of stainless steel of grade 308 for fabricating round components using the TW-SMD technique.

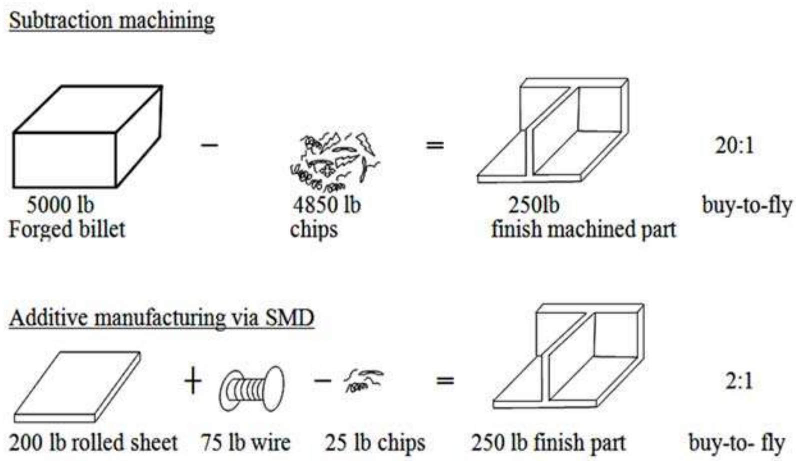

Figure 2. 7 Comparison of traditional machining process vs AM process in terms of BTF

SMD can help significantly reduce high Buy-To-Fly (BTF) ratios of the cast, forged, and machined parts in the aerospace industry. BTF ratio reflects the material efficiency of manufactured components and it is often referred by the aerospace community to establish an amount of material needed to purchase rather than manufacture final "flying" part. BTF ratio is the weight ratio between the raw material used for a component and the weight of the component itself [2, 22]. Traditional machining methods typically produce components with BTF ratios of 5:1, but sometimes greater than 20:1 due to a large amount of waste and difficult-to-recycle material [95]. Figure 2.7 shows an example of a comparison of BTF ratio between traditional and WT-SMD technology. The finished part has a weight of 250 Ib and to machine from a forged billet would require a starting billet weight of 5000Ib which gives a BTF ratio of over 20. This method is extremely wasteful in terms of material. In contrast, using some processes in AM technology the substrate has a weight of 200 lb as a rolled sheet and 75lb of wire which is added with 25 lb machined away to get the final profile. This gives BTF ratio near to 2 and saving materials of 4825 lb. The SMD technique helps to effectively minimize the amount of material required for the final shape of the component.

2.4 Control of SMD Process

2.4.1 Monitoring and sensing technologies

This section presents the literature concerning with development of the closed loop, sensing, real-time and other control systems. These systems are used for controlling the deposition process and improving the manufactured part quality. It was found that the surface quality of the deposited components can be improved by using temperature control of the part at the starting point of each pass [40]. Further investigations were done in the Robotics Institute and the Engineering Design Research Centre of Carnegie Mellon University. Robotic deposition systems were used in several thermal deposition processes in order to direct fabricate prototype metal shapes [60]. In RAPOLAC, the fully automatic welding system was improved by a closed-loop welding controller, which uses image processing and a video feedback control. The working variables have been identified in four fundamental key parameters; such as welding current, wire feed speed (WFS), travel speed (TV), and the thickness of each layer (the step height between two subsequent layers SH) [43]. For the frame of the RAPOLAC European project, further studies were investigated for the control of SMD systems. The proposed system aimed to show the software interface of an experimental system adopted to investigate control strategies for rapid manufacturing of aerospace components [41, 42, and 59].

Wang et al. [96] offered a WAAM system based on a 3D-TIG technique for producing shaped parts made of aluminum alloys as Al-5356 and Al-4043. In their study, they used on-line monitoring and control systems for controlling process parameters in order to achieve good-quality parts. Zhang et.al. [60] employed STL files for slicing and planning RP system using the 3D-MIG technique. A CAD surface or a solid model in the standard of IGES format was used to facilitate the controlling on the part to be deposited. It was shown that the control of the deposition parameters helps to control of ignition, minimize ignition times, and crater filling control. Figure 2.8 shows the effects of the application of the control system in start and end portions [97]. It was shown that the control of the size, flux and thermal states to the droplet effect on improving the quality of the deposition. Besides an adaptive robotic control (TIG-welding) SMD, the process was developed by Ding and others [98] in order to enhance the weld quality with full penetration of Al-depositions. Another WAAM technology, which was provided by ready-to-use additive manufacturing (RUAM) project opened new routes to fabricating large parts. This work includes a robotic

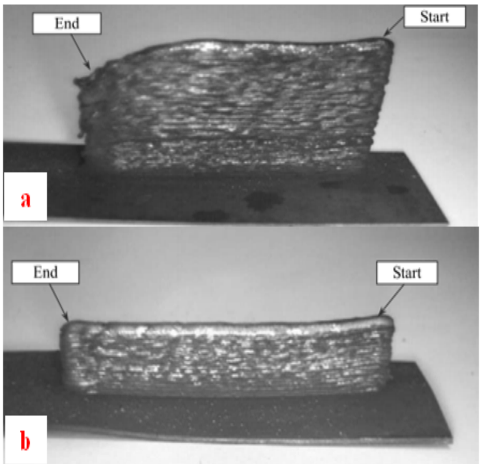

Figure 2. 8. Effects of the control system on the deposit quality (a) without control system the error is significant; (b) with a control system, the error is eliminated [60, 97].

welding SMD system. The researchers improved the process by using modern technologies such as cold metal transfer process and plasma welding [56, 99]. [100] applied a neural network and second regression analysis for predicting bead geometry of depositing parts, which was manufactured using a robotic SMD process representing 3D-TIG welding technique. The main findings of their study were that employing this analysis model can effectively be used to predict the desired bead geometry with high precision. Tėllez [101] used a fiber laser system to deposit a solid metal wire of SS308Lsi and Ti6Al4V. He investigated the effects of process parameters on the process and on the deposited bead geometry. A closed loop temperature control system was developed. The main finding of his work was that the developed system provides a means to perform stable and smooth wire metal deposition, achieving good mechanical properties. Heralić [55] used the laser deposition process using wire as an additive material. In the work, the first step was to develop a basic understanding of the process characteristics of the used system, regarding deposition stability and formation of defects. Control strategies were developed, such that they enable automatic control of the deposition process with process stability and good geometrical fit of the production parts.

2.4.2 Deposition Path Machine Control

A deposition path machine plays the major role in the SMD capabilities; therefore, a large body of the literature was performed using complicated systems of 6-axis robots linked to a 2-axis rotary table.

The TW-SMD system requires designing and developing integrated systems, which are able to reduce the time-consuming and boring task of the deposition process. In the literature, the works [40, 47] used complex systems to produce Ti-6Al-4V components with two geometries, namely cylindrical part and straight walls. They fabricated around parts using rotating table and holding the torch as fixed while the wall components were done using the robot's movements. Some studies [47, 48, 51] used the same complicated systems to deposit round and square Ti-6Al-4V components. Whereas, some studies used robotic systems with WAAM to produce walls, squares, and round components of SS308 alloy [45, 60]. Some of the studies developed pre-programmed robot systems for WAAM techniques [31, 41, 42, 56, 59, 74, 98, 100, 102]. Besides some of them have used special mechanical systems such as 4-axis CNC milling machines or 3D- positioned CNC machines [43, 44, 61, 97].

In the literature, it was experienced that the integrated systems used are really complicated and limited to special codes and machine languages, which mean that these systems are considered as closed systems used for generating the deposition paths. Actual robot paths are directly calculated from the CAD geometry. There are some of the difficulties, which may appear during the deposition process such as producing wall crossing due to the weld beads overlap at the crossing point. Most of the existing systems begin with a model created based on a CAD packages e.g. CAD surface or solid modeler to generate an output file such as STL file. Subsequently, the STL file is sliced using a special format into uniform layers, and afterward, these layers consider as path trajectories used for building the part layer by layer.

Mehnen et al. [56] developed a robot path generation program RUAMROB in Matlab®. This system contains two main modules, a slicing module, and a robot generation module. The program slices the part and generates the path code for a Fanuc robot. Bonaccorso et al. [41, 42, 59] designed and implemented a user interface to investigate the control on process stability using Labview. They used feedback controller to control on the bead geometry. The work of Ribeiro and Norish et al. [90, 91] introduced a new fabrication approach by developing a manufacturing system. Their system was capable of creating solid metal parts directly from CAD models. All the systems are used CAD packages to create the part's shape and then creating a program to read these CAD files and transform them into a robot program. The TIG welding based metal deposition process requires a special interface between the modeled data and the deposition system. Hence, the interface used must allow the process parameters to be controlled and tuned during the deposition process, which is difficult to get using the systems depend on the off-line programming method.

In industrial robots, the programming of these systems is still very difficult, time-consuming, and expensive. There are two main types of robotic programming methods, which are online programming and off-line programming (OLP). The OLP method is more reliable and provides more flexibility to the changes of the product design [103]. This method of programming shifts the programming task from the robot operator in the workshop of the software engineering in the office.

2.4.3. Path Planning Strategy

For the near net shaped metal testing, a special rapid metal manufacturing (RMM) system is required, including hardware and software comprises the path planning steps of creating the part drawing, slicing that drawing, and tool path generation for each layer. The path pattern is the trajectory of the deposition tool to fill the boundary and interior of each sliced layer. It is an important factor to determine the surface quality, strength of the building model, and efficiency of the deposition process [83]. Many studies investigated RMM with emphasis on materials, path planning software, and system design. Heralić [55] developed a robotized laser and metal-wire deposition system. This system can slice the CAD drawing into layers of uniform height using Labview® format.

Research work by Zhang et al [60] introduced an experimental study to investigate the RMM through using a new interface between the modeling data, and the deposition process based on the IGES format. A welding deposition system (MIG-welding SMD) was established with a new interface between the modeling data and the deposition process. The system was computer controlled to provide the welding torch with the desired path and angle. In their study, they proposed a rotating planning model which allows changing the orientation of each layer for reducing the accumulated error as shown in Figure 2.9 [60]. Topçu et al [104] used a modern STL slicing file and G-Code generation algorithm software to create slice data of any given 3-D model. There are some problems existed in RMM include poor surface accuracy extensive fabrication process. There is a strong desire to reduce build time and enhance surface accuracy significantly through improved software and hardware [83]. Zhang et al [14] used laser metal deposition shaping with filler metal in powder form to deposit a rotary table part. They converted the CAD model to STL file; then the solid model was sliced by utilizing slicing software, thereafter; the layered geometric information was output in the form of CLI file. In their study, the deposition process was done using two path patterns, namely spiral and zigzag pattern. Ibrahim et al [105] investigated the roughness surface of the parts produced by RMM technology. They showed that the poor surface quality is mainly generated by tessellation of the original CAD model and slicing during the RMM process. So components fabricated by RMM techniques when compared to other conventional

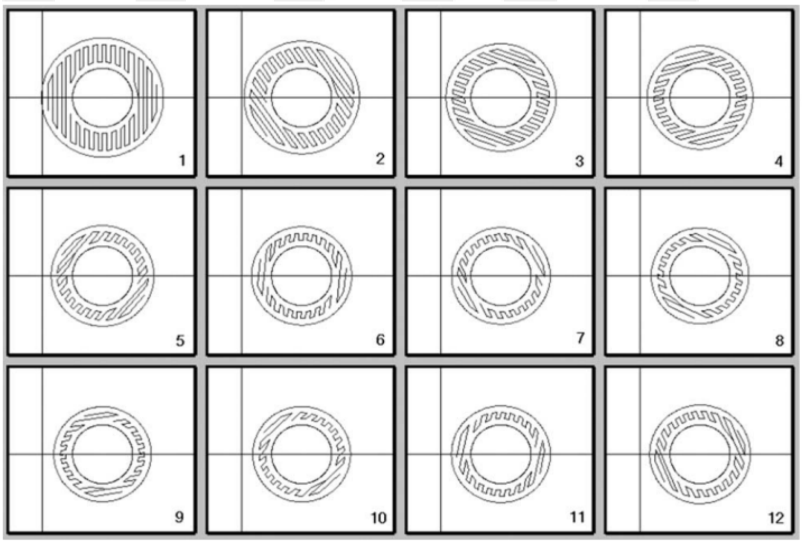

Figure 2. 9. Sketches illustrate the rotated weld path for different layers [97]

manufacturing processes can be inferior in terms of surface quality. Thivillon et al. [79] utilized laser-assisted direct metal deposition to fabricate cubic shape of a metal part by raster fill pattern They used a powder filler metal for fabricating the part in deposition directions of two consecutive layers are perpendicular.

Geometrically, the filling path patterns can be classified into the following common patterns for generating deposition –paths (see Figure 2.10):

- Zig-zag paths: with paths parallel to a pre-determined direction consisting of back and forth motions [14, 83,106].
- Spiral/contour paths: they comprise of a series of contours that are parallel to the boundary of the 2-D cross-section [14, 83, 107, 108].

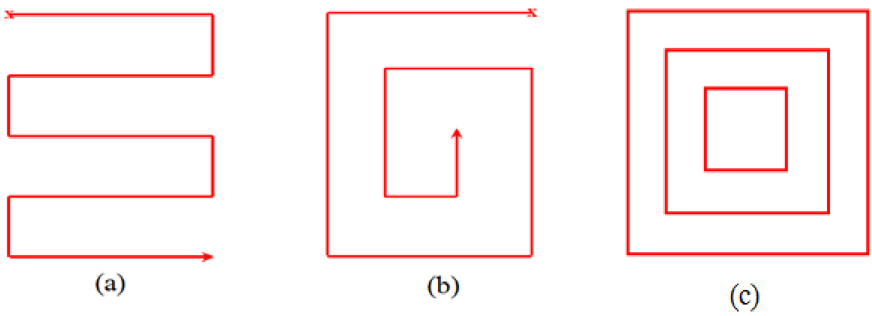

Figure 2. 10. Toolpath generation techniques (a) Zigzag/ raster path pattern; (b) spiral path pattern; (c) contour path pattern.

- Raster paths: they comprise of a series of the contiguous or overlapping straight lines segments [79, 97, 109], it is suitable for laser deposition processes.
- Combined paths of raster, contour, and space filling curves. This filling strategy is suggested to use theTW-SMD technique since it is possible to generate a various of deposition path patterns from the aforementioned paths.

High flexibility and usability of the SMD technique can be achieved if the system is automated by using the robot, CNC machine, or other manipulators based on good path planning strategies.

2.5 Development of Microstructure and Effects on Final Mechanical Characteristics in CCSMD and PCSMD Techniques

The following literature mainly focuses on the works concerning with microstructure characteristics of samples were prepared by SMD processes represented by 3D-welding techniques for different materials. It is obvious that microstructural properties both affect the further mechanical properties and quality of the parts. As it was previously discussed that SMD techniques perform by feeding a metal wire into a local melt pool by arc beam, electron beam, or laser beam. After that the solidification will occur and that is producing microstructures which are significantly affected by thermal cycles [54, 74, 98,100,110, 111]. The deposited material is thermally affected by the deposition of subsequent layers, resulting in complex thermal histories, which lead to problems of residual stresses and distortions. Furthermore, SMD process parameters can also influence the constitute microstructure and its specifications [62, 98]. Many studies investigated the microstructure of deposited materials and their mechanical properties of different materials. A large body of literature focused on Ti-6Al-4V which is one of the most important Ti-alloys [31]. In the works of Baufeld et al.[46, 47, 54], an SMD technique using a robotic TIG welding which is enclosed in an airtight chamber filled with pure argon gas was presented. Argon is controlled to 99.999% purity and moisture is also controlled at a minimum amount. Deposition material was a Ti-6Al-4V wire with 1.2 mm in diameter. The microstructure examinations showed that the layered structure is reflecting SMD layers and large elongated grains which are shown in Figure 2.11. These grains grew epitaxial, inclined in a direction to the layers following the temperature gradient resulting from the movement of the component relative to the welding head. These grains are also visible on the etched cross-sections of the components as shown in Figure 2.12.

Microstructural heterogeneity or banding in the titanium AM is a result of the repeated thermal cycles experienced by the solidified material, with a reducing peak temperature, as the heated source is passed across the surface each time a new layer is consolidated as shown in Figure 2.12.

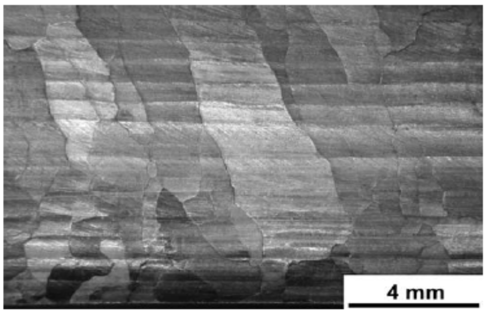

Figure 2. 11. SMD layers and large elongated grains [46, 54].

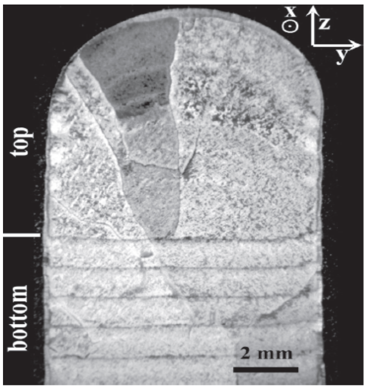

Figure 2. 12. Etched cross-section (y-z plane) of a component exhibiting the top region and the bottom region with bands parallel to the base plate [46, 47].

The formation of banding in wire plus laser AM process for Ti6AL4V alloy was discussed by Kelly and Kampe [28]. Banding is caused by cyclic thermal effects and inhomogeneous distribution of microstructure with a change in the local variation in hardness see Figure 2.13. Generally, fluctuation of hardness in single beads results from differences in thermal history and chemical composition [74]. SMD components exhibit two different appearing regions: a bottom region, which is a coarse Widmastätten structure with circular lamellae, and a top region with a fine, needle-like structure exists in cross-section as shown in Figure 2.14(a). The height of the top region is not very sensitive to the height of the whole component. The microstructure of the both regions consists of α phase laths in a β matrix, but their morphology is different in both regions as indicated in Figure 2.14.

Thus, it has been reported that the SMD components show periodic bulges that reflect the separate layers of each deposit and the large thermally grooved columnar grain [48]. The fine Widmanstätten structure at the top and a coarse widmanstätten structure in the bottom region results from the repeated heat treatment by SMD.

Mechanical tests (tensile test and hardness test) showed that the ultimate tensile strength (σ_u) of the specimens in the horizontal orientations is slightly higher than the specimens with a vertical orientation. Ultimate tensile strength (σ_u) and ductility depend only slightly on the orientation, location, and also heat treatment.

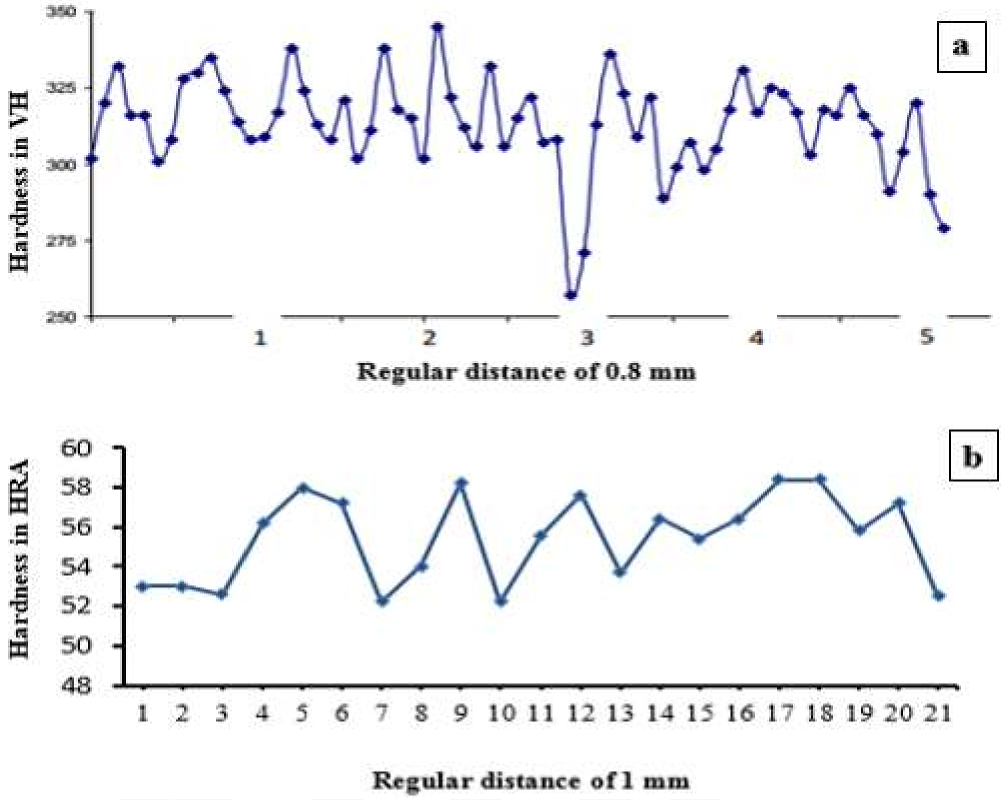

Figure 2. 13. Cyclic changes in hardness values at a regular distance along the deposition direction; (a) for Ti6Al4V [28]; (b) SS308LSi.

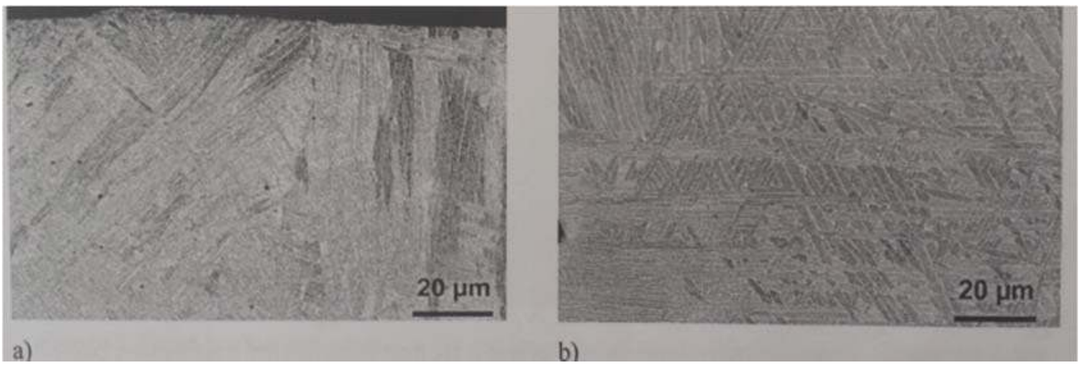

Figure 2. 14. Microstructures of component from the top (a) and the bottom region (b) (y-z plane) [48, 54].

Microhardness tests showed that there is no obvious dependence on the wall height. The heat treatment with the β-phase increases the σ_u and decreases the ductility. The mechanical properties vary to some extent with the variation of welding parameters [46- 48].

The work [46] showed that anisotropic mechanical properties are expected due to anisotropic microstructure. While the results presented in Baufeld et al.[48, 54] claimed that the microstructure exhibits large, columnar prior-β grains with a gradient in the individual α-lath thickness between the deposited layers, except for in the last three layers of Ti6Al4V alloy. The cooling rate in a newly deposited layer decreases as the number of additional layers increases [28]. The thermal cycle is responsible for the formation of the characteristic layer in a layer *n* due to the deposition of the next layer; *n+1* and *n+3*. They showed that upon deposition of layer *n+3*, only a narrow region near the top of layer *n* will see an excursion into the β-phase field as shown in Figure 2.15 [2, 28].

Zhao et al. [31] used SMD process represented by 3D-MAG welding for producing parts of H08Mn2Si steel wire. In their study, researchers combined experiments and numerical model of 3D transient heat transfer. An interaction exists between the pre-heating of four layers and post-heating of the rear layer. It has been an inter-layer metallurgy bonding requirement satisfied by re-melting process between every two adjacent layers. It was also shown that the direction of deposition effects on the temperature gradient state, where the same deposition direction has larger than the

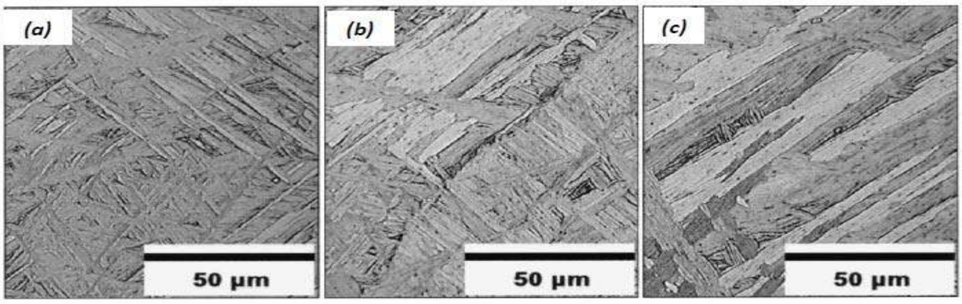

Figure 2. 15. Micrographs from the last 3 layers deposited (a) represent the (n+1) showing a fine basket weave and fine colony widmanstatten α, (b) (n+2) shows a fine colony α with some areas of fine basket weave widmanstatten α, and (c) (n+3) exhibiting predominate [2, 28].

reverse depositing direction. Also, the heat diffusion condition could be improved by optimizing the deposition direction, in the case of keeping other parameters constant. Clark et al. [49] used SMD process represented by 3D-MIG welding to produce developmental ring rolled combustion casing incorporating an internal circumferential

SMD flange, which can be used for an aero engine made of Inconel 718 alloy. They showed that the microstructural conditions of the features are highly dependent on welding parameters and practices.

Austenitic stainless steel (ASS) contribute properties and characteristics which are otherwise unavailable within the alloy systems of various ferrous alloy groups. They have a useful combination of properties such mechanical properties and high corrosion resistance, excellent cryogenic properties, good high-temperature strength, good weldability, and high ductility [112-114]. The grade used in this study is AISI 308LSi, lower carbon, and higher silicon than grade 308 [115]. There were some of the works done using the stainless steel in additive manufacturing but the authors used metal powders with a laser [16, 115]. Other researchers used stainless steel wires as filler materials and used the laser as a melting source. Tellez [101] used fiber laser as melting method to deposit SS308LSi solid wire.

The first attempt to use the ASS in TW-SMD process was by Skiba et al [45], they used CCSMD process for manufacturing test specimens of 308 stainless sheets of steel to gain steel components with high corrosion resistance and better mechanical properties. They showed that the microstructure of the components consists mainly of

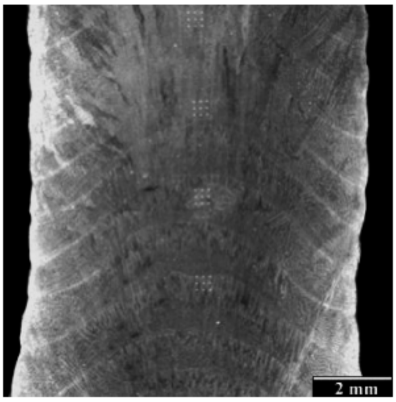

Figure 2. 16. Optical microscopy; cross-section of the 308 stainless steel component, showing the wavy bands coinless steel component, showing the wavy bands corresponding to the deposition layers [45]

austenite and ferrite and the cross-section revealed wavy bands as shown in Figure 2.16.

The mechanical properties value comparable to that of the material prepared by conventional techniques. But they did not refer to the orientation of testing in their study. Although some of the researchers used the pulsed current in welding processes of ASS to improve the mechanical properties of the weldments, especially for the Type 304 ASS [117-123], but the attempts to use PCSMD process is still limited or non-existent for austenitic stainless steels especially grade 308LSi. Wang et.al [52] investigated the effects of pulsed gas tungsten arc welding parameters on the morphology of additive layer manufactured Ti6Al4V. They studied only the macrostructure of the deposited specimens for comparing the columnar grains morphology.

Microstructure anisotropy and hence the mechanical properties inhomogeneous of the component may be obtained due to adopted deposition rote in TW-SMD components. Therefore, for the adoption of this manufacturing method in the manufacturing field, further understanding is required to ensure routine fabrication of robust components with desired properties. This requires investigation and control of the material behavior during component deposition and solidification and understanding the mechanical properties of the manufactured components especially with using the pulsed current technique.

2.6 Grain Refinement Attempts in SMD Processes

In the aforementioned microstructural and mechanical properties section, the parts manufactured by SMD techniques tend to be with large and elongated grains as shown in Figures 2.11 and Figure 2.12. So the mechanical properties vary with the direction of the test since it may result in the anisotropic phenomenon. Hence, there is a need to study and control the grain sizes during SMD methods by the common methods of grain refining such as inoculation method through adding of nucleating agent or inoculants to the liquid metal to get very fine equiaxed grains [124-126]. Other researchers used external excitation techniques for the purpose of grain refinements, such as weld pool stirring, arc oscillation, ultrasonic vibration, and arc pulsation [22, 124, 127, and 128]. Figure 2.17 (a) shows the effect of the arc oscillation by vibrating the welding torch [129]. Figure 2.17 (b) shows the effect of the arc oscillation on the grain refinement. In the pulsed arc technique, the low-current cycle or background current which is sometimes less than 50% of the peak current, so that a sudden reduction in heat input occurs which leads to refining the grains as shown in Figure 2.18 [130-135].

Wang et al. [52] investigated the effects of direct current pulse GTAW parameters on the morphology of the Ti6Al4V. They concluded that there is no any grain refinement in the WAAM parts of Ti6Al4V alloy deposited at both low and/or high frequency pulsed current due to the manner in which the titanium solidifies by planar and cellular rather than dendritic growth. While the work [136] stated that AC was much more effective than DC in refining the FZ of Ti-6Al-4V welds since the pulsed AC causes a greater agitation in the weld pool. Authors of the works [56, 99] employed inter-pulse GTAW system as a heat source for the fabrication of large structural Ti-6Al-4V components.

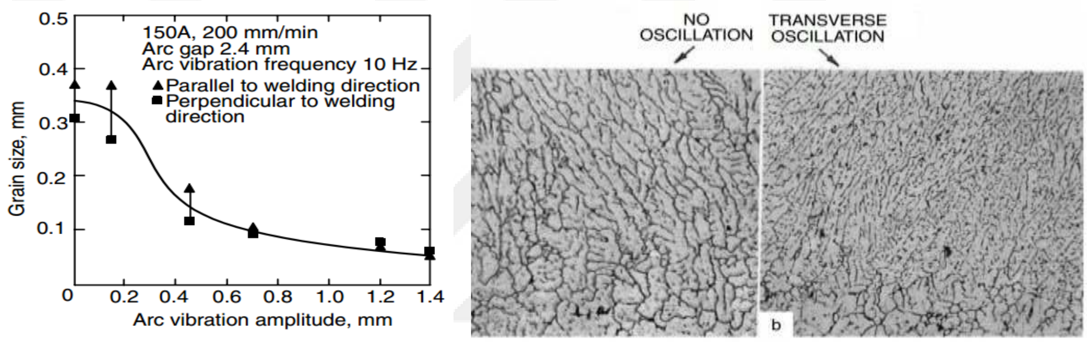

(a) (b)

Figure 2. 17. (a) Effect of arc vibration amplitude on grain size in Al-2,5 Mg, (b) Effect of oscillation process in refining the dendrites in the fusion zone [124]

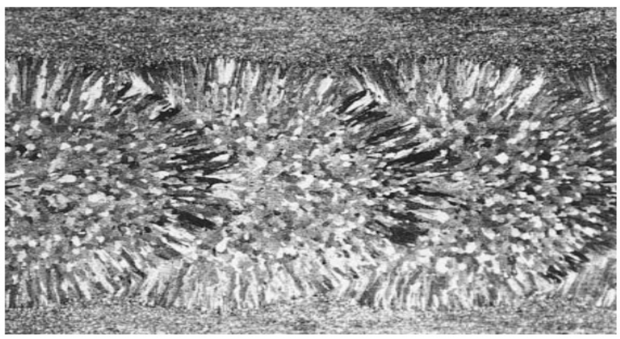

Figure 2. 18. Equiaxed grains in pulsed arc weld of 6061 Al-alloy [131,137]

2.7 SMD Bead Geometries

The bead geometries were affected by the process parameters. Geometry, and hence the surface quality and thickness of the machined layer (TML). The proper selection of process parameters leads to getting good bead geometries resulting in minimum TML and good surface. Thus, more studies are required to evaluate the relationship among geometric features and process variables in multi-layered components [138]. In multi-layered part, the major drawback faced is the controlling the process parameters to get controlled bead dimensions [139]. Gurev et al. [140] showed that heat input significantly affected on the bead width in a direct relationship. Escobar-Palafox et al. [141] used SMD cell to carry out their empirical models for predicting part geometry. They showed process parameters (I and TS) have significant effects on wall thickness and surface finish of the deposited parts. Baufeld et al. [54] showed that the thickness and height of the deposited components by TW-SMD depend on the deposition parameters, where the variation of process parameter lead to variation in wall thickness of the deposited parts.

Muscato et al. [42, 43] developed a TW-SMD system to be automatic control the deposition process by automatic controlling on the wire feed rate and step height to make the process more stable. Sequeira-Almeida et al. [99] used MW-SMD process to fabricate wall specimens of Ti6Al4V. In their study, they aimed to develop a process model that enables the prediction of weld bead geometry from the process parameters. They used a systematic experimental approach (SEA) based on a regression analysis. Hoye et al. [53] used Taguchi DOE technique to analysis the results of their study using the TW-SMD method to deposit Ti6Al4V wall specimens. They showed that average thickness is a function of I and TS while the average height is primarily related to WFS. Adebayo [102] studied the effects of the interaction of the process parameters on the bead geometry of a mild steel material used MW-SMD technique. He focused on wall width, height and perpendicularity through comparing these geometries for the three machine used in the study. Tėllez [101] investigated the influence of process parameters on the bead geometry of the fabricated samples using laser and wire SMD technique for SS308Lsi stainless steel and Ti6Al4V filler wires.

2.8 Weld bead Imperfection and Defects

The weld defects refer to any departure in welded structure from specified requirements. These imperfections impair the strength of welded or deposited parts and may result in the failure of the whole structure during service. The defects are generally due to the use of sub-standard materials, defective welding equipment etc. There are some of the imperfections which can consider as serious defects in the 3D-welding based SMD, such as porosity, cracks, lack of fusion, inclusions, undercut, excessive melting, and bead humping [142].

2.8.1 Porosity

A porous weld is one in which gas pockets or voids are included in the weld. The pores are in the form of small spherical cavities which may result from [143, 144]:

- Rust, greases, moisture and other contaminants on the substrate or on the deposited wire.
- İmpurities in the shielding gases.
- High travel speed may affect the protect gas envelope around the molten pool.

The porosity can exist in the AM components which were deposited using the powders as filler materials. The powders are consolidated by either laser beam or electron beam to fabricate the final solid parts, and hence, the porosity amount must be controlled by controlling the process parameters and conditions. The porosity may be reduced to minimum amount in electron beam technique as choosing suitable process parameters [145, 146]. Whereas, in the case of arc beam and wire-shaped metal deposition method, a fully dense component can be achieved. When the cooling rate is sufficiently high, it may prevent the molten metal filling the blowholes that created by the plasma jet [94].

The porosity may be exited between the layers of multilayer walls due to the formation serration in the case of rear wire feeding direction to the molten pool zone during deposition process [109].

2.8.2 Lack of Fusion

Lack of fusion (LOF) refers to the condition where boundaries of unfused metal existed between layers due to insufficient input power and presence of dirt, slag, oxide or other non-metallic substances. Or it is sometimes due to inadvertent interruptions in the progress of welding.

2.8.3 Shallower Penetration between substrate and deposited walls

In some cases, the weld metal does not completely penetrate the substrate due to low heat input because using high travel speed or low welding current.

2.8.4 Bead humping

The humping defect refers to the hump and valley which appear on the bead surface as shown in Figure 2.19. It may be caused by a relatively high travel speed. It makes the weld bead to be undulated. The humming may appear in some of the weld processes such as GMA welding technique [102], in laser welding process [147], in electron beam welding [148], and in GTA welding process [149]. In the present study, hump defect was investigated as a function of travel speed TS in TW-SMD technique

Figure 2. 19. Photograph illustrates the bead humping in TW-SMD process

2.9 Austenitic Stainless Steels

2.9.1 Characteristics and Applications of Stainless Steels

Stainless steel is a complex group of iron-based alloys containing at least 10.5 wt% chromium (to be stainless) and no more than 1.5 wt % carbon [113, 150]. Stainless steels are used in chemical, nuclear and petroleum industries where corrosion resistance is an important factor [151]. The stainless steel corrosion resistance is obtained with the presence of an oxide protector film on its surface and welding operations can affect the material [152]. Stainless steels contribute properties and characteristics which are otherwise unavailable within the alloy systems of the various ferrous alloy groups [152].

There are several different systems currently used to designate stainless steel. The various specifying bodies categorize stainless steels according to chemical composition and other properties. For example, the American Iron and Steel Institute (AISI) lists more than 40 approved wrought stainless steel compositions. In the AISI system, austenitic grades are in the 200 and 300 series, ferritic and martensitic grades are in 400 series. These grades can be seen schematically in the Figure 2.20. The major reason for the selection of stainless steel was corrosion resistance and heat resistance. Other reasons offered included strength, cryogenic properties, weldability, machinability, and cost advantage 114]. The choice of a material is not simply based on a single requirement. The selection of a specific stainless steel may depend on corrosion resistance, mechanical properties in specific temperature ranges, fabrication characteristics, and physical properties.

Ferritic Stainless steels: These grade of steels consist of a microstructure of alpha ferrite which has a body- centered cubic (BCC) crystal structure with chromium contents varying from 14.5% Cr to approximately 27% Cr [152]. These alloys cannot be strengthened by heat treatment since they do not transform to any other phase up to the melting point. They can be cold-worked and annealed. As a group, they are more corrosion resistant than the martensitic grades but generally inferior to the austenitic. They available in 400 series, which include 405, 409, 430,439, 442 etc.

Martensitic stainless steels: They are similar in composition to the ferritic group but contain higher carbon and lower chromium. These alloys include 403, 410, 414, 416, 420, 422, etc. They are magnetic and can be hardened by treatment. They contain chromium up to 18% and carbon (may exceed 1.2%). However, these alloys are not as corrosion resistant as the ferritic or austenitic groups. [114].

Precipitation-Hardenable stainless steels: The ordinary stainless steels of the 300 series are not heat treatable and give up strength for corrosion resistance, while the 400 series contain higher carbon contents, and therefore higher strength, but have reduced resistance to the environment. The precipitation-hardenable grades exhibit a unique

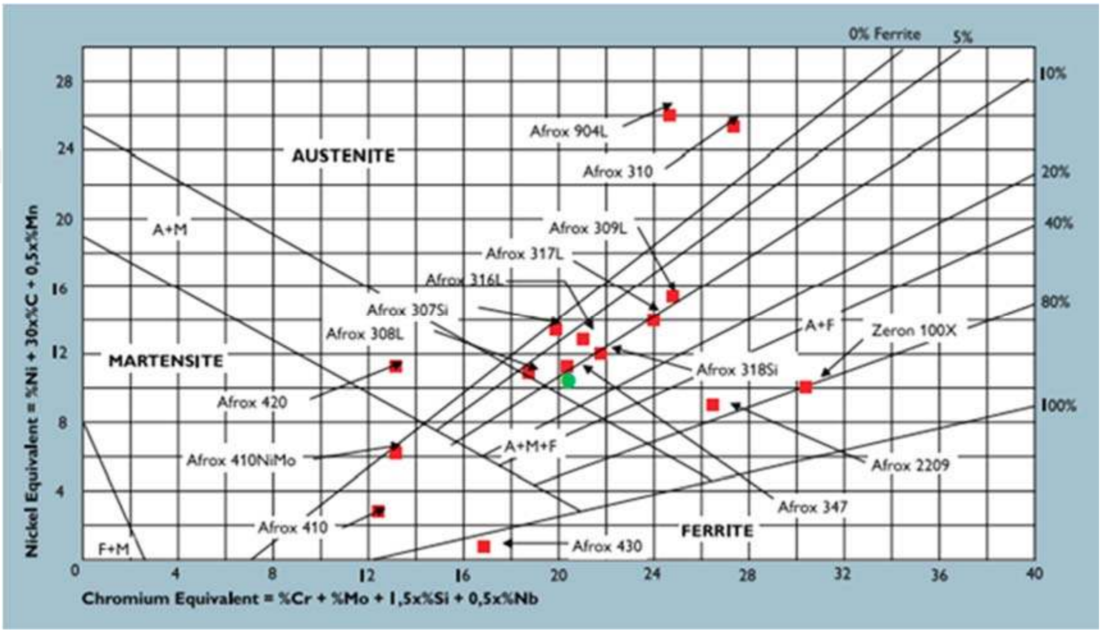

Figure 2. 20. Families of stainless steel presented on Schaeffler diagram of 1949 [153].

the combination of strength, ease of heat treatment and corrosion resistance that are not found in any class of materials.

Duplex stainless steels: These grades are the newest of the stainless steels, which contain both ferrite and austenite. They have good corrosion resistance and higher tensile strengths than austenitic grades [112, 152]

Austenitic Stainless steels (ASS): These grades cannot be hardened to form martensitic by quenching. Whatever the cooling rate, they are austenitic at room temperature. Nor do they undergo a transformation on heating to below the melting range. ASS are non-magnetic and can be retained at room temperature by appropriate alloying. Both chromium and nickel contents can be increased to improve corrosion resistance [114]. ASS contain maximum carbon up to 0.15 wt%. The most common austenitic alloys are iron- chromium-nickel steels and are widely known as the 300 series. These austenitic stainless steels, because of their high chromium and nickel content, are the most corrosion resistant of the stainless steels group. AISI 300 series include: 301, 302, 303Se, 304, 304L, 304LN, 308, 308L, 309,310, 316, 316L, 316LN, 320, 330, 337, etc., containing chromium (16-26%) and nickel (5-18%) mainly AISI 200 series include 201, 202, 205, etc. [114, 152]. The important specifications of these grades include: they can be hardened by cold work, excellent cryogenic properties, high ductility, and high-temperature strength [112]

2.9.2 Welding of Austenitic Stainless Steels

The 200- and 300- series austenitic compositions are the most weldable grades and producing welded joints with high toughness [112]. The problems that arise related mainly to the possibilities of sensitization in the heat-affected-zone. No preheating is necessary, post-heating is usually for the purpose of re-dissolving precipitated carbides and so restoring corrosion resistance. However, post-heating treatment is also used for the stress relief of comments that are to be used environments that may cause stress corrosion cracking and for the stress relief of parts that are fabricated from a clad material [114]. Susceptibility to sensitization is minimal in the extra-low-carbon grade (designated L) and in the stabilized grades 347 and 321; it increases in other grades as the ratio of carbon to chromium increases.

Sensitization is a term used to describe the depletion of chromium content brought about by the precipitation of chromium-rich carbide at the grain boundaries and this causes the formation a chromium depleted zone in the immediate vicinity of the boundary [151]. It is the major pitfall in the austenitic class. When ASS are heated between 450-850 °C, subsequent performance in a corrosive environment is marred by the inter-granular attack. The most critical temperature is about 650 °C, where holding for only for a few seconds may be sufficient to permit subsequent deterioration. Chromium and carbon, originally distributed through the austenitic structure, combine to form chromium carbide (see Figure 2.21). The temperature at which this occurs most rapidly is about 650°C at low temperatures diffusion rates of the atoms are less; at higher temperature, there is an effective reverse process [114].

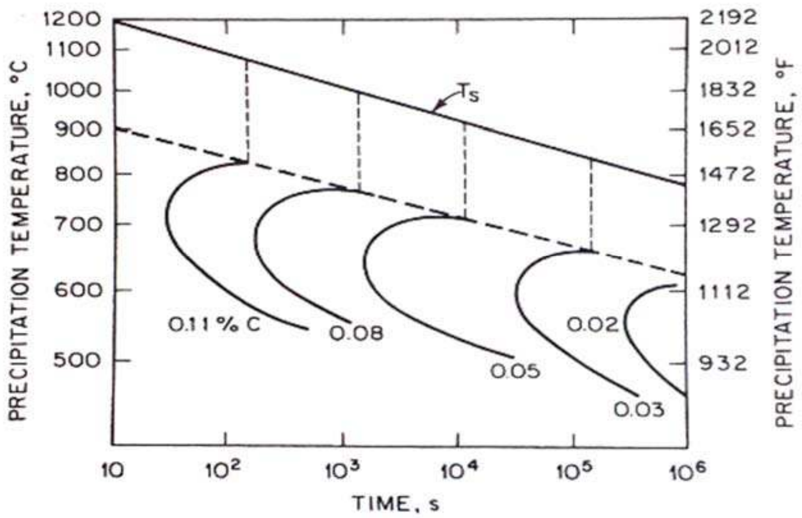

Figure 2. 21. Effect of carbon content on M23C6 precipitation in 18Cr-9Ni stainless steel, as detected by intergranular corrosion tests (H_2SO_4-Cu_2SO_4) [152].

Sigma (σ) is formed from high-chromium ferrite, and hence, we might anticipate that it should not appear in the austenitic alloys. However, some of the austenitic alloys are not entirely austenitic, and, in welding austenitic stainless steels, some ferrite is usually purposely allowed to form [114]. σ is a hard and brittle, nonmagnetic phase with a tetragonal unit cell, forms at temperatures 400-900 ^{o}c in alloys containing 17-70 % chromium [154].

The austenitic grades may contain some ferrite. Ferrite commonly produced in an austenitic weld bead; the amount present depends on to an extent upon the cooling rate and subsequent heat treatment, but more upon the composition [114]. A continuous austenite matrix separated long, narrow, ferrite regions that were distributed in a cellular dendritic pattern. The ferrite distribution and orientation of the long axes of the grains vary with location within the weld, depending on the solidification growth direction.

The delta ferrite plays a significant role in the reduction of the hot cracking susceptibility of austenitic stainless steels with a duplex microstructure. Investigators contend that three to eight volume percent delta ferrite is required to reduce hot cracking susceptibility [155]. To ensure primary ferrite solidification, alloy composition must lie on the effective chromium-rich side of the liquidus projection line on the Fe-Cr-Ni phase diagram shown in Figure 2.22 [156]

Suutala et al. [157] determined the liquidus projection line as a function of modified nickel and chromium equivalent expression, as seen in Figure 2.23. They clearly distinguished the regions of primary ferrite and primary austenite. Delta ferrite amount, morphology, and distribution required to produce optimal weld strength were determined to be service temperature dependent. At low service, temperature dependent. At low service temperatures, delta ferrite has ductile-brittle transition temperature. At high temperatures, delta ferrite transformation to sigma phase, which is brittle. Therefore, low ferrite content (less than eight volume percent delta ferrite) with a non-continuous network is desired to limit brittle crack propagation [158].

The Fe-Cr-Ni ternary system provides the basis for predicting phase equilibrium in austenitic steels. Since most commercial stainless steels are composed of 16-25 wt% chromium and 8-20 wt% nickel, their compositions are localized in the iron-rich corner of the ternary diagram. The liquidus surface of the system can be represented by a series of isotherms which reach a minimum along a line running from the Fe-Ni peritectic reaction (Fe-4Ni) to the eutectic point at (49Cr-4Ni-8Fe) [154] as illustrated in Figure 2.24 [159].

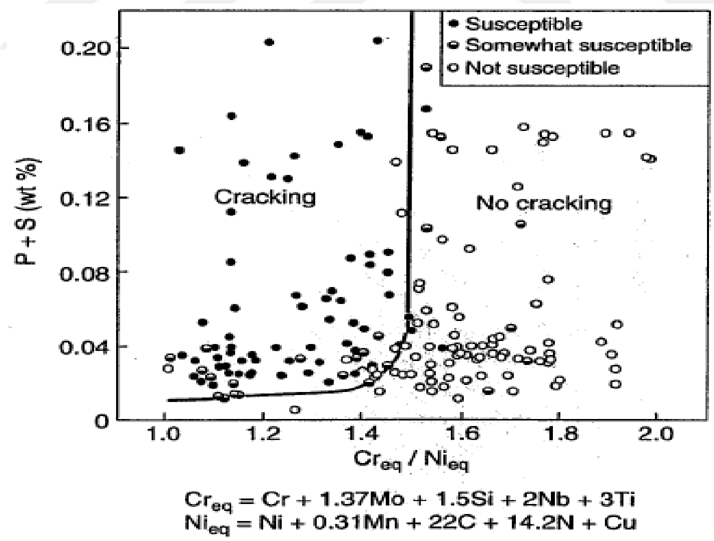

Figure 2. 22. Suutala diagram for predicting weld solidification cracking from weld metal composition [156]

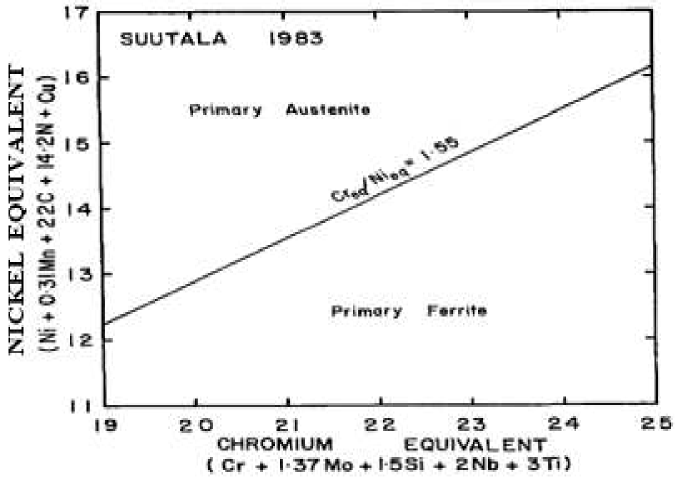

Figure 2. 23. The Suutala diagram indicates the liquidus projection line as a function of nickel and chromium equivalents [157].

There are four solidification and solid state transformation possibilities for austenitic stainless steel weld metal. The relative position of the four solidification modes is illustrated in the pseudo-binary diagram as shown in Figure 2.25. These reactions are related to Fe-Cr-Ni ternary phase diagram by use of Cr and Ni equivalents. Solidification mechanisms of austenitic stainless steels are shown as follow;

Austenite / A mode: $L \rightarrow L+\gamma \rightarrow \gamma$ $Cr_{eq}/Ni_{eq} < 1.25$

Primary Austenite/ AF mode: $L \rightarrow L + \gamma \rightarrow L + \gamma + \delta \rightarrow \gamma + \delta \rightarrow \gamma$ $Cr_{eq}/Ni_{eq} < 1.48$

Primary Ferrite/ FA mode: $L \rightarrow L + \delta \rightarrow L + \delta + \gamma \rightarrow \gamma + \delta \rightarrow \gamma$ $Cr_{eq}/Ni_{eq} < 1.95$

Ferrite/F mode: $L \rightarrow L + \delta \rightarrow \delta \rightarrow \gamma + \delta \rightarrow \gamma$ $Cr_{eq}/Ni_{eq} > 1.95$

Where L, δ, and γ represent liquid, delta ferrite and austenite respectively

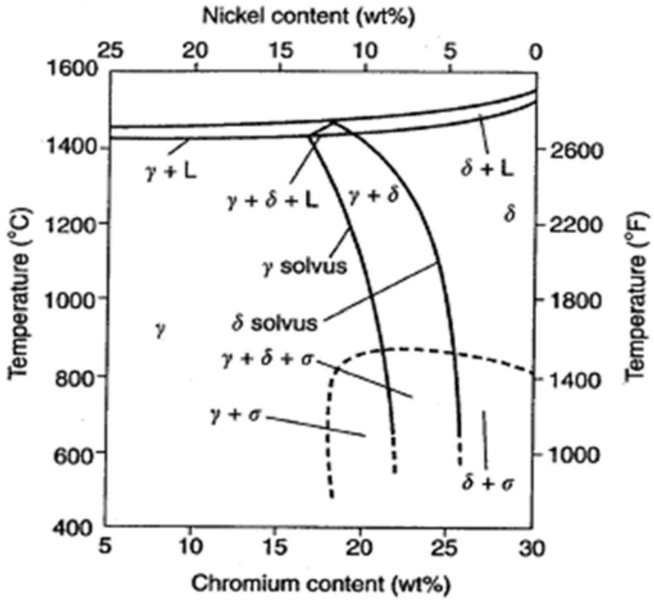

Figure 2. 24. Pseudobinary section of the Fe-Cr-Ni system at 70% iron [159].

Cr equivalent (Creq) = [%Cr] + [%Mo] + 1.5[%Si] + 0.5 [% Nb] …………(2.1)

Ni equivalent (Ni eq) = [%Ni] + 30[%C] + 0.5[% Mn]……………………..(2.2)

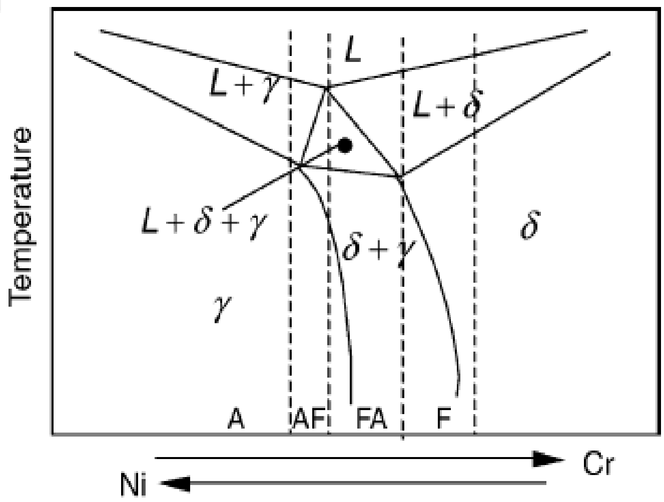

Figure 2. 25. The relative position of four solidification modes of stainless steels in pseudo-binary diagram [160].

Fully Austenite solidification (A): The metal entirely solidifies as austenite and remains in this phase to room temperature and exhibits a distinct solidification structure when viewed metallographically [113, 161].

Primary austenite solidification (AF): If some ferrite forms at the end of primary austenite solidification process via a eutectic reaction, solidification is termed Type AF. If the material cools down under equilibrium conditions, the ferrite will transform to austenite, but under rapid cooling ferrite will remain to room temperatures [113, 161].

Primary ferrite solidification (FA): When solidification occurs as primary ferrite and at the end of solidification some of the austenite forms, it is termed Type FA. When cooling down the metal under equilibrium conditions, the ferrite can be transformed to austenite. However, under rapid cooling rate, some of the ferrites will remain to room temperature.

Ferrite solidification (F): If solidification occurs completely as ferrite, it is termed Type F. in this case the microstructure is fully ferritic at the end of solidification as shown in Figure 2.6. When cooling down, it may transform partially or totally to austenite. [113, 161].

Stainless steels that solidify in the primary ferrite FA are the most resistant to hot cracking as shown in figure 2.3 and figure 2.4.

Actual measurements of ferrite can be made a magnetic analysis device. In welding and deposition processes, the ferrite number (FN) can be predicted using Schaeffler diagram (see Figure 2.26), which is normally used to predict the approximate amount of ferrite to be obtained in these processes, based on the chemical composition [112, 114]. The Schaeffler diagram was developed using shielded metal arc welding (SMAW) process, where the nominal nitrogen content as not considered as an alloying element. The diagram proved to be reasonably accurate for most 300 series alloys of his time, using conventional arc welding processes [113]. It was a major advancement for the prediction of weld microstructure and led to the development of other diagrams.

Ni_{eq} = [%Ni]+ 30{%C] + 0.5[Mn]

Cr_{eq} = [%Cr] + [%Mo] + 1.5[%Si] + 0.5[Nb]

where Ni_{eq}, Cr_{eq} represent a nickel equivalent and a chromium equivalent respectively. Using the Schaeffler equivalency relationships (Cr_{eq} and Ni_{eq}), Seferian [162] developed an expression for calculating the amount of delta ferrite present in austenitic weld metal:

Delta ferrite (δ) =3 (Cr_{eq} – 0.93 Ni_{eq} – 6.7)……………….(2.3)

At the present time, the WRC-1992 diagram is the most reliable and accurate diagram available for prediction of Ferrite Number FN in austenitic and duplex stainless steel weld metal as shown in Figure 2.27 [163].

2.9.3 Austenitic stainless steel grade 308L

Austenitic stainless steel 308L is the standard 19 9 L according to EN ISO 14343-A [115, 164]. It has excellent weldability and formability. It has also excellent corrosion resistance since it has a higher content of Cr and Ni.

The grade used in this work is 308LSi (19 9 L Si). It has low carbon content to increase the resistance to corrosion, avoid the intergranular corrosion due to sensitization, and maintain the mechanical properties. It is very easy to strike and restrike, so that very smooth, low spatter arc producing a finally rippled bead surface with excellent slag detachability. The high silicon levels improve arc characteristics and weld pool fluidity and flatten weld bead profile [112, 115.]. The mechanical and physical properties of the selected material were reported in Tables 2.2-2.3.

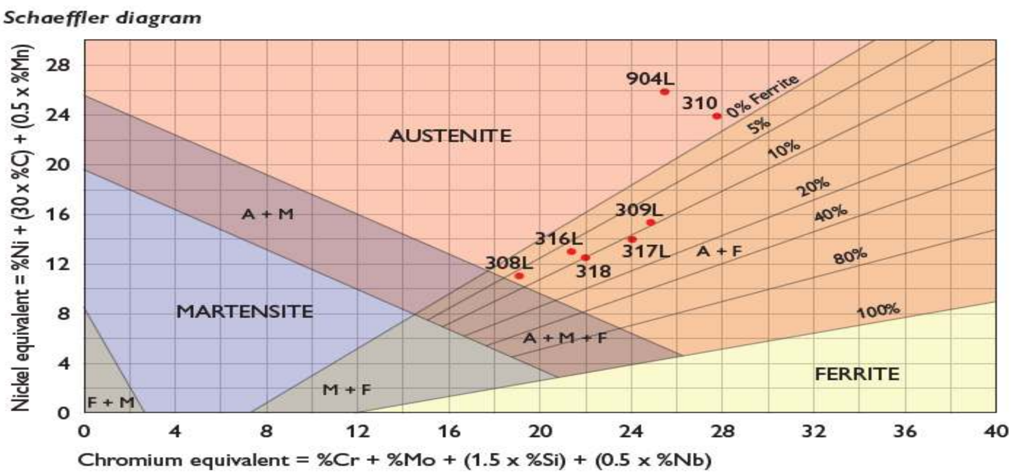

Figure 2. 26. Schaeffler diagram of 1949, which is still in use [153]

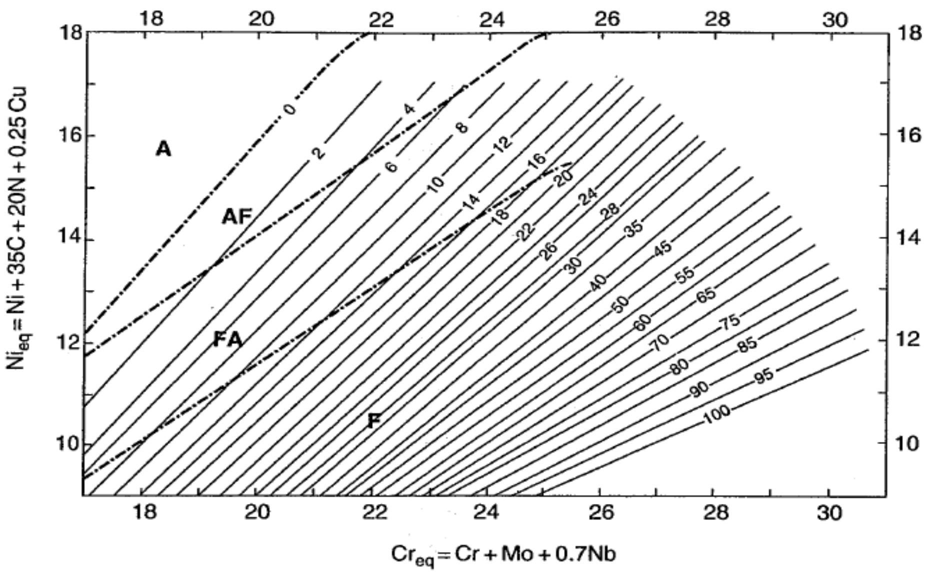

Figure 2. 27. WRC-1992 diagram [163]

Table 2. 2. Typical mechanical properties of 308L as wrought metal [112], as cast [152, 113, 114, 152,], and as all weld metal [115]

Specimen preparation method	Ultimate Tensile Strength (MPa) Min.	Yield strength 0.2% proof (MPa) Min.	Elongation %
Wrought Metal (WM)	515	205	40
Casting metal (CM)	530- 621	200 – 310	39 – 60
All weld by TIG welding (ATW)	510	320	30

Table 2. 3. Typical physical properties of stainless steel 308 [112]

Material	Density (kg/m3)	Elastic modulus (GPa)	Thermal conductivity at 100 °C (W/m k)	Thermal conductivity at 500 °C (W/m K)	Specific heat at 0-100 (J/kg k)	Melting range (°C)
SS 308	8000	193	15.2	21.6	500	1400-1420

2.10 Research Gaps in the related literature

TIG welding plus cold wire - based shaped metal deposition (TW-SMD) technique is a relatively new and immature technology. Therefore, there is a need for understanding the basic science of this process as most of the processing parameters to this point have been empirically derived, and hence there is need for more investigating and more understanding of the material properties of the parts produced by such innovative process to understand the material microstructure resulting from a particular thermal processing cycle.

The bead geometries and process stability need to be investigated. So that the system and process will be modeled and research be carried out to determine stable parameter windows for deposition different austenitic stainless steel components and discover the mechanical and microstructural properties of the resulting parts. The present investigation involved the conventional process using continuous current (CCSMD) and for the first time the pulsed current SMD (PCSMD).

There is a potential ability to improve the wall quality and minimize thickness of layer machined through controlling the optimized building parameters and building strategies

A Large body of research's in SMD field were done using systems which are somewhat complex and obeyed to special codes and machine languages. In order to shorten the production time and to eliminate the tedious process of teaching programs of these systems, there is a need to develop a new system to be more suitable for TW-SMD path planning strategies without such difficulties of other systems such these used robotic welding cell or the CNC milling machines.

One of the main challenges in the SMD technologies is growth columnar grains throughout the components as a result of the process procedure, which effects on the mechanical characteristics. There is a need to investigate the possibility of grain refinement and improve the properties of the built components. So, there is a research gap and practical need of introducing a new method to refine the grains in TW-SMD techniques by using arc pulsation process which may affect the grain growth and hence the mechanical properties of the built parts. The geometrical, metallurgical, and mechanical properties should be examined and compared to conventional TW-SMD process.

CHAPTER 3

EXPERIMENTAL SETUP, MATERIALS, AND PROCEDURES

3.1 Introduction

This chapter describes the designing, constructing, and controlling of Shaped Metal Deposition machine (SMDM). Moreover, the chapter specifies the base materials, dimensions, welding consumables, and procedure utilized during the research study. It also includes the substrate preparation and details about the operation conditions and the welding setup used in the study, including power supply and welding rigs.

3.2 SMD System Design (System Hardware)

An SMD system generally consists of the following main parts:

1. Melting source, which refers to the electrical arc machine in WAAM
2. Deposition metal supplier, which refers to the metal solid wires using wire feeder machines.
3. Deposition path machine, which may be welding robots, CNC positioned or any machine which is able to generate the deposition paths.
4. Control system and software. The mechanical system in WAAM is carefully controlled since it is responsible for the deposited part features.

In this study, the main units of the SMD-system are shown in Figure 3.1. SMD machine with 3 linear axes (x-y-z) is used for depositing melted wire to produce 3D solid parts. Arc heat is produced via welding machine that has a capability of producing AC/DC, pulsed /non-pulsed current TIG welding. Deposition tool (DT) unit is used to attach the welding torch and the wire feed nozzle. The wire is fed and controlled by wire feeding unit. The control system was designed and programmed only the SMD machine axes movements. A general hardware structure of the SMD system is shown in Figure 3.2. The dotted arrows represent the ideal situation work. The SMD machine (SMDM) represents the central part of the SMD hardware system.

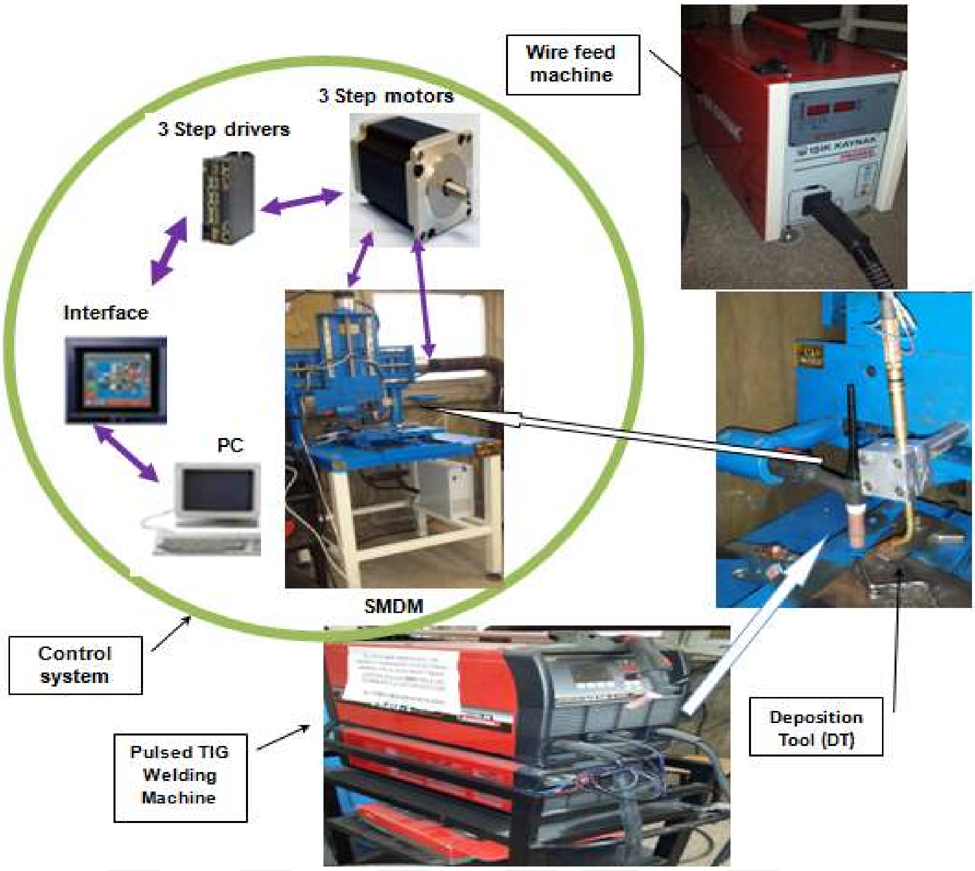

Figure 3. 1. Main integrated units in SMD system

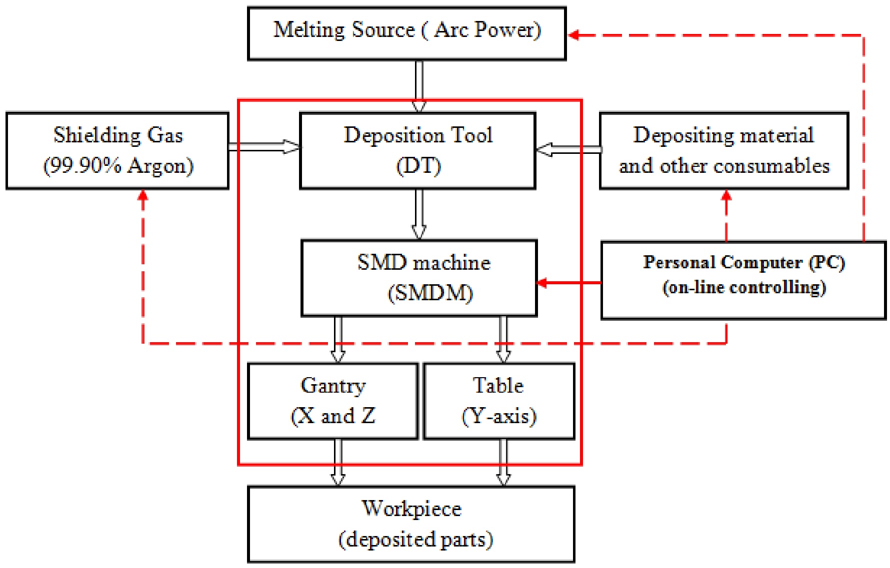

Figure 3. 2. Work cell structure in CAMDM hardware.

3.2.1 Shaped Metal Deposition Machine Designing and Constructing

This section explains designing and constructing of the developed SMD system. Due to the importance of using manipulating arms (CNC machines, gantries, or robots) as a major factor in additive manufacturing technologies. A new 3-axes machine was designed and fabricated for the purpose of facilitating the shaped metal deposition. It is a computer aided metal deposition machine (CAMDM) with 3-axes positioning, which can be used for SMD processes, especially for TIG and MIG welding deposition techniques. At first, a feasible design for the proposed SMD machine was prepared.

The design was performed using a CAD software using industry experience and according to the valid standards. The design includes machine body, gantry part which holds the DT and moves it in the X- and Z-axes, movable work table, which holds the substrate plates and moves in the Y-direction to grant the system high flexibility concerning the size and the condition of the manufacturing component with smooth movement at this counsel, and adjustable fixtures which are utilized for holding torches of DT. These fixtures allow changing the angles and positions of the torches with respect to each other. Figure 3.3 (a) and (b) shows the first design of the CAMDM which was then improved during the manufacturing of these parts. All parts were fabricated and then assembled into the final configuration of CAMDM after finishing processes. Figure 3.3(c) shows the general view of the CAMDM.

The machine is actuated by three stepper motors, which are connected along the x-, y-, and z-direction. It is necessary to mention that the materials used in the manufacturing of all parts were selected as hardened steels and stainless steels in order to be stable, strong, tough, and heat resistant to withstand the different work conditions during deposition processes. Stepper motors were selected according to the designed weight constraints and movement accuracies as well as motor specifications, e.g. it's power, rating on handling the torque, and rotating speed. The most suitable one for this machine was stepper motor of 86HS45 series hybrid, which has handled the torque of 4.5 N.M, 300 w, and (200-2400) RPM [165].

The maximum working area was designed as 400x400x400 mm^3. A 2D mechanical motion of the x-y plane is used to define the geometry of each layer, and the third axis is affected by pulling the DT up vertically in the z-direction. The substrate is mounted on the work table, whereas the DT is coupled to the gantry part of the CAMDM.

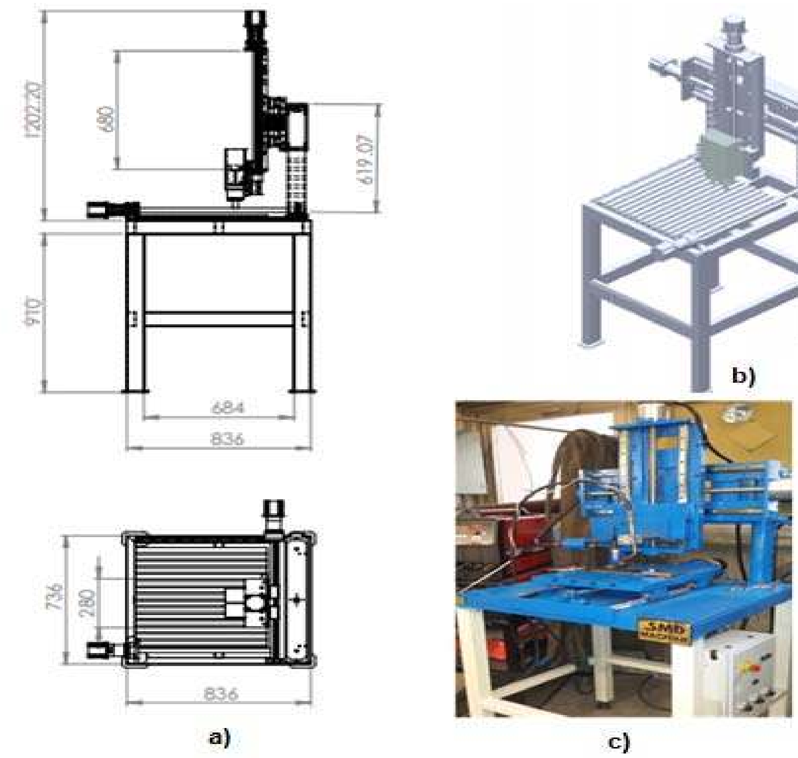

Figure 3. 3. (a) Multi-views of the designed construction, (b) isometric view of the model, (c) photograph of the assembled SMD system

3.2.2 SMDM Controlling Process

The system is a feed forward (open-loop), which means that the information about the welding process well known before without feedback to be used. The SMD system in this study includes the development of 3D model object based on CAD drawing, planning and slicing of the pattern in uniform thickness layers. The CAD drawing is imported to an on-line programming method. So the desired geometry according to the CAD-specification is sliced into layers of uniform height. For each layer the paths along which the beads should be deposited to fill the layer [166]. The deposition process has been established with an interface between the modeling data and the deposition tool. Where, after the model is validated, it is sliced from the bottom to the top with uniform layer thickness. This was done by slicing the complicated 3D geometry into simple 2D features and designing of the SMDM paths and deposition parameters. The process parameters were selected based on some of the preliminary experiments as shown in Figure 3.4.

In the present SMD system, on-line programming method utilizes 3D CAD data of a part to generate and simulate the SMDM programs. On-line programming is selected since it is not with high cost as in the off-line programming (OLP) package, especially for smaller product volumes. OLP software is time-consuming and requires high-level programming skills, and the on-line is less complex as in OLP [103].

Before the generated program is done in the real CAMDM, the deposition paths are tested in a simulated machine in order to show and sure that the motions are applicable to the equipment. The CAMDM is represented by 3 axes Cartesian robot for simulation and visualization from solid model points. Cartesian trajectories are generated (x, y, z) and $(\dot{x}, \dot{y}, \dot{z})$, that means the points of motion and velocities are specified, then the machine is animated in the graphical procedure. Figure 3.5 shows the main steps that were followed in the present work. The first step is the CAD software to draw and define the part geometry graphically. CAM sliced the part model into layers and the layers are converted into lines. Lines are regarded as paths to be followed and these paths are simulated in the control software. The deposition control parameters are set on the welding machine and wire feeder. Finally, the modeled part is built via defined paths on the substrate. In that case, one of the benefits of the developed SMD system is that the actual paths are directly calculated from the CAD geometry. Thus, time-consuming and tedious task of teaching the robot can significantly be reduced by the developed CAMDM software

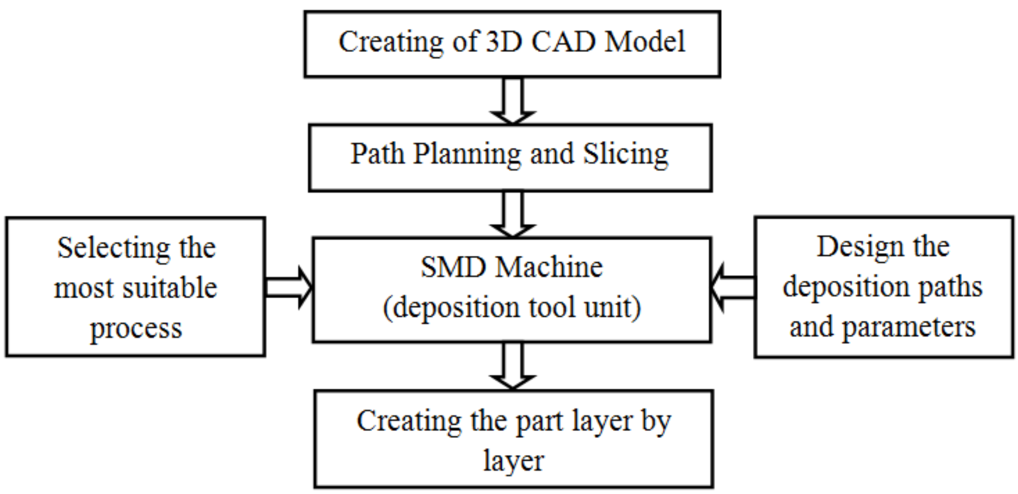

Figure 3. 4. Building part flow in SMD.

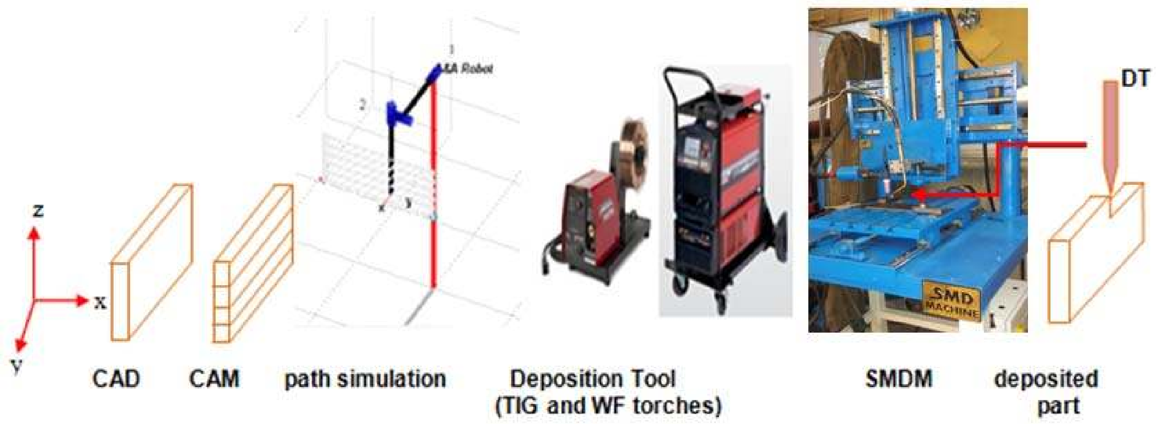

Figure 3. 5. Part manufacturing steps in SMD system.

3.2.3. Software Architecture (Control Unit)

The architecture of block diagram that is used for studying and controlling the process is constructed by PC Interface Program, Control Unit, and SMD machine. The block diagram of the system is shown in Figure 3.6 (a). The PC- interface program is a user interface panel as shown in Figure 3.6 (b). It is projected with the graphical user interface development environment (GUIDE) of MATLAB. MATLAB is a high-level technical computing language, and it is an interactive environment for algorithm development and data visualization [167]. This software is practiced because of the system requirement to play at the online process that is supported by MATLAB real-time signal processing.

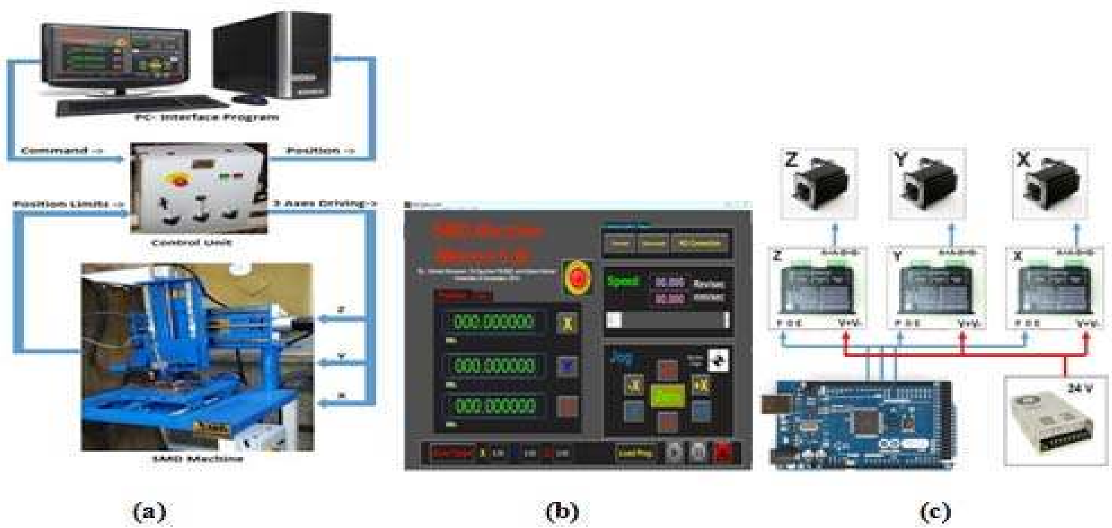

Figure 3. 6. (a) Block diagram of system, (b) user interface and (c) the control unit circuit.

The control unit is constructed to receive commands from computer programs and to send the current position of machine axes as a feedback. The connection between the control unit and the computer is by USB port. The control unit has an **open-source** simple microcontroller board (Arduino Mega 2560). The open - source program is a low-level program, which gives the CAMDM flexibility to alter and edit the operation program. The microcontroller is programmed by C++ language, where the C++ program was written to receive a high-level machine code from PC and convert it digital binary form to control the digital step motor driver. The digital step motor drivers area 2-phase step motor drivers. They generate a micro-step up to 51200 steps/rev and an output current of 2.1A to 5.6A [165]. The power supply gives the required voltage for the control unit. Figure 3.6 (c) shows the structure of the control unit.

The CAMDM path generation has been created in MATLAB program. The CAD model is firstly transformed by a GUIDE program to be input to the user interface after slicing the CAD model into ISO-line paths and building a sequence of the part. The operator can define the main points of shape, layer height, and a number of layers. Afterward, a translational transform between points is created (x-y path), the layers are built by increasing z-axes by layer height for the x-y path. The solid model is expressed as points (x, y, z). The pattern points can be saved as the m-file type and can be loaded on machine user interface program for experiment implementation.

The paths can be translated into binary format and uploading the binary code into the SMDM controller. PC-Interface Program is a computer aided manufacturing (CAM) program, which is used for controlling machine torch movements relative to machine workspace. The program receives the CAD output file (m-file) and converts it to low-level machine code. The user can control machine manually by JOG, apply machine zeroing, monitor the change of the parameters of the machine, and load sequential program for the machine.

3.3 Materials and welding consumables

The experiments were conducted on as rolled low carbon steel type “St. 3” according to DIN standard [168] substrates. Two types of deposition materials used in this study, the first wire was a 1.2 mm diameter, copper-coated, solid mild steel wire. Its grade was chosen according to AWS specification, so the wire grade is “ER70S-6”.

Maximum nominal composition in wt.% of the deposited wire metal, which is taken from the AWS specification [169]. These materials are low cost and widespread application in the structural fabrication such as bridge components, power plants, wind tower components, as well as different tools and die/mold repair. Table 3.1 shows the nominal and actual laboratory results of chemical composition (in wt. %). The other deposited wire was a 0.8 mm diameter, a smooth arc, a low carbon grades solid stainless steel wire. Its grade was chosen according to AWS A5.9-95 specification, so the wire grade is "ER308LSi" [164]. These materials have good arc characteristics, weld pool fluidity as it contains higher Si, and flatten weld bead profile. It is suited for welding or depositing on mild steels and 18Cr8Ni type stainless steels such as 304 and 304L.

Austenitic stainless steels have good strength and high corrosion resistance as well as they are weldable and less embrittlement in the welded structure. They are widely used in thermal power plan, pressure vessels, and medical industry. So this group of stainless steels is considered suitable for additive manufacturing. Table 3.1 shows the standard compositions and actual laboratory results of chemical composition using spectrometer analysis device shown in Figure A.1 in Appendix A.

3.3.1 Substrate Preparation

The substrates were sheet metals with dimensions 100 x 200 x 6 mm and 200 x 250 x 6 mm. They were mechanically cleaned using stainless steel wire brush to remove the top surface iron, grease, paint, rust, etc. from the base plate before deposition process, degreased with ethanol, and then dried. The thermocouples were embedded in the selected positions on the substrate.

3.3.2 Cooling System and Clamping Arrangements

The substrate had to be clamped very strongly to a fixture in order to avoid deformation and also to enable efficient heat dissipation. In order to provide a larger heat sink to the substrate plate, a water cooled copper backing plate was used, which was machined as shown in Figure 3.7. The cooling plate helps to improve the heat flow during the deposition process and reducing the waiting time between the subsequent layers.

Table 3. 1. The chemical composition of the substrates and the filler materials (in wt. %)

Element	%C	%Si	%Mn	%S	%P	%Mo	%Ni	%Cr	% Fe	Others
Plate nominal comp.	0.1 max	0.03-0.15	0.2-0.45	0.04	0.04	--	--	--	Rem.	--
Plate (St. 3) actual comp.	0.067	0.025	0.249	0.01	0.012	0.006	0.015	0.01	Rem.	--
ER70S-6 Nominal comp.	0.07-0.15	0.8-0.15	1.4-1.85	0.035	0.025	-----	----	----	Rem.	Cu=0.5
ER70S-6 Measured comp	1.0	1.0	1.5	0.029	0.02	------	-----	-----	Rem.	Cu=0.3
ER308LSi typical composition	0.012	0.85	1.9	0.002	0.02	0.05	10.5	19.5	Rem.	--
ER308LSi as deposited composition	0.018	0.56	1.358	0.0331	0.033	0.115	9.412	19.557	Rem.	Co=0.941 Cu= 0.181 Ti=0.057

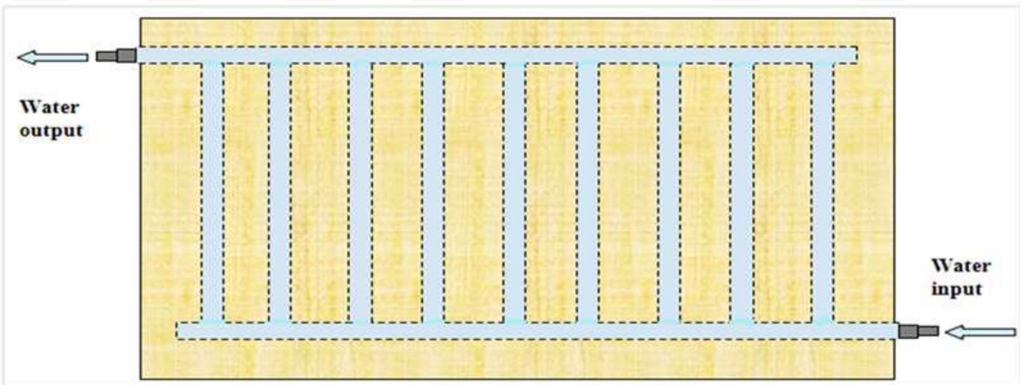

Figure 3. 7. Water-cooled copper backing plate.

3.4 Continuous Current TIG Welding –SMD (CCTSMD) Technique

The developed SMD machine is used together with other parts of the SMD cell to construct an integrated work cell. The melting source was conducted using water cooled LINCOLN V320-T AC/DC welding machine Figure 3.8(a). It can supply welding current with the range of 5-320 A (see also the Appendix B). The TIG torch is LincTorch (LT18W) water cooled duty cycle, 100%, 1.8 cm cup size with 2% throated tungsten. The tungsten electrode distance from the tipping point till the ceramic cup is recommended to be between 4-9 mm [171]. An arc of plasma is formed between the electrode and the substrate [109].

The deposited material is supplied by a cold wire which is fed into the melting zone through an annular feed nozzle connected to PROMIG (4T) wire feed machine see Figure 3.8(b). It independently provides the cold wire to the DT, it can be manipulated manually. The DT was coupled to the pre-programmed SMDM through using special fixtures, the fixtures are responsible for giving the TIG electrode and wire feeds the desired feed angles and positions in order to obtain a stable process.

The inert gas used for this work was shield Argon with a 99.90%, which is used on the top side to avoid oxidation and other contaminants of the component due to reacting with atmospheric gases. The shielding gas (Ar) which surrounds the electrode and the weld pool, forms an inert atmosphere which protects the electrode and the workpiece from atmosphere oxidation and favor in the ignition and stability of the arc [171]. The shielding gas, flow rate, and other constant conditions are detailed in Table 3.2.

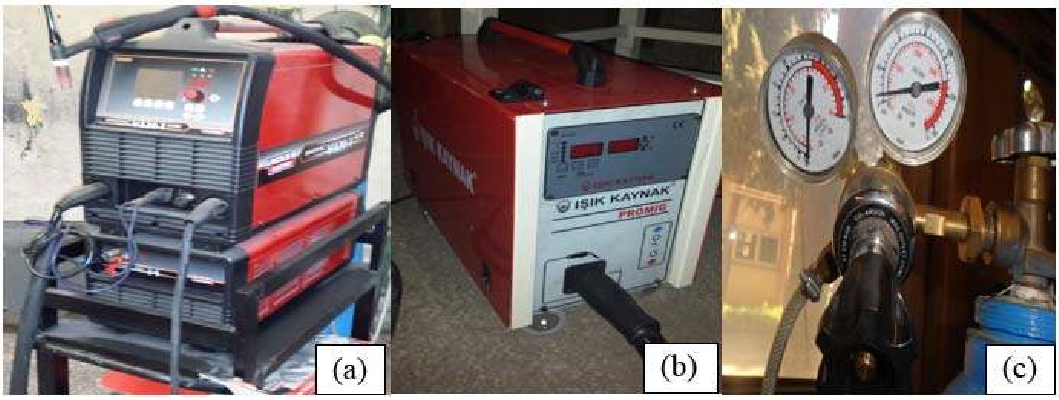

Figure 3. 8. (a) Lincoln TIG welding machine; (b) Wire feeder machine; and (c) Argon regulator Gauges.

Table 3. 2. Nominal pre-set operating conditions utilized for conventional TIG- SMD

Shielding Gas	Welding grade Argon
Flow rate	12 l/min
Pre-flow duration	3 Sec
Post flow duration	15 Sec
Starting current	30 A
Finishing Current	30 A
Polarity	DCEN (or DCSP)
Electrode	2% thoriated*, 3.2 mm diameter
Upslope duration	0.5 Sec
Downslope duration	5.5 Sec
Wire stick out	18 mm
Layer step height (hs)	0.5 mm for SS308lSi wire
Layer step height (hs)	1.0 mm for ER70S-6 wire

*The 2% thoriated electrode gives a good arc striking characteristics at low DC current values [170]

3.4.1 Preliminary Experiments for Developing the Process Model

The present SMD system has the capabilities to fabricate fully dense components using solid wire material in a layer by layer manner. Prior to the deposition, it is necessary to carefully tune the main process parameters and conditions such as arc current (I), arc length (L), travel speed (TS), and wire feed speed (WFS). It is essential to know that these factors have to be chosen as suitable as a combination to reach process stability. There are other important conditions which also affect the deposition quality such as shielding gas flow rate, the wire's feeding angle (α), wire feed direction), and position of the wire tip in the weld pool. These parameters control the amount of heat input, metal deposition rate, and the beads geometry.

Several experiments were done in order for tuning the main parameters and conditions. These preliminary experiments were done using filler wires of ER70S-6 and SS308LSi in order to know the main parameter and other conditions' limits and their effects on the bead geometry. All the experiments were conducted without using a chamber (no inert gas chamber). The method of experiment was selecting a combination of arc current and travel speed, deposit beads with different wire feed speeds starting from 0.8 m/min and increasing it by 0.4 m/min until the deposition process shows an excess of wire. Then the procedure was repeated for the other sets of arc current and Traverse speed.

3.4.2 Tuning the Feeding Angles and Deposition Directions

This section consists of the experiments of depositing specimens for evaluating the feeding angles and directions using the information shown in Table 3.3. On that point, there are various delivery angles as shown in Figure 3.9. Most of the researchers focused on the study of Laser and powder and laser with wires for cladding or single layer analysis [38, 75, 172]. Up to the author's knowledge, no detailed research has been done to study the influence of the wire feeding angle and feeding directions for the SMD-TIG method through multilayer parts. The main objective of this section is to study the effects of feeding angle amounts on the bead characteristics and process stability for the design SMD work-cell. The experiments were carried out using filler wire of 0.8 mm in diameter SS308LSi throughout producing straight walls with 20 layers high.

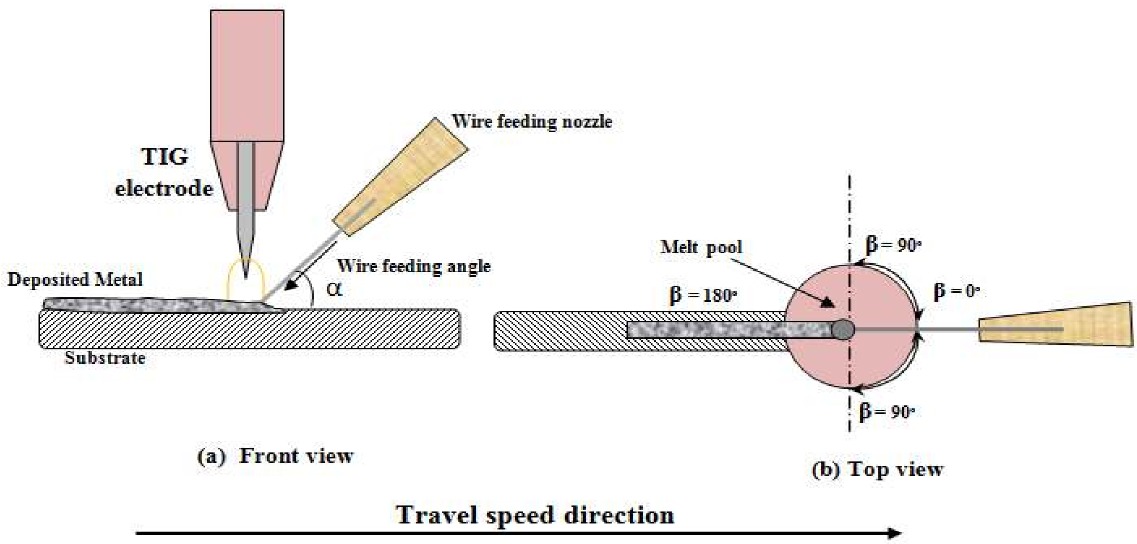

Figure 3. 9. Schematic shows feeding angle α (a); and (b) feeding directions, when β=0° front feeding, β= 90° side feeding and when β= 180° rear feeding direction.

Table 3. 3. The deposition parameters used for feeding angles analysis

Feeding direction	Current I (A)	Travel speed TS (mm/s)	Wire feed speed WFS (m/min)	Arc length L (mm)	Feeding angle α (°)
Front direction	150	4	2.0	5	30; 45
Side direction	150	4	2.0	5	30; 45
Rear direction	150	4	2.0	5	30; 45

3.4.3. Bead-On-Plate Experiments

There are two experiments have been carried out in this study using the setup described in sections 3.3.2 and 3.4:

3.4.3.1 Single –Layer Experiment for Finding the Process Window

In order to prevent the occurrence of the porosity, the substrates were prepared prior to the deposition process and restrained to the work- table of the SMD cell. The TIG torch was kept to be normal to the substrate surface in all the experiments. The beads on the plate were deposited next to each other parallel to the welding direction (moving in the x-direction). The distance between the bead centerlines was constant at 15 mm (see Figure 3.10). The deposits were approximately 180 mm in length. The substrates were preheated before depositing the beads. The temperature of substrates during deposition was kept about 200 °C to reduce the impact of the high cooling rate on the deposit profile. Temperatures were monitored using an industrial data logger device. Figure C.1 in appendix C shows an industrial data logger device used for measuring the temperature and record it with time. The objective of these experiments was to find the operational process window for a bead on a plate for SMD-TIG of stainless steel filler wires. The welding conditions used are summarized in Table 3.4. The other conditions were kept constant such as arc length L= 4 mm, α = 35°, forward feeding direction, and efficiency (η = 0.83) [124].

Table 3. 4. Summary of the welding conditions for experiments

Parameter(s)	Levels							
	1	2	3	4	5	6	7	8
Current (A)	140	160	180					
Travel Speed (mm/s)	2	3	5	7				
Wire feed speed (m/min)	1	1.5	2	2.5	3	3.5	4	4.5

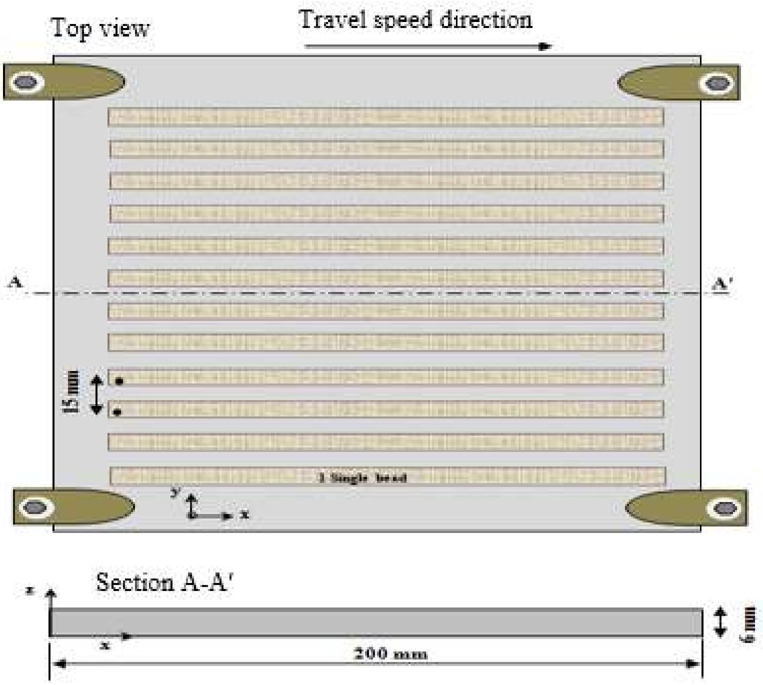

Figure 3. 10. Schematic illustration of the substrate restraining arrangement and single layer deposition (top and cross section views).

3.4.3.2 Effects of Travel Speed and Wire Feed Speed to Travel Speed Ratio on the Deposited Bead and Penetration Characteristics and Process Stability

In this study, the materials and welding consumables described in section 3.3 and section 3.4 were utilized to produce single layer deposits using wire diameter of 0.8 mm SS308LSi. Substrates were prepared before deposition as detailed in section 3.3.1 and clamped tightly onto the movable working table of the CAMDM. The objective of this experiment was to show the effects of TS and WFS on the bead geometry, the penetration, and the deposited bead humping (or to show the TS limits). Figure 3.11 shows the important output parameters of the deposited single layer such as bead height (H), bead width (W), and penetration depth (P). The experiment was conducted using non-pulsed current TIG welding method. The pre-set operating conditions utilized through this study are summarized in Table 3.5. In addition, welding condition used in this study can also be found in Table 3.6. The width, height, and penetration of the deposited beads were measured using calipers and digital vernier. The height measurements were determined by measuring the total height and subtracting the average thickness of the substrate plate. The measurements of width and penetration were determined after preparations the specimens for metallographic tests.

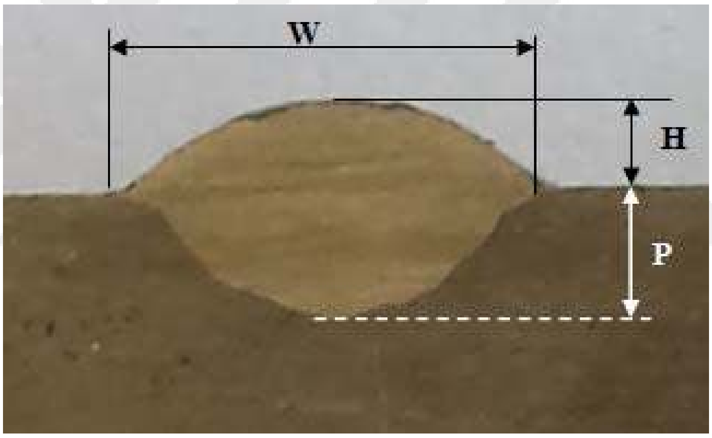

Figure 3. 11. Single bead transverse cross section showing the measured outputs.

Table 3. 5. Nominal pre-set operating conditions

Parameter	Value
Electric current (A)	175
Arc length (mm)	4
Feeding angle α	35°
Gas flow rate L/min	12
Feeding direction	Forward

Table 3. 6. Experimental welding conditions

Trial	TS	WFS/TS	WFS	Trial	TS	WFS/TS	WFS
1	0.18	4	0.72	13	0.18	10	1.8
2	0.3	4	1.2	14	0.3	10	3
3	0.42	4	1.68	15	0.42	10	4.2
4	0.54	4	2.2	16	0.54	10	5.4
5	0.18	6	1.08	17	0.18	12	2.16
6	0.3	6	1.8	18	0.3	12	3.6
7	0.42	6	2.52	19	0.42	12	5.04
8	0.54	6	3.2	20	0.54	12	6.5
9	0.18	8	1.44				
10	0.3	8	2.4				
11	0.42	8	3.36				
12	0.54	8	4.3				

3.4.4 Multilayer of Metal deposition experiments

The experiments were carried out using the materials and the SMD-work cell described in the sections 3.2, 3.3, and 3.4. Based on the results of the section 3.4.3, a new experimental plan depended to investigate multi-layer deposition geometries and other features. The welding wire used in these experiments is 0.8 mm in diameter SS308LSi wire spools. The substrates were prepared before deposition process and clamped to the water cooled copper backing plate. Before depositing the first layer, the substrate was preheated using the same electric arc at the same travel speed used in experiments until the temperature reaches nearly 200 ^{o}C. Continuous weld beads of approximately 180 mm in length were deposited and one layer at a time in the inverse directions (±X) (see Figure 3.12).

3.4.4.1 Effects of Main Process Parameters on the Deposited Bead Profile Characteristics

The most important factors for SMD are welding current I, travel speed TS, and wire feed speed WFS [46, 51, 54, 74,]. And also the wire feeding angles α [37, 172]. These factors have to be in the right combination for getting a stable and reliable process. In this study, another parameter was introduced, namely, the arc length L. The metal wire is fed into the melt pool so that it is important to choose the suitable arc power for the selected wire material. An SS308LSi wire electrode with 0.8 mm in diameter utilized through this experiment for the manufacturing of 20 layers high walls. The interface temperature was held constant at 200 ^{o}C for all produced specimens. The nominal pre-set operating conditions are summarized in Table 3.2 and Table 3.7. This experiment was planned with the DOE methodology. Taguchi methodology was used to determine the welding parameters with the best optimal weld pool geometry. It helps to determine best levels of the parameter used to analyze the best performance of the process. The Taguchi approach developed rules to carry out experiments, which further simplified and standardized the design of the experiment, along with minimizing the number of factor combinations that would be required to test for the factor effects. The values of the welding parameters at the different levels are listed in Table 3.8. In this study, an L16 orthogonal array with 16 welding process parameters combinations. Therefore, only 16 experiments are required to study the entire welding process parameters space using the L16 orthogonal array. The experimental layout for the depositing process parameters using the standard L16 orthogonal array is shown in Table 3.9.

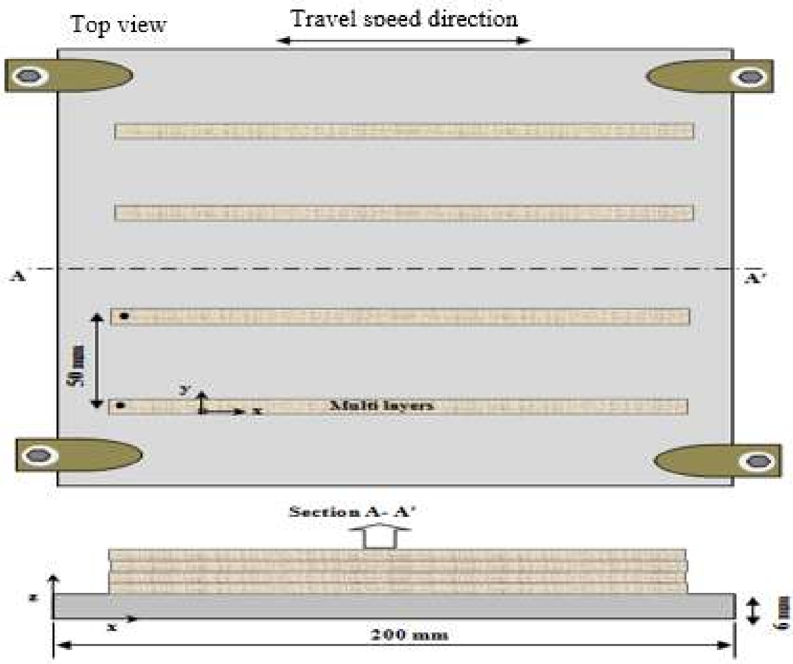

Figure 3. 12. Schematic illustration of the substrate dimensions and multi-layer deposition.

Table 3. 7. Nominal pre-set operating conditions

Parameter	**Value**
Feeding angle (α)	35°, with a reversed feeding direction
Number of layers	20
Arc efficiency (η)	0.83 [124]

Table 3. 8. Identified factors with levels

Input parameter		**Levels**			
	Unit	**1**	**2**	**3**	**4**
Welding Current (I)	A	125	150	175	200
Travel speed (TS)	mm/s	3	5	6	7
Wire feed speed (WFS)	m/min	1.5	2.0	2.5	3
Arc length (L)	mm	3	4	5	6

Table 3. 9. Experimental layout of parameters

Exp. No.	I (A)	TS (mm/s)	WFS (m/min)	L (mm)
1	125	3	1.5	3
2	125	5	2	4
3	125	6	2.5	5
4	125	7	3	6
5	150	3	2	5
6	150	5	1.5	6
7	150	6	3	3
8	150	7	2.5	4
9	175	3	2.5	6
10	175	5	3	5
11	175	6	1.5	4
12	175	7	2	3
13	200	3	3	4
14	200	5	2.5	3
15	200	6	2	6
16	200	7	1.5	5

3.4.4.2 Effects of Interpass Temperature and WFS/TS Ratio on the Bead Characteristics and Surface Quality

In order to investigate the influence of interface temperature (T) and WFS/TS ratio on the deposition characteristics such as total wall height H, effective wall width EWW, and machining layer thickness MLT (see Figure 3.13). The visual test was used to compare the side wall surface quality for some of one side photographed manufacturing specimens. The deposited material was a 0.8 mm in diameter SS308LSi wire that used to produce walls of 12 layers high. The experiment plan included the depositing of specimens at different substrate temperatures and WFS/TS ratios, whereas, the other factors were kept constant as summarized in Table 3.2 and Table 3.10. The experiment was done with a new DOE using Taguchi approach methodology. The identified factors with their levels are shown in Table 3.11 and Table 3.12 shows the standard L9 orthogonal array contains the experimental layout.

Table 3. 10. Nominal pre-set operation conditions utilized in non-pulsed TIG system

Current (I) A	Arc length (L) mm	Feeding angle (α) °	Layer number mm	Deposit length mm
175	4	35	12	100

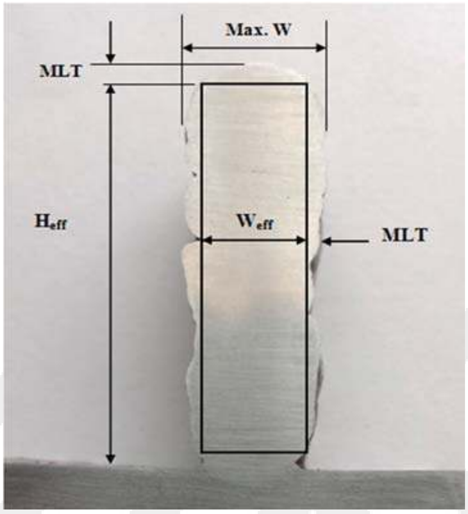

Figure 3. 13. Micrograph of a multi-layer transverse cross-section showing the measured output

Table 3. 11. Identified factors with levels

Input Parameter	Unit	Levels 1	2	3
Travel speed TS	m/min	0.18	0.30	0.42
WFS/TS	-----	6	8	10
Interpass temperature T	°C	40	200	300

Table 3. 12. L9 Experimental layout of factors with levels

Exp. No.	TS m/min	WFS/TS	T °C
1	0.18	6	40
2	0.18	8	200
3	0.18	10	300
4	0.3	6	200
5	0.3	8	300
6	0.3	10	40
7	0.42	6	300
8	0.42	8	40
9	0.42	10	200

3.5. Pulsed Current SMD (PCSMD) Technique

In the pulsed current deposition technique, the welding current rapidly alternates between two levels. The higher current limit is known as the peak (pulse) current, whereas the lower current state is known as background current. The fusion occurs at the pulse current state, while the background current I_b is necessary to maintain the electric arc.

In this study, the pulsed current TIG welding power source was water cooled LINCOLN V320-T AC/DC welding machine. The TIG torch is LincTorch (LT18W) water cooled duty cycle 100%. The primary parameters were shown in Figure 3.14. It can supply the following specifications with standard pulse current square waveform:

Peak current (I_p) = 5-320 A;
Back current (I_b) = 5-95 % of I_p
On-time-pulse = 5-95 %
Low frequency (LF) = 0.2-100 Hz
High frequency (HF) = 0.5- 2.5 KHz

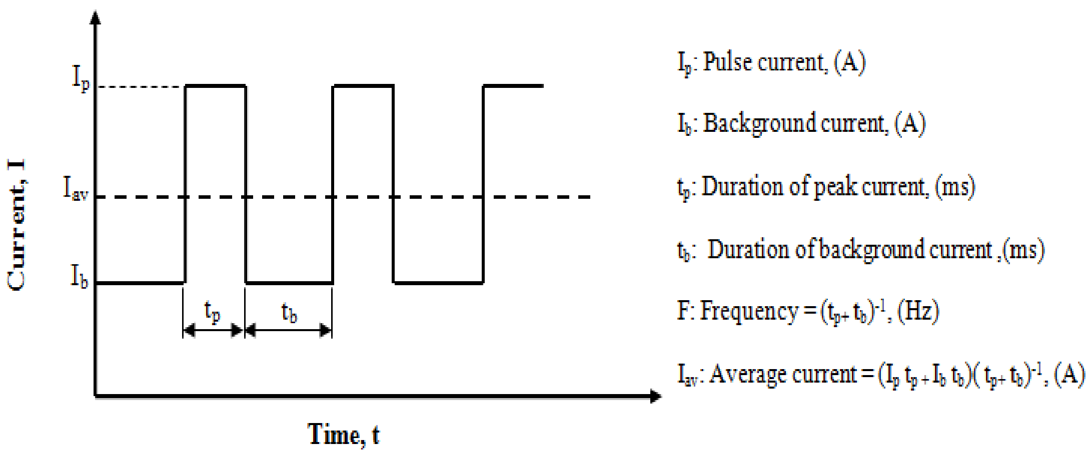

Figure 3. 14. Schematic diagram of a standard pulse current-time waveform in PTIG welding.

Table 3. 13. Preset parameters and operating conditions

Parameters and Consumables	Pulse- Current Machine Set-up Conditions
Arc length (L) = 5 mm	On-time-pulse = 50%
Wire feed speed WFS = 2.0 m/min and 2.5 m/min	Pre flow = 0.5 s Post flow = 0.2 s
Feeding angle (α) = 35°	Start current = 10A
Argon flow rate =12 l/min	Finish current= 51 A
Filler wire = SS308LSi	Downslope= 5.1 s
Wire diameter = 0.8 mm	Upslope = 0.3 s

3.5.1 Bead on Plate Experiments

The filler metal is fed into the melting pool by a cold- wire fashion, using PROMIG (4D) feeder machine. The welding electric source operation specifications and other pre-set parameters for all experiments are summarized in Table 3.13. Figure D (1-2) in Appendix D show the pulsed mode in the used machine.

In order to get defect free sample for testing a large number of trial runs were carried out using the same preparation method described in section 3.4.3.1 and also the deposits dimensions as shown in previous sections. The main objective of this experiment was to find out the feasible working limits of pulsed-current deposition parameters. Different combinations of parameters were tried. The bead profile, bead appearance, existence of defects, and other features were visually inspected in order to identify the real limits of the main parameters.

3.5.1.1 Single-Layer Using Different Welding Current and Frequency

In this experiment, take all the main parameters as constant to show the effect of the different combination of I_p and F on the deposition process. The travel speed (TS) was kept as 3 mm/s, WFS = 2.5 m/min, and I_p/I_b ratio = 2. The method for the experiment was: selecting a combination of I_p with different frequency starting from low frequency and increasing it until getting the maximum frequency of the machine. For example

For I_p: 120 A and F: 500, 1000, 1500, 2000, 2500.

The same procedure was repeated for the other combination.

3.5.1.2 Effects of frequency on the process stability and bead geometry

In order to investigate the effects of the pulse frequencies on the deposition process stability, surface quality, and deposit characteristics, a new experiment plan was carried out. The method of the experiment consisted of keeping all parameters as constant and varying the pulse frequency only starting from low frequency and increasing it to reach the maximum amount. Two experiments were done, the welding parameters used are shown in Table 3.14.

3.5.1.3 Effects of Travel Speed and I_p/I_b Ratio on the Process Stability and Bead Characteristics Using Low-Frequency (LF).

This experiment was carried out to investigate the effect of primary welding parameters of the current waveform, such as I_p, I_b, TS, and LF on the surface quality and arc stability of single layer deposits. This experiment was planned with the DOE methodology. Taguchi methodology was used to determine the welding parameters with the best optimal weld pool geometry. The values of the welding parameters at the different levels are listed in Table 3.15. In this study, an L9 orthogonal array with 9 welding process parameters combinations. The experimental layout for the depositing process parameters using the standard L9 orthogonal array is shown in Table 3.16.

Table 3. 14. Experimental parameters: (I_p of 160 A, TS of 3 mm/s, and WFS of 2 m/min) and II (I of 200 A, TS of 4 mm/s, and WFS of 2.5 m/min)

Exp. I	Exp. II	Exp. I	Exp. II	Exp. I	Exp. II
3	1.5	30	50	500	1000
5	3	50	70	600	1250
7	5	100	90	700	1500
9	10	200	100	800	1750
11	20	300	500	900	2000
17	30	400	750		2500

Table 3. 15. Process parameters and their levels

Input parameter	Units	Levels		
		1	2	3
Pulse current I_p	A	165	185	205
F	Hz	1.5	30	90
TS	mm/s	2	3	4
CR (I_p/I_b)	A/A	1.5	2	2.5

Table 3. 16. Experimental layout for the deposition process parameters

Exp. No.	I_p	F	TS	$R=I_p/I_b$
1	165	1.5	2	1.5
2	165	30	3	2
3	165	90	4	2.5
4	185	1.5	3	2.5
5	185	30	4	1.5
6	185	90	2	2
7	205	1.5	4	2
8	205	30	2	2.5
9	205	90	3	1.5

Table 3. 17. Process parameters and their levels

Input parameter		Units	Levels		
			1	2	3
Pulse current	I_p	A	165	185	205
Frequency	Fr	Hz	500	1500	2500
Travel speed	TS	mm/s	2	3	4
Current ratio	CR	A/A	1.5	2	2.5

Table 3. 18. Experimental layout for the deposition process parameters

Exp. No.	**I_p**	**Fr**	**TS**	**CR**
1	165	500	2	1.5
2	165	1500	3	2
3	165	2500	4	2.5
4	185	500	3	2.5
5	185	1500	4	1.5
6	185	2500	2	2
7	205	500	4	2
8	205	1500	2	2.5
9	205	2500	3	1.5

3.5.1.4 Effects of Travel Speed and I_p/I_b Ratio on the Process Stability and Bead Characteristics Using High-Frequency (HF)

This experiment was carried out to investigate the effect of primary welding parameters of the current waveform, such as I_p, Current Ratio (CR), TS, and HF on the surface quality and arc stability of single layer deposits. This experiment was planned with the DOE methodology. Taguchi methodology was used to determine the welding parameters with the best optimal weld pool geometry. The values of the welding parameters at the different levels are listed in Table 3.17. In this study, an L9 orthogonal array with 9 welding process parameters combinations. The experimental layout for the depositing process parameters using the standard L9 orthogonal array is shown in Table 3.18.

3.5.2 Multilayer Deposition Experiment

Following the study of single bead and according to the effects of the main parameters on the bead geometry and deposit quality as shown in section 3.5, a new experiment was followed to study the multi-layer deposition characteristics. Using the information in the previous Tables, the TIG-P machine was employed in the experiments of producing walls at different frequencies to produce multi-layer specimens.

3.5.2.1 Effects of Main Process Parameters on the Process Stability and Bead Characteristics Using Low-Frequency (LF)

This experiment was carried out to investigate the effect of primary welding parameters of the current waveform, such as I_p, I_b, TS, and LF on the surface quality and arc stability of single layer deposits. This experiment was planned with the design of the experiment, DOE using Taguchi approach methodology to determine the welding parameters with the best optimal weld pool geometry. The values of the welding parameters at the different levels are listed in Table 3.19. In this study, an L9 orthogonal array with 9 welding process parameters combinations. The experimental layout for the depositing process parameters using the standard L9 orthogonal array is shown in Table 4.20.

3.5.2.2 Multilayer Walls for Test Specimens

Once an initial understanding of the influence of the process parameters on the build quality was developed, large walls by 1 bead wide were built by adopting a reverse deposition direction. The mechanical and metallographic properties specimens were extracted. The sample of tensile and hardness are labeled by H when the tensile force is parallel to the deposition direction and by V when it is parallel to the building direction, i.e. perpendicular to the layer as shown in Figure 3.15, where T, HR, M denotes samples taken for tensile, Rockwell hardness, and microstructure respectively. The label H, V, T, B refers to the horizontal direction, Vertical direction, top region, and bottom region respectively. A wall was built for the continuous current TIG- SMD technique, Pulsed current TIG with low frequencies, and pulsed current TIG with high frequencies. Table 3.21. Shows the process parameters used for producing these walls.

Table 3. 19. Process parameters and their levels

Input parameter	Units	Levels		
		1	2	3
Pulse current I_p	A	165	185	205
Frequency Fr	Hz	1.5	30	90
Travel speed TS	mm/s	2	3	4
Current ratio CR	A/A	1.5	2	2.5

Table 3. 20. Experimental layout for the deposition process parameters

Exp. No.	I_p	Fr	TS	CR
1	165	1.5	2	1.5
2	165	30	3	2
3	165	90	4	2.5
4	185	1.5	3	2.5
5	185	30	4	1.5
6	185	90	2	2
7	205	1.5	4	2
8	205	30	2	2.5
9	205	90	3	1.5

Table 3. 21. The experimental parameters used to build walls in order for extracting different test samples

		Parameters						
ID	Process type	I_p A	TS mm/s	WFS m/min	Arc length mm	Feeding angle °α	I_b A	Fr Hz
1	CCSMD	175	4	3	4	35	-------	-----
2	PCSMD	175	4	3	4	35	75	5
3	PCSMD	175	4	3	4	35	75	30
4	PCSMD	175	4	3	4	35	75	500
5	PCSMD	175	4	3	4	35	75	2000

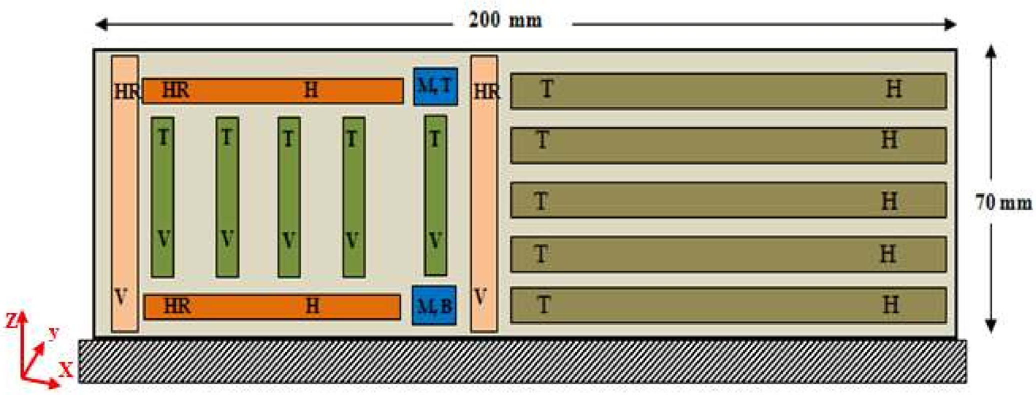

Figure 3. 15. Schematic diagram of a Large SS308LSi wall built with reversed direction, orientations and positions of the tensile and hardness samples

3.6. Deposition Path Planning Strategies

In this section, the current experiment highlights capabilities and limitations of the TW-SMD system through investigating the path planning strategies used for generating the most suitable deposition trajectories of the SMDM. Various path patterns were planned and implemented in the present study such as those used for depositing the tubular components, stiffener panels, different features of the hollow filling area, and solid filling area components.

3.6.1. Experimental Pattern and Procedure

3.6.1.1 3D TIG Welding Based SMD Process

The TW- SMD system consists of SMD machine and its control system, water cooled LINCOLN V320-TAC/DC welding machine, and deposition material is supplied by a cold wire which is fed into the melting zone through an annular feed nozzle connected to PROMIG (4T) wire feed machine. The shielding gas suggested in this study was Argon of 99.9% purity with a flow rate of 12 l/min. The deposited material was ∅0.8 mm stainless steel wire. Its grade was chosen according to AWS A5.9-95 specification so that the wire grade is ER308LSi. The SMD machine, which is a computer aided metal deposition machine (CAMDM), consists of a three axes movements actuated by 3 stepper motors.

In this system, the actual paths are directly calculated from CAD geometry and so time-consuming and the tedious task of teaching the robot or other CNC machines can significantly be reduced by the present SMDM software. In order to reduce the or eliminate the cumulative error, the SMDM paths can be adjusted manually after deposition of few layers. The typical deposition parameters used in experiments are shown in Table 3.22. These parameters were chosen depending on previous experiments.

Table 3. 22. Process Parameters Used for TIG-SMD Experiments.

	Welding current (A)	Travel speed (mm/s)	Wire feed speed (m/min)	Arc length (mm)	Feedin g angle (°)	Interpass temperatur e (°C)
Value	175	4	3	4	35	300

3.6.1.2 Model Preparation (CAD Program and Slicing Strategy)

The Figur 3.16 shows the main steps used for building up the parts in the present system. After the model is validated, it is then scaled and oriented with respect to the work table and the substrate sizes, taking into account the wire feed direction, feeding angle, and arc length (the distance from the substrate to the electrode tip). Thereafter, the model is sliced from bottom to the top with a suitable step height (hs) for each layer. The hs was selected depended on the set of the process parameters and the parameters as shown in Table 3.22, the hs is within the range (0.5-1.0 mm).

The simulation and implementation of SMDM were done which shows capable of creating deposition paths for complex shapes.

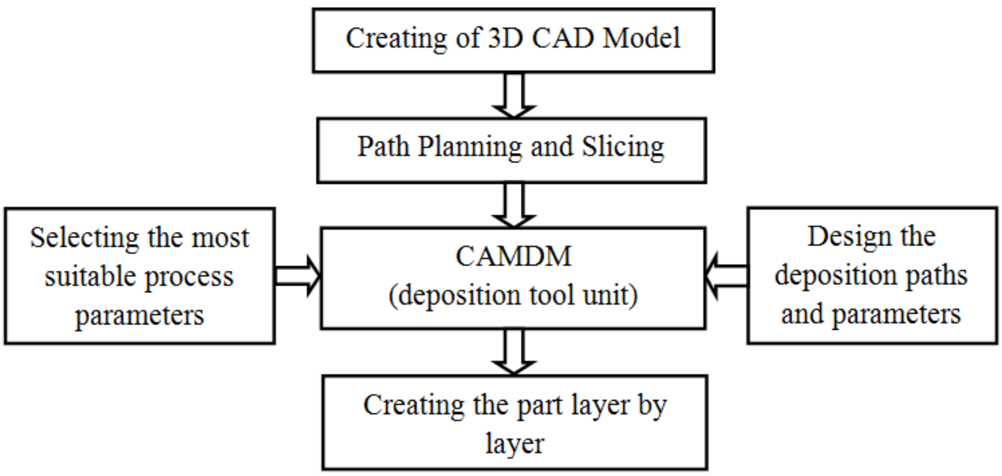

Figure 3. 16. Building up the part flow chart in SMD

The architecture of the block diagram used for studying and controlling the process is constructed by CAD module, PC Interface Program, Control Unit, and CAMDM as shown in Figure 3.17. The PC- interface program is a user interface panel, which is projected with the graphical user interface development environment (GUIDE) of MATLAB®.

The control unit is constructed to receive commands from computer programs and to send the current position of machine axes as a feedback. The connection between the control unit and the computer is by USB port. The control unit has an **open-source** simple microcontroller board (Arduino Mega 2560). The SMDM path generation has been created in MATLAB program.

The CAD model is firstly transformed by a GUIDE program to be input to the user interface after slicing the CAD model into ISO-line paths and building a sequence of the part. The operator can define the main points of shape, layer height, and a number of layers. Afterward, a translational transform between points is created (x-y path), the layers are built by increasing z-axes by layer height for the x-y path. The solid model is expressed as points (x, y, z). The pattern points can be saved as the m-file type and can be loaded on machine user interface program for experiment implementation. The paths can be translated into binary format and uploading the binary code into the SMDM controller. PC-Interface Program is a computer aided manufacturing (CAM) program, which is used for controlling machine torch movements relative to machine workspace. The program receives the CAD output file (m-file) and converts it to low-level machine code. The user can control machine manually by JOG, apply machine zeroing, monitor the change of the parameters of the machine, and load sequential program for the machine.

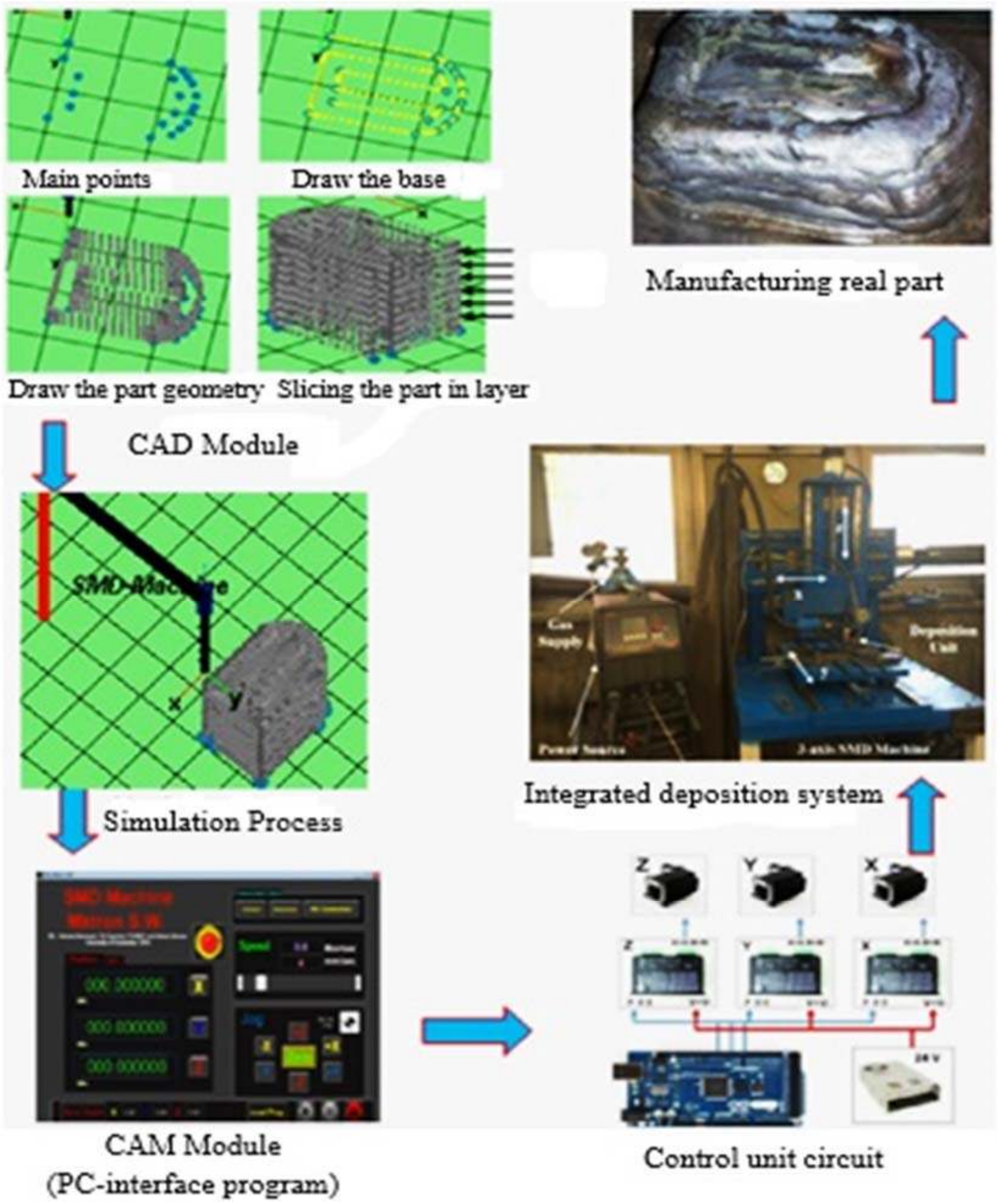

Figure 3. 17. Main units, integrated into the CAMDM system

3.6.1.3. Deposition-Path Strategy of the CAMDM

During TW- SMD process, the metal components are built by moving the deposition tool (DT) to melt the cold wire, which is fed externally into the melt pool, and fill all areas of the part on the metal substrate in layer by layer fashion. In order to reduce the surface roughness and errors, the outline of the path pattern was carried out using the contour/spiral pattern, whereas the inner space is filled with raster, zigzag, or spiral approach. From another side, the start and end points during the deposition process consider as heat concentration points and so the bead at these points seems wider and sometimes it over flows. Therefore, it is necessary to minimize the quantity of the arc start-ends (arc ignition and re-ignition) to as minimum as possible in this technique, thereby the precision improved and the total production time will be shortened.

3.6.2 Features of the Deposited Components

The present system is capable of producing various designs of tubular products, hollow parts, solid parts and other features such as walls, profile of blade part, and omega shape part.

i. Crossing Wall Feature

The literature [56] studied the possibility of using the MIG welding which associated with the robotic system to produce different designs for stiffeners panels, especially the wall crossing. They showed that there is the difficulty of producing this feature due to the buildup of peaks where the weld bead overlaps at the crossing points. So that they used a path pattern of opposite angles as shown in Figure 3.18. In the present study, the system controlling process allows overcoming the aforementioned problem it the cross wall feature. Two alternative patterns are prepared to deposit the cross wall feature as shown in Figure 3.19. The pattern represents in Figure 3.19(b) is the most suitable one since it leads to reduce the total deposition time, produce each layer with one arc ignition and can continue for the sequential layers, make the deposition process more stable, and eliminate the existing of the peak in the overlap pattern. The Figure 3.20 shows the CAD drawing and the real deposited crossing wall component.

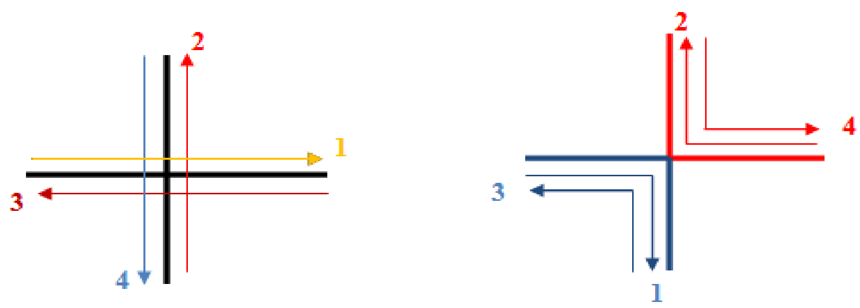

(a) (b)

Figure 3. 18. Deposition patterns of cross feature. (a) overlap pattern; (b) opposite

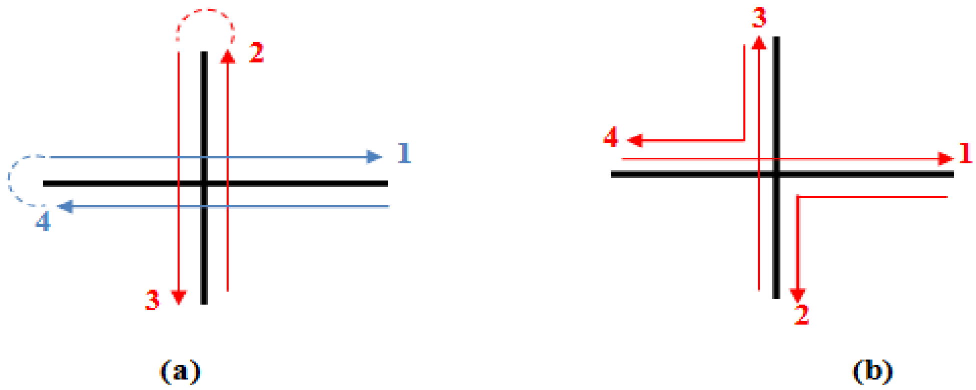

Figure 3. 19. Deposition patterns of cross wall feature, (a) overlap with two start-ends of the arc; (b) overlap pattern with continuous ignition arc.

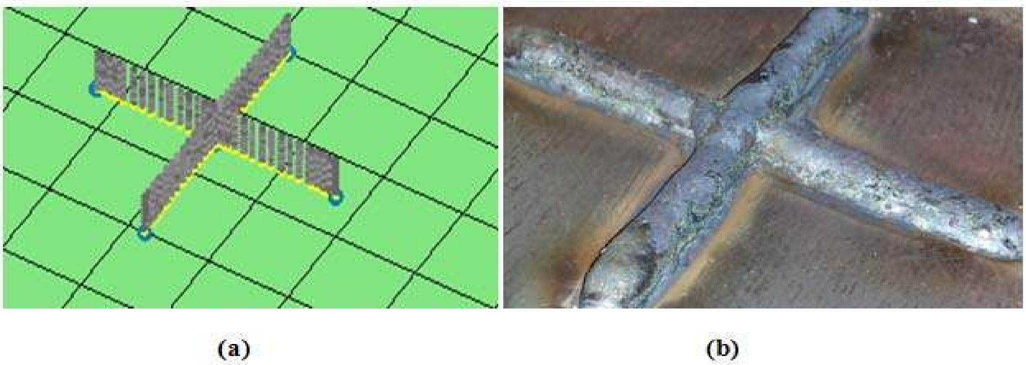

Figure 3. 20. Examples of crossing wall feature produced using the continuous ignition arc, (a) CAD drawing; (b) deposited part

ii. Solid Filling Area Feature Parts

Figure 3.21 presents a comparison of the deposition methods used for the solid filling area of the part shown in Figure 3.21(a), which was produced using some of the additive manufacturing methods namely, the laser assisted direct metal deposition (DMD) [107] as shown in Figure 3.21(b), MIG welding based shaped metal deposition [79] as shown in Figure 3.21(c), and the current CAMDM system as shown in Figure 3.21(d-f). In order to compare the two types of path patterns, deposition of solid circular feature part was performed using spiral pattern and zigzag pattern as shown in

Figure 3.22 (a-b) respectively. Figure 3.22 (c) presents the first few layers of the real deposited part

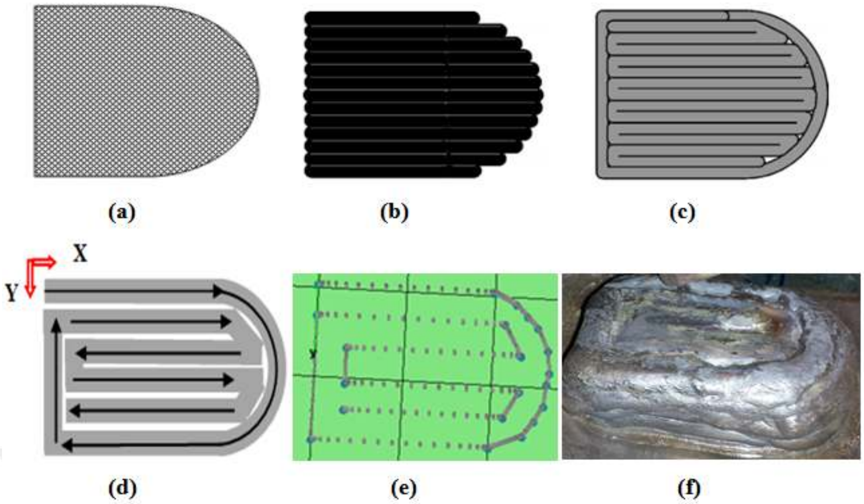

Figure 3. 21. (a) A solid filling part; (b) raster file for DMD; (c) contour and raster fill for MIG- SMD; (d) combined paths fill for TW-SMD; (e) CAD drawing; and (f) real deposited part using TW-SMD method.

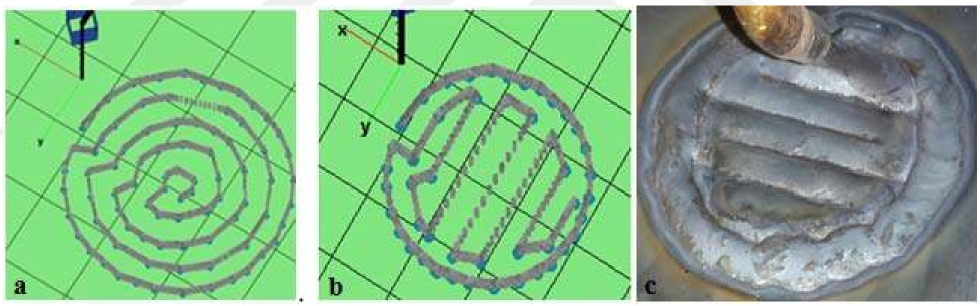

Figure 3. 22. Combined path pattern for solid filling cylindrical part, (a) CAD drawing of the combined path pattern by spiral strategy; (b) CAD drawing of the combined path pattern by zigzag/raster strategy; and (c) the first deposited layers using the zigzag/raste

iii. Hollow Filling Area Feature Parts

In order to compare the two types of path patterns, deposition of the hollow rectangular part was performed using spiral pattern and zigzag pattern. The deposition starts from the upper right side and complete the outline of the part configuration and then using either the spiral or zigzag movements to complete the filling of the first layer of the deposited area, thereafter reversed direction for deposited the sequential layers and so on. Figure 3.23 shows the generated deposition path used to manufacture a hollow filling area of a square part using the spiral pattern. While the Figure 3.24 illustrates another path pattern used to manufacture the same part using the combined pattern of contour and zig-zag paths. The real deposited layer of this part is shown in Figure 3.24 (c). Spiral path pattern was most suitable for depositing a hollow filling circular feature as shown in Figure 3.25.

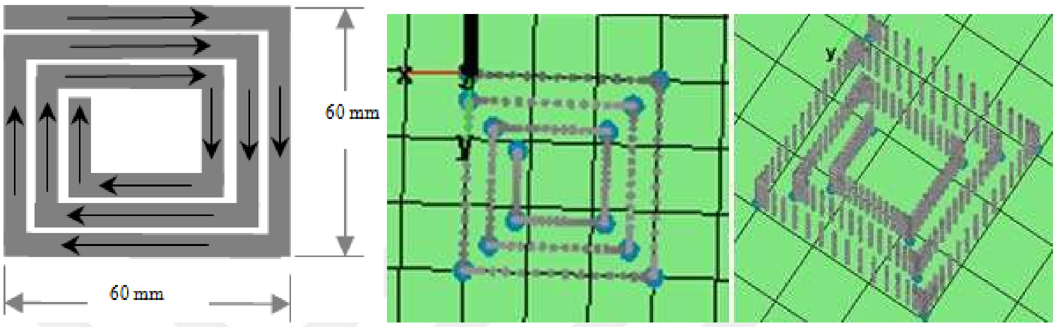

(a) (b) (c)

Figure 3. 23. Spiral path pattern for hollow filling the rectangular part, (a) spiral path pattern; (b and c) the CAD drawing and layer slices.

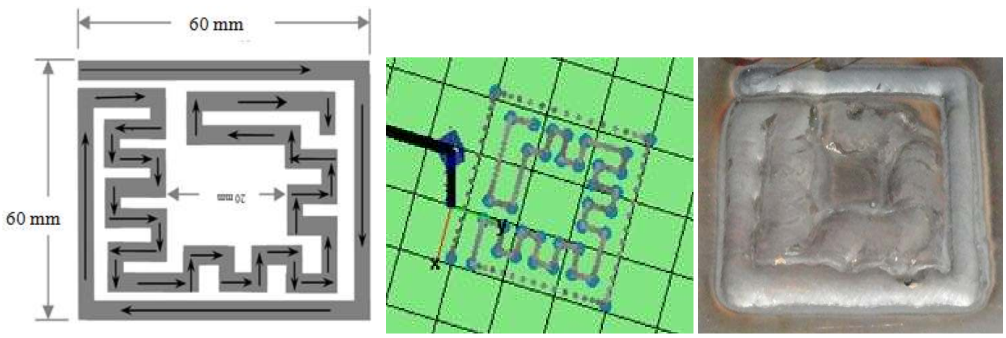

(a) (b) (c)

Figure 3. 24. Deposition of hollow filling rectangular part, (a) contour and zigzag/raster path pattern; (b) the CAD drawing and (c) single deposited layer using the TW-SMD method

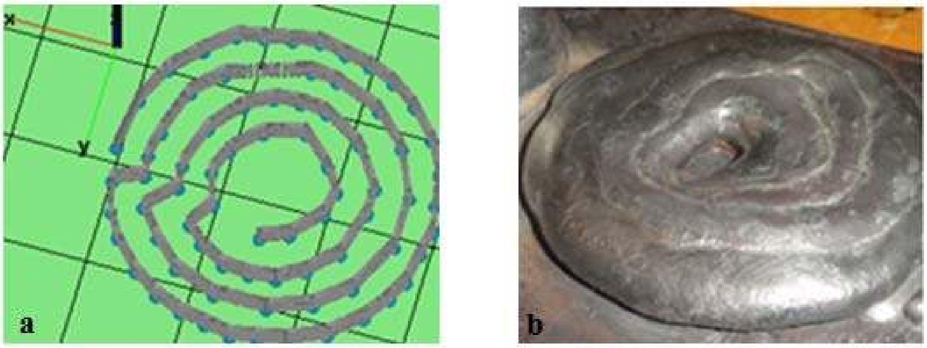

Figure 3. 25. Path pattern for hollow filling cylindrical part, (a) CAD drawing of the combined path pattern by spiral strategy; (b) the real deposited part using the spiral path pattern after some of the layers.

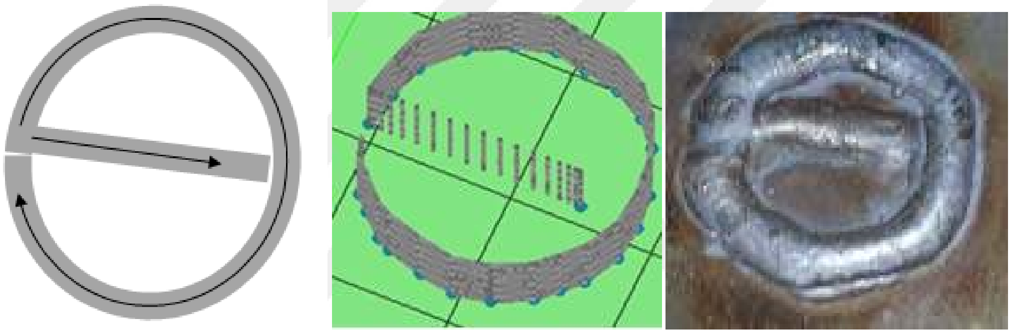

Figure 3. 26. Production procedure of a tubular part with an internal obstacle.

Figure 3. 27. Photograph of component in the form of (a) a zig-zag wall; (b) a straight wall; and (c) a low Tube with rectangular base.

iv. Tubular and Wall Parts

The present system can be used to fabricate different tubular components such as square, rectangular, circular and so on. Figure 3.26 shows the procedure followed to produce a cylindrical component having an internal obstacle. Additionally, all tubular, zig-zag and straight shapes (see Figure 3.27) can be manufactured using the CAMDM system.

v. Manufacturing of Industrial Parts

Finally, the current system can be used to fabricate special parts as near net shaped components, such as a profile of blade (Figure 3.28) and omega shape part (see Figure 3.29).

3.7. Production 3-D TIG Part from CAD to Finishing Real Part Processes

In this section, the common methods to fabricate a typical aerospace part was described. The necessary steps followed through building an SMD component from CAD model to real component were investigated. The main methods for making this part fall into three broad categories:

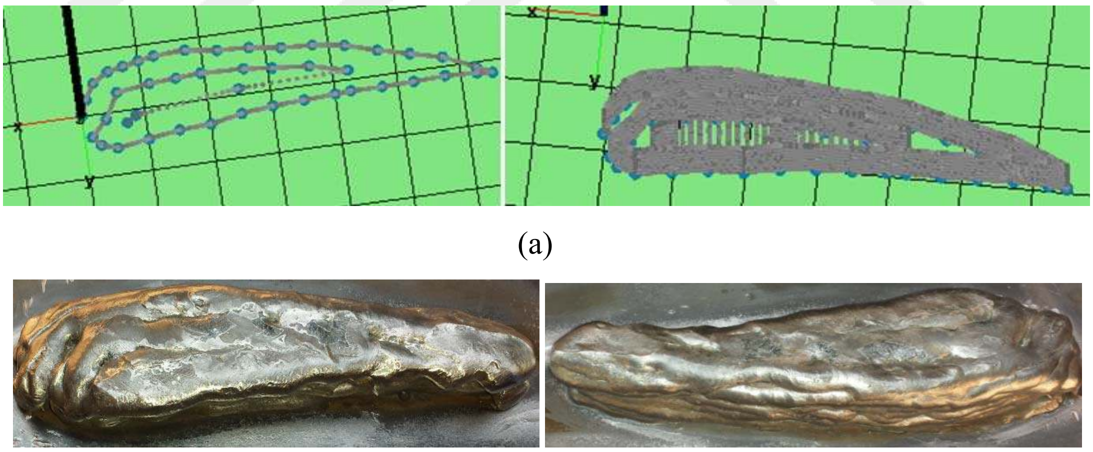

(a)

(b)

Figure 3. 28. Combined path pattern for profile of blade part, (a) CAD drawing of the combined path pattern by spiral strategy; (b) the real deposited part using the spiral path pattern.

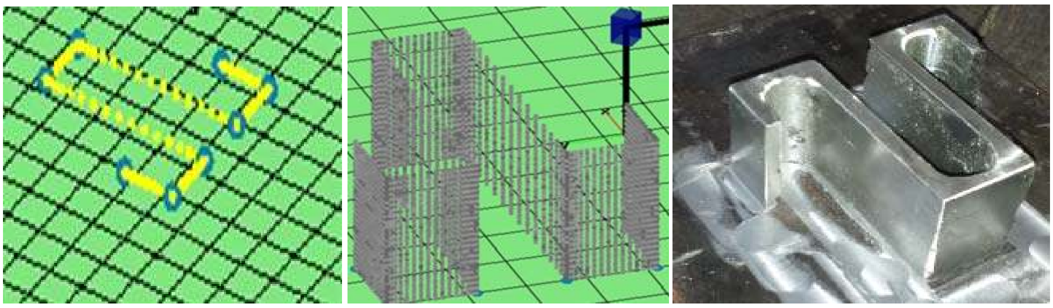

(a) (b) (c)

Figure 3. 29. The procedure of producing the omega (Ω) part, (a) part path planning, (b) part creation, and (d) fabricated part.

3.7.1. Machining Processes (Subtractive Processes)

In this method, starting by cutting a piece of rectangular cross-section solid block of SS308LSi material. Using machining processes to produce the final finished part. This method always wastes a large amount of raw material and coolant and has high energy use. It can be very expensive to produce the component in terms of both financial and environmental cost; additionally, there is also a long production lead time.

3.7.2. Forming Processes (Forging and Casting).

The forging and casting processes are used to produce near net shaped components, which usually at the finished features by machining processes. So less raw material is used, therefore, less machining is necessary and less coolant, tooling, and energy use. It is knowing that casting and forging processes require a large amount of energy to create. Also, these techniques have process constraints, this means that they may be unable to produce very near shaped components. These methods are not flexible since they are expensive and time-consuming in molds and dies preparation.

3.7.3. Additive Layer Manufacturing (ALM) Technology

In AM, there are two types of net-shaped part processes namely, direct laser deposition (DLD) and SMD techniques [30, 47, 53, 173].

3.7.3.1. AM Based on Powders Material Method

These can be hazardous to work with. These methods are well suitable for depositing small components with fine details and high resolution but they are very expensive and limited for large scales.

3.7.3.2. AM Based on Wire Material Method

SMD can avoid many of the aforementioned problems since it can be as a newly net or near net shaped part production technique compared to the modern ALM techniques. It is able to produce large structural components, especially for aerospace parts by building them up from welded wire. This technique reduces raw material and removes the need for expensive tooling. SMD components require minimal machining for finishing the surface. So there is less energy use and coolant. However, the fabricated part usually requires more extensive machining than the powder base AM method.

3.7.4. 3-D TIG SMD Component Procedure

The experimental procedure consists of the following steps:

3.7.4.1. CAD Software

In the first step, CAD software covers 3D object modeling based on CAD drawing, planning and slicing of the pattern in uniform thickness layers. The CAD drawing is imported using an on-line programming method. So the desired geometry according to the CAD-specification is sliced into layers of uniform height. For each layer the paths along which the beads should be deposited to fill the layer. The input data for building up the CAD drawing of the omega part (Ω) part by the user through interning following points coordinates.

[0, 0, 0; -2,0,0;-2,2,0;4.8,2,0;4.8,4,0;-2,4,0;-2,6,0;0,6,0]

Step height (H) = 1 mm and number of layers (L) = 48

These data will specify the sites of the main points in the (Ω) part as shown in Figure 3.30(a), then the CAD program will star to draw the baseline of the part (the first layer) as shown in Figure 3.30(b). Whereas the Figure 3.31 refers to the CAD screen with complete (Ω) part drawing.

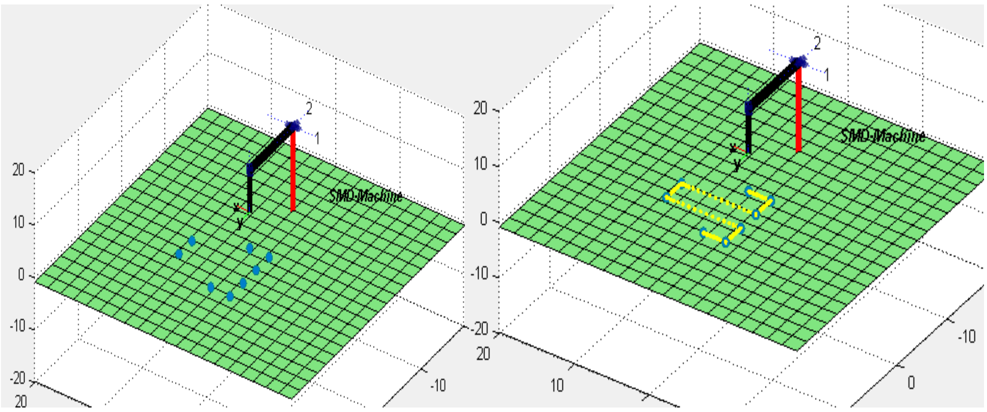

Figure 3. 30. (a) Shows the sites of the input points. (b) Drawing the base of the part to be deposited

.

3.7.4.2. SMD Path Planning and Pattern Slicing and Simulation

For the omega shape part (Ω) project, an SMDM path generation was designed depending on the one-layer (2-D) technique with one (start-end path) as shown in Figure 3.32. Applying the reverse direction method for the subsequent layer with a step height of 1 mm for each deposited layer. The CAD model is firstly transformed by a GUIDE program to be input to the user interface after slicing the CAD model into ISO-line paths and building a sequence of the part. The pattern points (CAD program) can be saved as the m-file type and can be loaded on machine user interface program (CAM) program for experiment implementation. Figure 3.33 shows the CAD model after slicing it into layers which represent the paths of the designed model to be built.

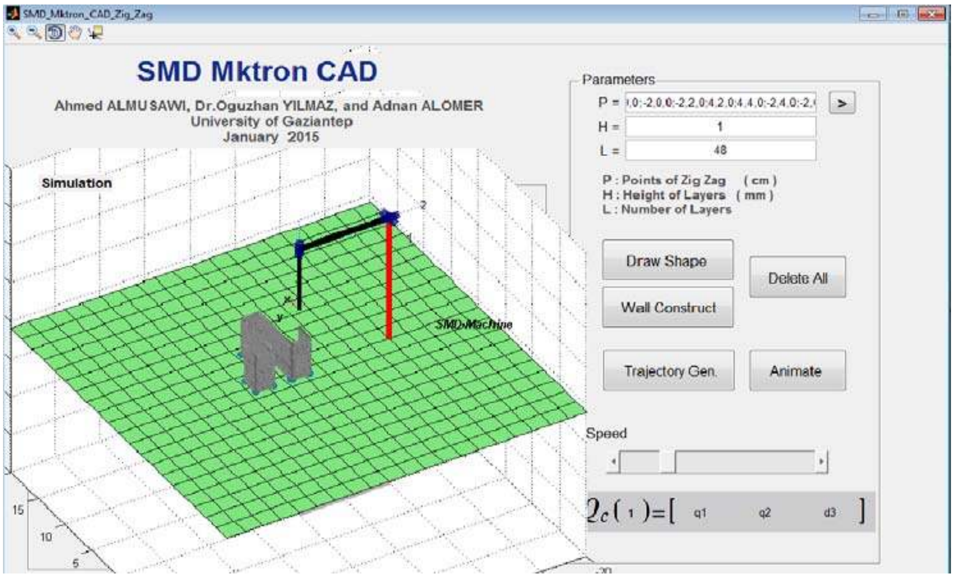

Figure 3. 31. CAD drawing of the omega part with 48 layers and step height of 1 mm.

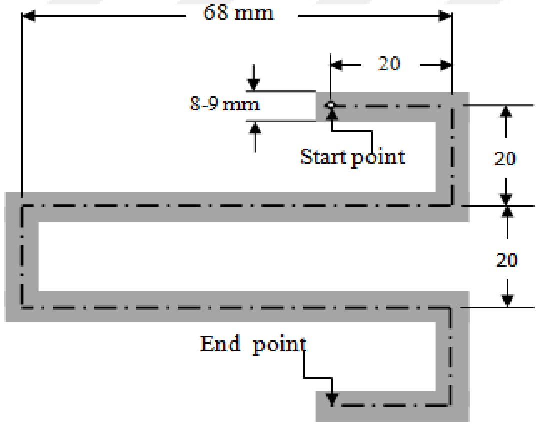

Figure 3. 32. Schematic representative of the path planning used for deposited the (Ω) part

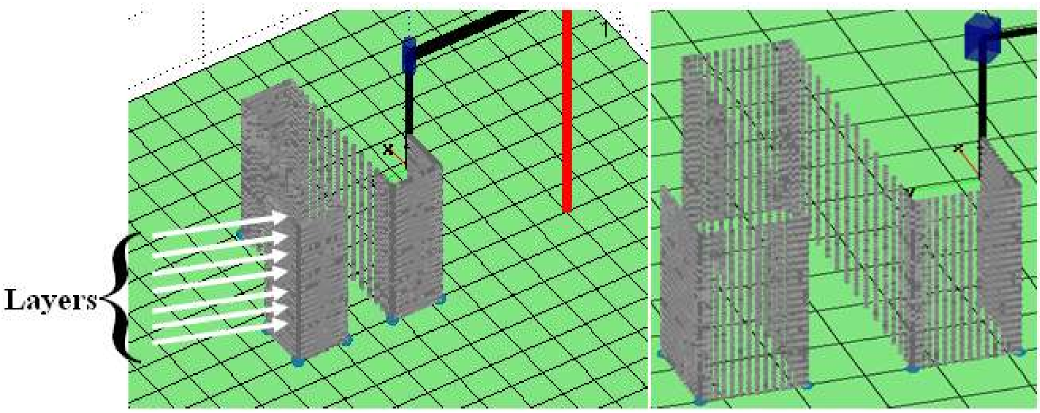

Figure 3. 33. The slicing of the CAD model into uniform layers from the base to the top

3.7.4.3. The Omega Shape (Ω) Part Deposition Process (CAM Program)

This step represents the real deposition process, which consists of the controlling of the mechanical system (SMDM), and the deposition parameters which refers to the controlling the welding parameters and wire feed system as well as the cooling system and the temperature control. The material used is austenitic stainless steel (details of the SS 308LSi has been described in section 2.10). By controlling the deposition process parameters, it is possible to control the deposition dimensions especially the wall width and wall side roughness. From the aforementioned experiments, the suitable set of combination of the parameters for deposing the part is as shown in Table 3.23. The expected wall width is within the range (8-10) mm.

The computer aided manufacturing (CAM) program, which is used for controlling machine torch movements relative to machine workspace. The program receives the CAD output file (m-file) and converts it to low-level machine code. Using the CAM program to control the SMDM movements and paths during the deposition process (see Figure 3.34)

Table 3. 23. The deposition process parameters

Parameter	Unit	Symbol	Value
Welding Current	A	I	170
Travel speed	mm/s	TS	4
Wire feed speed	m/min	WFS	3.5
Arc length	Mm	L	4-5
Feeding angle	º	A	30
Interpass temperature	°C	T_b	300

Figure 3. 34. PC-interface program (CAM) shows the amount of travel speed used (TS) = 4 mm/s.

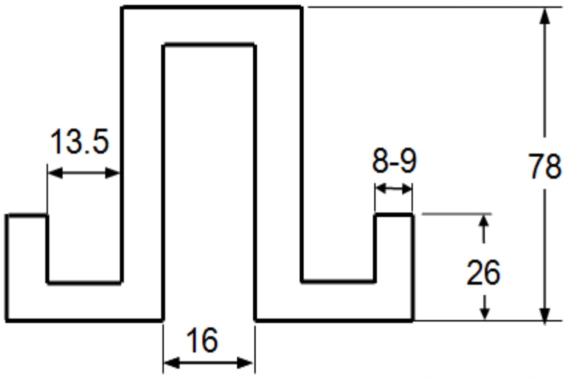

Figure 3. 35. Shows the real deposited part dimensions after the deposition process (dimensions are in mm).

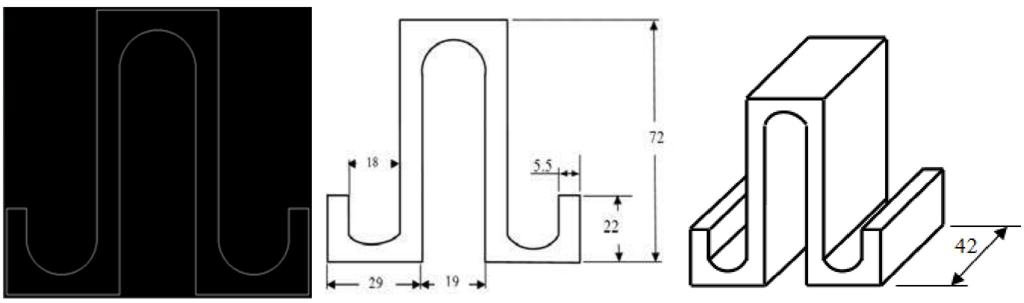

(a) **(b)** **(c)**

Figure 3. 36. (a) Diagram represents the dimensions (in mm) of the part used for preparing the CNC milling machine program; (b) sketch illustrates the cross-section of the final part after finishing processes; (c) Sketch shows the isometric view of the part.

3.7.4.4. Machining Process

In this step, the deposited part which has the average dimensions shown in Figure 3.35 was machining by preparing a suitable CAM program. Using CNC milling machine to finishing the deposited part to final dimensions as shown in Figure 3.36. The real finished omega part is shown in Figure 3.37.

Another CAM program was prepared to machine the same omega part from a solid block by machining processes. The first step was cutting a piece of the rectangular cross-section solid bar with dimensions as shown in the Figure 3.38. Then machining the part to the final dimensions as shown in Figure 3.36.

Figure 3. 37. Real deposited part after machining process

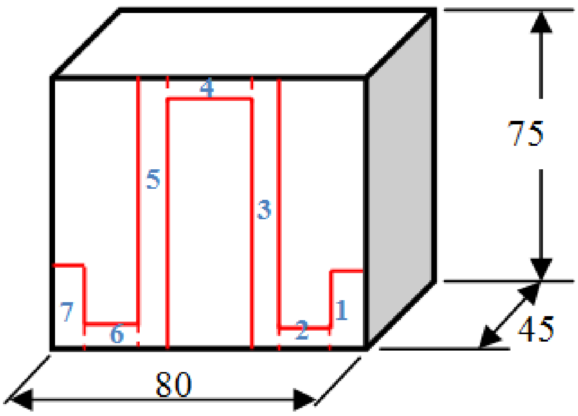

Figure 3. 38. Schematic illustration the dimensions of a solid block which used for machining the part. All dimensions are in mm.

3.8. Metallographic, Radiography, and Mechanical Properties of SMD Test Samples

3.8.1. Characterization of Microstructure Tests

The deposited samples were removed from the substrates and sectioned in the traverse cross section in the y-z plane and in the longitudinal direction (in the x-z plane). Macro- and microstructure analysis was carried out by optical microscopy. Samples with different sets of parameters, from different locations and prepared using CCSMD and PCSMD processes are discussed here.

3.8.1.1. Optical Microscopy

Optical microscopy was used to analyses the macro and microstructure of the deposited specimens. A microscope with a camera was used to investigate the unetched and etched microstructures. Sometimes, during the cutting of specimens severe thermal damage on the surface may occur which causing microstructural phase changes and as a result misleading metallographic characterization. To prevent occurring this problem a correct procedure was used with suitable speed and sufficient cooling fluid and the surface layer of the specimen is removed by grinding machine using abrasive silicon carbide cutting wheel. Samples were mounted in non-conductive black epoxy mounting resin. Large specimens were prepared without using the resin. Grinding was carried out by an automatic grinding/polishing machine. Mirror-smooth specimens for metallographic studies were prepared by first grinding with SiC abrasive papers at 150 rpm, for 1-2 minute, at each stage. The following grinding papers were used: 120 → 240→ 400→600→1200→2000. For the polishing stages, the samples were polished with 6, 1 µm diamond abrasive. In order to obtain a good polishing surface free of scratches, the preparation time varied depending on the specimen area. Manual polishing consists of three stages: rough, intermediate, and final polishing. Rough polishing is performed on a high-speed polishing wheel covered with a lintless rayon or silk cloth as shown in appendix F.1, using medium pressure and levigated 1- or 3-µm α-alumina (Al2O3). After the final polishing step, samples were cleaned using tap water and then with ethanol after that dried in hot air. Finally, the specimens were chemically etched with a suitable etchant. All specimens were electro-etched using 10gr oxalic acid with 100 ml distilled water at 9 V for 30-60 S. Olympus optical microscope with 60-400X magnification was used attached to digital camera for microscope replaces one of the microscope's eyepieces (see appendix F.2). The microstructures were revealed, examined and photographs were taken.

3.8.1.2 Effects of Process parameters on Metallography Aspects of CCSMD

In order to investigate the effects of main process parameters on the macro- and microstructure of the deposited samples using CCSMD process, Table 3.24 presents the set combinations of these parameters used for producing the testing samples. To investigate effects of TS on Microstructure of the specimens prepared using CCSMD, the other parameters were kept as constants and only the TS was changed as shown in Table 3.24 (1st case). Thus, to investigate the effects of Hi on the microstructure, two experiments of differing rent Hi amounts were done as shown in Table 3.24 (2nd case). Additionally, two experiments were carried out to investigate the effects of deposition rate on the microstructure of the specimens prepared using CCSMD process as shown in Table 3.24 (3rd case). To investigate the effects of the substrate temperature on the microstructure, two experiments were done using the sets of parameters shown in Table 3.24 (4th case).

Table 3. 24. Process parameters used for preparing the test specimens of CCSMD

Case	I (A)	WFS (m/min)	TS (m/min	Tsub. (^oC)
1st	175	3.5	0.24	200
	175	3.5	0.42	200
2nd	150	3	0.36	200
	200	2	0.30	200
3rd	175	2	0.30	200
	175	3.5	0.30	200
4th	175	3	0.30	40
	175	3	0.30	300

3.8.1.3 Effects of Process parameters on Metallography Aspects of PCSMD

In order to investigate the effects of main process parameters on the macro- and microstructure of the deposited samples using CCSMD process, Table 3.25 presents the set combinations of these parameters used for producing the testing samples.

To investigate the effects of traveling speed of melting source on the microstructure, two experiments were carried out using the process parameters shown in the Table 3.25 (1^{st} case). To investigate the effects of heat input to the deposited part on the microstructure, two experiments were carried out using the process parameters shown in the Table 3.25 (2^{nd} case). To investigate the effects of peak current on the microstructure, two experiments were carried out using the process parameters shown in the Table 3.25 (3^{rd} case). To investigate the effects of the current ratio (CR) on the microstructure, two experiments were carried out using the process parameters shown in the Table 3.25 (4^{th} case). Finally, to investigate the effects of frequency (Fr) on the microstructure, two experiments were carried out using the process parameters shown in the Table 3.25 (5^{th} case).

Table 3. 25. Process parameters used for preparing the test specimens of PCSMD

Case	I (A)	WFS (m/min)	TS (m/min	CR (A/A)	Fr (HZ)
	185	2.5	0.24	2	30
1^{st}	185	2.5	0.12	2	30
	165	2.5	0.24	2.5	90
2^{nd}	205	2.5	0.12	2.5	30
	175	2.5	0.24	2	5
3^{rd}	205	2.5	0.24	2	5
	175	2.5	0.24	2.0	30
4^{th}	175	2.5	0.24	1.5	30
	175	2.5	0.24	2	5
5^{th}	175	2.5	0.24	2	2000

Table 3. 26. Process parameters used for preparing a sample for X-Ray tests.

ID	Process type	Parameters							No. of layers	Height mm
		I_p A	TS mm/s	WFS m/min	Arc length mm	Feeding angle °α	I_b A	Frequency Hz		
1	CCSMD	175	4	3.5	4	35	-------	-----	50	35
2	PCSMD	175	4	3	4	35	75	5	52	50
3	PCSMD	175	4	3	4	35	75	500	50	54
4	PCSMD	175	4	3	4	35	75	2000	50	58

Table 3. 27. X-Ray testing conditions

Specimen No.	V (kV)	I (μ A)	Time (Sec.)
1	140	1300	10
2	110	1200	10
3	110	1200	10
4	110	1200	10

3.8.2. Radiography Test

X-Ray test was used for examining the presence of internal porosity and other defects inside the specimens which were prepared using the process parameters reported in the Table 3.26. The four wall samples were machined from both sides in order to get correct results about only the internal flaws. The net wall thickness was more than 4 mm and length of 150 mm. The test conditions used for examining the specimens were shown in Table 3.27.

3.8.3. Mechanical Properties

3.8.3.1 Hardness Test

Hardness tests employed the Rockwell A scale on a (DIGIROCK) hardness tester with a flat anvil (see Figure E.1 in Appendix E). Each reading is an average of 3 point test where the indents were spaced to equal sides triangle in the center of the specimen. In order to ensure the reliability, after a certain number of tests a standard test block was tested. The tests were conducted during the study as mentioned in Figure 3.15 to show the variation of the hardness of the deposited walls with both the location and orientation for continuous and pulsed current techniques. The hardness test was conducted to show the effects of deposition parameters on the hardness.

Furthermore, stress relief heat treatment (RHT) was conducted using an electrical furnace with a temperature of about 550 ˚C for 1.5 – 2 hours. Using same testing procedure, the hardness test was reread to show the effects of RHT on the hardness of the deposited specimens.

3.8.3.2 Tensile Test Specimen

Two different types of tensile specimens were used in this study. A smaller specimens with a flat, dog-bone shape, has a gauge length of 10 mm and a 3x2 mm^2 cross-section within the gauge length have been prepared from different location and orientations according to ISO/ASTM 52900 standard [174] and a larger one was a sub size sheet specimen according to [175] with a gauge length of 35 mm, and cross-section within the gauge length of 4x2 mm^2. Two possible specimen orientation with respect to the build direction as shown in Figure 3.15. The smaller specimens were used for the vertical orientation while the larger used for horizontal specimens (See Figure 3.39). The specimens were tested using SHIMADZU testing machine (with a capacity of 300 kN) with a test speed of 1.0 $mm.min^{-1}$ (see Figures (E.2-E.4) in Appendix E).

In the experimental design for this test, two factors are considered: the condition of frequency used (4 levels) and the orientation of the sample with respect to the deposition direction (2 levels) as shown in Table 3.28. Three samples were tested for each case of vertical orientation and horizontal orientation.

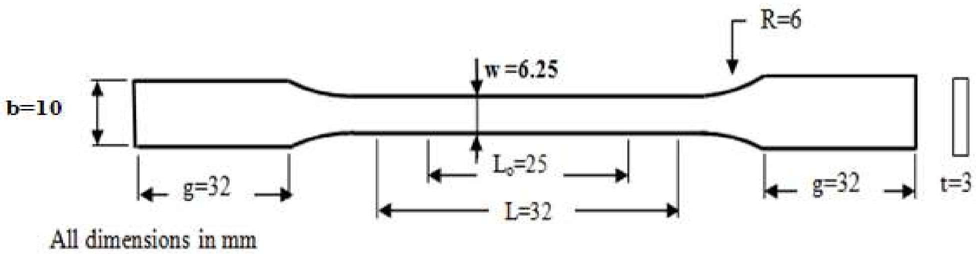

(a)

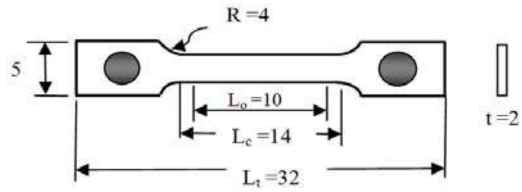

(b)

Figure 3. 39. Shows the standard tensile specimens, (a) subsize specimen[175]; (b) smaller specimen dog-bone shape [174]

Table 3. 28. The factors ant their levels

Factors	Levels			
	1	2	3	4
Frequency HZ (Fr)	0	5	500	2000
Orientation (Or)	H	V		

Table 3. 29. Experimental layout of factors with levels

Exp. No	Factors	
	Fr (Hz)	Orientation
1	0	H
2	0	V
3	5	H
4	5	V
5	500	H
6	500	V
7	2000	H
8	2000	V

The design of experiment methodology was performed using the full factorial design method. The experiment layout is shown in Table 3.29

The other design of experiment was to investigate effects the specimen location on the properties. In this experiment also two factors were considered: the condition of frequency used (4 levels) and the location of the sample with respect to the deposition height (3 levels) as shown in Table 3.30. To increase the test reliability, two samples were tested for each location. The response variables are the UTS, 0.2% YS, and ductility. The samples were machined from the wall samples according to the test specimen dimensions as shown in Figure 3.40, which shows the specimens cutting process and their labbles.

The design of experiment methodology was performed using the full factorial design method. The layout is shown in Table 3.31. Additionally, in order to investigate the effect of stress relief heat treatment on the mechanical properties (UTS & ductility) some of the PCSMD specimens were heat treated at 550 °C to about (1.5 - 2) hours and then cooled at the furnace.

Table 3. 30. Identified factors with levels

Factors	Levels			
	1	2	3	4
Frequency HZ	0	5	500	2000
Position	B	M	T	

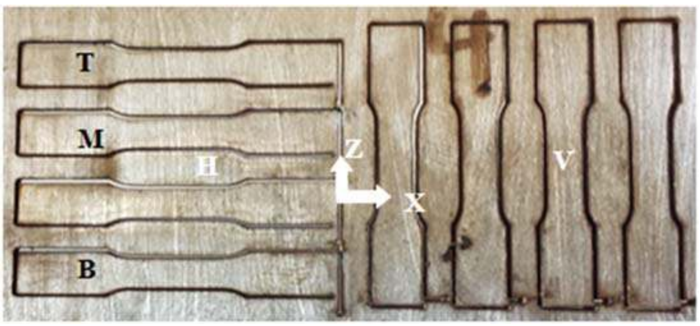

Figure 3. 40. Photograph illustrates the tension specimens' orientation

Table 3. 31. Experimental layout of factors with levels

		Factors	
StdOrder	RunOrder	Position	Fr (Hz)
1	1	B	0
2	2	B	5
3	3	B	500
4	4	B	2000
5	5	M	0
6	6	M	5
7	7	M	500
8	8	M	2000
9	9	T	0
10	10	T	5
11	11	T	500
12	12	T	2000

CHAPTER 4

RESULTS

This chapter shows the results of the experiments mentioned in chapter 3. These results are divided into twelve main sub-sections related to the experimental procedure in the previous chapter.

4.1 CAMDM Controlling

The computer aided metal deposition machine (CAMDM) path generation has been created in MATLAB program. The CAD model is firstly transformed by a GUIDE program to be input to the user interface after slicing the CAD model into ISO-line paths and building a sequence of the part. So, the operator can define the main points of shape, layer height (step height hs), and a number of layers as shown in Figure 4.1(a). Afterward, a translational transform between points is created (x-y path), the layers are built by increasing z-axes by layer height for the x-y path. The solid model is expressed as points (x, y, z). The pattern points can be saved as the m-file type and can be loaded on machine user interface program for experiment implementation.

The paths can be translated into binary format and uploading the binary code into the CAMDM controller. PC-Interface Program is a computer aided manufacturing (CAM) program, which is used for controlling machine torch movements relative to machine workspace. The program receives the CAD output file (m-file) and converts it to low-level machine code. The user can control machine manually by JOG, apply machine zeroing, monitor the change of the parameters of the machine, and load sequential program for the machine. Different solid parts such as straight walls, zigzag walls, circular walls, square walls, rectangular solid component, and other features were drawn and then sliced them in uniform layer height (see Figure 4.1(b)). Afterward, they were deposited in nearly finished configurations as shown in Figure 4.2. In the present study, the system developed to produce different geometries without such difficulties which can be countered in other systems, e.g. robots and CNC machines, since it is depending on the open source system, which gives the operator capability to tune the process parameters and control the deposition tool (DT) movements during the deposition process and give the system more flexibility to produce different geometries. So the current SMD system is appropriate for workshop working to fabricate small and medium size parts.

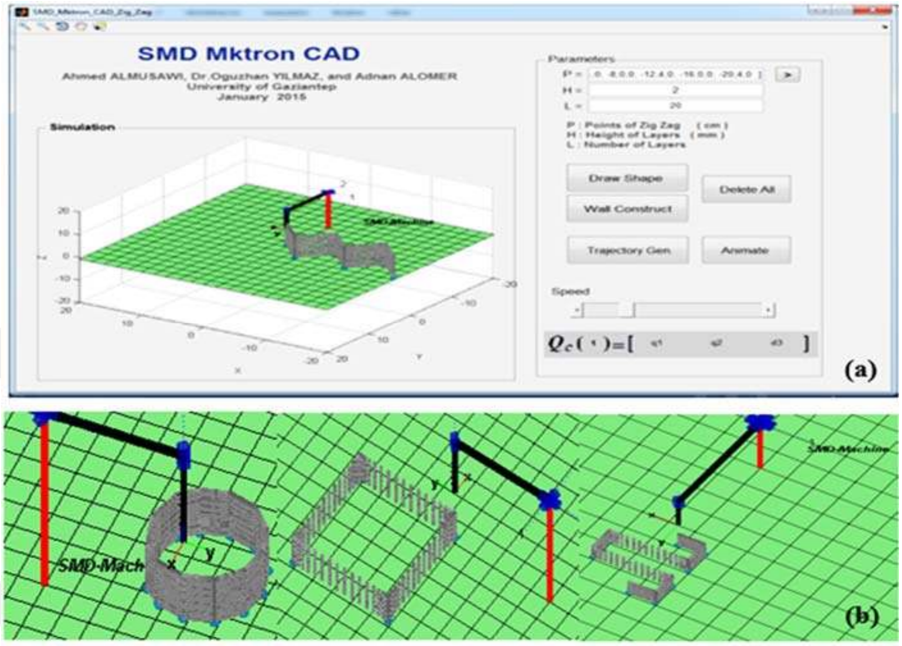

Figure 4. 1. (a) Control screen of the SMD machine; (b) different component geometries as sliced layers.

Figure 4. 2. Different solid near-net-shape deposited components using SMDM cell

4.2 Preliminary Experiments for Developing the Process Model of CCSMD Technique

Prior to deposition, the main parameters, and other operating conditions need to be tuned accordingly. Several experiments were carried out using the set-up, materials, and experiment method reported in this section were described in section 3.4.1. The depositing of uniform bead on the flat surface of substrate needs to consider the following parameters:

Arc power- one of the important parameters, which refers to the welding current and arc voltage. Depending on the arc power and travel speed, the heat input is decided. The arc power consists of the amount of current arc voltage (V_i) and welding current (I), so the input heat (**Hi**) can be calculated from the following relation:

$$\mathbf{Hi}\ \left(\frac{\mathbf{J}}{\mathbf{mm}}\right) = \eta \mathbf{I}\,\frac{\mathbf{Vav}}{\mathbf{TS}} \qquad \mathbf{(4.1)}$$

where Hi is the heat input per unit length; η is arc efficiency (assumed to be 0.83) for TIG welding [124], V_{av}: the average of the instantaneous arc voltage.

Wire feed rate- it is an important factor which is responsible for deposition rate and deposition volume DV see relation 4.2. It affects the bead geometry and other features and bead defects. So it should be chosen correctly.

$$\mathbf{DV}\ \left(\frac{\mathbf{mm3}}{\mathbf{mm}}\right) = \mathbf{A}.\frac{\mathbf{WFS}}{\mathbf{TS}} \qquad \mathbf{(4.\ 2)}$$

where DV is the deposition volume per unit distance, A; is the cross section area of the filler wire (mm^2), and WFS is the wire feed speed (mm/s),

TS is the travel speed (mm/s). It is a main factor in the deposition process since it decides the added mass per unit length and the input energy per unit length.

Feeding angle and feeding direction are also important parameters, where they affect the bead geometry and process stability.

It was important to note that for some of the experiments the metal deposition was impossible to perform, such as those with low current and high TS because an insufficient melting occurs (see Figure 4.3(a)) or due to excessive melting for the experiments in which the current is high and travel speed is slow as shown in Figure

4.3(b). For the experiments in which metal deposition was possible, only one run of each set was made during the experiments of parameters selection (see section 4.4).

4.3 Tuning the Feeding Angles and Deposition Directions

Using the mentioned parameters in Table 4.3, some of the experiments were accomplished using two feeding angles with the three types of wire feeding directions shown in Figure 4.10. Figure 5.4 shows the relation between wire tip and substrate angle, the feeding orientations, and also shows some cases of wire setup positions. During experiments, it was shown that when the wire is fed far away from the arc-substrate intersection point the drops may be generated and the bead becomes irregular and the process may be unstable (see Figure 4.4(e) and (f). Plunging also may be happened as shown in Figure 4.4(g). A suitable metal deposition was gutted when the wire was fed directly into the in the intersection point between the arc center and the weld pool (see Figure 4.4(h)). Parameters were set to be kept the same, and investigate the effect of both feeding angles and feeding directions on the bead characteristics (e.g. total height h, and maximum width w). Figure 4.5 explains the effect of the feeding angles on the bead geometries especially the average of total height and average of maximum width for the three nominal feeding directions. Preliminary experiments were carried out by changing the delivery angle (α°) (30°, 45° and 60°) and directions, whereas, the other parameters were set to be constant to show the effects of the feeding angle and directions only. The results with $\alpha = 60^{\circ}$ angle were not considered since it makes the process unstable due to the wire flow inside the melting zone is not free.

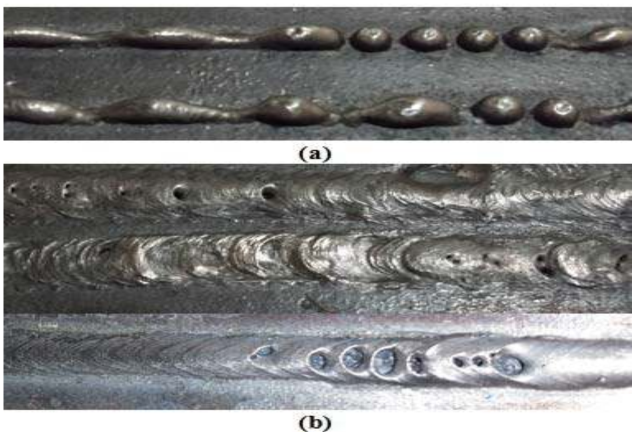

Figure 4. 3. (a) Insufficient melting deposits; (b) Excessive melting deposits

It is obvious that the delivery angle of 30° gives the highest height for each direction and the width is reduced for the same angle. It can see also that the side direction is more sensitive to increasing in feeding angle (45°- 60°) especially when the arc length becomes larger, where droplet phenomenon occurs, which may lead to producing irregular bead shapes and sometimes the wall becomes as skewed towards wire feeding side due to fall down the melted metal droplet by gravity before it reaches the wall surface see Figure 4.6. So the suitable angle is less than 30°. During the experiment, it was conducted that for small feeding angle the high deposition rate is more suitable than the large angles since the large angles are more sensitive for dripping mode and the wire might stick the substrate which makes the process doesn't smooth. It should be taken in mind that, the main variables are necessary to be tuned in order to reduce the effects of difference in height corresponding to the different feeding directions for the same parts especially during production of the square and rectangular components. The solution is to develop a suitable path planning software to control the height without the need for a closed feedback system. The front feeding direction is more stable than rear direction.

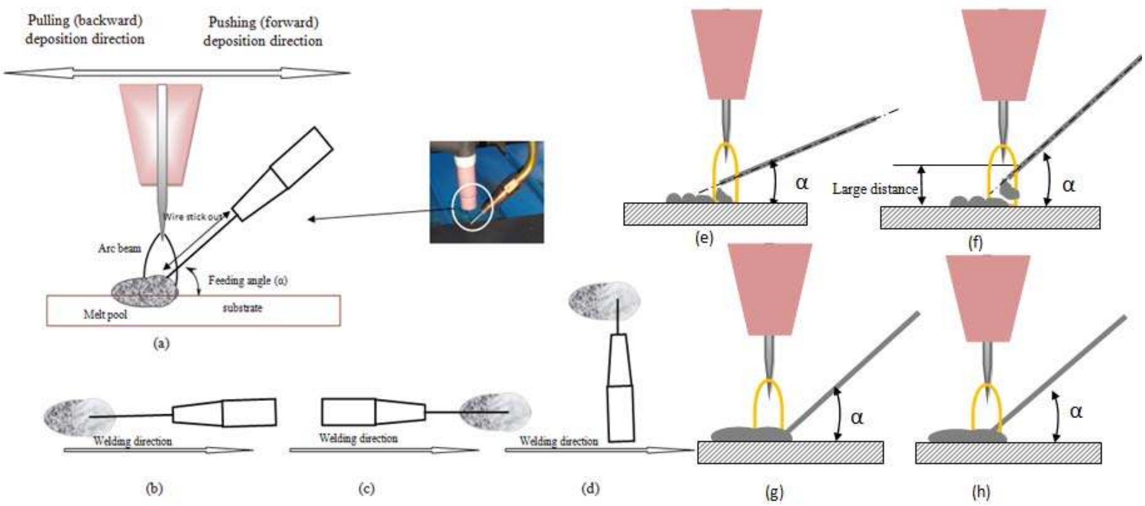

Figure 4. 4. (a) Shows the wire tip in relation to weld pool angle, (b) front feeding (forward direction), (c) back feeding (rear direction), (d) side feeding, (e) and (f) show the dropping mode due to improper setup of wire with respect to the intersection of arc

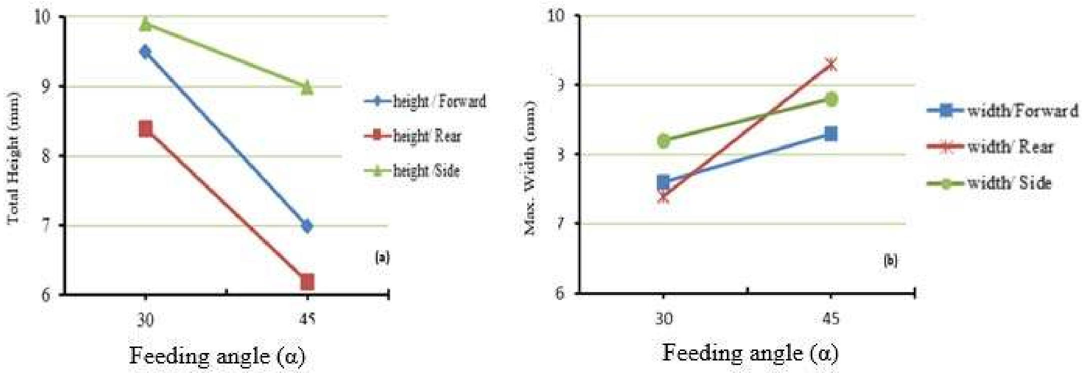

Figure 4. 5. Shows the relations between the wire feeding angles and the feed direction and effects on the (a) total height (h); (b) the max. width (w).

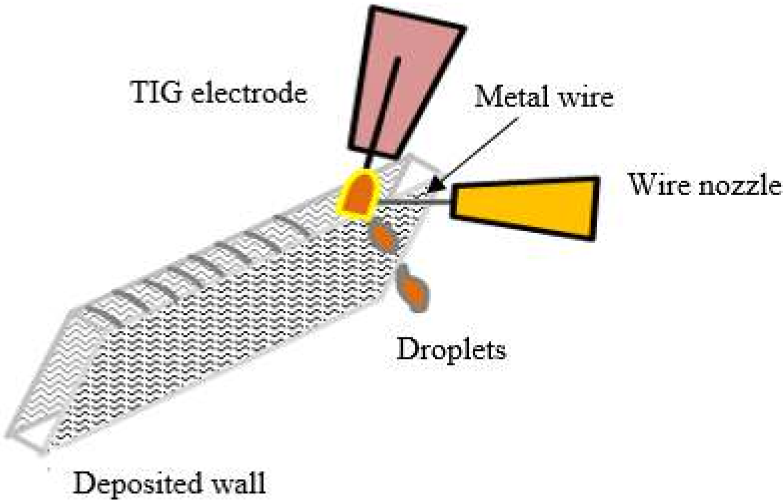

Figure 4. 6. Schematic illustration the droplet formation during side feeding with high feeding angle and long arc length.

4.4. Bead-On-Plate Metal Deposition Experiments

The set-up and experimental method employed for carrying out these experiments are described in section 3.4.3 of the experimental procedure

4.4.1. Single –Layer Experiment for Finding the Process Window

The experiments reported in this section were done according to the deposition procedure described in section 3.4.3.1. This experiment was planned with the DOE methodology. A factorial design was selected in order to be able to analyze possible interactions and also possible non-linear between the factors and the response variables. Two replicates were made, giving a total of 108 beads, which were deposited in random order. TS is a main parameter in the deposition process since it affects directly on the heat input and the deposition volume as was summarized in equations 1 and 2. Figure 4.7 shows the process window. It describes the dripping conditions, the excessive melting zone, the smooth bead region, the stubbing and oscillation conditions, and wavy zone.

The Figure 4.7 shows also the states of TS corresponding to the welding current. This process window is valid for filler wire of 0.8 mm diameter of stainless steel which is fed to the weld pool as shown in Figure 4.4(h), where the tip constructs with the arc center on the substrate surface point. Zone 2 of the process window represents the area in which an excessive melting and existence of porosities and blow-holes conditions may occur whereas zone 1 represents the excessive melting region. These zones depends mainly on the combination of low TS and low WFS at the present arc power, it is clearly seen at the experiments having parameters such as (I=160-180 A, TS= 2 mm/s, WFS 1-1.5 m/min) (see Figure 4.8 (a)). While the zone 7 of the process window represents the dripping area due to low WFS, which means that the wire takes a long time under the arc beam, so that it will melt before it reaches the deposition zone at the weld pool center, this leads to generate droplets (see Figure 4.8(b)) whereas zone 6 refers to the zone in which the dripping may be occur. With increasing WFS the smooth bead will be achieved as shown in region 3 in the diagram, which represents the most stable process with a uniform bead (see Figure 4.8(c)). Zone 4 refers to the stabbing and oscillation conditions, these may occur as WFS is high relatively, which means that the wire tip will spend too short time under arc beam so that it may be un-melted and will strike the substrate surface under the weld pool which may lead to oscillating or to stub. In region 5, due to too much wire is fed into the melt pool, the wire will cause to build up a higher and wider bead, sometimes the wire is forced to turn out the deposition region these cases make the process unstable (see Figure 4.8(d)). Region 8 shows the wavy conditions may occur. Whereas when the TS is too high and WFS is low at relatively low current, the wavy bead occurs as shown in zone 9, e.g. the following set of the combination: I= 140 A, TS = 7 mm/s, WFS = 1.5-2.5 m/min (see Figure 4.8(e)).

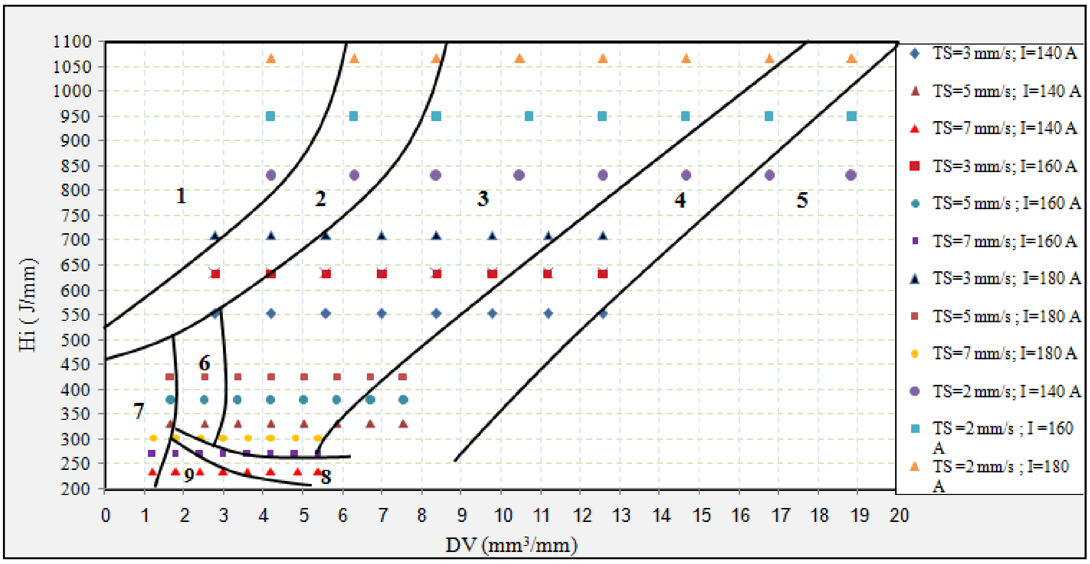

Figure 4. 7. Schematic illustrates the SMD process window: (1) Excessive melting, (2) Excessive melting may occur, (3) Stable process and smooth bead deposition, (4) Stubbing and humping may occur, (5) Stubbing occurs, (6) Droplets may appear, (7) Dripping occurs, (8) the wavy bead may occur, and (9) Wavily occurs.

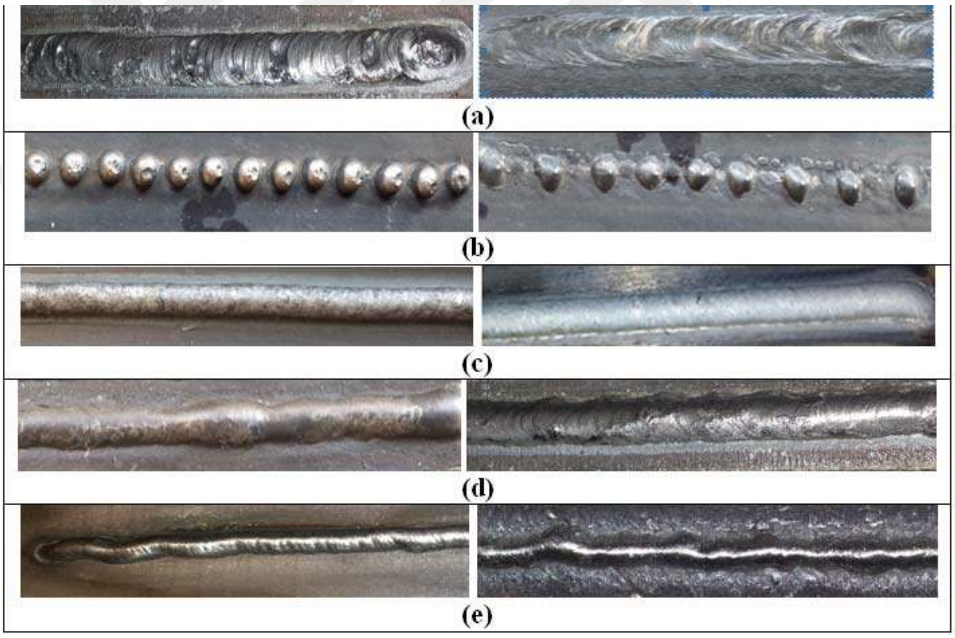

Figure 4. 8. (a) Excessive melting, (b) Dripping formation, (c) Smooth deposition beads, (d) Stubbing bead deposition, (e) Wavy bead.

4.4.2 Effects of TS and WFS/ TS Ratio on the Deposit Bead Penetration Characteristics

This section shows the effects of the TS and WFS/TS ratios on the bead geometry and penetration. In addition, this section investigates the effects of TS on the humping defect during depositing bead on the plate. This study was done based on the experiment described in section 3.4.3.2. The design of experiment here was carried out using a full factorial design in order to cover all possible ways related to the humping existence with respect to TS and WFS/TS ratio. Table 4.1 shows the experiments layout with the values of welding parameters used.

4.4.2.1 Effects on Bead Height

To identify the significant factor effects, an analysis of variance is used. The result of the ANOVA for the bead height is shown in Table G.1 in Appendix G.

From Table G.1 it easy to recognize the most important factors, which have a smaller P-value (or bigger F-value). With a significant level of $\alpha = 0.95$ a factor is significant if its P-value ≤ 0.05. From the Table G.1, the most important factor is WFS/TS, and the factor TS is also affected in the response but less than WFS/TS. It is also possible to analyze graphically the main factors as shown in Figure 4.9.

Table 4. 1. Shows the experimental input parameters, output variables measurements, and visual notation of process state

Trial No	Process parameters			Bead profile characteristics			Visual inspection
	TS	**WFS/TS**	**WFS**	**W_{av}**	**h_{av}**	**P**	**Process state**
1	0.18	4	0.72	6.35	0.8	1.6	No defect
2	0.3	4	1.2	5.2	0.83	0.8	No defect
3	0.42	4	1.68	4.5	0.95	0.7	No defect
4	0.54	4	2.2	3.63	1.1	0.3	Defect
5	0.18	6	1.08	6.4	1.23	1.47	No defect
6	0.3	6	1.8	5.1	1.15	0.9	No defect
7	0.42	6	2.52	4.2	1.3	0.6	No defect
8	0.54	6	3.2	3.2	1.45	0.4	Defect
9	0.18	8	1.44	5.95	1.4	1.3	No defect
10	0.3	8	2.4	4.9	1.5	0.7	No defect
11	0.42	8	3.36	3.5	2.1	0.3	Defect
12	0.54	8	4.3	2.56	2.45	1.8	Defect
13	0.18	10	1.8	5.7	1.6	0.8	No defect
14	0.3	10	3	4.7	2.25	0.6	No Defect
15	0.42	10	4.2	3.1	2.5	0.5	Defect
16	0.54	10	5.4	2.52	3.5	0.5	Defect
17	0.18	12	2.16	5.45	1.8	1.8	No defect
18	0.3	12	3.6	3.8	2.55	0.6	Defect
19	0.42	12	5.04	2.83	3	0.25	Defect
20	0.54	12	6.5	2.53	3	0.2	Defect

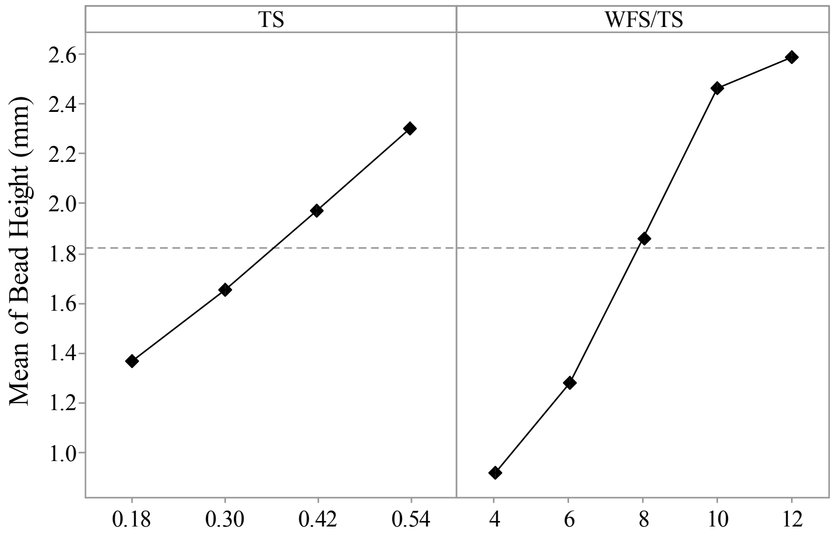

Figure 4. 9. Main effects plot for bead height

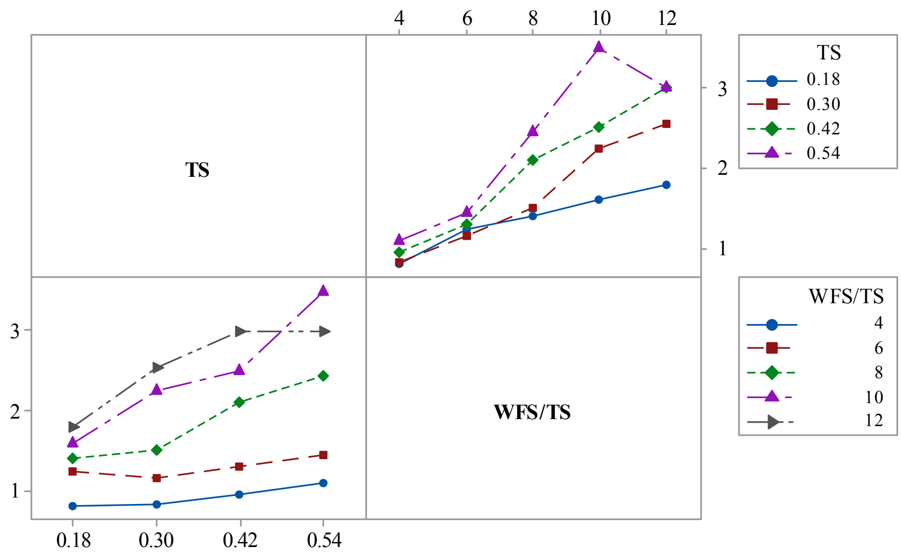

Figure 4. 10. Interaction plot for the bead height.

It is also possible to analyze graphically the interactions of the factors. An interaction occurs when the difference between the levels of one factor is not the same at all levels of the other factors [101]. Graphically, an interaction can be identified when the lines are not parallel in the interaction plot. Figure 4.10 shows the interaction plot for bead height. It can be seen, in the plot of the interaction between WFS/TS and TS, the lines are nearly parallel, indicating that the interaction is low. For that, the analysis will focus on the two main factors.

It is also possible to calculate a regression equation for the height, using the method of lead squares. The result of the equation is:

$$H = -0.868 + 0.2287\ WFS/TS + 2.397\ TS \qquad \textbf{(4. 3)}$$

4.4.2.2. Effects on Bead Width

Using the same method of analysis for the bead width. The result of the ANOVA is shown in Table G.2 as shown in Appendix G. From this initial analysis, it is possible to identify the most significant factor is TS followed by the WFS/TS. Figure 4.11 shows the main effects of the two control factors. From Figure 4.12, it can be seen that most of the lines are fairly parallel. The significance of the interactions between factors is ignored and focused on the main two control factors.

It is also possible to calculate a regression equation for the height, using the method of least squares. The result of the equation is:

$$W = 8.618 - 0.1604\ WFS/TS - 8.425\ TS \qquad \textbf{(4. 4)}$$

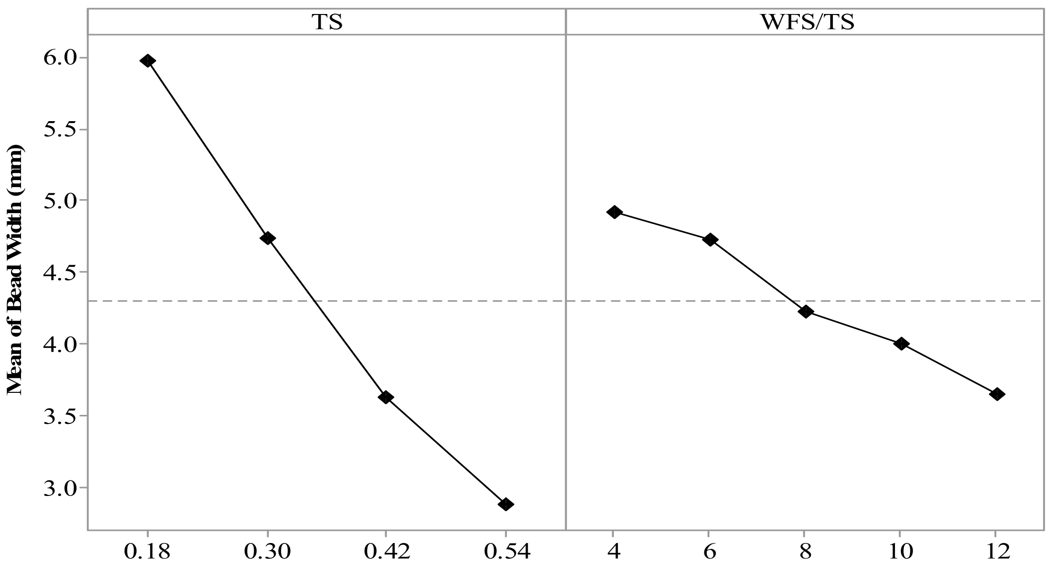

Figure 4. 11. Main effects plot for bead width, w

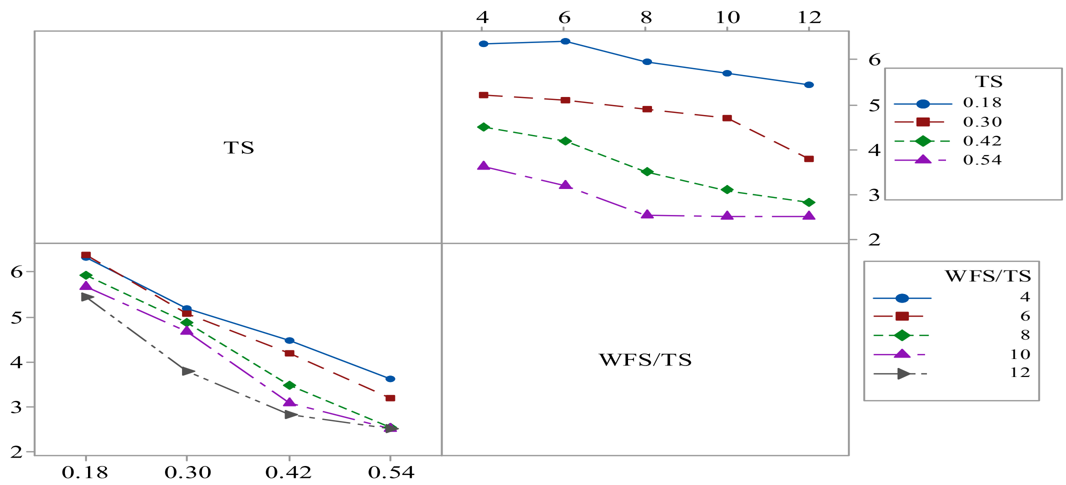

Figure 4. 12. Interaction plot for bead width

4.4.2.3. Effects on Penetration

The result of analysis of variance is shown in Table G.3 as given in Appendix G. From the initial analysis, it is possible to identify the most important factor is TS whereas, the WFS/TS is not significant. Figure 4.13 shows the main effects of the two control factors. It is obvious that the effect of TS on the penetration, especially with slow welding speeds. Figure 4.14 shows the interaction between the factors. There is a small interaction between WFS/TS and TS.

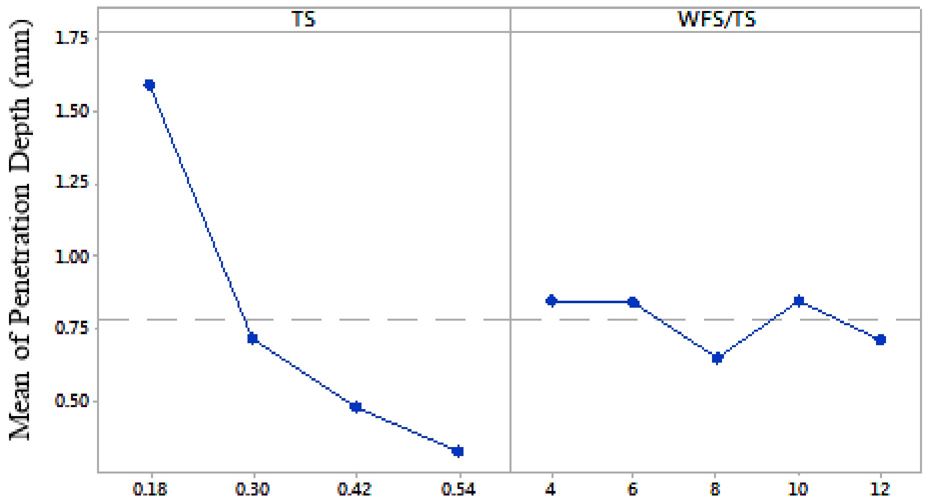

Figure 4. 13. Main effect plots for penetration p.

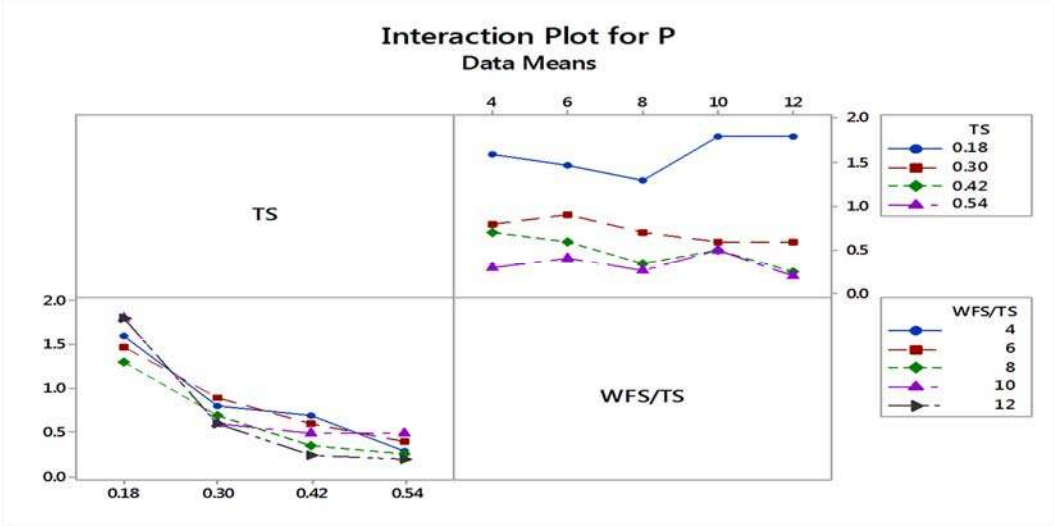

Figure 4. 14. Interaction plots for penetration

It is also possible to calculate a regression equation for the height, using the method of least squares. The result of the equation is:

P = 2.104 - 0.0143 WFS/TS - 3.351 TS **(4.5)**

4.4.2.4. Effects on Weld Bead Humps

During the deposition of beads experiment, some of the beads contain hump defects which make the deposition process unstable process. Table 4.1 illustrates the summary of the controlling parameters and the results of this experiment. It was described in process window Figure 4.7, that even when the heat input per unit distance is kept constant, the continuous increasing in the wire feed speed may lead to unstable process as a result of deterioration of the deposit quality. Figure 4.15 shows the effects of the TS on the quality of deposited beads. The travel speed plays the vital role in the formation of the humping defect. Figure 4.16 shows the experiment parametric plot limiting the regions where process parameters either acceptant quality beads or defective beads and unstable process

4.5 Multilayer of Metal Deposition Experiments

The set-up, welding conditions, and experiment method utilized to carry out the experiments described in this section are detailed in section 3.4.4 (see chapter three).

4.5.1 Effects of Main Parameters on the Deposited Bead Characteristics and Surface Quality.

This section reports the influence of the main parameters on the bead geometry. In addition, the thickness of the machined metal layer from the wall sides of the deposited samples. The deposition volume per unit distance was also calculated. The measured bead profile, namely bead width, average of total wall height, and the machining layer thickness and other results are reported in Table 4.2

Figure 4. 15. (a) Beads of experiments 5 and 6, smooth beads ; (b) beads of experiments 19 and 20, humping beads.

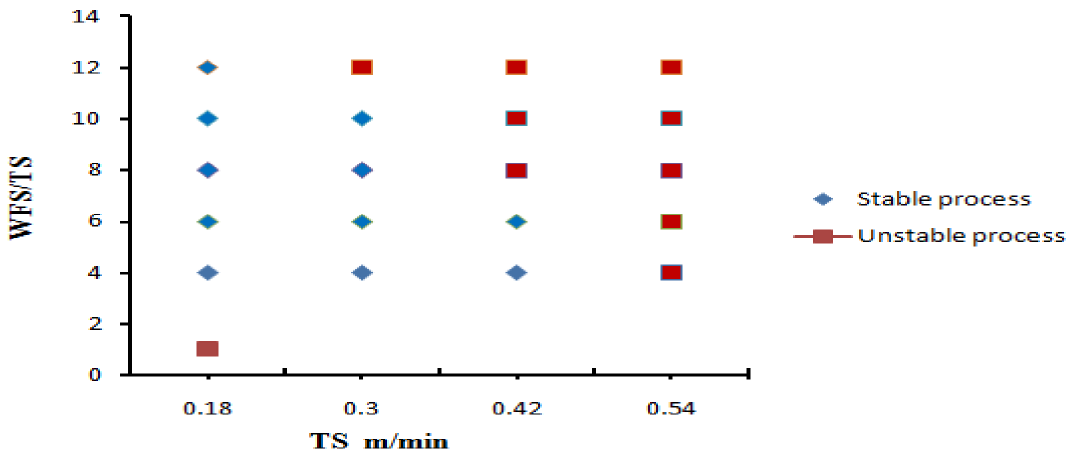

Figure 4. 16. Parametric diagram of the TS Versus WFS/TS showing the limits of a stable process with TS limits.

Table 4. 2. Measured values from the test specimens as per L16 orthogonal array.

Exp. No.	Input Parameters				Responses				
	I A	TS mm/s	WFS m/min	L mm	H_{av} mm	$W_{max.}$ mm	DV mm^3/mm	MLT mm	Measured hardness HRA(Kgf)
1	125	3	1.5	3	7.8	6.9	4.189	1.3	51.5
2	125	5	2	4	10.83	6.23	3.3506	0.45	52.8
3	125	6	2.5	5	4.8	7.3	3.4902	0.59	54
4	125	7	3	6	9.8	7.5	3.59	1.125	46.6
5	150	3	2	5	9	12.6	5.5844	1.03	47.9
6	150	5	1.5	6	7.13	6.73	2.513	1.015	52
7	150	6	3	3	14.13	7.33	4.1883	0.565	53.4
8	150	7	2.5	4	9.4	7.53	2.9916	1.1	52.4
9	175	3	2.5	6	12.56	11.93	6.9805	1.3	49.4
10	175	5	3	5	10.43	10.2	5.026	1.15	51
11	175	6	1.5	4	5.4	7.1	2.094	0.95	53.7
12	175	7	2	3	8.4	7.26	2.3933	0.5	51.5
13	200	3	3	4	15	11.97	8.3766	0.75	51.3
14	200	5	2.5	3	9.5	9.23	4.1883	0.55	47.5
15	200	6	2	6	7.97	9.67	2.7922	1.085	49.6
16	200	7	1.5	5	8	5.97	1.795	0.985	49.5

As mentioned in Section 3.4.4.1, Taguchi approach was used for designing the experiment and L16 orthogonal array. The filler metal was 0.8 mm diameter SS308LSi. The analysis of variance is a statically based decision tool used for interpreting experimental data and making the necessary decisions.

4.5.1.1 Effects on Wall Height, h_{av}

The result of ANOVA for the wall height is shown in Table H.1 as given in Appendix H. From the Table H.1, it is easy to identify the most important factor which effects on the wall height is the WFS and TS has a small effect, whereas the other parameters are not significant. It can be seen that in the Figure 4.17. When the WFS increases, which means that increasing the metal deposition so that the total height of the wall increases. From the Figure 4.18, it can be seen that in the plot of the interaction between the factors is also significant. Welding current and arc length have the smallest effect on wall height. The mathematical model to establish the relationships between the total height and input parameters was developed based on the experimental data collected from Table 5.5 and taguchi L16 orthogonal array. The model was developed using the least squares approach based on multiple regression with four regressor variables (i.e. I, TS, WFS, and L) [176]. The regression equation thus obtained is as follows:

$$H = 4.29 + 0.0188\, I - 0.593\, TS + 3.163\, WFS - 0.419\, L \quad \textbf{(4.6)}$$

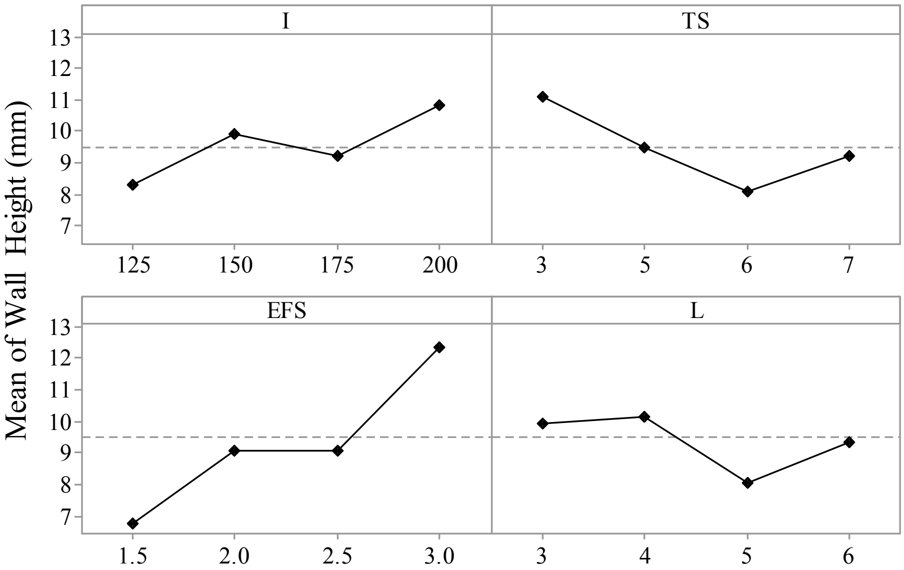

Figure 4. 17. Plot of main factors for wall height

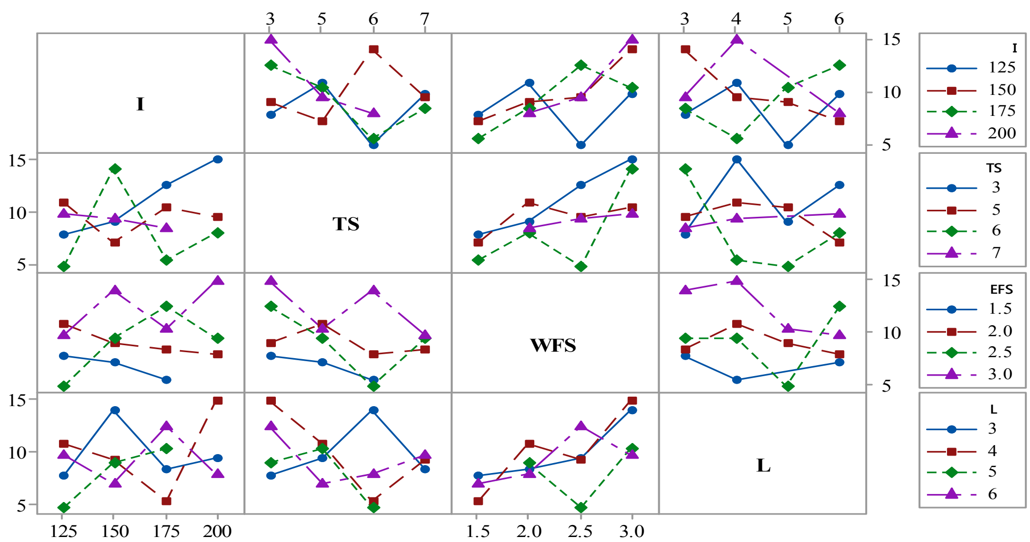

Figure 4. 18. Interaction plots for wall height

4.5.1.2. Effects on wall width

The maximum wall width is described in Figure 3.13. The experimental parts built ranges from 7.13 to 15 mm maximum wall width. The result of ANOVA is shown in Table H.2

From this initial analysis, it is possible to conclude that the most significant factors are: traverse speed, wire feed speed, and welding current, whereas the arc length, is less effect on the wall width. These effects can be seen graphically as shown in Figure 4.19

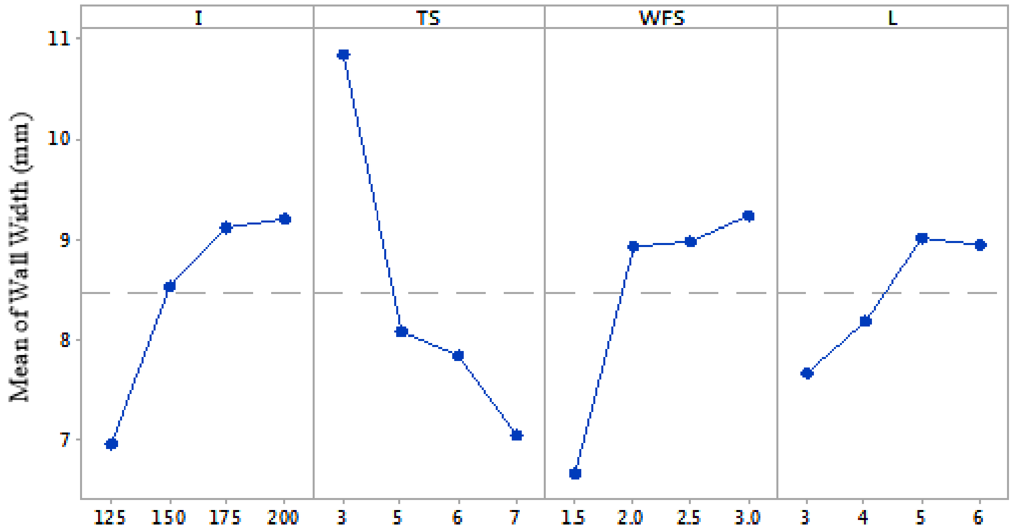

Figure 4. 19. Main effects plot for wall width

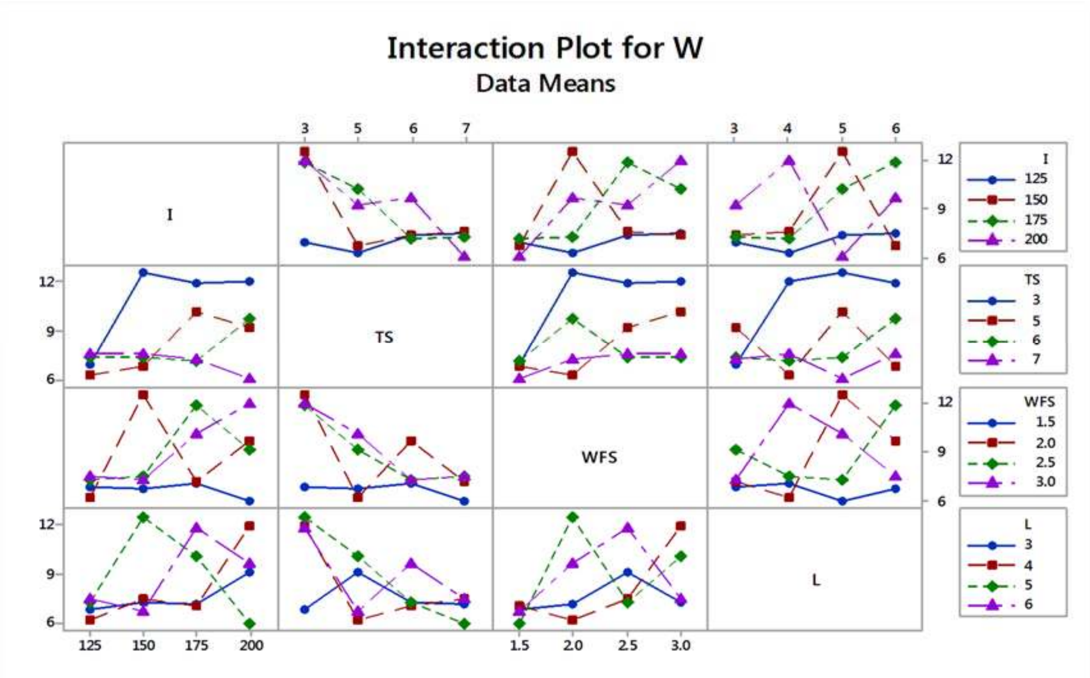

Figure 4. 20. Interaction plots for wall width.

The wall width is directly proportional to the heat input per unit distance, which mainly depends on the arc power and travel speed. From the Figure 4.19, it is clear that the wall width decreases rapidly with the increase in travel speed. The increasing in WFS leads to the increasing in deposition volume so that the wall width increases. Figure 4.20 shows the interaction plot for wall width. It can be seen that in the plots there are interactions between all the main factors.

The mathematical model to establish the relationships between the maximum wall width and input parameters was developed based on the experimental data collected from Table 4.2 Taguchi L16 orthogonal array. The model was developed using the least squares approach based on multiple regression with four regressor variables (i.e. I, TS, WFS, and L). The regression equation thus obtained is as follows:

$$W = 3.07 + 0.02903\ I - 0.935\ TS + 1.557\ WFS + 0.464\ L \quad \textbf{(4.7)}$$

4.5.1.3. Effects on Machining Layer Thickness

The machining layer thickness (MLT) was described in Figure 3.13. It is a measure of apparent surface of the build-up which was defined as the maximum thickness of material required to be removed to bring the deposit back to a solid continuous vertical surface [53]. The result of the analysis of variance of the main four factors is shown in Table H.3. In contrast, the ANOVA results for the MLT show a strong dependence on arc length as a most significant factor, with travel speed a lesser influence. Whereas the current and wire feed rate are not significant. It can analyze graphically the main effects of factors as shown in Figure 4.21. It is clear the effect of arc length on the thickness of the machined layer from the wall side or the sidewall profile. This gives an indication that large arc length leads to bad deposit quality since it produces a larger thickness of metal to be removed as well as the effects on the sidewall profile. Figure 4.22 shows a comparison between the Experiment 9 and Experiment 12.

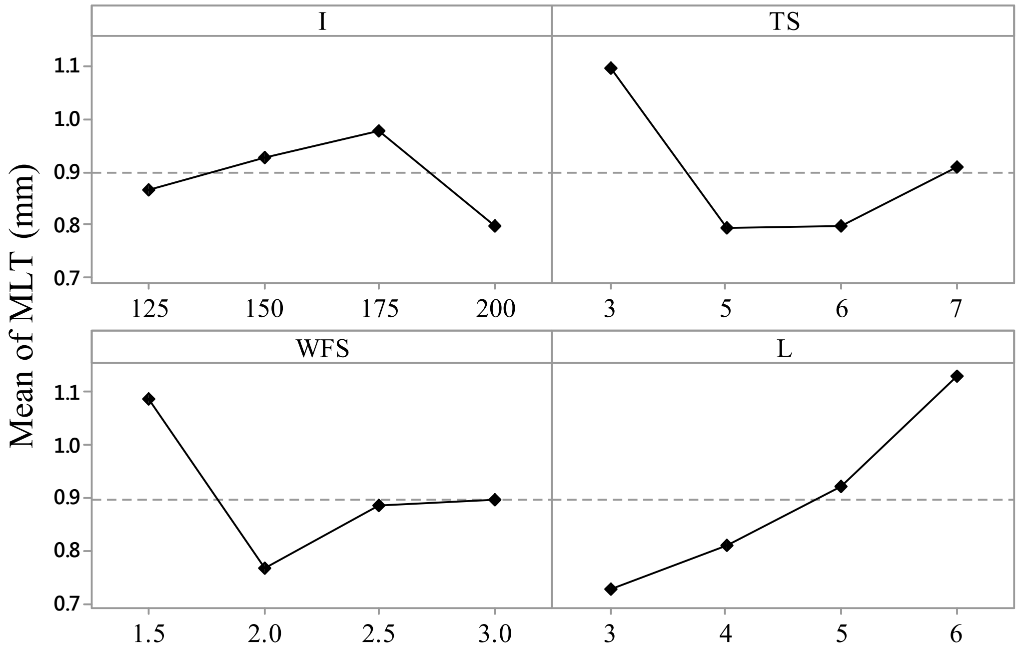

Figure 4. 21. Main effects plot for MLT

Figure 4. 22. Variation in wall surface quality for (a) Experiment 9; and (b) Experiment 12.

The mathematical model to establish the relationships between the machining layer thickness and input parameters was developed based on the experimental data collected from Table 4.2 Taguchi L16 orthogonal array. The model was developed using the least squares approach based on multiple regression with four regressor variables (i.e. I, TS, WFS, and L). The regression equation thus obtained is as follows:

$$MLT = 0.752 - 0.00009\, I - 0.0503\, TS - 0.075\, WFS + 0.1334\, L \quad \textbf{(4.8)}$$

4.5.1.4 Effects on deposition volume

DV refers to the amount of metal deposited per unit distance, which can calculate using Equation 2 as it was mentioned in chapter four. The experimental parts built range from 2.091 to 8.376 mm^3/mm deposition volume. The result of the analysis of variance of the main four factors is shown in Table H.4 as given in Appendix H.

From this initial analysis, it is possible to conclude that the most significant factors are: traverse speed, wire feed speed, and whereas the current is having less effect on the metal deposition volume, and the arc length is insignificant. These effects can be seen graphically as shown in Figure 4.23. Figure 4.24 shows the interaction plot for the DV. The deposition volume DV must be controlled with the suitable state since when it becomes more, then the wall quality is affected and the MLT may be increased too much. Figure 4.25 shows a comparison between tow experiments with different DV.

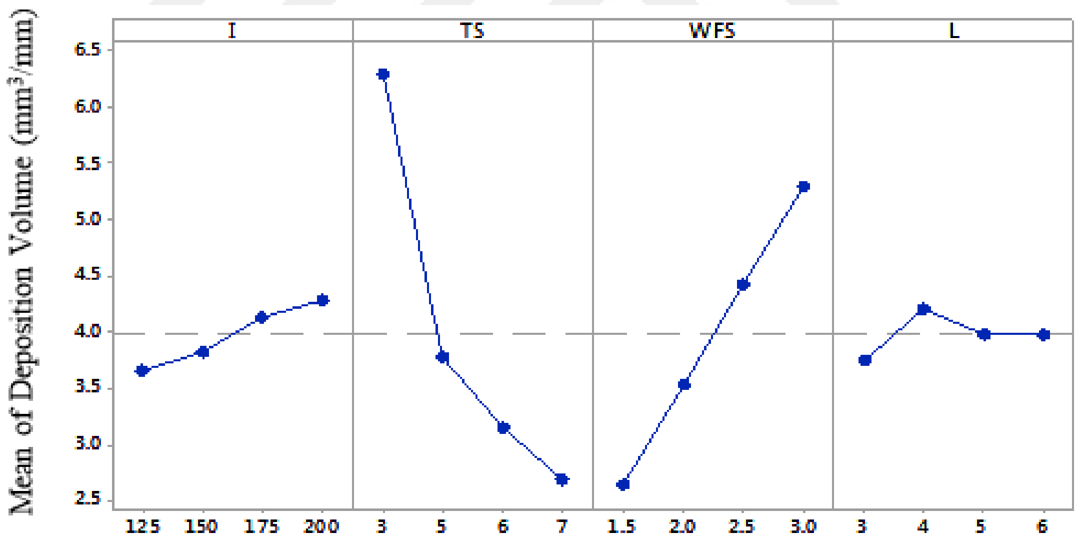

Figure 4. 23. Main effects plot for DV

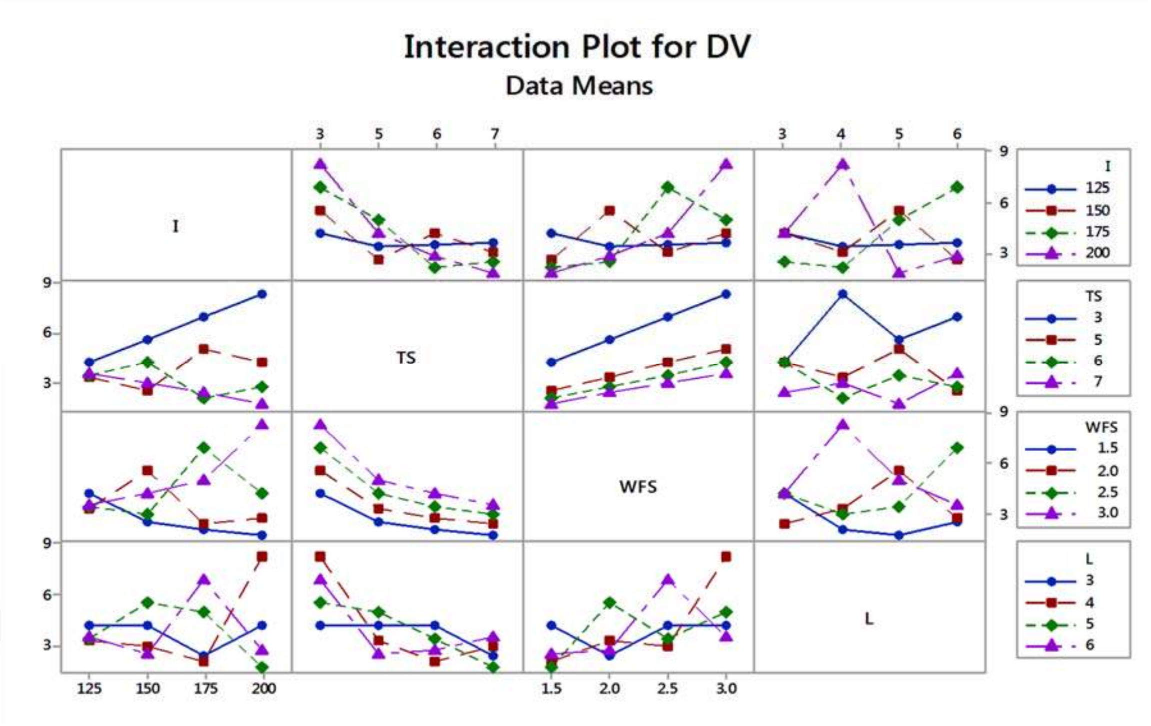

Figure 4. 24. Interactions Plot for DV

Figure 4. 25. Samples from experiments

.

The mathematical model to establish the relationships between the deposition volume per unit distance and input parameters was developed based on the experimental data collected from Table 4.2 using Taguchi L16 orthogonal array. The model was developed using the least squares approach based on multiple regression with four regressor variables (i.e. I, TS, WFS, and L). The regression equation thus obtained is as follows:

$$DV = 3.17 + 0.00881\ I - 0.9155\ TS + 1.765\ WFS + 0.046\ L \tag{4.9}$$

4.5.1.5 Effects on Hardness

This section reports the influence of the main parameters on the hardness. The experiments reported in this subsection were carried out according to set-up and the method described in section 3.8.3 (Chapter 3). The deposited walls were sectioned in traverse direction and the specimens prepared for the hardness test. The hardness was measured at the center of the wall in the cross section area at least three readings were averaged. The result of the analysis of variance of the main four factors and interactions are shown in Table H.5 as given in Appendix H.

From this initial analysis, it is possible to identify that there is no evident significant factor of the main parameters and their interaction. The arc length has small significance. These effects can be seen graphically in the main effects plot as shown in Figure 4.26.

From Figure 4.27, it can be noticed the effects of travel speed on the hardness. Maximum hardness obtained at TS = 6 mm/s (see Figure 4.27(a)) and also the minimum HRA was measured as L is a larger range (see Figure 4.27(b)).

The regression equation:

$$HRA = 57.58 - 0.0211\ I + 0.199\ TS - 0.59\ WFS - 0.668\ L \tag{4.10}$$

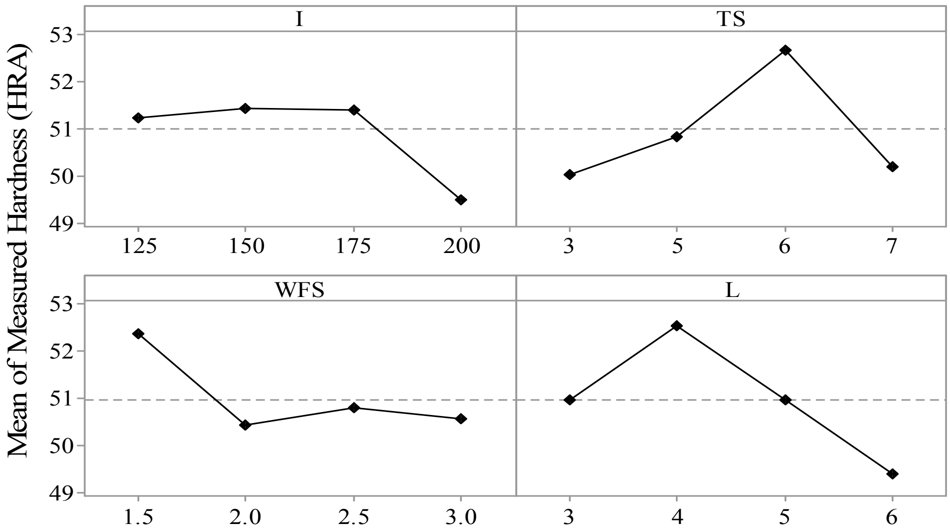

Figure 4. 26. Main effects plot for hardness

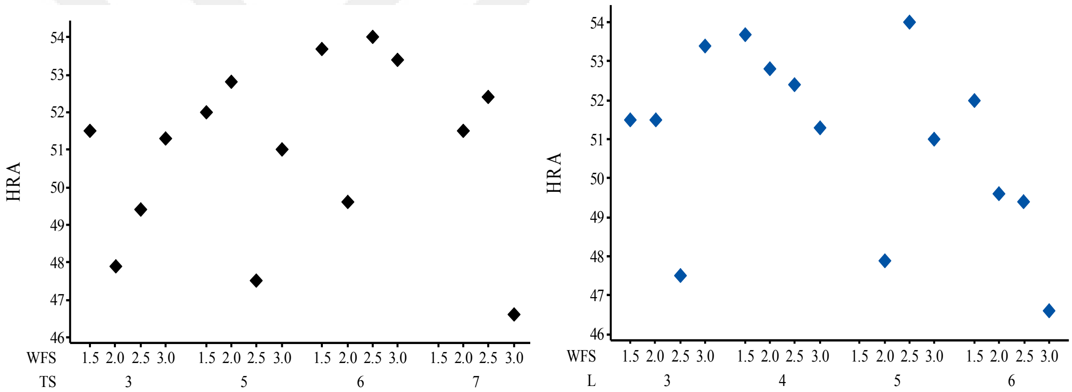

(a) **(b)**

Figure 4. 27. Plot of effects of Interactions on HRA

4.5.2 Effects of Interpass Temperature T_{sub}, TS, and WFS/TS Ratio on the Bead Characteristics and Surface Quality.

This section reports the influence of interpass temperature $T_{sub,}$ TS, and WFS/TS on the deposited sample's characteristics such as effective wall width Weff., wall height in vertical multi-layer overlapped walls, H and machined layer thickness, MLT. The investigation was carried out according to the nominal welding condition in Section 3.4.4.2. The experimental design with the measurement results is shown in Table 4.3. Walls with 12 layers high were produced.

4.5.2.1 Effects on EWW

The effects of TS and WFS/TS on the effective wall thickness (EWW) are shown in Figure 4.28(a) and the effect of the TS on EWW at constant substrate temperature Tsub. It is apparent that the EWW increases as TS decrease for all WFS/TS and T_{sub} ranges. EWW depends significantly on the TS, however, with a larger gradient at higher WFS/TS and also for higher T_{sub}, where it drops rapidly from a maximum amount at low TS to a minimum value at high TS. It can be seen that the EWW increases with increasing T_{sub} for constant TS. A positive linear relationship between EWW and T_{sub} can be concluded from the Figure 4.28(b) for all ranges of TS studied. From the analysis of variance results, it can be seen the most effect parameter is the TS, whereas the others are less significant (see Figure 4.29). The increased width of the deposited wall is consistent with low translation speed since this allows for the greater volume of deposit material per length of the deposit.

Table 4. 3. L9 experimental layout of factors and results

Exp. No.	TS m/min	WFS/TS	T ^{o}C	MLT mm	EWW mm	H mm
1	0.18	6	40	0.3	7	4.25
2	0.18	8	200	0.4	8	6.67
3	0.18	10	300	0.25	8.4	9.70
4	0.3	6	200	0.33	6.6	11.40
5	0.3	8	300	0.165	7.2	9.30
6	0.3	10	40	0.25	6.7	8.30
7	0.42	6	300	0.3	5.9	5.20
8	0.42	8	40	0.4	5.4	9.20
9	0.42	10	200	0.5	5.5	6.60

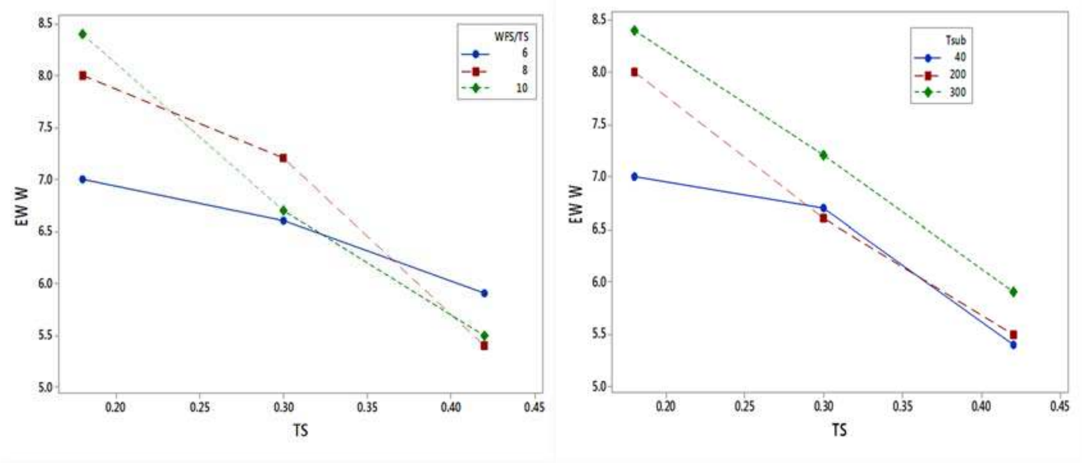

(a) **(b)**

Figure 4. 28. Influences of (a) TS and WFS/TS and (b) TS and Tsub on the EWW

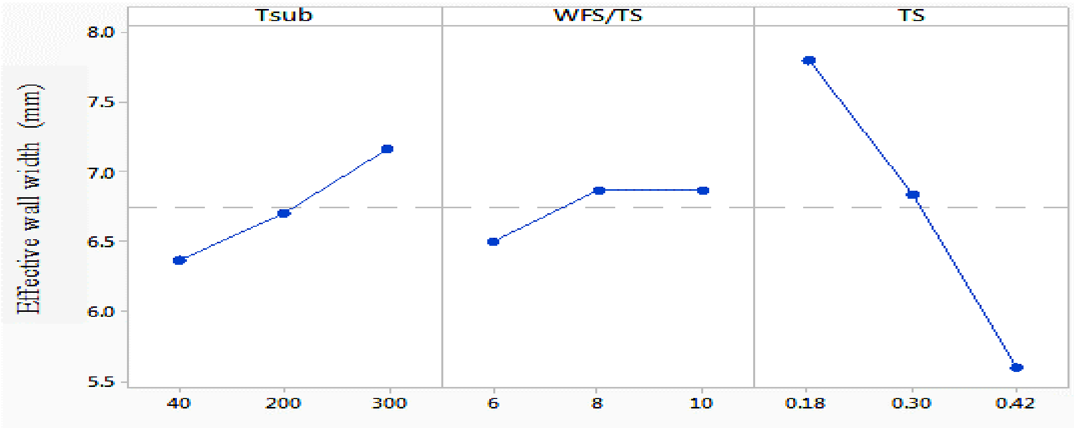

Figure 4. 29. Main effects plot for EWW

4.5.2.2 Effects on MLT

The effects of TS and WFS/TS on the surface quality, which was expressed as the machined layer thickness MLT, is shown in Figure 4.30(a). While the effects of Ts and T_{sub} on the MLT is shown in Figure 5.30(b). From the Figure 5.30, it is clear that there no linear association between TS and both WFS/TS and T_{sub} with the thickness of the layer to be machined from the sidewall. There is no obvious significant factor as also summarized in ANOVA results in Table H.6 as ginen in Appendix H.

Figure 4.31 compares the sidewall surface quality of the walls produced at different interpass temperatures at constant WFS/TS (see Experiment 3, 6, and 9 in Table 4.3). The results show that the T_{sub} has an effective effect on the sidewall characteristics such as MLT and EWW. It is important to see that the MLT of the Experiments 3 and 6 was 0.25 mm and for experiment 9 was 0.5 mm. These were depending on the TS and T_{sub} as shown in Figure 4.30.

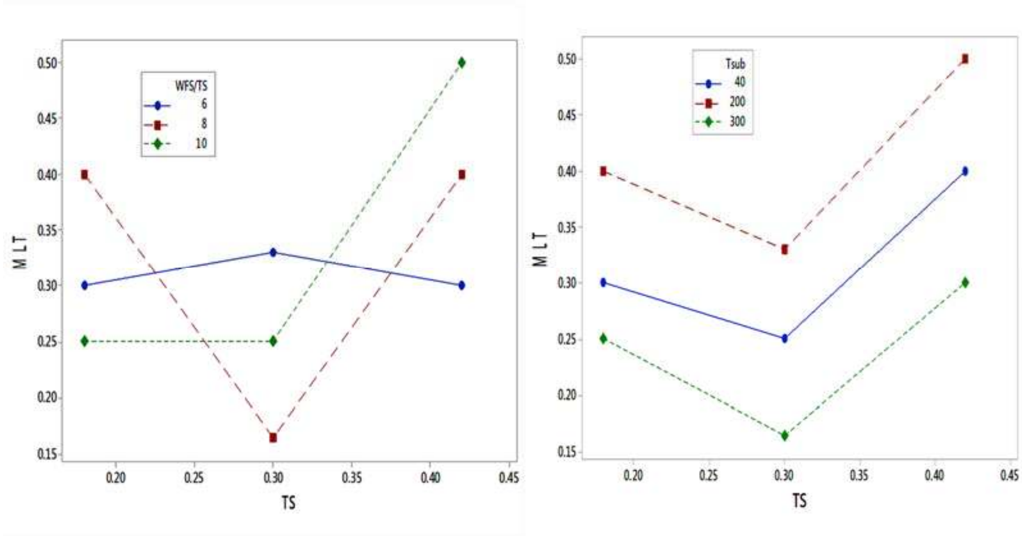

(a) **(b)**

Figure 4. 30. Influences of (a) TS and WFS/TS and (b) TS and T_{sub} on the MLT

Figure 4. 31. Effects of Tsub and TS on the sidewall surface facet

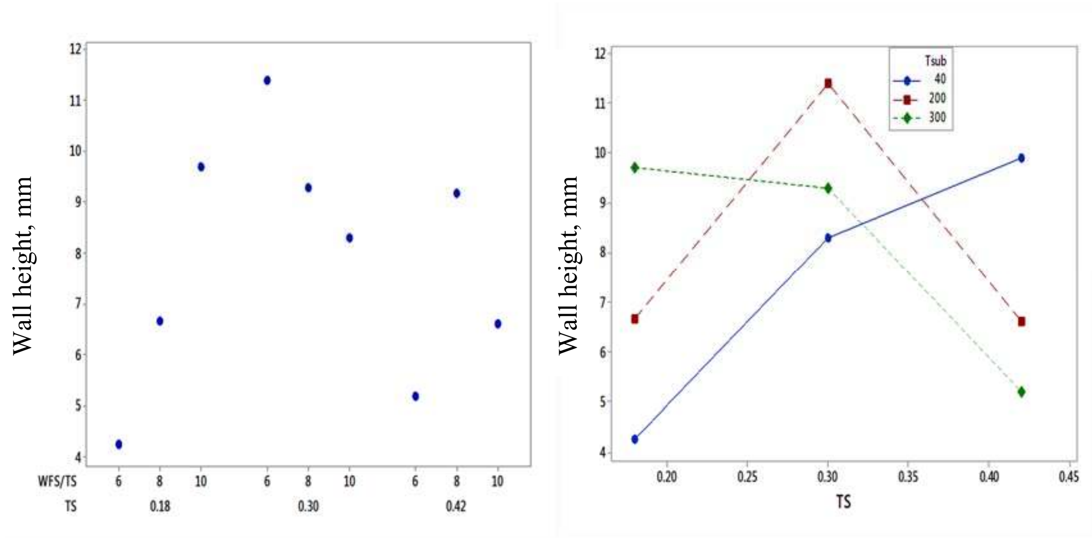

(a) **(b)**

Figure 4. 32. Influences of (a) TS and WFS/TS and (b) TS and T_{sub} on the H.

4.5.2.3 Effects on Height

The effects of TS and WFS/TS on the total wall height are shown in Figure 4.32(a). While the effects of Ts and T_{sub} on the total height H are shown in Figure 4.32(b). It is clear that WFS/TS has a noticeable effect on the total height at constant TS. The maximum height of the deposited wall can be got as the TS is equal or less than (0.3 m/min). The wall height decreases with increasing the heat input (current and voltage of the welding source) when the DV remains constant. The TS would have the same effect, but here the DV wouldbe changed (see equation 2). So reducing the TS will increase DV and as a result, the height may increase as shown in Figure 4.32(a). The T_{sub} has less effect on the H as compared with WFS/TS parameter at constant TS (see Figure 4.32(b)), but the main effect of the T_{sub} was on the sidewall quality especially with high temperatures (200-300)°C as summarized in Figure 4.30 and 4.31.

The mathematical model to establish the relationships between the responses and input parameters was developed based on the experimental data collected from Table 4.3 and taguchi L9 orthogonal array. The model was developed using the least squares approach based on multiple regression with four regressor variables (i.e. TS, WFS/TS, and T_{sub}). As a general form, geometrical output variables, represented by the response parameter Y, are related to the key three input parameters. This yielded equation is of the form of;

$$Y = K + aX1 + bX2 + cX3 \quad \textbf{(4.11)}$$

.

where: Y is any output variable such as EWW, MLT, and H, X1-X3 represent the input parameters of TS, WFS/TS, and Tsub respectively. a, b, c and k are modeling constants

These modeling constants are calculated for each response using the multiple regression techniques, with these results presented in the following equations.

$$EWW\ (mm) = 8.224 + 0.002984\ T_{sub} + 0.0917\ WFS/TS - 9.167\ TS \quad \textbf{(4.12)}$$

$$MLT\ (mm) = 0.210 - 0.000219\ T_{sub} + 0.0058\ WFS/TS + 0.347\ TS \quad \textbf{(4.13)}$$

$$Wall\ height\ (mm) = 4.57 + 0.00341\ T_{sub} + 0.313\ WFS/TS + 0.53\ TS \quad \textbf{(4.14)}$$

4.5.2.4 Effects of Continuous Deposition Process on the Sidewall Quality

Throughout the experiments of deposition walls, it was discerned that there is a correlation between the interpass temperature and the sidewall quality. It was noticed that in the case of depositing the subsequent layers on the previous one when it with high temperature helps to produce walls with fewer surface waves of sidewalls. But from the other side, it is important to control the amount of heat input to the weld pool and the deposited wall and to prevent increasing it due to the cumulative heat because the continuity of adding the layers. This problem may be overcomed using an efficient cooling system and a suitable traveling speed. Figure 4.33 compares the two walls, one wall was produced by using the idle time between layers to bring the deposited layer to the ambient temperature, whereas the other wall was carried out by the continuous deposition process. Both walls were done using the same welding parameters and other conditions (see Table 3.11). Figure 4.34 presents the steps of machining the wall side by removing a layer of thickness between (0.25-0.85) mm to get completely vertical machined top and side wall surfaces.

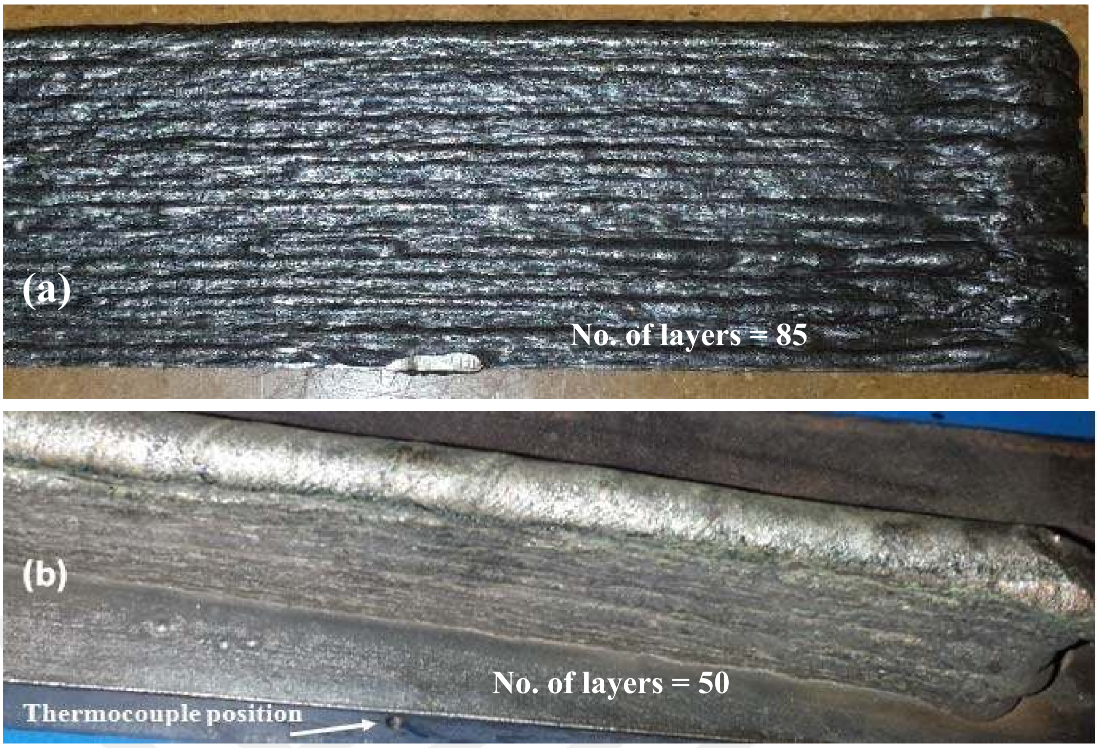

Figure 4. 33. Compares the sidewall roughness between two samples from experiments (a) using idle time each four layers; (b) continuous deposition without idle time in between layers

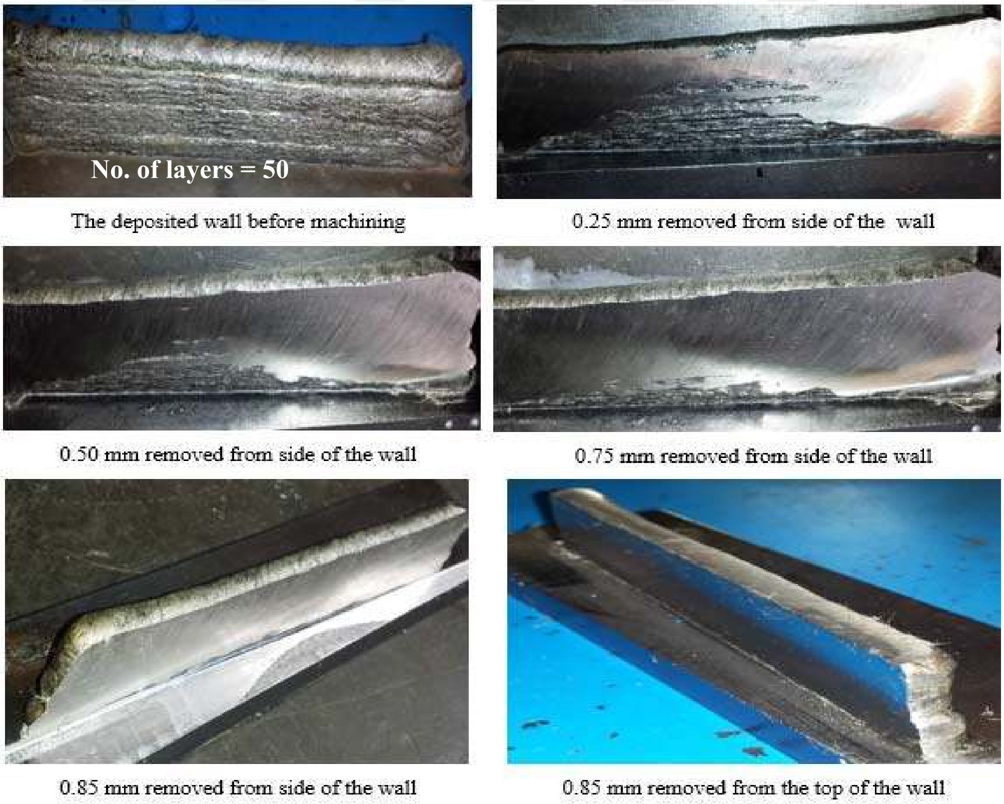

Figure 4. 34. Photos illustrate the machining layer thickness (MLT) by milling of the deposited wall.

Regarding the thermal histories within the deposited layers of the wall in Figure 5.33b. A K-type thermocouple was attached to the midpoint of the deposited wall of 200 mm in length, 50 layers, and 30 mm in height as shown in Figure 4.33(b). The thermocouple was positioned into the pre-machined drill to a distance near to the weld pool center, but underneath the surface of the substrate. The thermocouple was connected via industrial data logger (see Figure C.1 (c)). The Figure 4.35 shows the temperature variation on the underneath surface in the midpoint of the substrate. The substrate temperature was increased to 200°C before deposition to start. The oscillation was the evident characteristic of the temperature measurements. Figure 4.36 shows the temperature variation of Experiment 6 in Table 4.3. In this case the idle time between subsequent layers, so the temperature varies between 40 °C and maximum as shown in Figure 5.32.

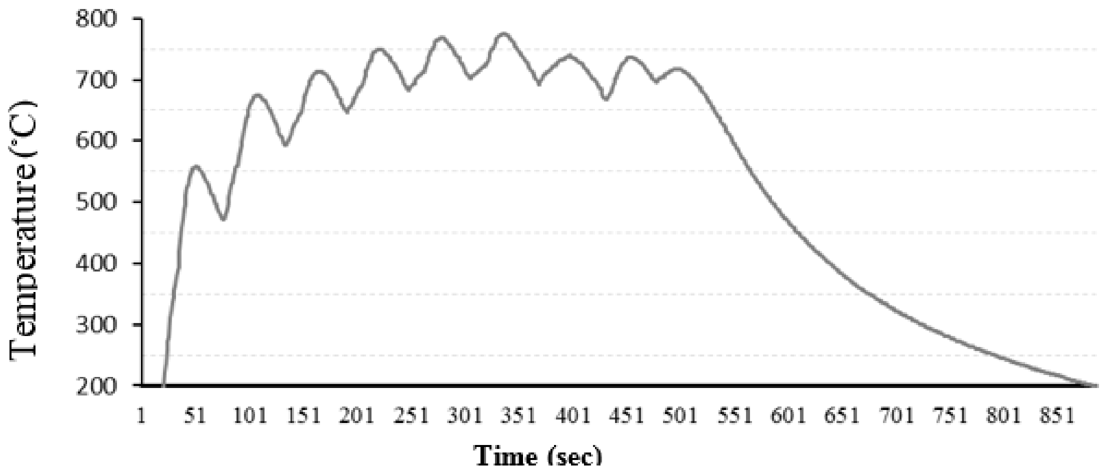

Figure 4. 35. Thermal history of the underneath surface of the first deposited layer, while 80 subsequent layers are deposited.

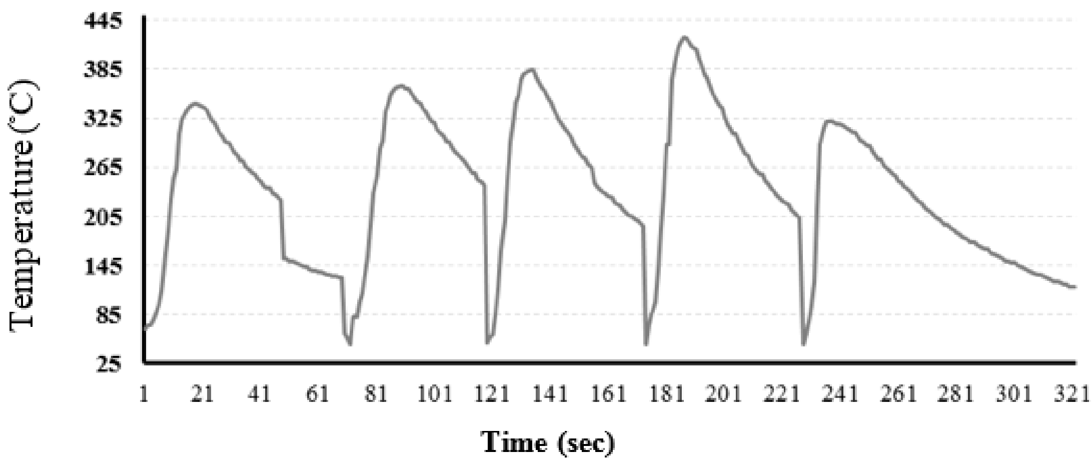

Figure 4. 36. Temperature history on the underneath surface of the first deposited layer, during the multi-bead stacks produced by Experiment 6. The substrate temperature maintains at 40 °C.

4.6. Preliminary Experiments for Developing the Process Model of PCSMD Technique

A large number of trial runs were conducted to find out the working limits of the process parameters. The bead contour, appearance, and quality of the weld joint were inspected in order to identify the welding parameters. The preliminary trials were done by a bead on plate method to determine the peak pulsed current. Figure 4.37 represents such bead-on-plate. It can be seen that if the current is less than 160A, the deposition process is difficult and dripping bead appears as shown in Figure 4.38 in the case of low currents. Also, it can be seen that as the peak current (I_p) is more than 210 A, the deposition process becomes unstable and with high spatter, undercut, and excessive melting may appear. So the suitable range of I_p is (160-210 A). If CR (I_p/I_b) less than 1.5, the deposition process becomes unstable since this leads to high heat input and overheating. At the same time if CR greater than 2.5, the heat input is very less and leads to incomplete melting. From another side when the frequency is very less (i.e. less than 1.5 Hz), unstable bead results, bad bead quality, and humping appear such as shown in Figure 4.38. At the same time at the high frequencies, the harsh sound emanated from the welding machine. If the travel speed (TS) is less than 2 mm/s, the quality of the bead is not acceptable due to the excessive fusion of the deposited metal. At high TS that is greater than 5 mm/s, the process becomes unstable since the time is not enough to melt the metal wire.

4.6.1 Effects of Frequency on the Process Stability and Bead Geometry

The results in this subsection were obtained using the pulsed current welding machine described in Section 3.5.1. The deposition condition selected in this experiments are given in Section 3.5.1.1. Table 4.4 shows the experiment design and the bead geometry results for the first experiment and Table 4.5 shows the results of the second experiment which were mentioned in Section 3.5.1.1 and Table 3.14.

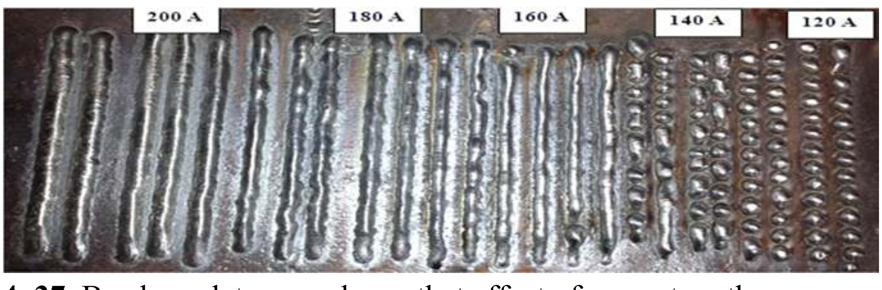

Figure 4. 37. Bead on plate runs shows that effect of current on the process stability and deposition possibility.

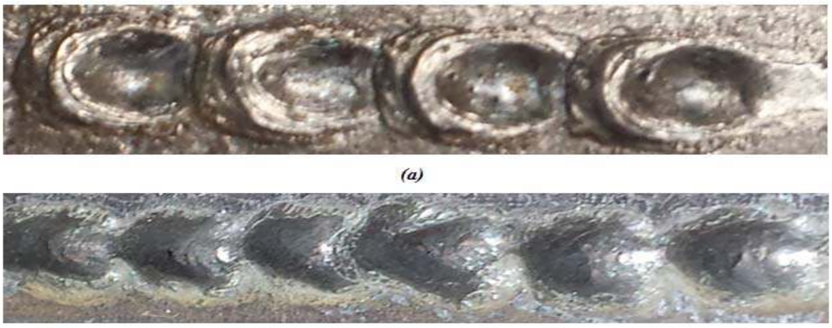

(a)

(b)

Figure 4. 38. Pictures illustrate the bead humps due to low frequency, (a) (Fr=0.5 Hz); (b) (Fr=1.0 Hz)

Table 4. 4. Bead geometry and penetration results for each frequency used in the first experiment.

Exp. No.	Frequencies Hz	$W_{av.}$	H_{av}	P_{av}
1	3	3.75	3	0.5
2	5	3.9	2.9	0.6
3	7	3.7	2.93	0.5
4	9	3.76	2.83	0.6
5	11	3.5	2.8	0.65
6	17	3.36	2.8	0.55
7	30	3.5	2.7	0.55
8	50	3.4	2.96	0.9
9	100	3.33	2.86	0.65
10	200	3.4	2.83	1.1
11	300	3.76	2.86	0.7
12	400	4.03	2.86	0.65
13	500	4.16	2.73	0.45
14	600	4.13	2.8	0.5
15	700	4.06	2.8	0.8
16	800	4.2	2.8	0.6
17	900	4.3	2.73	0.64

The main effects of the frequency on the bead width, height and the penetration for the two experiments are shown in Figure 4.39(a - b). It can be seen that the width of the bead reduces slightly with increasing the frequency in low-frequency regions at the low current experiment and increases slightly with the frequency in the high-frequency regions at high current experiment as shown in Figure 4.40. In the process of low frequencies for both experiments, the more suitable frequency values which give a reasonable bead width are 5, 9, 30, and 90 Hz. Whereas for the high-frequency process are 500, 1750, and 2000 Hz. There is no evident effect of the frequency on the bead height in both experiments and for low and high frequencies. The penetration increases slightly with the frequency at high welding current as shown in Figure 4.41 (b).

Table 4. 5. Bead geometry and penetration results for each frequency used in the second experiment.

Exp. No.	Frequencies Hz	W av.	H_{av}	P_{av}
1	1.5	4.3	2	1.1
2	3	4.5	1.88	0.9
3	5	4.6	2	0.95
4	10	4.75	2.15	0.8
5	20	4.55	2	0.7
6	30	4.23	1.8	0.9
7	50	4.43	1.9	1
8	70	4.3	1.8	1.2
9	90	4.6	1.95	1.1
10	100	4.43	1.83	1.2
11	500	4.7	1.8	1.3
12	750	4.6	1.85	1.1
13	1000	4.76	1.8	1.2
14	1250	4.8	1.65	1
15	1500	4.8	1.8	1.1
16	1750	5	1.85	1.3
17	2000	4.9	1.88	1.2
18	2500	4.8	1.7	1.3

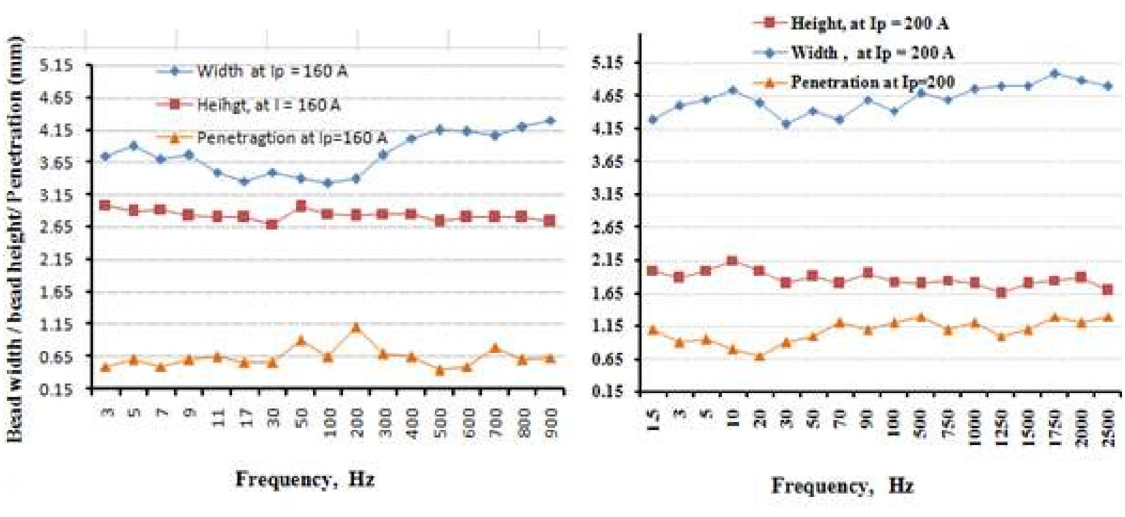

(a) (b)

Figure 4. 39. Effects of Fr on bead geometry at two set of parameter combinations: (a) Ip =160 A, TS = 3 mm/s, and WFS =2 m/min; (b) Ip = 200 A, Ts mm/s =4, And WFS= 2.5 m/min.

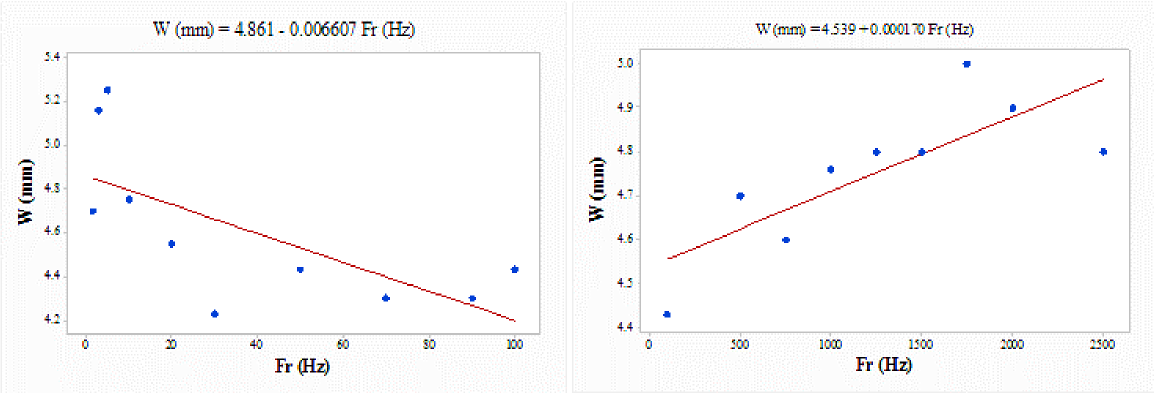

(a) **(b)**

Figure 4. 40. Effects of Fr on bead width at two set of parameter combinations: (a) low frequency region (b) high frequency region.

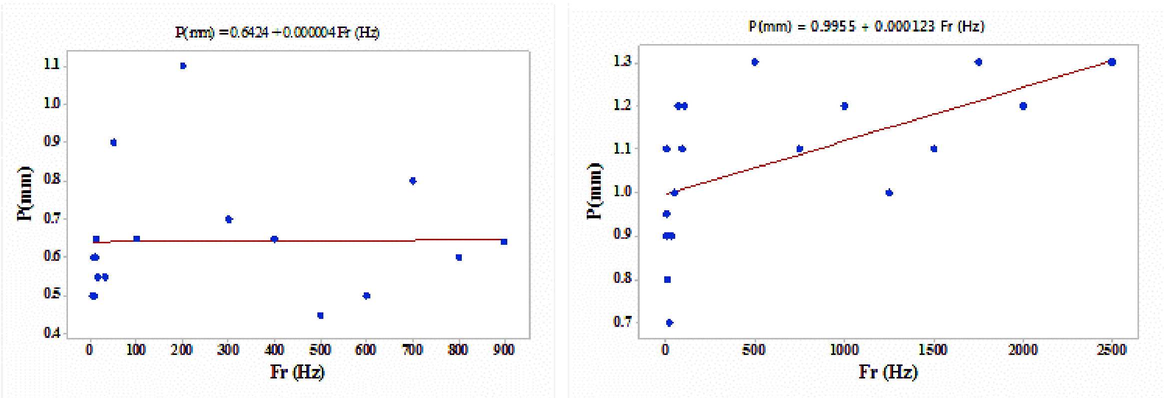

(a) **(b)**

Figure 4. 41. Effects of Fr on the penetration amount: (a) Ip =160 A, TS = 3 mm/s, and WFS =2 m/min; (b) Ip = 200 A, Ts mm/s =4, And WFS= 2.5 m/min

4.6.2 Effects of Travel Speed and I_p/I_b Ratio on the Process Stability and Bead Characteristics Using Low-Frequency (LF).

The experiments reported in this section were carried out according to the set-up, deposition conditions, and experimental method detailed in Section 3.5.1.3 (Chapter 3). The experimental design is detailed in Table 4.6, together with penetration and deposited bead shape response data. As mentioned in Section 3.5.1.3, Taguchi approach was used for designing the experiment and L9 orthogonal array. The filler metal was 0.8 mm diameter SS308LSi. The analysis of variance is a statically based decision tool used for interpreting experimental data and make the necessary decision.

4.6.2.1 Effects on Wall Width $W_{av.}$

The result of ANOVA for the wall height is shown in Table I.1 as given in Appendix I. From this initial analysis, it is possible to conclude that the most significant factors are: welding current, and the current ratio, whereas the travel speed and the frequency are fewer effects on the wall width. These effects can be seen graphically as shown in Figure 4.42. The effects of the frequency on the width of the bead at different currents is shown in Figure 4.43. It confirms the same truth in Figure 4.40.

Table 4. 6. Deposition conditions used and bead geometry and penetration with low frequency

Exp.	Input Parameters				Responses			
No.	I_p	Fr	TS	CR	W_{av}	$H_{av.}$	$P_{av.}$	AR
1	165	1.5	2	1.5	4.46	2.3	1.5	2.97
2	165	30	3	2	3.8	2.5	0.25	15.2
3	165	90	4	2.5	3.16	2.8	0.7	4.51
4	185	1.5	3	2.5	4.33	2.96	0.95	4.56
5	185	30	4	1.5	4.1	2	0.7	5.86
6	185	90	2	2	4.8	3.15	1.4	3.43
7	205	1.5	4	2	4.7	1.65	1	4.7
8	205	30	2	2.5	4.85	3.05	1.35	3.59
9	205	90	3	1.5	6.66	1.66	0.85	7.83

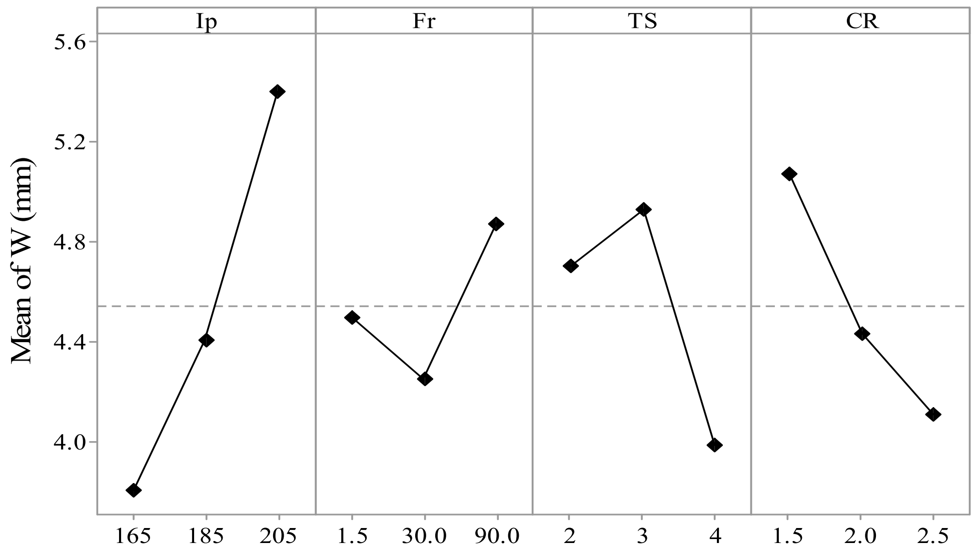

Figure 4. 42. Main effects plot for wall height

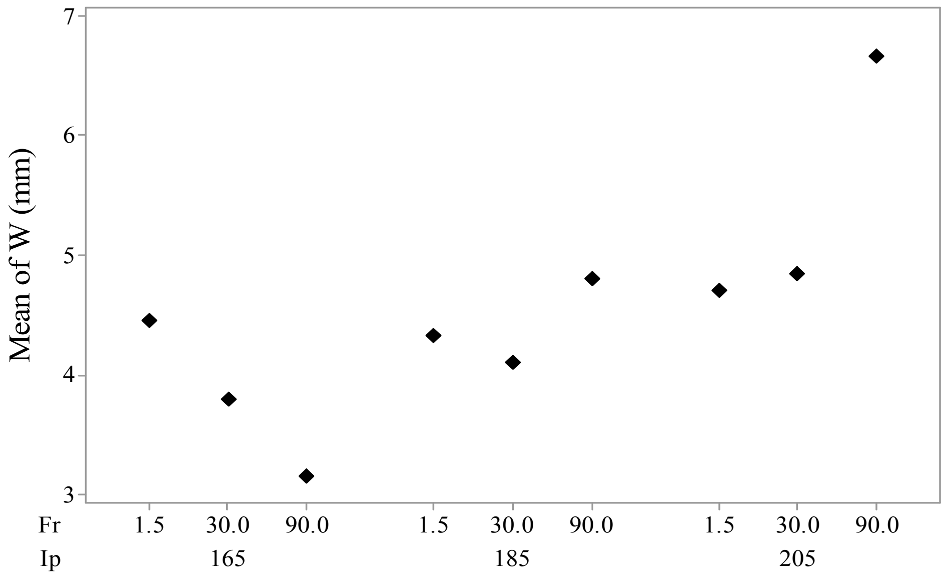

Figure 4. 43. The individual values of W corresponding to the I_p and Fr.

4.6.2.2 Effects on Bead Height H_{av}.

The result of ANOVA for the wall height is shown in Table I.2 as given in Appendix I. From this initial analysis, it is possible to conclude that the most significant factors are current ratio (CR) and then travel speed, whereas the welding current and the frequency are less effects on the wall width. These effects can be seen graphically as shown in Figure 4.44. When the current ratio is increased then the bead height increases. This effect is due to the amount of heat input to the deposition zone that significantly decreases at low base current (I_b).

4.6.2.3 Effects on Depth of Penetration P_{av}

The result of ANOVA for the depth of penetration is shown in Table I.3 as given in Appendix I. From this initial analysis, it is possible to identify that there is no evident significant factor of the main parameters and their interaction. The travel speed has small significance. These effects can be seen graphically in the main effects plot as shown in Figure 4.45.

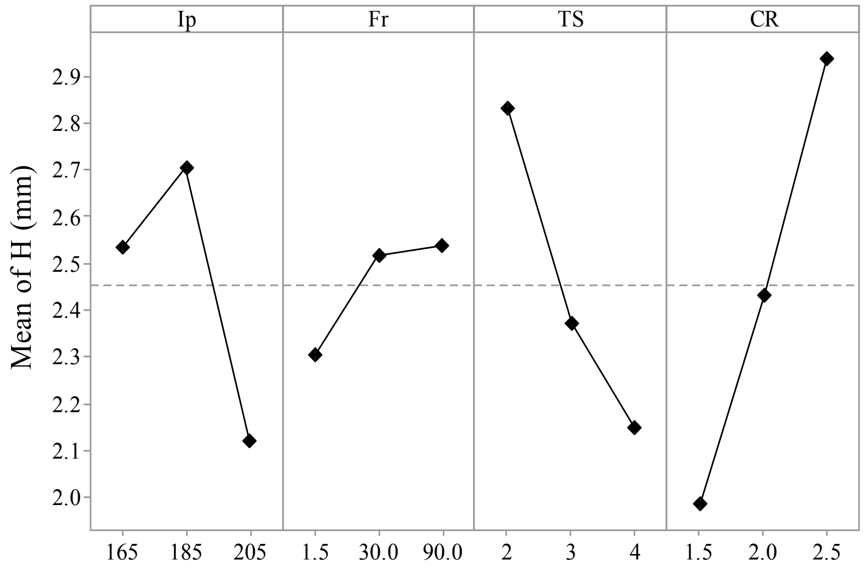

Figure 4. 44. Main effects plot for wall height

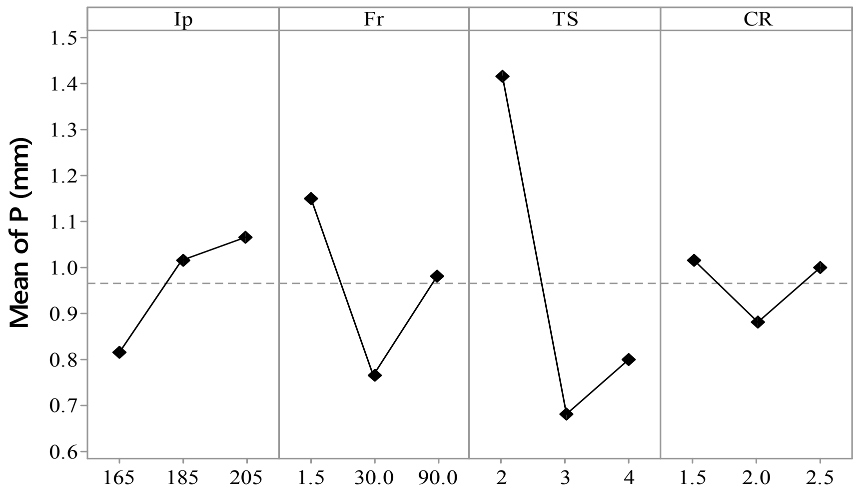

Figure 4. 45. Main effects plot for penetration

.

4.6.3 Effects of TS and I_p/I_b Ratio on the Process Stability and Bead Characteristics Using High-Frequency (HF).

This section reports the influence of the main parameters on the bead geometry. In addition, the thickness of the penetration of the deposited samples. The measured bead profile, namely bead width, average of total wall height, and the penetration depth are reported in Table 4.7

Table 4. 7. Experimental layout for the deposition process parameters and results at HF

Exp. No.	I_p	Fr	TS	CR	$W_{av.}$	$H_{av.}$	$P_{av.}$	Aspect ratio (AR)
1	165	500	2	1.5	4.633	3.06	0.40	5.15
2	165	1500	3	2.0	3.530	2.55	0.45	10.09
3	165	2500	4	2.5	3.360	2.00	0.60	5.6
4	185	500	3	2.5	4.360	2.36	0.35	12.45
5	185	1500	4	1.5	4.560	1.60	0.65	7.02
6	185	2500	2	2.0	5.760	1.70	0.80	7.2
7	205	500	4	2.0	4.700	1.70	0.55	18.8
8	205	1500	2	2.5	6.230	2.80	0.80	7.78
9	205	2500	3	1.5	6.630	1.45	1.10	6.03

As mentioned in section 3.5.1.4, Taguchi approach was used for designing the experiment and L9 orthogonal array. The filler metal was 0.8 mm diameter SS308LSi. In a similar procedure in section 4.1.2, the analysis of variance is a statically based decision tool used for interpreting experimental data and make the necessary decision.

4.6.3.1 Effects on Bead Width, W_{av}

The result of ANOVA for the bead width is shown in Table I.4. From this initial analysis, it is possible to conclude that the most significant factors are: welding current, travel speed, followed by the frequency and current ratio. These effects can be seen graphically as shown in Figure 4.46. It is obvious that all the parameters have significant effects on the bead width. From the Figures 4.46 and 4.47, it can be discerned that the frequency of 500 Hz produces a more stability in bead width at different current values.

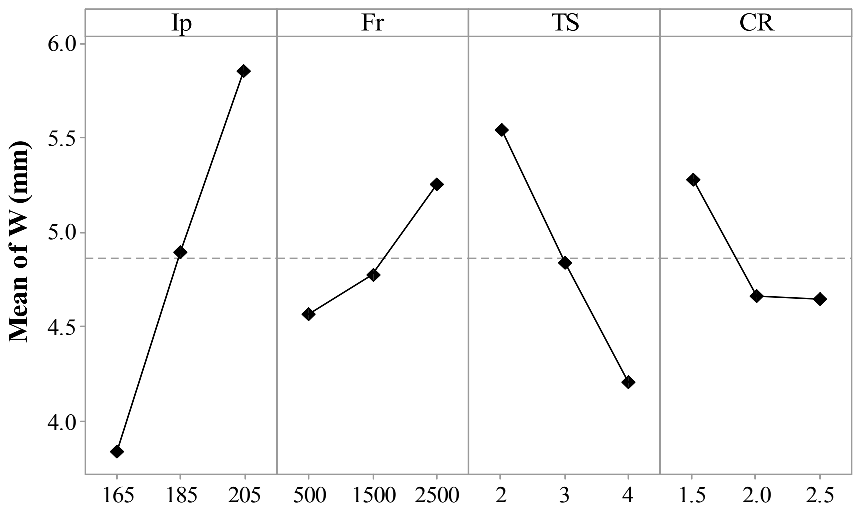

Figure 4. 46. Main effects plot for bead width

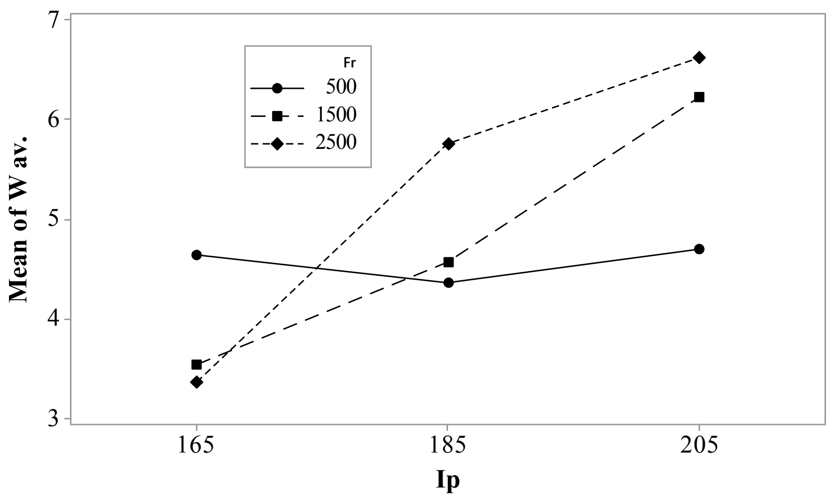

Figure 4. 47. Interaction effects between Ip and Fr on the bead width

4.6.3.2 Effects on Bead Height, H_{av}

The result of ANOVA for the bead width is shown in Table I.5 as given in Appendix I. From this initial analysis, it is possible to conclude that the most significant factors are travel speed and frequency while the welding current and current ratio have less effects. These effects can be seen graphically as shown in Figure 4.48. The suitable value of current is about 185 A as shown in Figure 4.49, which produces layer with height does not exceed 2 mm.

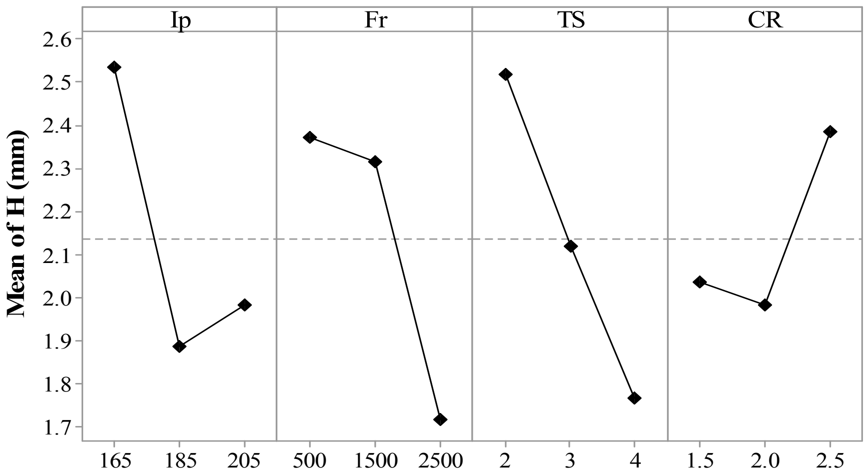

Figure 4. 48. Main effects plot for bead height

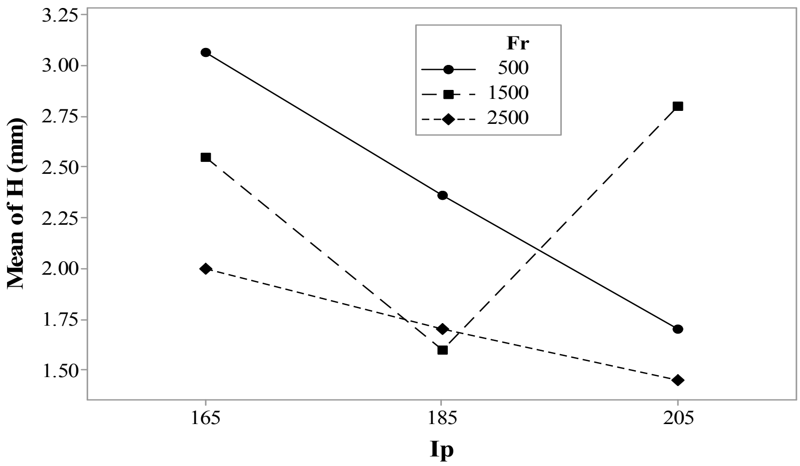

Figure 4. 49. Interaction effects between Ip and Fr on the bead height

4.6.3.3 Effects on depth penetration, P_{av}.

The result of ANOVA for the depth of penetration is shown in Table I.6 as given in Appendix I. From this initial analysis, it is possible to conclude that the most significant factors are welding current and frequency while the travel speed and current ratio have less effects. These effects can be seen in Figure 4.50. The penetration is shallower at 500 Hz frequency for all current sets and the penetration depth amounts range is between 0.25-1.1 mm.

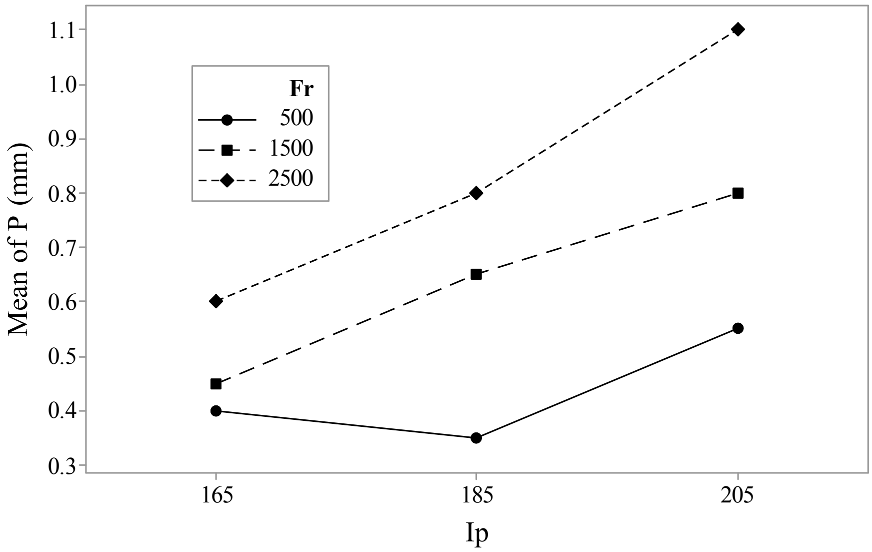

Figure 4. 50. Effects of current and frequency on the depth of penetration

.

Table 4. 8. Experimental layout for the deposition process parameters and results.

	Input factors				Responses			
Exp. No.	I_p	Fr	TS	CR	W	H	P	HRA kg_f
1	165	1.5	2	1.5	12.70	10.670	1.10	56.3
2	165	30	3	2	11.55	9.500	0.80	55.266
3	165	90	4	2.5	7.63	10.000	0.30	57.6
4	185	1.5	3	2.5	10.56	10.700	0.90	56.175
5	185	30	4	1.5	9.50	8.800	1.20	55.35
6	185	90	2	2	12.00	11.600	1.25	52.08
7	205	1.5	4	2	9.64	8.125	1.35	53.766
8	205	30	2	2.5	12.00	11.700	1.70	52.18
9	205	90	3	1.5	14.00	8.125	1.65	53.46

4.7 Multilayer Deposition Experiment

4.7.1 Effects of Main Process Parameters on the Process Stability, Hardness and Bead Characteristics Using Low-Frequency (LF)

The experiments reported in this section were carried out according to the set-up, deposition conditions, and experimental method detailed in Section 3.5.2.1 (Chapter 3). The experimental design is detailed in Table 4.8, together with penetration, hardness, and deposited bead shape responses. All the reported outputs' values were taken as an average of (4-5) readings for each response. As mentioned in section 3.5.2.1, Taguchi approach was used for designing the experiment and L9 orthogonal array. The filler metal was 0.8 mm diameter SS308LSi. The analysis of variance is a statically based decision tool used for interpreting experimental data and make the necessary decision.

4.7.1.1 Effects on wall width, W_{av}.

The result of ANOVA for the wall width is shown in Table J.1 as given in Appendix J. From this initial analysis, it is possible to conclude that the most significant factors are travel speed, followed by the current ratio, whereas the welding current and the frequency are less effects on the wall width. These effects can be seen graphically as shown in Figure 4.51.

4.7.1.2 Effects on Wall Height H_{av}.

The result of ANOVA for the wall height is shown in Table J.2. From this initial analysis, it is possible to conclude that the most significant factors are: travel speed, followed by the current ratio, whereas the welding current is less effect on the wall width and the frequency has no sensible effect on the total wall height. These effects can be seen graphically as shown in Figure 4.52

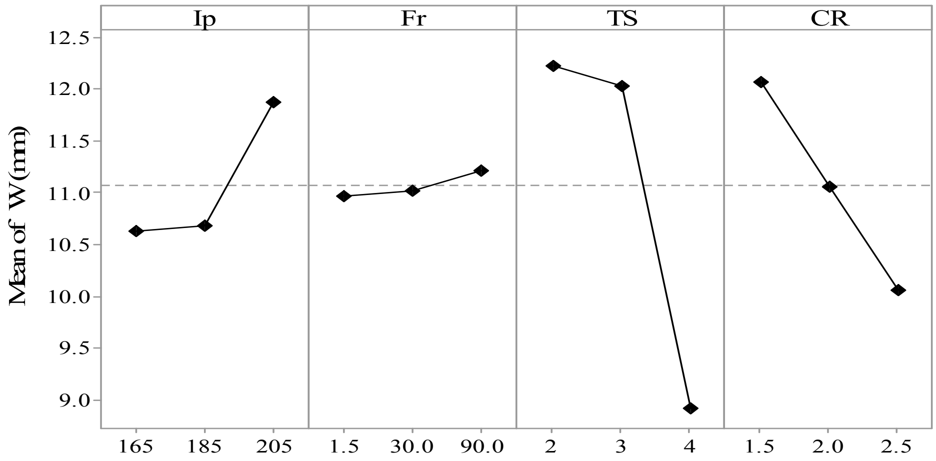

Figure 4. 51. Main effects plot for wall width

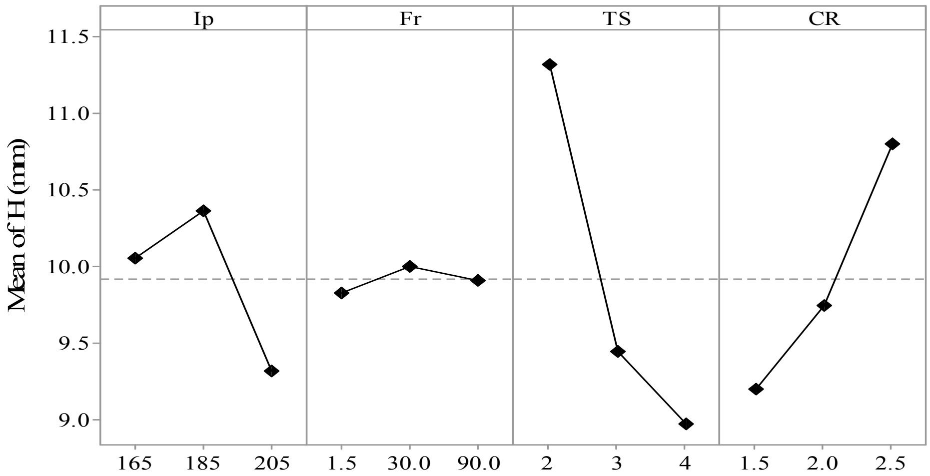

Figure 4. 52. Main effects plot for wall height

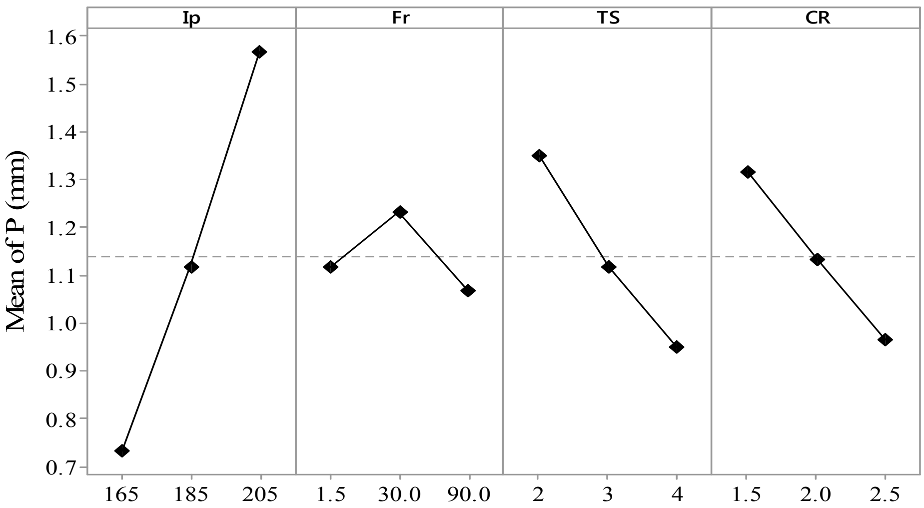

Figure 4. 53. Main effects plot for penetration.

4.7.1.3 Effects on the Depth of Penetration P_{av}.

The result of ANOVA for the penetration is shown in Table J.3. From this initial analysis, it is possible to conclude that the most significant factors are welding current, travel speed followed by the current ratio, whereas the frequency has no sensible effect on the penetration depth. These effects can be seen graphically as shown in Figure 4.53.

From the results of this experiment, it can be discerned that the Fr has a low effect on the wall geometry and also the penetration. So the frequency of 5 Hz may be suitable since it is not generating a harsh sound as in the 90 Hz, at the same time they give the same effects to the wall geometry. From another side, the CR has a significant effect on the wall geometry and the depth of penetration. So the most suitable CR is 2 since this amount gives the stability to the deposition process. For that reason, the recommended CR is 2 for all experiments of pulsed current TIG + wire SMD (PTW-SMD) process.

4.7.1.4 Effects on Hardness.

The result of ANOVA for the wall cross-section hardness HRA is shown in Table J.4 as given in Appendix J. From this initial analysis, it is possible to conclude that the most significant factors are: welding current, followed by the travel speed, whereas the current ratio and the frequency are less effects on the hardness. These effects can be seen graphically as shown in Figure 4.54.

The hardness readings were taken as an average of 5 readings at the center of the deposited samples. It can be seen that the hardness significantly depends on the heat input during the deposition process especially the peak welding current and the travel speed. At the case of low current or high speed (low heat input) the cooling rate is high and so the grains expected to be fine which leads to increase the hardness.

4.8 Metallography Testing Results

The process parameters affect the surface morphology and microstructure of the deposited parts using CCSMD and PCSMD processes. This Section mainly focuses on the influence of process parameters on the transformation of primary ferrite grain structure formed in the TIG plus wire SMD (TW-SMD) processes. The TW-SMD process which is relatively a newer technology still under development and considerably immature, in terms of the current understanding of the influence of the process parameters on the morphology and microstructure. The main parameters consist of the arc current, travel speed of the melting source, wire feed speed, and type of power used whether is pulsed current or continuous current type. These parameters can have significant effects on the final macro- and microstructure of the manufactured parts.

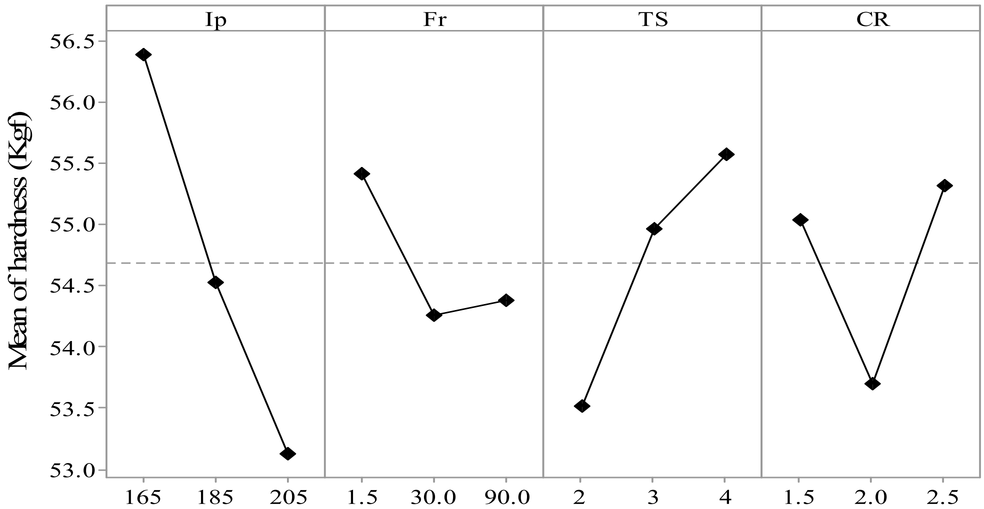

Figure 4. 54. Main effects plot for hardness

4.8.1. Continuous Current Shaped Metal Deposition CCSMD

4.8.1.1 Morphology of the Surface (Macrostructure Results)

Etched cross-section and side view of all specimens exhibit a layered structure, reflecting the layers bands and typical large columnar grain as shown in Figure 4.55. It is possible to distinguish parallel bands in the side view and wavy bands in the cross-section. Figure 4.56 reveals the elongated grains, which grow epitaxially from the substrate, pervading the weld layers. These grains grow vertically in the deposit center of the cross-section specimens (see Figure 4.55), whereas they inclined along the steepest temperature gradient during deposition and solidification in the side view specimens.

All the specimens revealed two distinct parts a bottom part with parallel bands and top part as shown in Figure 4.57 and Figure 4.58. The banding structure in the austenitic stainless steel SS308 type is a result of the repeated thermal cycles experienced by the solidified material. In the top part, the time is relatively short so that there is no bands appeared.

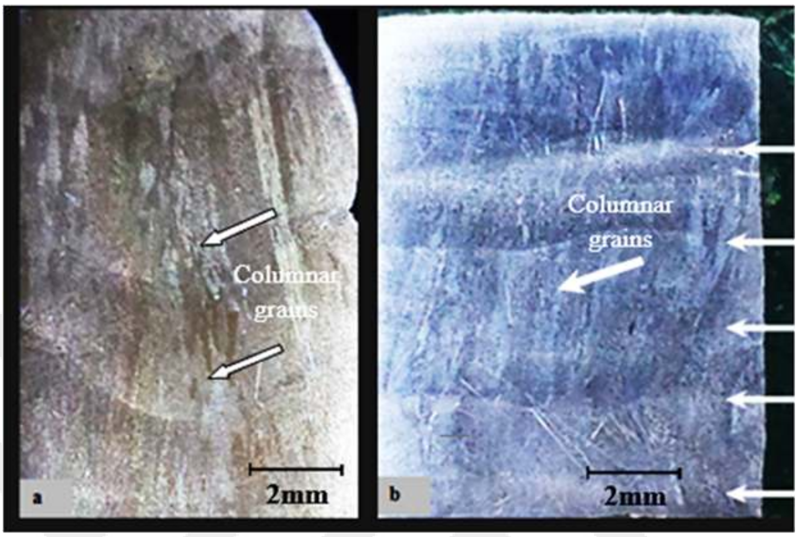

Figure 4. 55. Macrograph of the etched CCSMD component (a) cross-section (y-z plane) and (b) Side view (x-z plane) on the surface of specimens

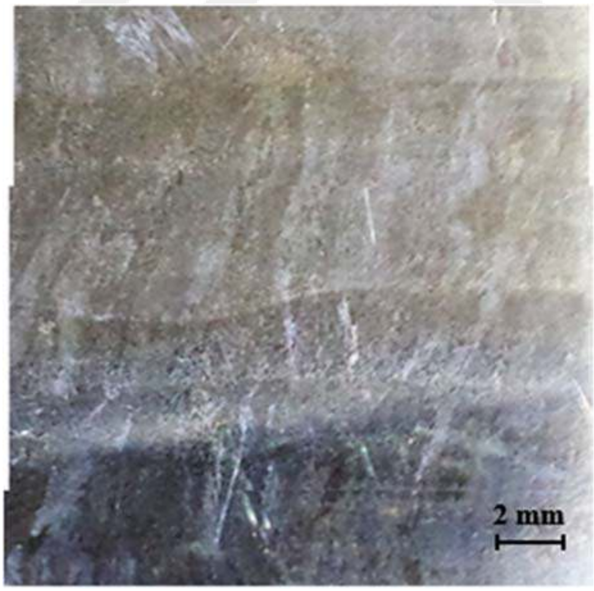

Figure 4. 56. Montage of macrostructure of CCSMD deposition of SS308LSi inside view of the wall with direct current 175 A, Travel speed 4mm/s, and WFS 3.5 m/min shows large columnar growth grains

4.8.1.2 Microstructure Analysis

As it was shown in Figure 4.55 and Figure 4.56, the columnar grains grew vertically in the cross-section of the wall specimen and inclined in the side view. Figure 4.57 show the microstructure at cross-section and side view of the top part and bottom part. The grains seem to be a randomly oriented structure at the top surface and tend to be vertical direction structure at the center of the wall. The microstructure of the top part, the structure mainly consists of two phases ferrite and austenite as predominant phases throughout the part (see Figure 4.58). The rapid cooling region near the surface affects to form of solid-state transformation producing smooth austenite-ferrite interface. These are called acicular or Widmansttãten austenite structure which are denoted as (W). Vermicular delta ferrite (V) appears as the dark- etching phase.

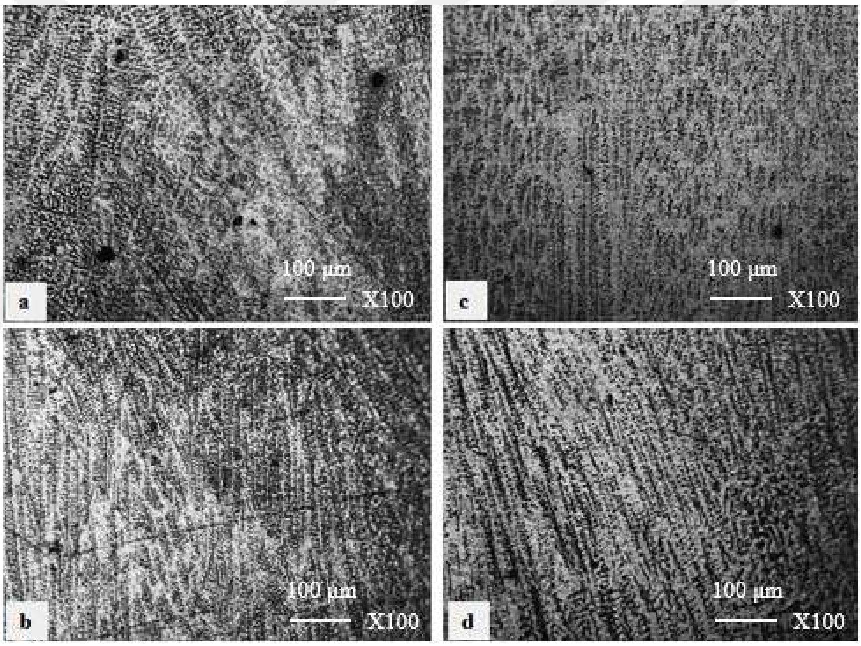

Figure 4. 57. Photomicrographs represent the microstructure of CCSMD wall specimens (a) cross-section at top part, (b) side at top part, (c) cross-section at the bottom part, and the (d) side wall at the bottom part. Original X100

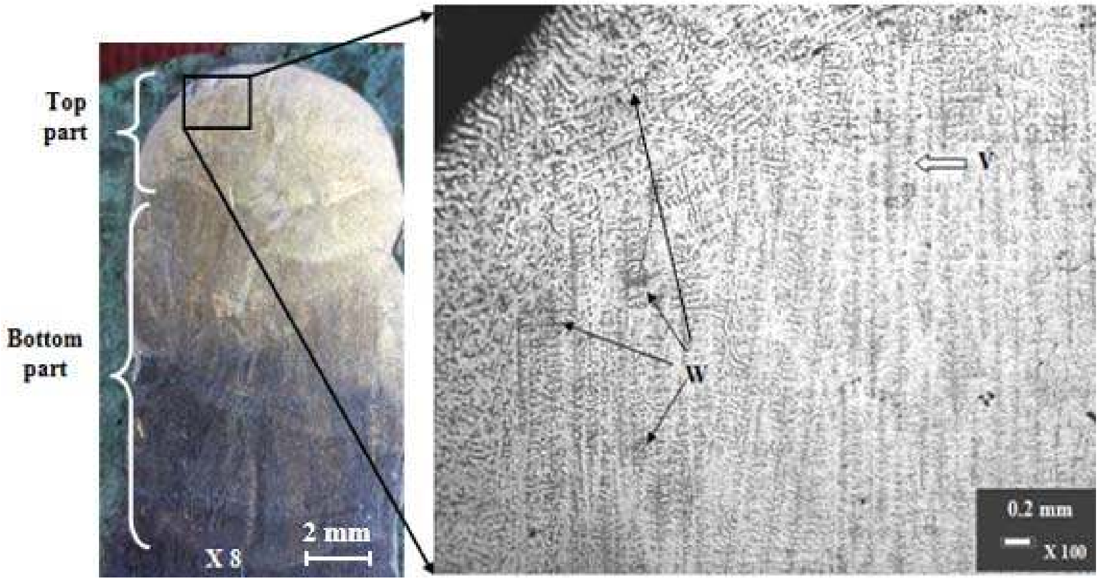

Figure 4. 58. The left side represents macrograph of the deposited wall reveals the top and bottom parts, and right side represents microstructure of the top part, showing the phases existed in that part.

4.8.1.2.1 Effect of TS on Microstructure of CCSMD

As the deposition travel speed increased from 0.24 m/min to 0.42 m/min and remain all the other parameters constant as explained before in Section 3.8.1.2, the microstructure of the deposited part changed from coarse dendrites to fine dendrites as shown in Figure 4.59. The changes in microstructure associated with the amount of heat input (Hi) to weld pool during the deposition process according to the Equation (4.1). And also the changes in microstructure may be attributed to the reduction in the ratio of a temperature gradient to the solidification rate [177].

Evaluation of the microstructure of the two samples did not reveal any intermetallic phases, which gives an indication that the deposition process would significantly improve the corrosion resistance.

4.8.1.2.2 Influence of Heat Input Hi on the Microstructure (FN) in CCSMD

The amount of ferrite content in the deposit depends on some of the parameters such as chemical composition of the filler material, welding procedure and amount of heat input [178].To investigate the effects of Hi on the microstructure, two experiments of different Hi amounts were done as were aforementioned in section 3.8.1.2. The first sample was prepared using I =150 A, TS= 0.36 m/min, and WFS = 3 m/min and so the Hi = 249 J/mm. Whereas the second specimen was prepared using I= 200A, TS = 0.3 m/min, WFS = 2 m/min and so the Hi = 398.4 J/mm. At high cooling rate (low Hi) the transformation of ferrite to austenite is suppressed and higher residual ferrite content in the deposition expected. Figure 4.60(a) shows the ferrite morphologies observed at low and high Hi. The ferrite morphology was extremely fine at Hi of 249 j/mm. The ferrite structure was skeletal with a continuous interconnected network of ferrite. Photomicrograph in Figure 4.60(b) showed that the ferrite morphology grew in the solidification direction with existing of some Widmansttãten austenite, which grew due the extended the cooling time with increasing Hi that allowed the nucleation and growth of austenite within the ferrite.

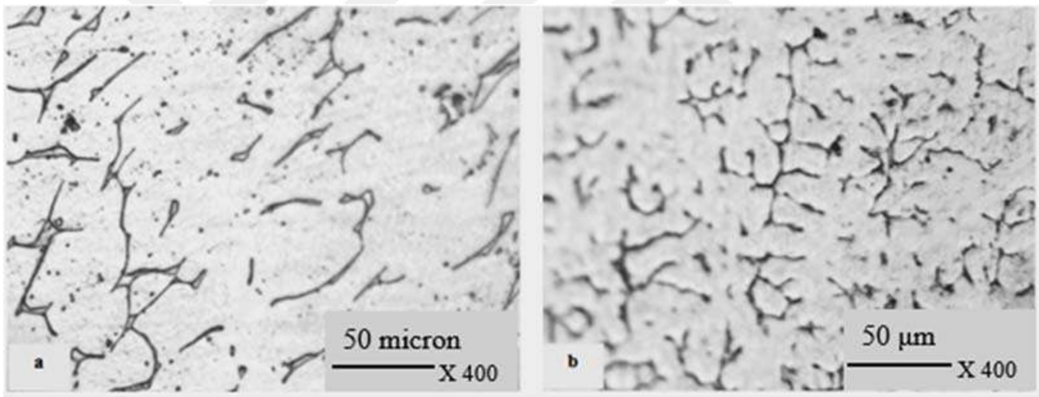

Figure 4. 59. Micrographs illustrate the microstructure at (a) TS = 0.24 m/min and (b) TS = 0.42 m/min

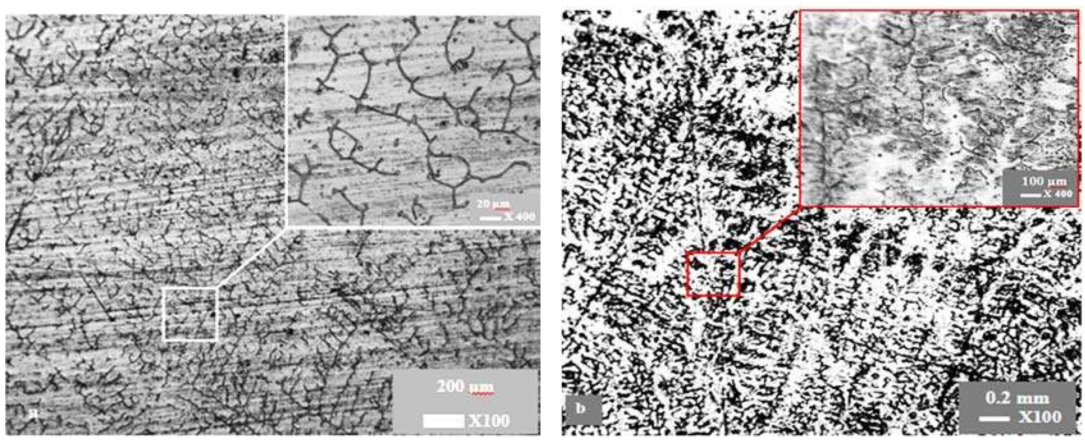

Figure 4. 60. Optical Micrographs illustrate the microstructure of the CCSMD specimen of (a) Hi = 249J/mm and (b) Hi = 398.4 J/mm

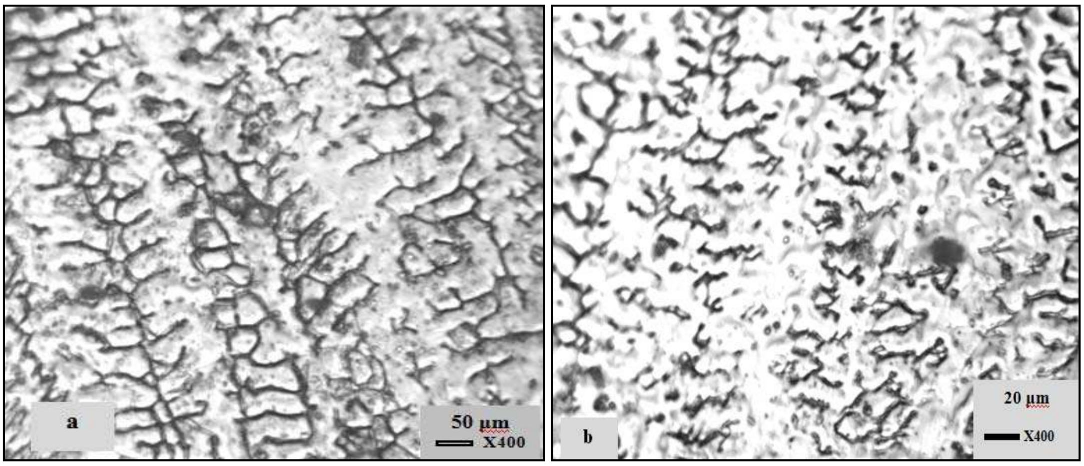

Figure 4. 61. MO. Micrographs illustrate the effects of WFS on the grains (a) WFS =2 m/min reveals skeletal ferrite structure and (b) WFS =3.5 m/min reveals fine star vermicular ferrite structure

4.8.1.2.3 Influence of Wire Feed Rate on the Microstructure (FN) in CCSMD

As WFS increases from 2 m/min to 3.5 m/min, the microstructure changes also from columnar dendrite structure to fine vermicular structure as shown in Figure 4.61. Showing that the increasing in the metal deposition rate produce finer grains and prevents producing of long dendrites grains. This attributes to the reduction in the thermal gradient in the deposition pool due to cooling the melt pool by increasing the feed rate of cold metal into weld pool, which may increase the heterogeneous nucleation.

4.8.1.2.4 Influence of Interface Temperature on the Microstructure (FN) in CCSMD

The idle time between the successive layers is important to prevent the developing of cumulative temperature in the built parts, which effects on the bead geometry and also the microstructure of the deposited parts. To show the effects of the substrate temperature between subsequent layers, two experiments with two different substrate temperature were used. Figure 4.62(a) shows the microstructure resulted from using 40 ^{o}C between the layers, it is seen that the grains tend to be fine. Figure 4.62(b) reveals the columnar grains grew in the direction of melting source movement orientation since the cooling rate is relatively long as a comparison with the first case.

4.8.2 Pulsed Current Shaped Metal Deposition PCSMD

4.8.2.1 Macrostructure (Surface Morphology)

Similar to CCSMD the etched cross-section and side view of all specimens exhibits a layered structure, reflecting the layers bands and typical columnar grain as shown in Figure 4.63. It is possible to distinguish the bands in parallel form in side view Fig. 63b, and take waveform at the center of the cross-section of wall Figure 4.63(a). Figure 4.64 shows a montage of macrostructure through the wall specimens prepared using PCSMD process at low and high frequency showing the band layers structure and the columnar grains.

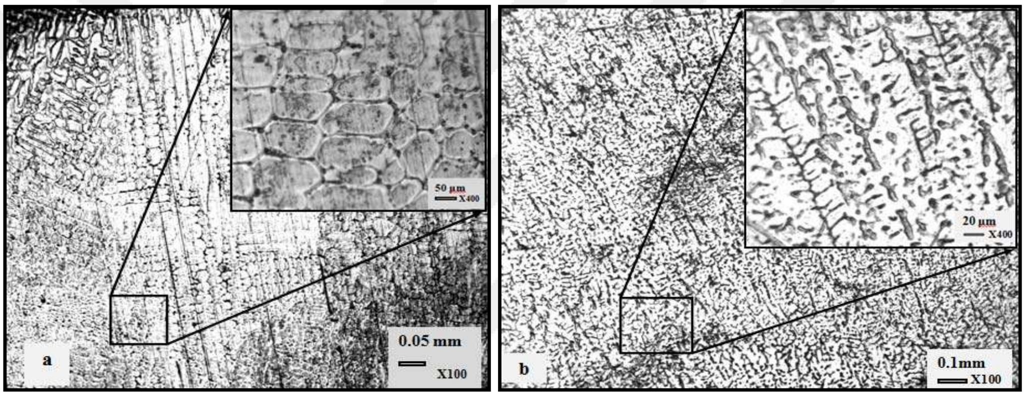

Figure 4. 62. Micrographs illustrate the effects of substrate temperature on the microstructure near the top region at different substrate temperature between subsequent layers (a) 40 °C and (b) 300 °C

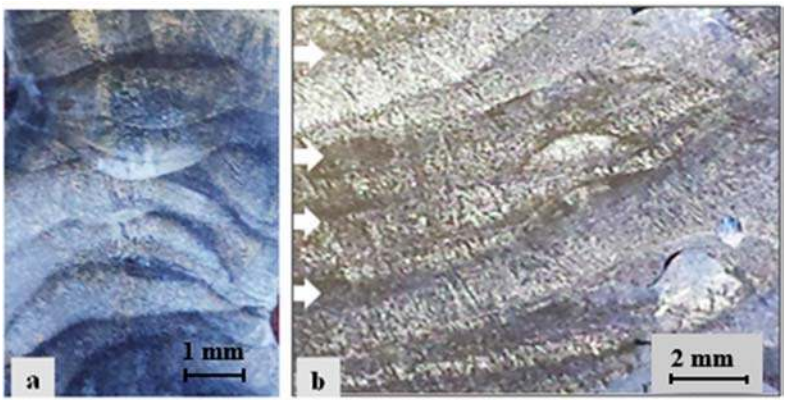

Figure 4. 63. Macrographs of etched PCSMD specimens showing the layers band on (a) cross-section and (b) Side view on the surface of the specimen.

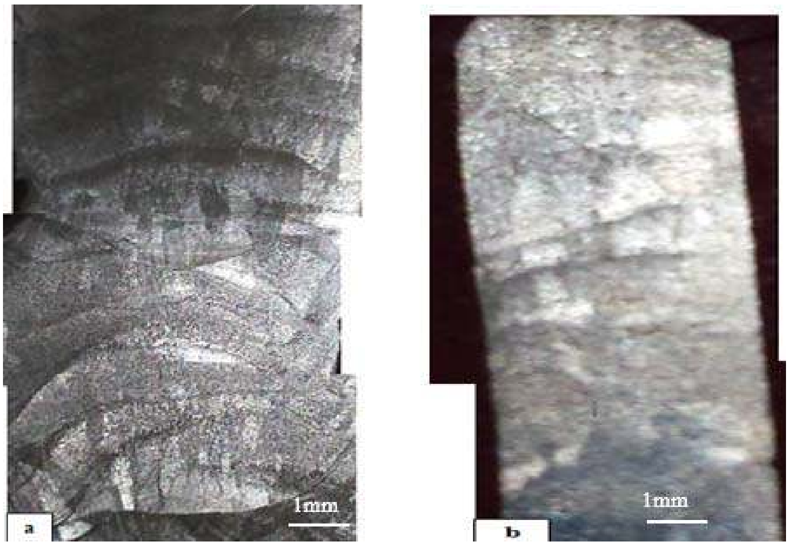

Figure 4. 64. Montage of the macrostructure of PCSMD deposition of the SS308LSi wall with direct current 175 A, Travel speed 4mm/s and WFS 2.5 m/min (a) Fr 2000HZ and CR 2, (b) Fr 30 Hz and CR 1.5; show large columnar grains have been blocked to grow at all frequencies

It is possible to see that the growth of columnar grains was broken at PCSMD process using the same process parameters as in the conventional CCSMD process as shown in Figure 4.65. The heat input to the deposition zone was 453.906 J/mm in conventional process whereas 340.43 J/mm in the pulsed current method. All specimens reveal two distinct parts a bottom part with parallel bands and top part as shown in Figure 4.66. The banding structure in the austenitic stainless steel SS308 type is a result of the repeated thermal cycles experienced by the solidified material. In the top part, the time is relatively short so that there are no bands appeared

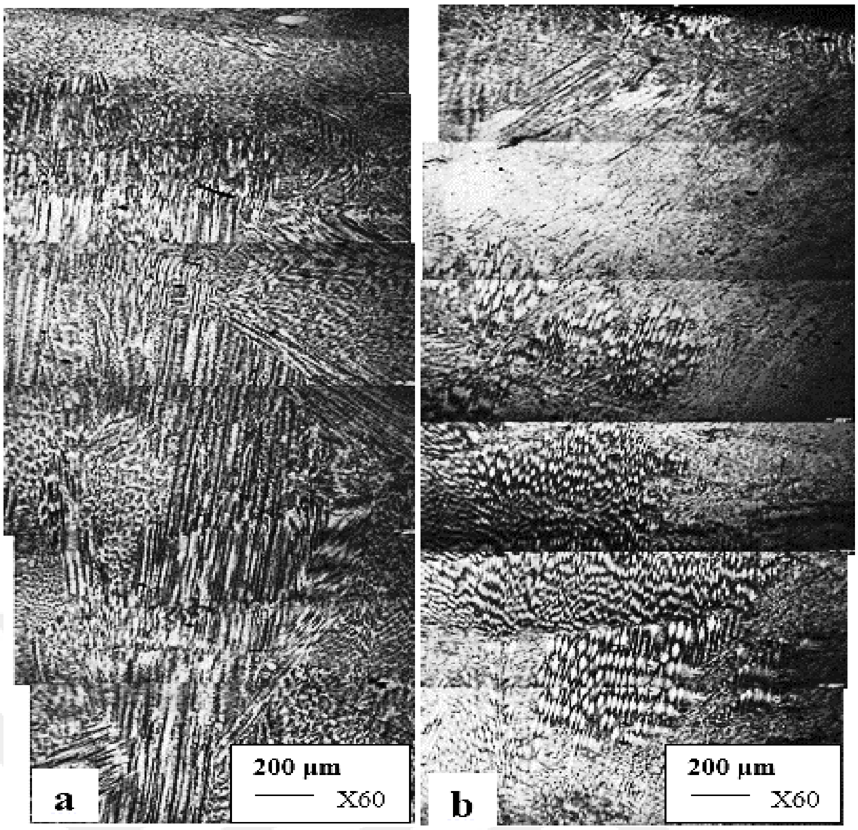

Figure 4. 65. Montage of microstructure for CCSMD and PCSMD wall specimens using process parameters of Ip 175A, CR 2, TS 4mm/s, WFS 2.5 m/min with (a) 0 HZ and (b) 2000 HZ, Ib 87.5A and the on-time of 50%.

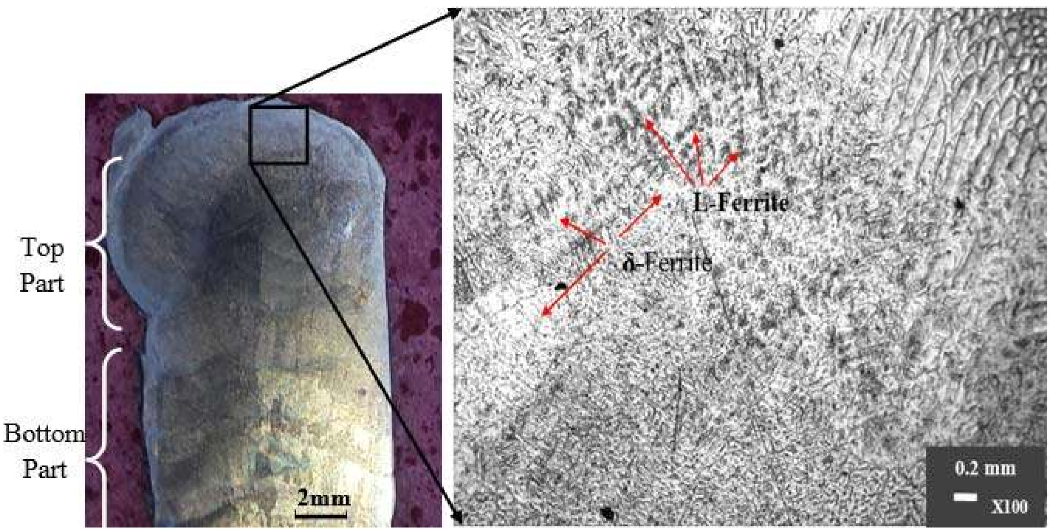

Figure 4. 66. Macrograph and micrograph of an etched PCSMD specimen : Left showing the distinct two regions, Right shows the microstructure of the top part which seems to be lathy ferrite structure

4.8.2.2 Microstructure Characteristics

Figure 4.67 shows the microstructure at cross-section and side view of the top part and bottom part. At top part, the grains seem to be a randomly oriented structure at the top surface and tend to be vertical direction structure at the center of the wall. The microstructure of the top part is mainly consisting of two phases ferrite and austenite as predominant phases throughout the part. The rapid cooling region near the surface and the frequency effects on the heat input to the deposited part lead to prevent the completing of ferrite transformation and so high residual ferrite will appear in form lathy structure (L-ferrite) or skeletal ferrite structure in the matrix of predominant phase austenite. Vermicular delta ferrite (δ-ferrite) may appear throughout the microstructure.

TW-SMD processes (CCSMD and PCSMD) were successfully used for producing defect free, and good metallurgical bonding SS308LSi components. Figure 5.68 shows the optical micrograph in cross-section of the deposited wall. It reveals good bonding between the tracks. No common defects were found between the layers of part prepared using CCSMD and PCSMD methods.

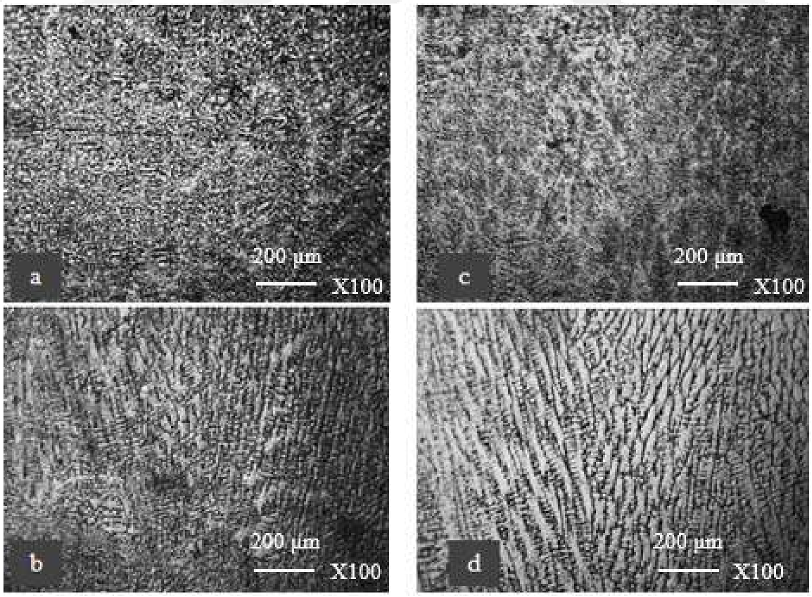

Figure 4. 67. Macrographs represent the microstructure of PCSMD wall specimens, (a) cross-section at top part, (b) side at top part, (c) cross-section of bottom part, and (d) side wall at the bottom part.

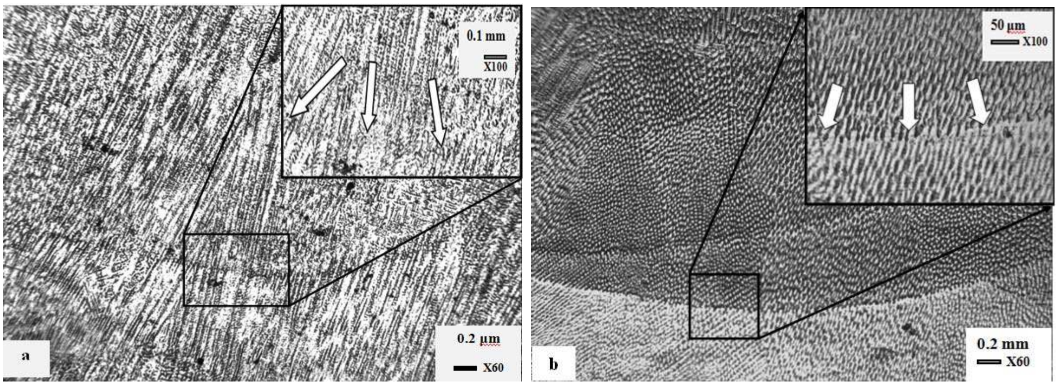

Figure 4. 68. OM: Micrograph illustrates the interaction between successive layers (a) CCSMD and (b) PCSMD, there are no defects such as lack of fusion, crack, oxidation or inclusions

4.8.2.2.1 Influence of Changing in TS on the Microstructure of PCSMD

To investigate the effect of the travel speed of melting source on the surface morphology and microstructure, using the process parameters which mentioned before in Section (3.8.1.3) for building wall specimens. Figure 4.69 presents the effects of TS on the columnar grains. These grains seem to be larger and pervade the layers bands at low TS due to the high heat interred to the deposited part about 719.477 J/mm. High residual ferrite with fine structure can be seen when using high TS as shown in Figure 5.70a, the heat input here is about 359.878 J/mm, whereas the low TS leads to large austenite grain since the heat input is doubled to about 719.477J/mm (see Figure 4.70(b)). In the pulsed current process, the heat input can be calculated using the Equation (4.15). The average peak current for pulsed current can be calculated using Equation (4.16) [179-182].

$$\mathrm{Hi}\left(\frac{\mathrm{J}}{\mathrm{mm}}\right) = \eta \mathrm{Iav}\frac{\mathrm{Vav}}{\mathrm{TS}} \quad \textbf{(4.15)}$$

$$\mathrm{I_{av}}(\mathrm{A}) = \frac{\mathrm{I_p\, t_p + I_b\, t_b}}{\mathrm{t_p + t_b}} \quad \textbf{(4.16)}$$

where I_{av} the average current for pulse current TIG welding, t_p is the peak time (s) and t_b is the base current duration (s), I_p is the peak current and I_b is the base current.

Let express the cycle time by k ($k = t_p + t_b$), and express the peak time percentage as d ($d = tp/k$) then sub. Equations 3 in 2 to get finally the Equation (4.17)

$$\text{Hi}\left(\frac{\text{J}}{\text{mm}}\right) = \eta\frac{V_{av}}{\text{TS}}\ \text{I}_\text{p}\left(\text{d} + \frac{1-\text{d}}{\text{CR}}\right) \tag{4.17}$$

where CR is the I_p/I_b ratio.

The peak duration (d) was kept as 50% throughout the study in order to investigate the effects of the other parameters. The heat input depends mainly on the TS, I_p , and CR.

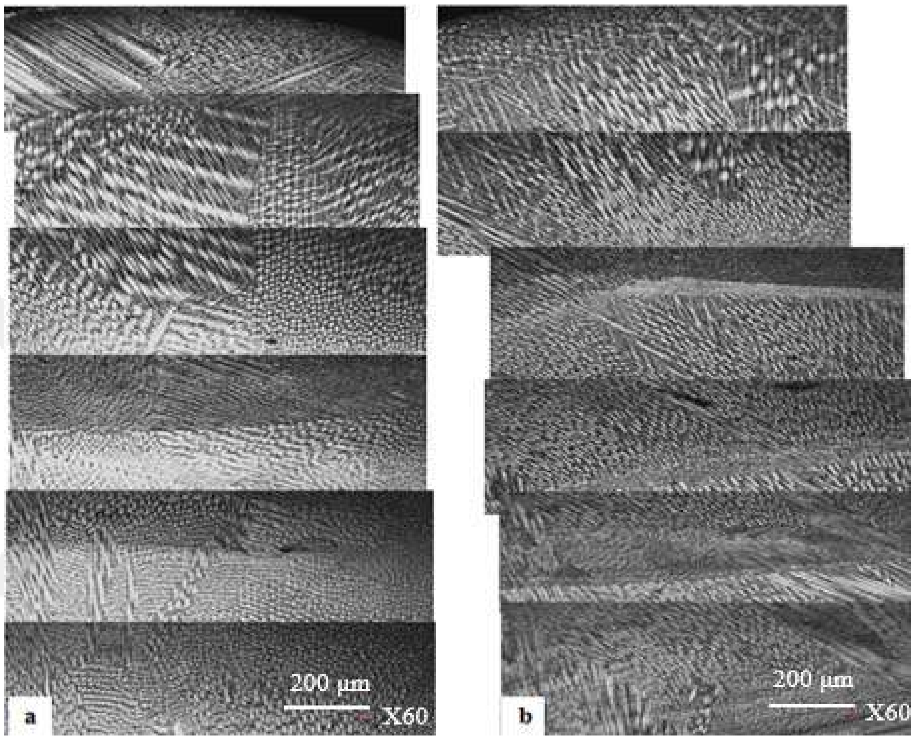

Figure 4. 69. Montage of photomicrographs illustrates the effects of TS on the morphology (a) TS=4mm/s (b) TS=2 mm/s.

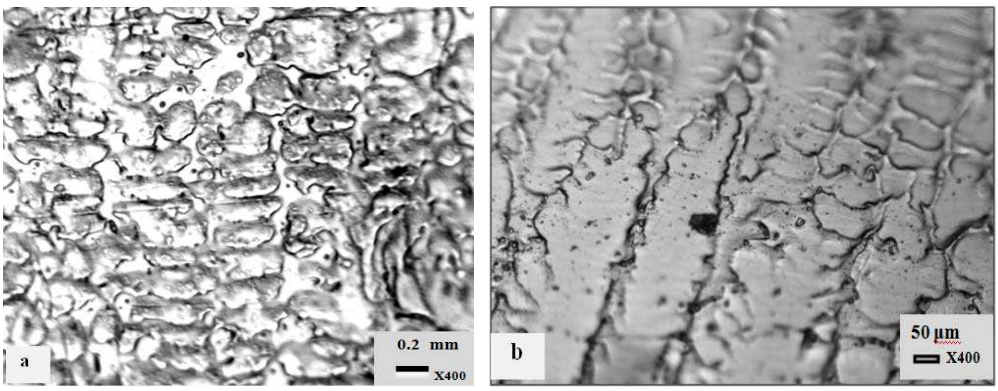

Figure 4. 70. Micrographs illustrate the effects of TS on the microstructure (a) TS=4mm/s and (b) TS=2 mm/s, showing the high residual amount of ferrite at high TS.

4.8.2.2.2 Influence of Heat Input on the Microstructure of PCSMD

To investigate the effects of Hi on the microstructure, two experiments of different Hi amounts were done as were aforementioned in section (3.8.1.3). The first sample was prepared using I_p =205 A, TS= 0.12 m/min, I_b = 82 A, Fr = 30 Hz and WFS = 2.5 m/min so the heat input is about 744.108 J/mm. Whereas the second specimen was prepared using I_p= 165 A, TS = 0.24 m/min, I_b = 66A, Fr = 90 Hz and WFS = 2 m/min and so the heat input of 269.62 J/mm. The microstructure of the deposited part changed from coarse dendrites to fine dendrites as shown in Figure 4.71. The changes in microstructure associated with the amount of heat input (Hi) to weld pool during the deposition process according to the equation 4.17.

4.8.2.2.3 Influence in of Peak Current on the Microstructure of PCSMD

Two experiments were carried out using the high current value of 205 A and low value of 175A and keeping all the other parameters as constant. As the current increased from 175A to 205 A, the heat input increased as well. There is no obvious difference in surface morphology between the two experiments as shown in Figure 4.72. The microstructure is changed based on the peak current used, it changed from the high skeletal ferrite structure at low current to the large austenite structure at high peak current as shown in Figure 4.73. This may be attributed to the change in Hi from 340.43 J/mm to 398.7 J/mm.

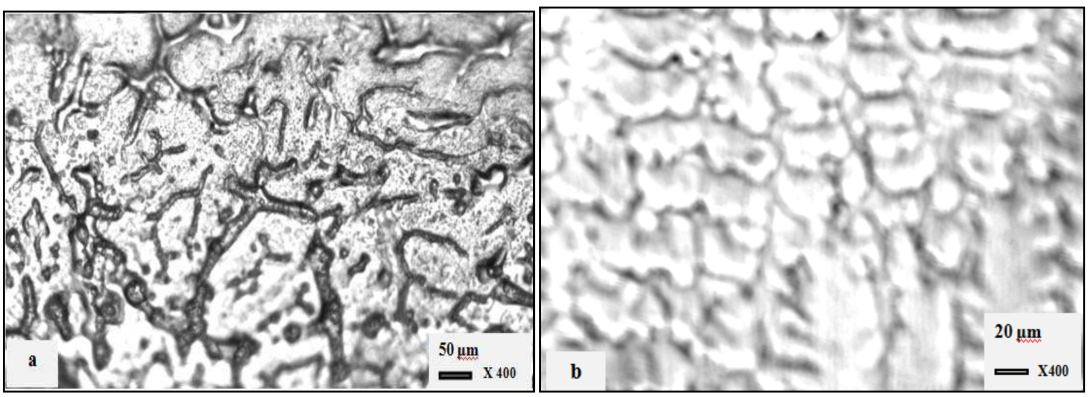

Figure 4. 71. Microstructure of specimen deposited at (a) high Hi (Ip =205A, Ib= 82A, WFS =2.5m/min, Fr=30 Hz, and TS=2mm/s), and (b) low Hi (Ip= 165A, Ib =66A, WFS = 2.5 m/min, Fr = 90 HZ, and TS = 4 mm/s)

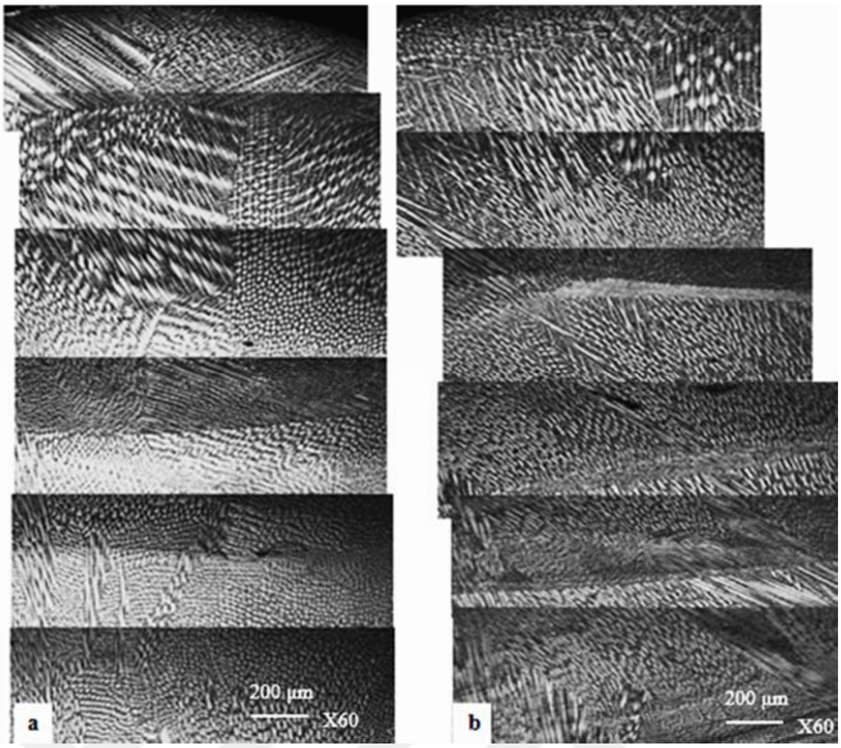

Figure 4. 72. Montage of micrographs of (a) the high Peak current specimen 205 A, and (b) low peak current Ip 175 A, show the blocking of columnar grain growth. There is no evident effect of the peak current on the morphology

.

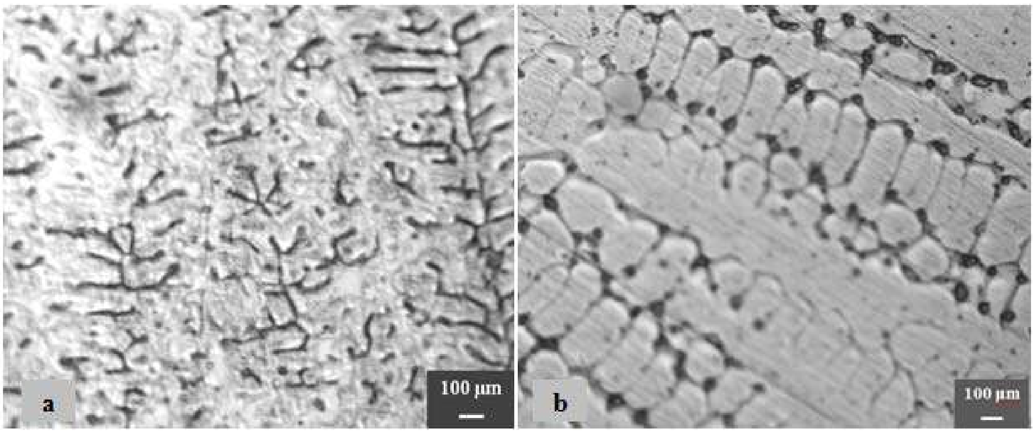

Figure 4. 73. Micrographs illustrate the effects of Ip on microstructure near the top part at (a) Ip = 175 A and (b) Ip=205A. Original X 400.

4.8.2.2.4 Influence in of Current Ratio on the Microstructure of PCSMD

Multilayer specimens were built at CR of 1.5 and 2. Other deposition parameters were kept at Fr 30 Hz, I_p 175A, and TS 4 mm/s. Figure 4.74 shows the montage of the low magnification microstructure, no significant changes can be seen, except the grains were larger with CR 1.5 and the columnar grains bulges grew in random orientations. The grain bulges were also stopped and prevented from growing more in CR 2 due to the high arc pressure as shown in Figure 4.74(a), whereas these grains were relatively larger with CR 1.5. The microstructure changes with changing the current ratio, where it consists of a large amount of residual ferrite in vermicular structure as shown in Figure 4.75 (a). Decreasing the current ratio from 2 to1.5 means that the background current increases from 87.5A to 116.7A respectively. So that the Hi increases as well from 340.43 to 529.466 J/mm, which affects the grain size of the final microstructure (see Figure 4.75(b)).

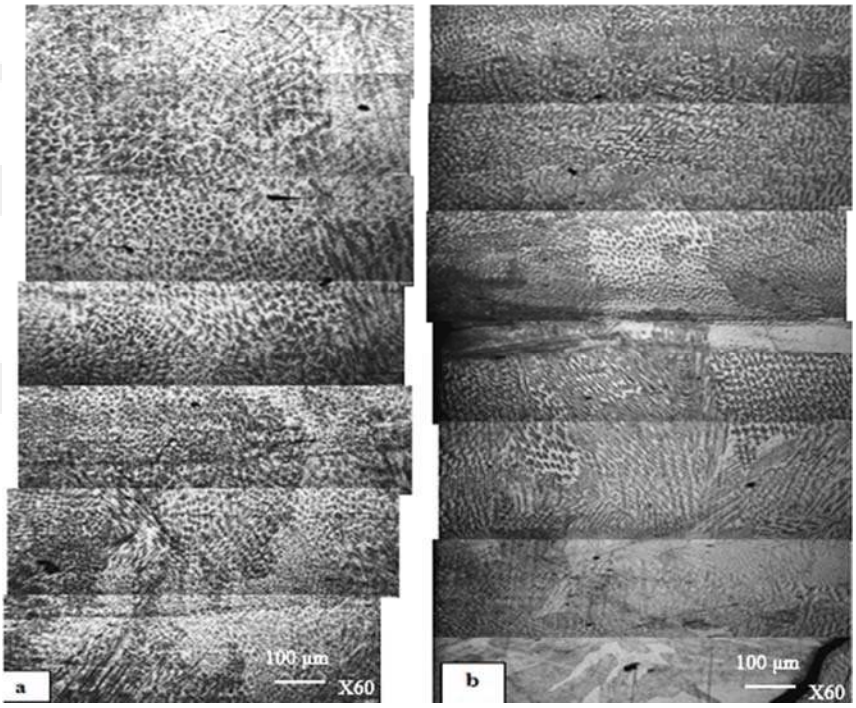

Figure 4. 74. Montage for the effects of CR on the morphology at (a) CR 2 and (b) CR 1.5.

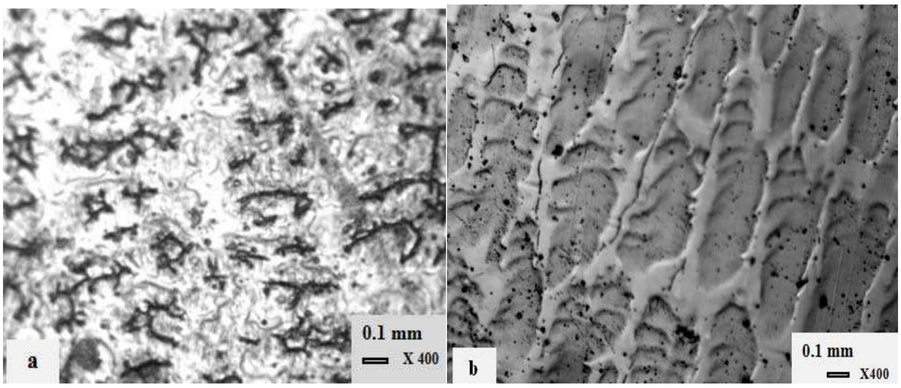

Figure 4. 75. Effects of current ratio on the microstructure (a) CR=2 and (b) CR=1.5

4.8.2.2.5 Influence of Pulse Frequency on the Microstructure of PCSMD

Using the experiment condition was mentioned in Table 3.25 (5^{th} case), two multilayer wall specimens were done under low- and high- frequency pulsed current. Other parameters were kept constant during this experiment in order to investigate the effects of pulse frequency on the surface morphology and microstructure of the deposited parts. The surface morphology of the deposited samples at 5 Hz and 2000 Hz are shown in Figure 4.76(a) and (b) respectively. It can be seen that pulse frequency has a great effect on the grain structure since the columnar grains were strongly broken by high frequency as shown in Figure 4.76. The arc pressure is depending on the pulse frequency which leads to refining the grain size of the deposited parts, and so affects the mechanical properties.

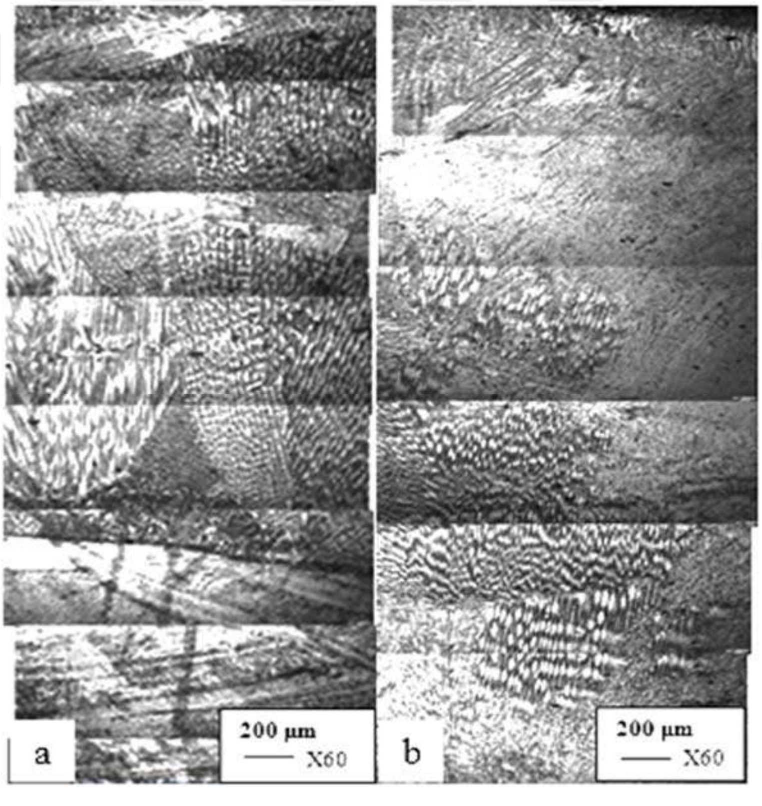

Figure 4. 76. Montage of Microstructure of Parts Prepared Using Ip 175A, CR 2, TS 4mm/s, WFS 2.5 m/min and Fr of (a) 5 HZ and (b) 2000HZ

4.8.3 Effects the Process Parameters on Precipitation

In order to examine the types of materials that exist inside the boundary grains of microstructures for both CCSMD and PCSMD processes, the three-phase diagram Figure 4.77 has been used [183]. According to the chemical analysis of the as-deposited part, the carbon percentage exists of about 0.018 % and chromium percentage of 19.557 %, so that the deposited part will have ferrite and very small amount of carbide ($M_{23}C_6$) after cooling.

Figure 4.78(a) shows the microstructure of the deposited specimen resulting from CCSMD technique. These boundary grains are much less than those in Figure 4.78(b-d) (PCSMD). Figure 4.78(b) describes the microstructure of the deposition of a specimen prepared using frequency of 5 HZ. As can be observed, the number of ferrite on the grain boundaries, in this case, is more compared to the Figure 4.78(a) case but less than in the other cases. Figure 4.78(c) shows the microstructure of the weld metal region resulting from the depositing of the part under the frequency of 500 HZ. Figure 4.78(d) illustrates the microstructure of the specimen prepared using frequency of 2000 HZ. Compared to the other cases, this microstructure enjoys more vermicular ferrite structure with greater distribution, which explains the fact that in this case, the noted mechanical properties are higher. No significant intergranular precipitation can be seen in all the tested specimens since the material used contains a low amount of carbon (see Figure 4.79).

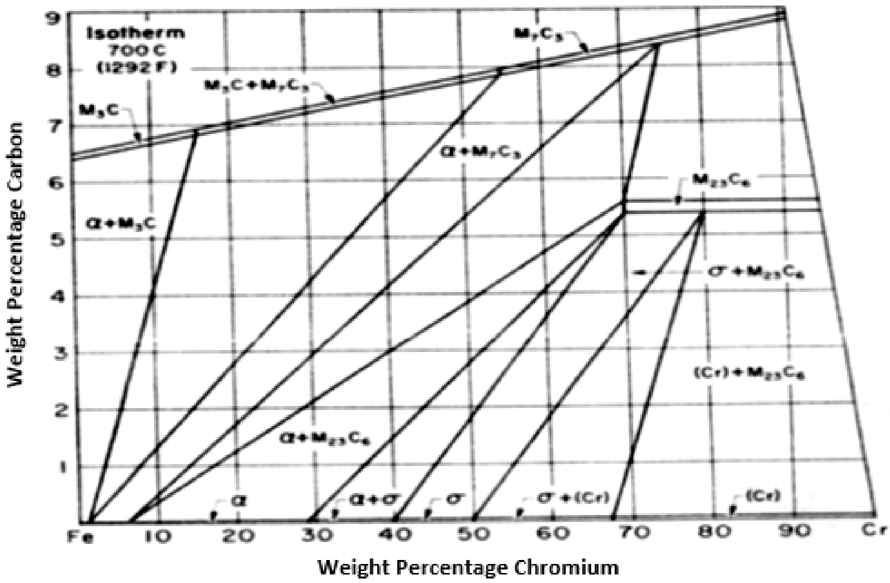

Figure 4. 77. Isotherm Equilibrium Diagram of Fe–Cr–C [183]

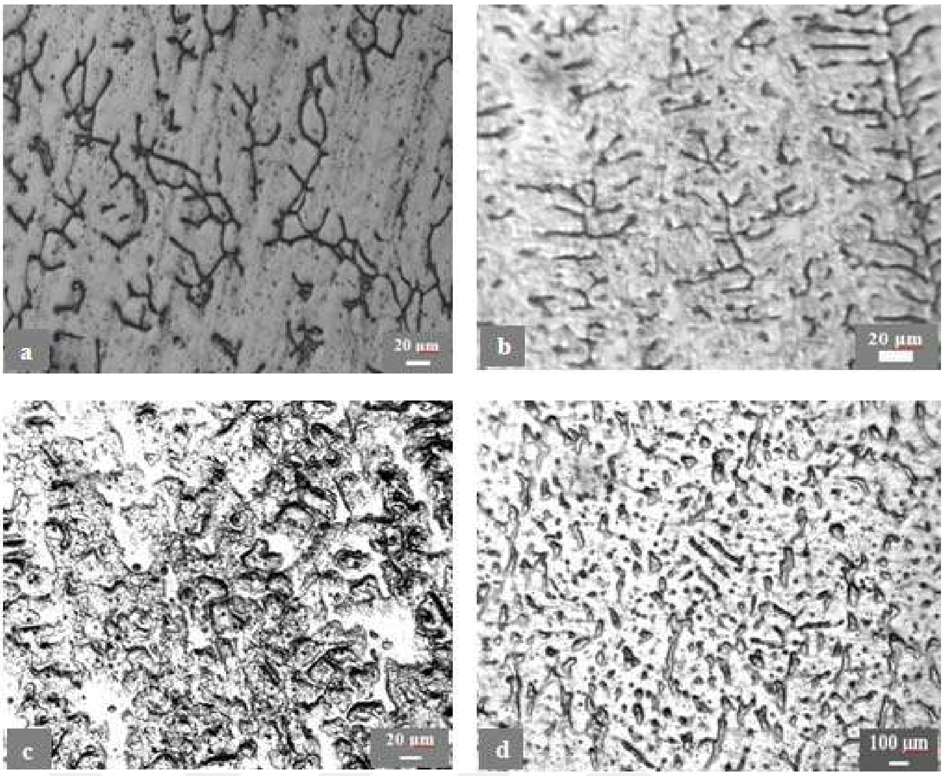

Figure 4. 78. (a) Non-pulsed (0 HZ), (b) 5 HZ, (c) 500HZ, and (d) 2000 HZ (X400)

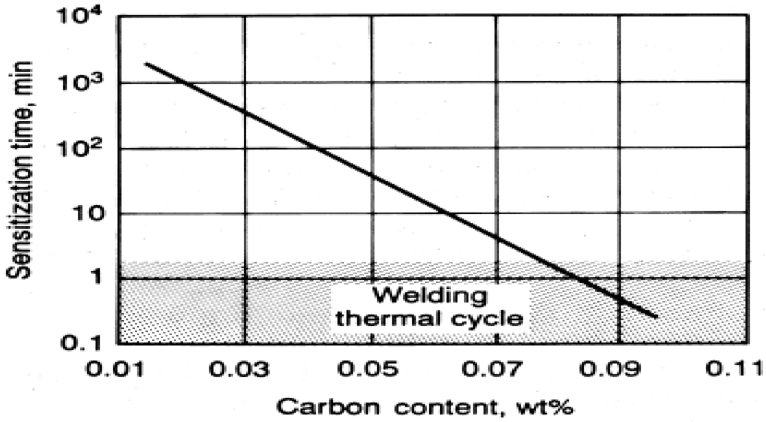

Figure 4. 79. Minimum sensitization time from a time-temperature sensitization diagram as a function of carbon content for a typical 300-series stainless steel alloy [152]

4.9 Radiography Tests

The results of the X-Ray tests showed that porosity defect was largely spread through the specimens of high frequency (2000 HZ) and less porosity appeared in the case of medium and low frequencies processes as shown in the Figure 4.80 (1-4).

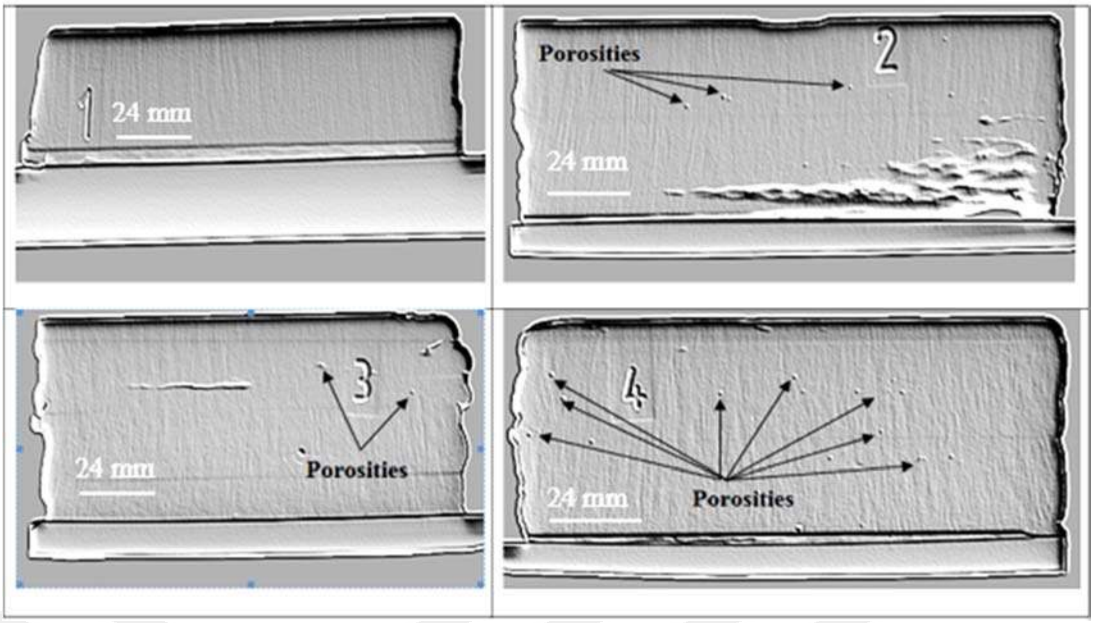

Figure 4. 80. X-ray photographs of (1) CCSMD process wall no porosity, (2) PCSMD with 5HZ process wall some of porous existed, (3) PCSMD process of 500 HZ wall some of porous were found, and (4) PCSMD process of 2000HZ wall large number of porous appeared in the specimen

.

4.10 Mechanical Properties

The experiments reported in this section were carried out according to the set-up, deposition conditions, and experimental method detailed in section 3.5.2 (chapter 3).

4.10.1. Hardness Tests

The experiments reported in this subsection were carried out according to set-up and the method described in Section 3.8.3.1 (Chapter 3). The deposited walls were sectioned in traverse direction and the specimens prepared for the hardness test. The results of the hardness were divided into two subsections as follows:

4.10.1.1 Hardness Test for CCSMD Specimens

Extensive macro hardness (HRA) tests in the vertical orientation and horizontal direction at top and bottom locations were performed as pointed in Figure 4.81. The results of hardness tests are shown in Figure 4.82. There is the significant dependence of hardness on the height is observed, where the average value of HRA near the substrate (bottom zone) is 56.37, whereas the average value of HRA near the top region is 52.08.

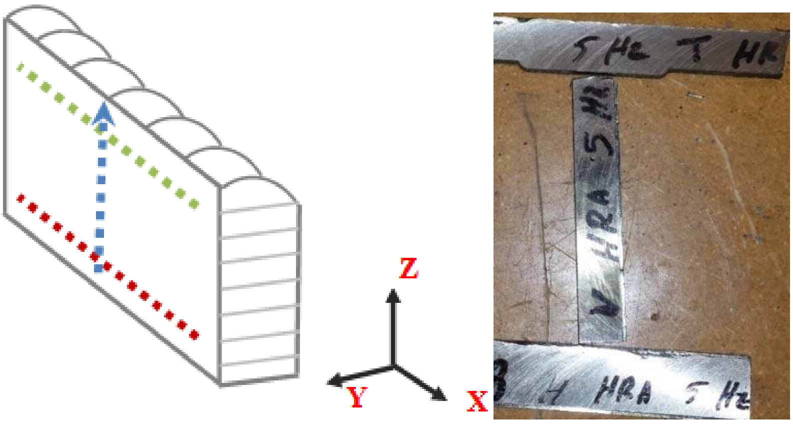

Figure 4. 81. Hardness measurement directions on the machined side of the deposited wall sample.

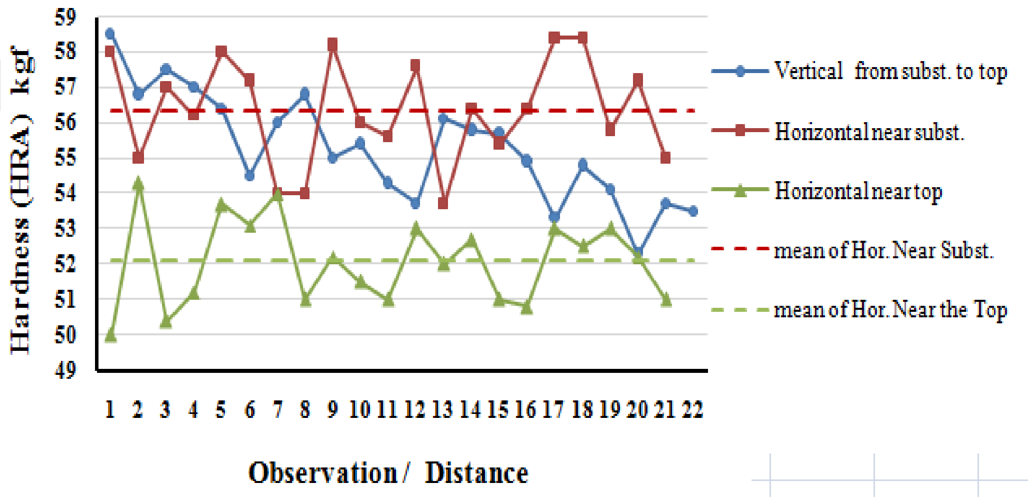

Figure 4. 82. Hardness versus distance/ observation

The hardness tests also show that the hardness of the deposited part is highest near at bottom zone of the wall, in the first few millimeters. Since in this zone, the substrate acts as a heat sink, which dissipates quickly the heat from the melt pool and increasing the cooling rate. Fast cooling rate always leads to fine microstructure and higher hardness since the rapid heating and cooling cycles associated with TIG plus wire deposition process increase the thermal stress and, as a result, the dislocation density [116].

4.10.1.2 Hardness Test for PCSMD Specimens

In a similar procedure to that was aforementioned in the previous section, the hardness tests were carried out in two directions and at top and bottom locations and this procedure was repeated for specimens that prepared using the deposition parameters reported in Table 3.14.

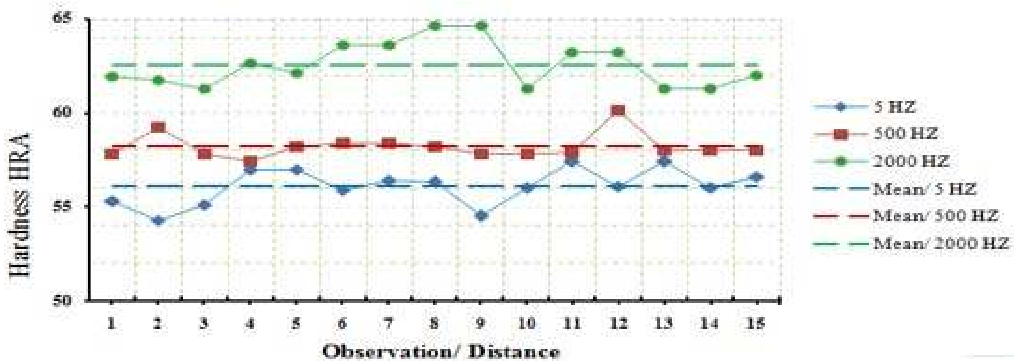

Figure 4. 83. Hardness results in horizontal direction near the substrate surface for specimens prepared using different frequencies.

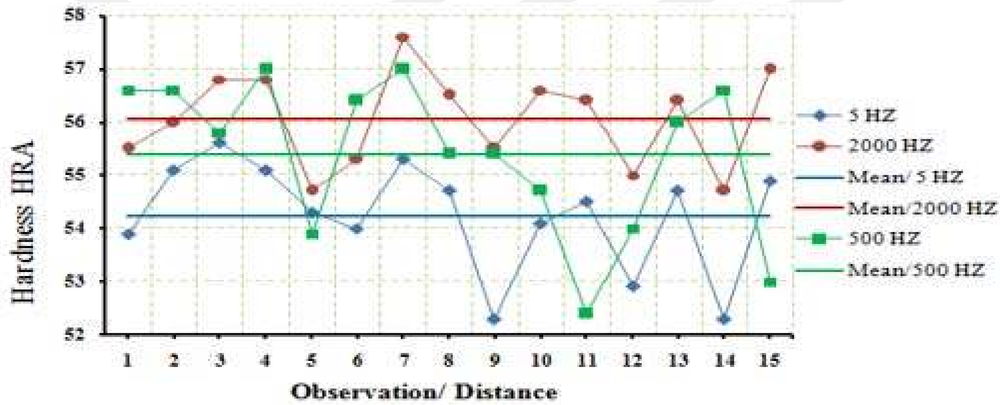

Figure 4. 84. Hardness results in horizontal direction near the top surface of specimens prepared using different frequencies.

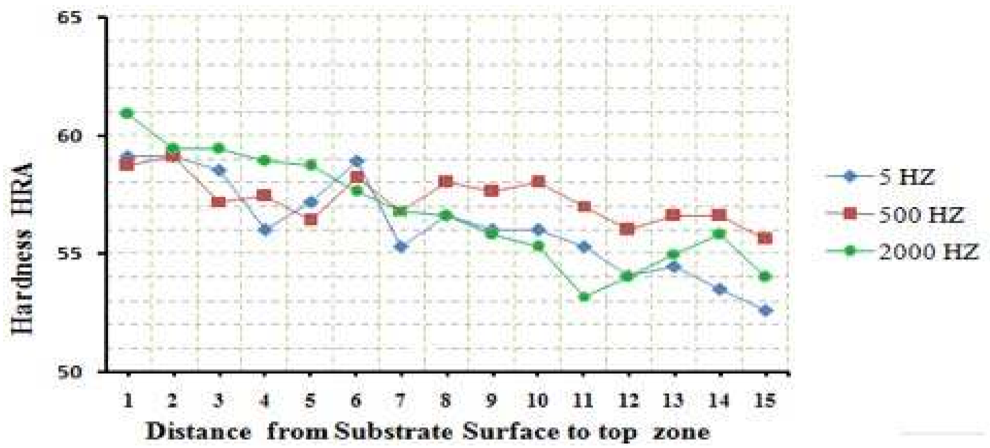

Figure 4. 85. Hardness results in the vertical direction from the substrate surface to the top region for specimens prepared using different frequencies.

Figure 4.83 illustrates the hardnesses of deposited specimens which were measured near the bottom of the sample wall. The hardness of sample prepared with high frequency is relatively the highest one and the sample of 5 Hz has the lowest value. And the same state for the hardness values near the top region, the sample of 2000 Hz has the highest hardness value and the sample of 5 Hz has the lowest hardness value as shown in Figure 4.84. Additionally, the hardness values at the bottom locations are higher than those of the top locations as shown in Figure 4.85. At top regions of the wall specimens, the heat transfer from the melt pool is reduce since the wall layers acts as a barrier between the substrate and this region and also the temperature of the wall increase due to the accumulated gradients so that leads to producing a slower cooling rate and reduce the hardness at top zone. The results have already published in the literature [23] showing that the residual stresses reduce with increasing the distance from the substrate. Thus, the hardness reduces with increasing the distance from the substrate as shown in Figures 4.82 and 4.85.

From a graphical comparison between the conventional and pulsed processes which is shown in Figure 4.86 and plots in Figure 4.87, it is obvious that the PCSMD process with high frequency produces components slightly harder than that of the conventional process. Also, the hardness of the wall prepared using high frequency is higher than that of 5 Hz. The well explaining for such case is that at high frequency the heat input to the deposited part is less as compared to that of the unpulsed process and those of the low frequency. Low heat input results the finer grains that produces the high strength and high hardness. From the Figure 4.88 and Figure 4.89, it can be seen that there is no significant difference in the hardness after relief heat treatment.

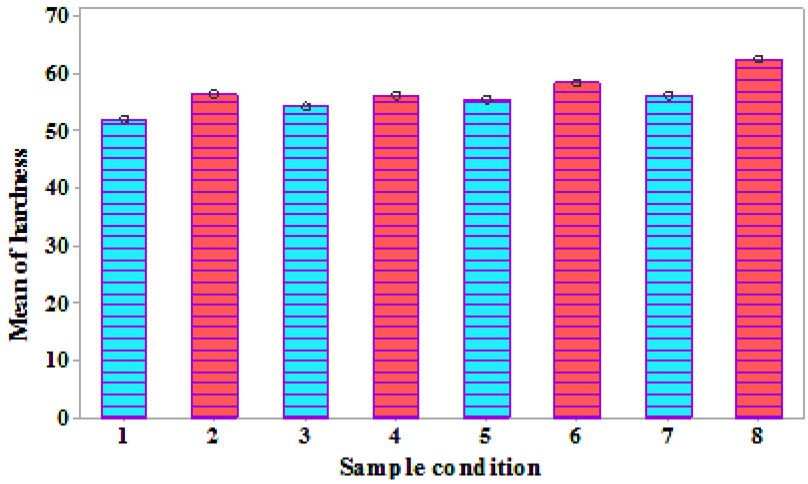

Figure 4. 86. Plots illustrate the comparison of hardness for different sample conditions: (1) CCSMD/0 Hz near top zone; (2) CCSMD/0 Hz near the bottom zone; (3) PCSMD/ 5 Hz near the top zone; (4) PCSMD /5Hznear bottom zone; (5) PCSMD / 500 Hz near top zone; (6) PCSMD / 500 Hz near the bottom zone; (7) PCSMD / 2000 Hz near top zone; and (8) PCSMD / 2000 Hz near the bottom zone.

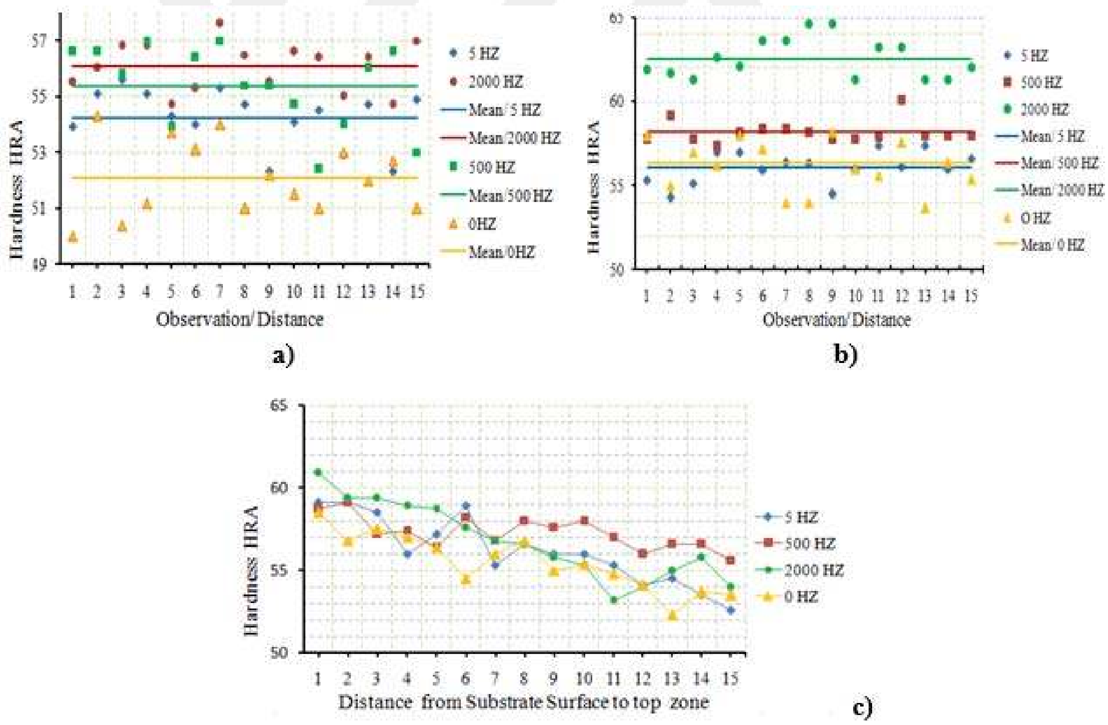

Figure 4. 87. Comparison the hardness values between CCSMD and PCSMD at different locations (a) near the top part; (b) near the bottom part; and (c) in the vertical direction from the base toward the top part

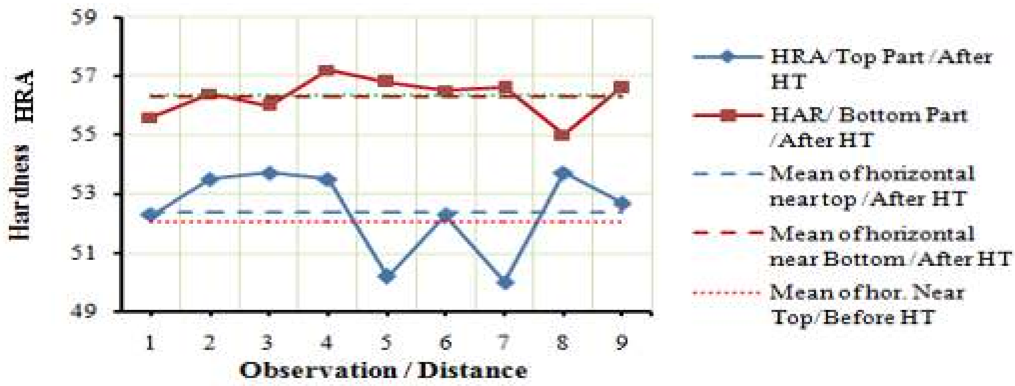

Figure 4. 88. Comparison the hardness at Bottom and top parts before and after HT.

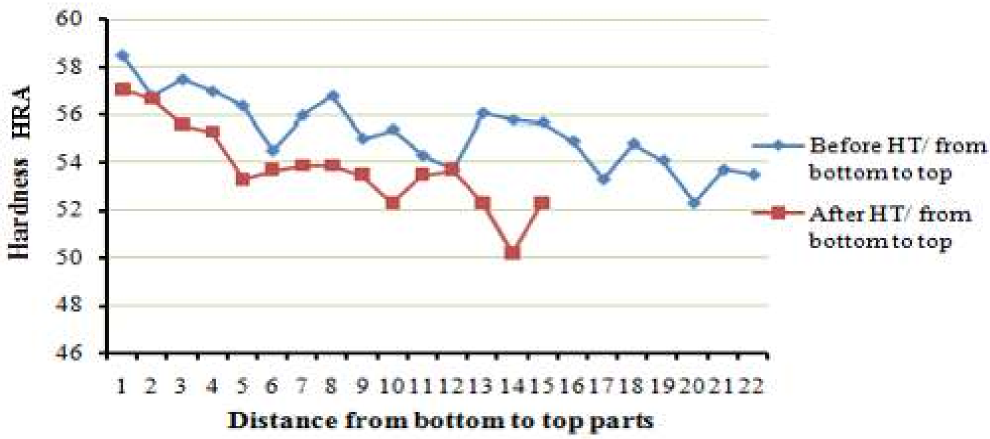

Figure 4. 89. Comparison the hardness from Bottom to the top before and after HT.

4.10.2. Tensile Testing Results

This study was done based on the experiment described in Section 3.8.3.2. The design of experiment was carried out using a full factorial design in order to cover all possible ways related to the properties with respect to Fr, orientation, and location. Table 4.9 shows the experiments layout with the values of UTS. While Table 4.10 shows the experiments layout with the values of ductility. The main effects of the frequency and test orientation on the deposited part tensile strength (UTS) are shown in Figure 4.90. It can be seen that the UTS increases slightly with increasing the frequency. Additionally, UTS in the H orientation is higher than that in V orientation (see Figure 4.91).

Table 4. 9. Experimental layout of factors with levels and resulted in UTS

	Factors		Results of UTS (MPa)			
Exp. No	Fr (Hz)	Orientation	1	2	3	**Mean**
1	0	H	616.7	585.51	604.42	**602.21**
2	0	V	580.4	602.77	610.07	**597.766**
3	5	H	696.19	685.61	694.73	**692.815**
4	5	V	638.08	677.109	719.75	**678.254**
5	500	H	712.45	746.7	719.03	**724.015**
6	500	V	647.91	698.84	674.031	**673.375**
7	2000	H	670.184	697.214	737.225	**710.4625**
8	2000	V	685.83	677.7	665.26	**676.263**

Table 4. 10. The experimental layout of factors with levels and resulted in Ductility

	Factors		Results of Ductility %			
Exp. No	Fr (Hz)	Orientation	1	2	3	**Mean**
1	0	H	50	45	45	46.667
2	0	V	52	50	51	51
3	5	H	55	53	60	57
4	5	V	60	56	57	57.67
5	500	H	60	65	60	61.67
6	500	V	60	65	67	64
7	2000	H	60	60	57	59
8	2000	V	60	60	65	61.667

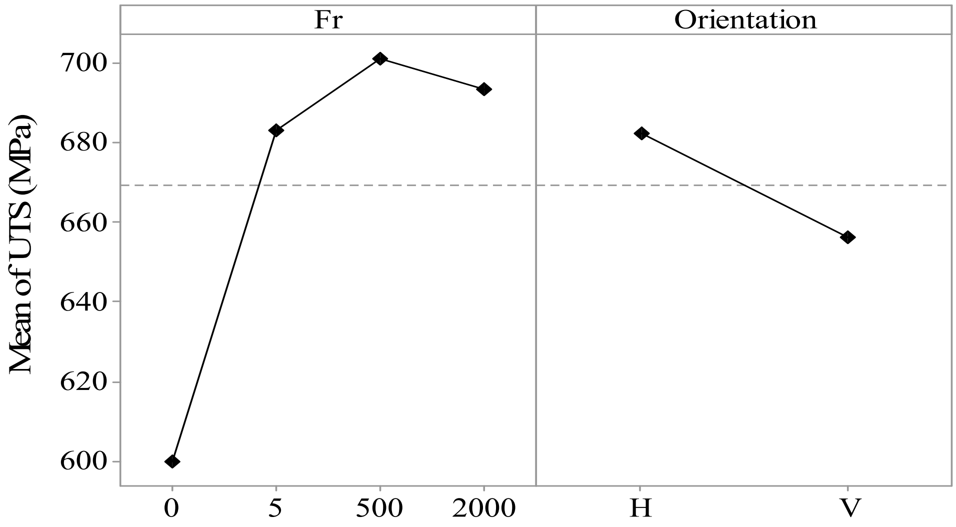

Figure 4. 90. Plot shows the effects of Fr and test orientation of the UTS

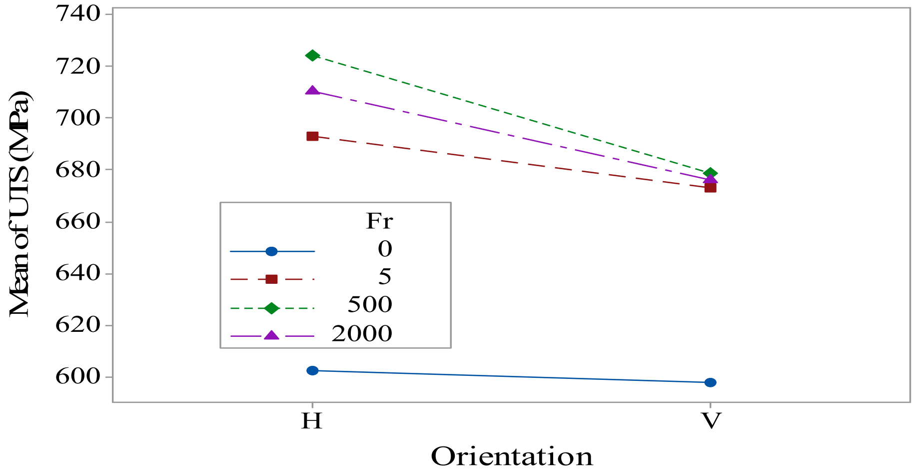

Figure 4. 91. The plot illustrates the effects of the interaction of the Fr and orientation on the UTS.

The ductility also increases in a similar manner to the UTS, with increasing the frequency of pulsed current and for both test orientations as shown in Figure 4.92. However, it was seen that the ductility seems to be larger in transverse direction than that in longitudinal direction (see Figure 4.93)

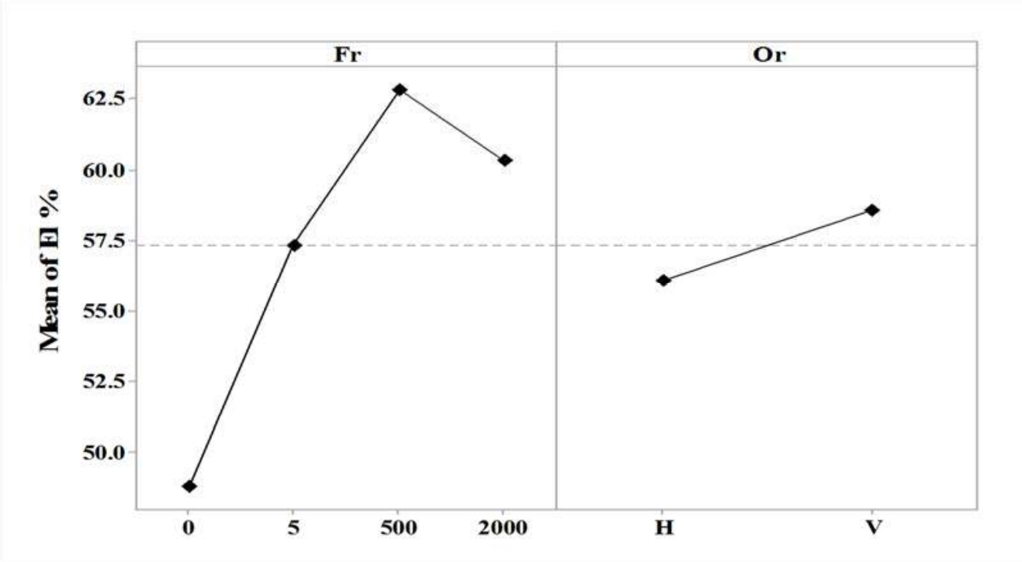

Figure 4. 92. The plot illustrates the relationship between pulse frequency and the ductility of the deposited components and how it varies with longitudinal (H) or transverse (V) orientations.

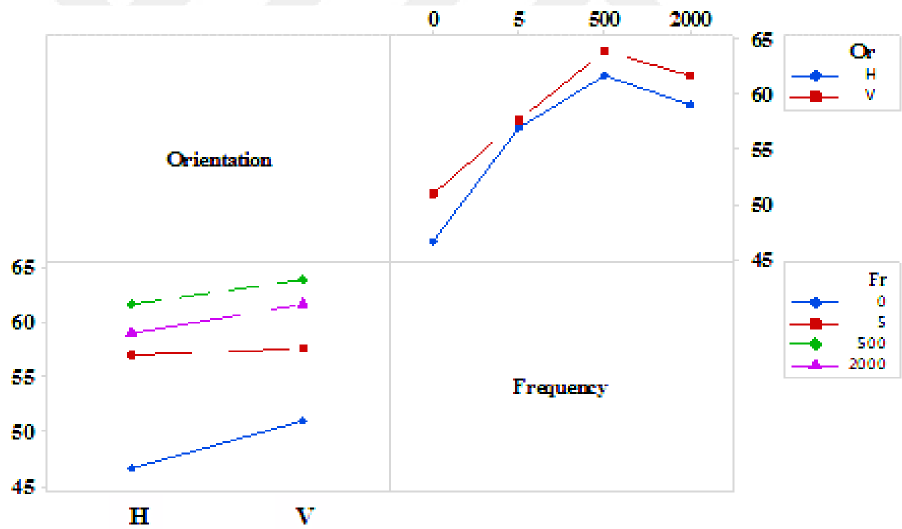

Figure 4. 93. Plots illustrate the interaction between the frequency and the orientation and their effects on the ductility of the deposited components.

From the results of the tensile test, it can be seen that the samples prepared with conventional method have lower UTS than those prepared with the pulsed current method and for all frequencies. The samples which were tested in the longitudinal direction have higher UTS than those tested in the vertical direction, and these results were consistent with those obtained in the literature [184]. Large variety in UTS values obtained with variation in the pulse frequency values as shown in Figure 4.90. The maximum UTS was obtained with specimen prepared using 500 HZ and longitudinal direction (see Figure 4.91). The tension test graphs are shown in Figure 4.94.

In order to investigate the influence of specimens location on the mechanical properties, another experiment was carried out. The objective of this experiments is to determine whether there is any difference between the UTS results for different frequencies and in the different location on the specimen height.

The specimens were machined from three positions which are taken from near the bottom of the wall (B), middle of the wall (M), and near the top part (T). The results of this experiment are summarized in Appendix K (Table K.1-K.2). The results of the test were shown in Figure 4.95.

It can be seen that no significant dependence of the properties on the specimens position as shown in Figure 4.95(a-b). However, there was a slightly decreasing in ductility with increasing in height as shown in Figure 4.95(c). This attributed to the fact that the grains near the bottom and middle of the wall subjected to repeated high temperature during depositing the subsequent layers which act a stress relief in these regions [29]. The ductility increased from about 50% to the CCSMD to above 60% with increasing the frequency in correspondingly with UTS, which also increased from about 600 MPa in CCSMD to the highest value of above 700 MPa in PCSMD.

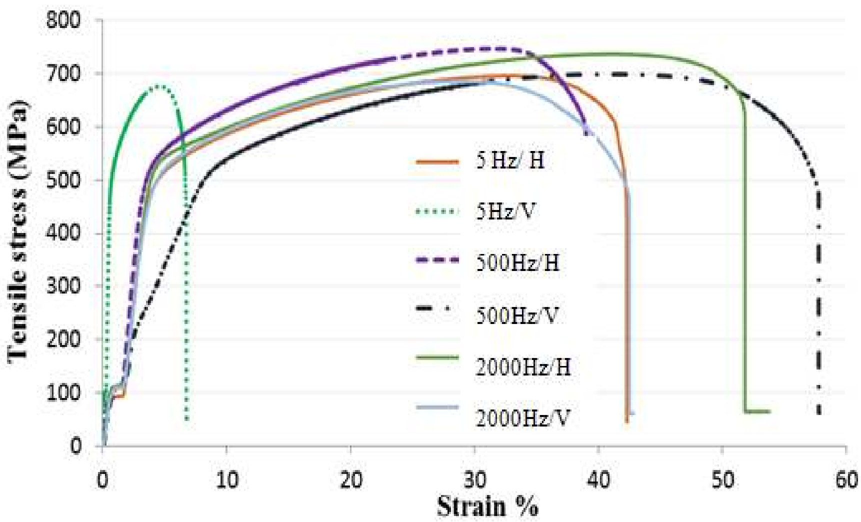

Figure 4. 94. Stress-strain diagram for PCSMD specimen tested in horizontal and vertical orientation.

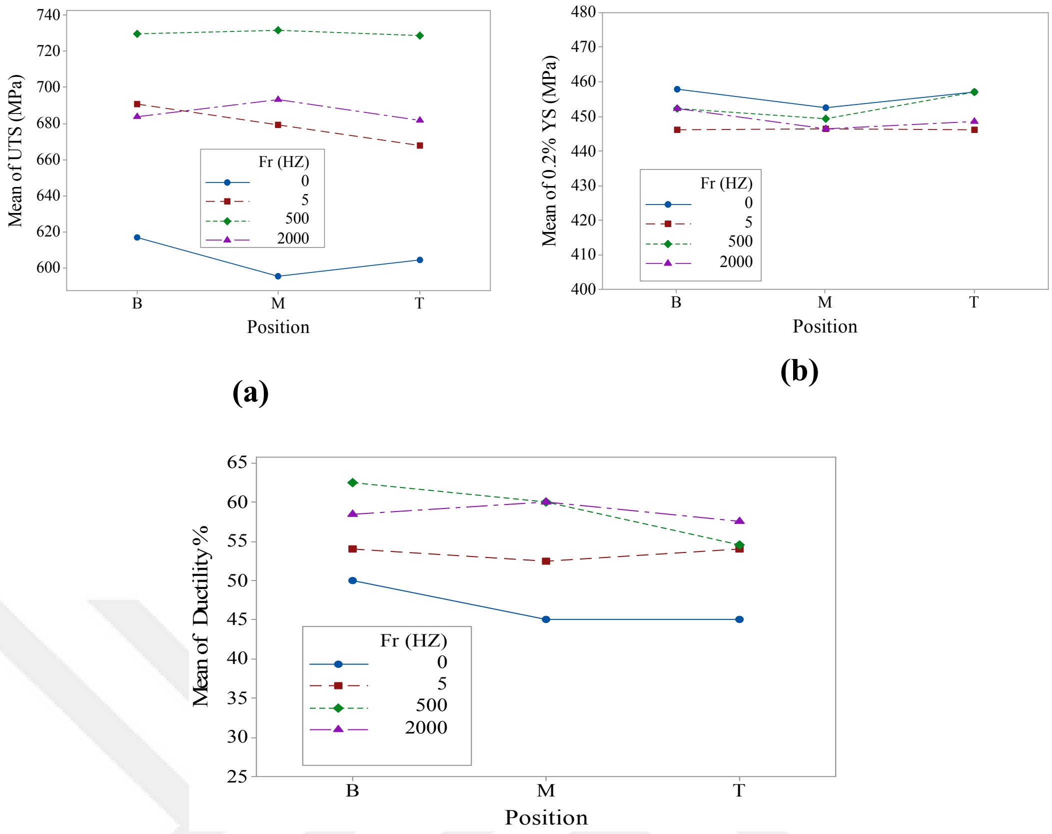

(a) (b) (c)

Figure 4. 95. Plots illustrate the variation of mechanical properties with the position of test specimens whereas near to base (B), at the middle of the wall (M) and near the top part (T) (a) Ultimate tensile strength, (b) 0.2% yield strength and (c) the ductility %

The ultimate strength and ductility of the present manufacturing method were compared to the reported results of wrought Type 308L stainless steel [15], as-cast austenitic stainless steel [113, 114, 152] all weld metal using TIG welding method [113, 115] as shown in Figure 4.96.

In order to show the effect of the stress relief heat treatment on the mechanical properties of the deposited parts using PCSMD process. The specimens were heat treated using electrical furnace and the temperature was maintained at 550 C for about 2 hours and then cooled inside the furnace. The experiment was performed using the same standard specimens aforementioned above. However, the only transverse direction was selected for comparing the results. There is no significant difference between the properties before and after the treatment (see Table K.2)

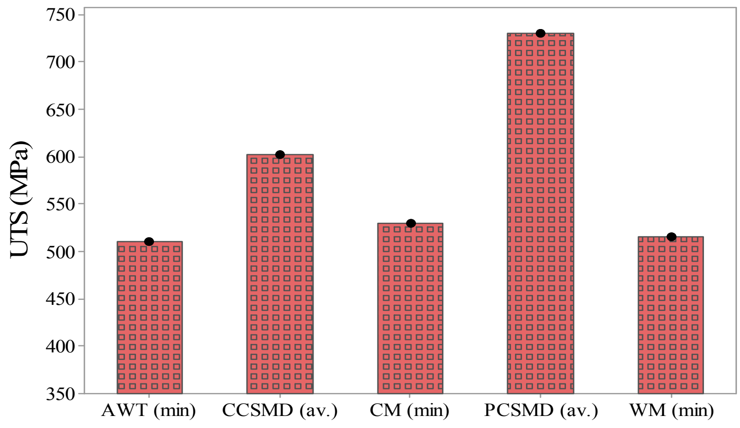

(a)

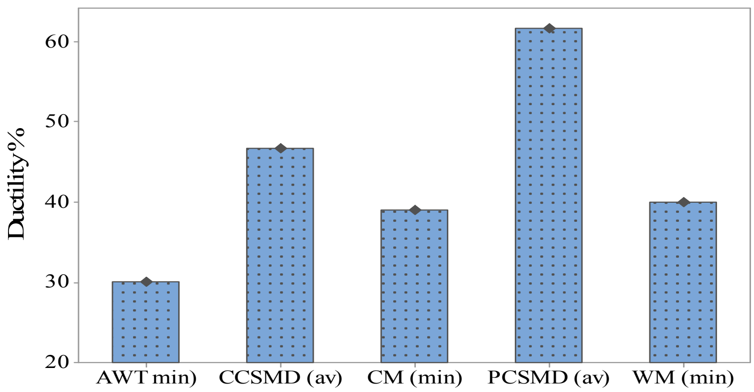

(b)

Figure 4. 96. Diagrams illustrate a comparison between the present method with standard values of wrought metal (WM), cast metal (CM), and all weld metal by TIG welding of (a) UTS and (b) ductility %

4.11. Deposition Path planning Strategies

The developed interfacing of CAMDM system was used to deposited different parts, which were deposited in a single stringer/multiple layers walls (Figure 3.27(a-b), single stringer/multiple layers tubular components (Figure 3.27(c)), solid filling area featured parts (Figures 3.21- 3.22), and hollow filling area (Figures 3.23-3.25).

The effects of the utilized path strategies on the improvement of the geometrical accuracy and side wall roughness were demonstrated. In the present TW-SMD process, for obtaining a stable deposition process with uniform beads, the deposition process has to be with continuous arc ignition without any stoppage during the deposition since it leads to concentrate the heat input at stop points and thus excessive melting may exist and flow the melted metal may occur. So, for the tubular products and all parts with polygon shape such as in Figure 3.27(c), the continuity in the same direction for the sequential layers is more preferable, since this technique will significantly reduce the accumulated error at these points. From another hand, the reverse direction technique becomes the most suitable choice for depositing the disconnected features parts such as walls and solid filling area parts. Figure 5.97 shows effects of the deposition directions on the wall ends. In Figure 97(a), the error in the end of the forward direction deposition process increases with increasing of the deposited layers due to the flow of the molten metal at this sites. At the start portion, the substrate is cool and acts as a heat sink to dissipate the heat. So the bead height is high with shallower penetration, whereas at the end portion of the deposited pass the temperature gradient is slow which leads to reducing the bead height at this position. Thereby, after a few layers, a significant deviation in bead height will occur due to the flow of molten metal. This error can be eliminated using the reverse direction method (see Figure 4.97(b)). For that reasons, the continuous arc deposition method during the deposition process of the crossing is the most proper technique for producing similar features, because this method will eliminate the arc ignition and re-ignition process and produce well wall profile and also the total deposition time will be significantly shortened.

Due to the physical nature of the present system, the control unit used which is an open-source one, and suitable path strategy used the developed CAMDM system is used for manufacturing the stiffened panel features, especially the crossing wall (Figures 3.19 and 3.20) without the difficulty which may be countered in other systems.

(a) (b)

Figure 4. 97. Photographs illustrate deposited walls using (a) one direction during deposition and (b) reverse direction deposition method

From the Figure 3.21, it can be seen that there were different path planning strategies can be used for manufacturing the same solid part. The deposition path strategy sued in Figure 3.21(b) is appropriate for DMD technique and it is not suitable for the current process since this method requires multi- arc ignition and re-ignition it and also the surface quality of the deposited part is very bad. The deposition-path strategy shown in Figure 3.21(c) is also unsuitable for the current system because it comprises of contour for the outside boundary and zig-zag pattern for the filling area, however, it also requires multi arc-ignition. So, the most convenient path strategy for the developed CAMDM system is shown in Figure 3.21(d), since it can deposit the first layer with one arc ignition and hence can deposit the part with one ignition.

Figure 4.98 shows a part with a relatively complex shape which fabricated by the present system. It shows the deposition of solid filling areas. In this part, all planning strategies were applied to manufacturing it in a satisfactory feature. In the solid filling area path planning, better results were achieved when the contiguous layers were attached to each other and no discontinuities were observed. Therefore, in some cases, the combined path planning strategies are applied to reduce or eliminate the voids or lack of fusion between the contiguous beads. Voids may occur during deposition of the layers at the turned points and start-ends points. The path strategy in the TW-SMD process was suggested to be combined paths of contour, raster, and space filling curves. The comparison of some measured values respectively gained by finishing a single layer filling with the spiral/contour pattern for an outer boundary and inner spaces are filled with a spiral or zigzag/raster pattern

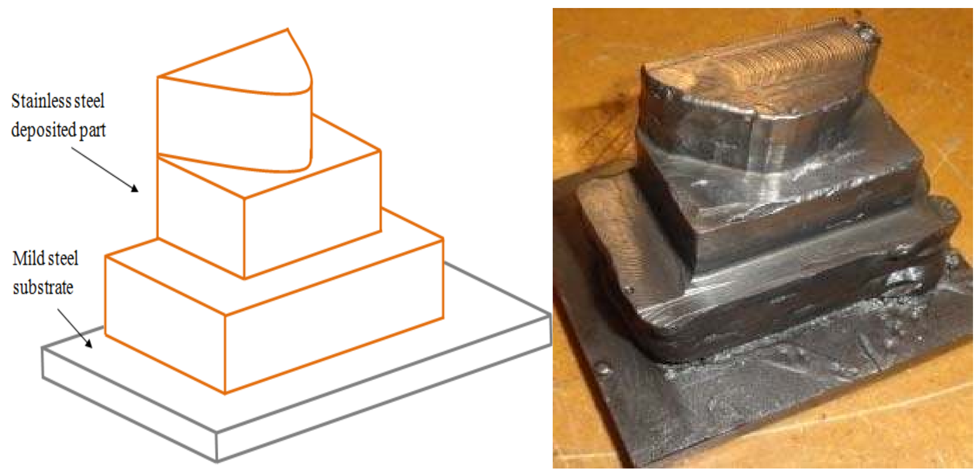

Figure 4. 98. Near net shaped stainless steel part by applying the combined path patterns procedure in TW-SMD technique.

Table 4. 11. Comparison between the Spiral and zigzag pattern for some of the deposited components

Sample part	Filling path type	Total length of the deposited path (mm)	Single layer deposition time (Sec)
Solid cylindrical part	Spiral fill path	528	132
	Zigzag/raster fill path	472	118
Hollow square part	Spiral fill path	520	130
	Zigzag/raster fill path	560	140

for the different deposited feature are reported in Table 4.11. From the results in Table 4.11, the zigzag/raster path pattern (Figure 3.22(b)) is more suitable for fabricating the circular sections parts since it provides a short trajectory for filling the internal spaces of the part with the shortest time. Whereas, the spiral/contour path strategy (Figure 3.23) is more proper for manufacturing of the square parts since it allows to manufacturing the part with shorter time as compared to zigzag pattern and also the inner surface quality of the part was butter than the zig-zag one. This means that the productivity is relatively increased. Additionally, the heat input to the component is lowered and this leads to improve the part accuracy and reduce the effects of the high rates of heat input.

4.12. Comparison Between TIG + Wire SMD and Machining Method by Calculating the (BTF) ratio.

Finally, the typical aerospace part used as a case study to evaluate the cost and time savings which are possible using TIG + Wire SMD and to assess the environment benefits of the process.

The time consuming during deposit each layer of the part is 53 seconds. So the total deposition time is 42.4 minutes. Whereas the machining time consuming during finishing the part is 32 minutes. Therefore, the total time for producing finished part is 1 hour and 14.4 minutes. The time consuming during machining process of the finished part from the solid block is 56 minutes without calculating the time of cutting process for the piece from a desired shaft or billet.

The volume of the solid block (V) = L*H*T =8.0*7.5*4.5 =270 cm^3.

Mass of the block = V* ρ =270 * 8.03 = 2168.1 gr.

Where ρ is the density of SS308Lsi in gr/cm^3.

Volume of machined part (Vm) can be calculated based on the Figurer 3.36 and Figure 3.38

Vm = volume of [1 +2+3+4+5+6+7] = 56.133 cm^3 and mass of the machined part = Vm* ρ =56.133 * 8.03 =450.748 gr. Thus the waste material as chips during machining process = 1717.352 gr

Volume of the deposited part (V_d) before machining can be calculated based on the Figure 3.35

V_d = 89.505 cm^3 and mass of the deposited part = 718.725 gr. Thus the waste material as chips during finishing process = 267.977 gr

The buy-to-fly (BTF) ratio reflects the material efficiency of a manufactured components and is often referred to within the aerospace community to establish the amount of material needed to purchase in order to manufacture the final "flying" part. BTF ratio is the weight ratio between the raw material used for a component and the weight of the component itself [2]. Traditional machining methods typically produce components with BTF ratios of 5:1, but sometimes greater than 20:1 due to a large amount of waste and difficult- to recycle material [185]. Figure 4.99 shows an example of a comparison of the buy-to-fly ratio between traditional and AM technologies. The finished part has a weight of 450.748 gr and to machine from a forged billet would require a starting billet weight of 2168.1 gr which gives a buy-to-fly ratio near 5. This method is extremely wasteful in terms of material. In contrast, using TIG + wire SMD technique the deposited part has a weight of 718.725gr as a cold wire which is added with 267.977 gr machined away to get the final profile. This gives a buy-to-fly ratio of near to 2 and saving materials of 1446.655 gr.

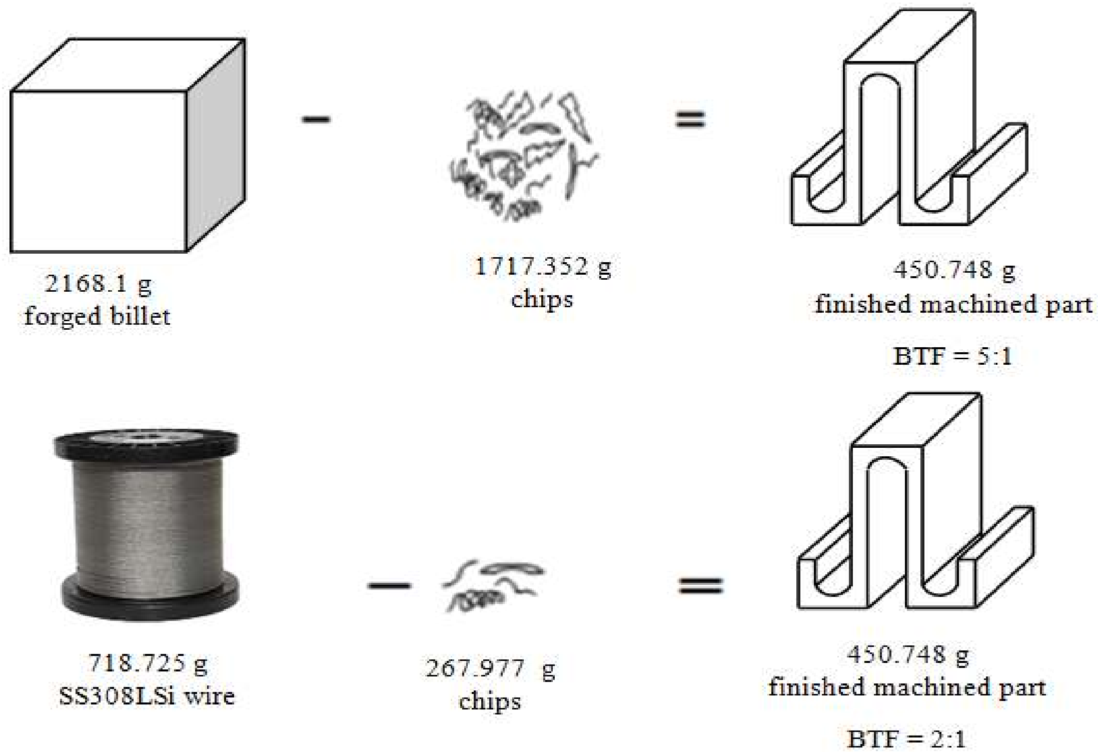

Figure 4. 99. Comparison of traditional machining process vs SMD process in terms of buy-to-fly ratio

CHAPTER 5

DISCUSSIONS

This chapter discusses the results of the experiments mentioned in the previous chapters. Initially, the discussion presents the CAMDM control, the effects of the process parameters on both bead geometry and the penetration in a single bead, tuning the feed angles, process window, and bead defects e.i humping using the CCSMD and PCSMD processes. The discussion then concentrates upon effects of the main parameters on the wall geometry and hardness, effects of interface temperature on the wall characteristics in multilayer deposits of SS308Lsi using CCSMD and PCSMD processes. Finally, the discussion focuses on the optimization of the proposed single and multilayer using the statistical techniques. Additionally, the mechanical and metallurgical tests were discussed in this chapter.

5.1 CAMDM Controlling

The current TW-SMD process comprises designing and developing an integrated system which is able to reduce the time-consuming and boring task of the deposition process. In this system, the deposition path machine acts the main role in the SMD techniques capabilities, therefore, a large body of the studies was done using complicated systems of 6-axis robots linked to a 2-axis rotary table. Most of the existing systems begin with a model created on a CAD packages e.g. CAD surface or solid modeler to generate an output file such as STL file. Then the STL file is sliced using special format into uniform layers, and then these layers consider as path trajectories used for building the part layer by layer. In the present system a new workshop size SMD system was developed which was adopted TIG welding deposition technique. In this system, a computer aided metal deposition machine (CAMDM) was designed, constructed and controlled only for the purpose of the TW-SMD process which was integrated with TIG welding machine and wire feeding mechanism to study the whole process parameters and to produce net or near-net-shaped products as was aforementioned in earlier chapters. The CAMDM control system was designed to have an open-source controller board type, which gives the deposition process flexibility to develop and edit the operation program as well as allows controlling and tuning of the process parameters during the online deposition process. In addition, the current system is characterized by its ability to reduce or eliminate the time-consuming of programming, which is consumed in teaching pendant, CAD packages, slicing format programs, and path generating of the robot. All these programs are replaced by the new program of CAMDM system.

5.2 CCSMD process

5.2.1 Single Layer Beads

5.2.1.1 Process Window

In this study, the effects of the main process parameters on the process states were studies using stainless steel wire of 0.8 mm diameter. The process window has been found, specifying the parameters ranges that lead to four deposition states which may exist during deposition processes such as dripping conditions, smooth deposition, stubbing deposition, and wavy deposition. (see Figure 4.7 and Figure 4.8). The zone 3 in the process window diagram represents the allowable parameter combinations that make the depositing process is stable and the resulted bead profile is satisfied.

5.2.1.2 Effects of Main Parameters on Bead Penetration and Characteristics

In this study, the travel speed and wire feed speed were investigated and keeping the other parameters as aforementioned in section 4.4.2. The results of this work indicate that TS and WFS/TS ratio are very influential parameters in determining the bead geometry, penetration, and bead humping.

5.2.1.2.1. Bead Geometry and Penetration

This study was carried out to show the effects of TS and WFS/TS ratio on the physical bead geometry characteristics (bead width W and bead height H) and the plate fusion amount (P).

Bead Height: In the present study, WFS/TS is the most important factor in determining the H. The WFS has a stronger effect on height at higher WFS/TS values, but the influence becomes less significant with lower ratios as is observed in Figure 4.9.

Bead Width: In this study, the most significant factor is TS in the determining the bead width as shown in Figure 4.11. The strong influence on the width can be obtained at lower TS of 0.18 m/min to be about 6 mm, but this amount may be reduced to the half with increasing the TS to about 0.54 m/min. This attributes to the Equation 4.1. At low TS values, the heat input to the weld pool is higher than that in the case of high TS. Thereby, the melted metal at the melt zone takes enough time for flow to the sides of the pool.

Penetration: In this study, it is possible to identify the most important factor is TS, whereas the WFS/TS is not significant that is clear obvious in Figures 4.13 and 4.14. This also attributes to the increasing in heat input with decreasing the TS. It is obvious that higher TS (0.54 m/min) leads to making the plate fusion (penetration) be shallower, which may result in separate the deposition part from the substrate.

5.2.1.2.2. Bead Defects (Bead Humps)

The results of this study demonstrate the existence of limiting travel speed TS for humping defect to occur in TW-SMD process. Some studies have been done previously on humping, but all were done using the MIG welding. The humping defect is mainly associated with TS, especially at higher rates. So, this phenomenon restricts the production rate of the TW-SMD process. Table 4.1 summarized the correlation between the process parameters (TS & WFS/TS ratio) and the humping defects. Figure 4.15 shows two set of parameters and the resulted beads. The humping defect and hence unstable deposition process tended to increase with increasing the TS and WFS/TS ratio. From Figure 4.16, it was clear that when the WFS/TS ratio increases up to 10, the humping appears even at low travel speeds. Thus, the bead may be humped at TS of 0.3 m/min when the WFS/TS ratio is 12. The travel speed may increase to be 0.42 m/min without defects when the WFS/TS ratio does not exceed 6.

5.2.2. Multilayer Wall Features

5.2.2.1 Effects of Main Parameters on the Deposited Bead Characteristics and Surface Quality

The purpose of this study was to investigate the influences of the main process parameters, such as I, TS, WFS, L on the wall width, wall height, machining layer thickness, deposition volume, and the hardness. This study provides additional insight on how the main parameters and interpass temperatures effect on the multilayer responses such as $W_{av.}$, H_{av}, MLT, DV, and HRA.

In this study, it was found that the responses are especially sensitive to the effects of deposition parameters as well as interpass temperatures.The results of this study showed that the average wall height (Hav) is greatly affected by WFS. It can be seen that when the WFS increases, which means that increasing the metal deposition so that the total height of the wall increases as it was obvious in Figure 4.17. The analysis also established that multilayer wall height is sensitive to the WFS/TS, which has a significant effect on the Hav at constant TS (see Figure 4.32). In the case of decreasing TS, the deposition volume per unit length (DV) will increase according to the Eq. 2 and so the wall height will increase (see Figure 4.32(a)).

The results of this study showed that the multilayer wall width (Wav) is significantly affected by TS (see Figure 4.19). the Wav is directly proportional to the heat input per unit distance, which mainly depends on the arc power and travel speed according to Eq.1. Another explanation for this might be that Wav increases with increasing of WFS/TS ratio ant constant TS (Figure 4.28).

Another very important aspect of this study was the effects of the arc length (L) on the wall geometry and surface quality. From the results of this study, it is clear that the effect of arc length on the thickness of the machined layer from the wall side or the sidewall profile. This gives an indicate that large arc length leads to bad deposit quality since it produces a larger thickness of metal to be removed as well as the effects on the sidewall profile (see Figures 4.21 and 4.22).

The results of the present study also showed that the most significant factors affecting on the DV are traversed speed and wire feed speed (Figure 4.23) and this is exactly consistent with the Eq. 2. As TS decreases and/or WFS increases then the DV increases as observed in Figure 4.25.

TS and L appear to be important factors in determining the HRA of the deposited wall specimens. The HRA tends to be scattered about the mean. But HRA generally is high as the travel speed TS is high due to heat input is lower (see Figure 4.26). Maximum average hardness (**52.7**) obtained at TS = 6 mm/s (see figure 4.27(a)) and also the minimum average HRA. This attributed to the grain refinement in case of low heat input to the deposition zone. The analysis also established that arc length effects on the HRA where the HRA reduces as L increases. This may belong to increasing the arc voltage with increasing the L and so the heat input becomes higher, which leads to reducing the hardness (HRA).

The multilayer depsition results showed that the wall characteristics such as H_{av} and W_{av} are significantly affected by T_{sub} when the TS is held constant. It was seen that the first layers are with small W_{av} and more H_{av}. This can be attributed to the faster cooling rate occurs during deposit the first layers on the substrate, which acts as high efficient heat sink to dissipate the welding heat away from. So the molten metal directly solidifies in relatively high H_{av} and small W_{av}. However, the previous layers act as a thermal barrier for the subsequent layer which leads to prevent the heat dissipation and as a result the W_{av} significantly increases. Therefore, for reducing that the substrate has to preheat to a suitable temperature before deposition the first layer.

The experimental results of the present study also showed another very interesting aspect that MLT of the side wall surface was found to be affected by T_{sub}. The results show that MLT reduced to the minimum amount when the T_{sub} is 300°C (see Figure 4.30). However, the increasing in T_{sub} leads to increase the W_{av} also (see Figure 4.29). In this study, higher T_{sub} leads to increase the wall width and improve the surface quality since the sidewall waves are reduced. Thus, the continuous deposition process without using the idle time between the layers leads to reduce the thickness of the machined layer from the sidewall during the finishing machining processes (see Figure 4.33).

5.3 PCSMD Process

5.3.1 Single Layer Beads

In this study, the preliminary results showed that there are certain limits for the main parameters used in PCSMD such as CR, I_p, and Fr. The CR is an important factor which effects on the amount of heat input and hence the microstructure and other properties of the deposited components. CR should be within the range (1.5-2.5) since at low ratios (less than 1.5), the heat input increases and excessive fusion occurs and so the process becomes unstable. Whereas at high ratios (more than 2.5), the heat input becomes extremely less and hence less melting the filler metal which makes the deposition process is difficult or impossible especially with low peak current process. The results showed that the operating range of frequency is more than the frequencies (0.2-1.0) Hz since the deposition process is unstable and the deposition quality is bad due to the formation of humps as shown in Figure 4.37. There are no limits for the frequency within the range (1.5- 2500)Hz. However, at high frequency (above 2000

Hz) the emanated sound in welding machine becomes very harsh sound. From another side, the very high Fr affects the flow of the shielding gas and in some cases, it leads to the formation of microporosity through the deposition as shown in Figure 4.79.

In PCSMD process, the preliminary tests showed that the deposition process is difficult when using peak current (Ip) lower than 160A especially with high frequencies (more than 500 HZ) as noticed in Figure 4.36. Thus, the higher allowable current is less than 210 A, since above this value the process becomes unstable.

This study was carried out for increasing the understanding upon the influence of main parameters such as pulse frequency Fr, I_p, TS, WFS/TS, and CR on the physical bead geometry characteristics such as bed width W, bead height H, and penetration P.

5.3.1.1 Effects of Fr and I_p on Bead Characteristics

Low frequency has low effects on the bead height and bead width. There is no evident effect of the Fr on the bead height in both low-frequency LF and high-frequency HF processes as observed in Figures 4.38, 4.41 and 4.45. The W increases slightly with increasing Fr at high peak current (Ip=205 A) and decreases with increasing Fr at low peak current (Ip=165 A). The results showed also that high-frequency HF and high current generates more penetration depth in the substrate plate comparing to low current and LF as observed in Figure 4.40.

These effects attribute to the amount of heat input into the deposition zone. In the case of high current (Ip=205A), the heat input amount is relatively higher and so the solidification takes more time to occur. From the other hand, the pulse arc pressure becomes higher with high frequencies which lead to pushing the molten metal ahead and side, which lead to increase the mean of bead width. Opposite state may occur low current (Ip=165A) and low frequency , where at increasing the frequency from 1.5 -90 Hz the width decreases. These effects attribute to the fact that the increasing of pulse frequency leads to decrease the heat input and hence accelerate the solidification of the molten metal especially, at low peak current (Ip =165A).

The overall mean of the penetration depth for the low frequency is significantly larger than that of high frequency (see Figure 5.1). Additionally, from the Figures 5.2 and 5.3, it can be discerned that the low-frequency state is more suitable for deposition process since the effects on the bead geometry do not change the deposition process stability as compared to the high-frequency state.

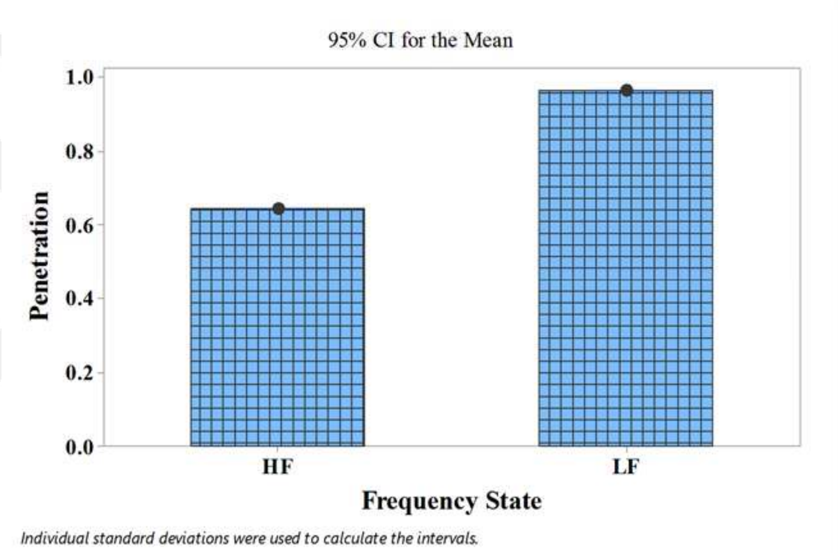

Figure 5. 1. Comparison of penetration depth between LF and HF states

.

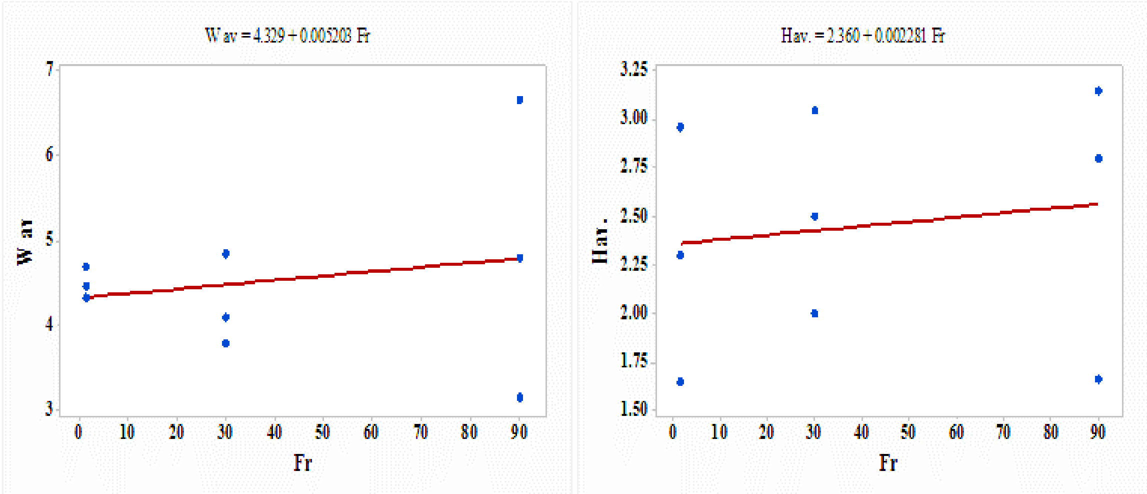

(a) (b)

Figure 5. 2. Effects of low Frequency (LF) on the bead geometry: (a) bead width; (b) bead height.

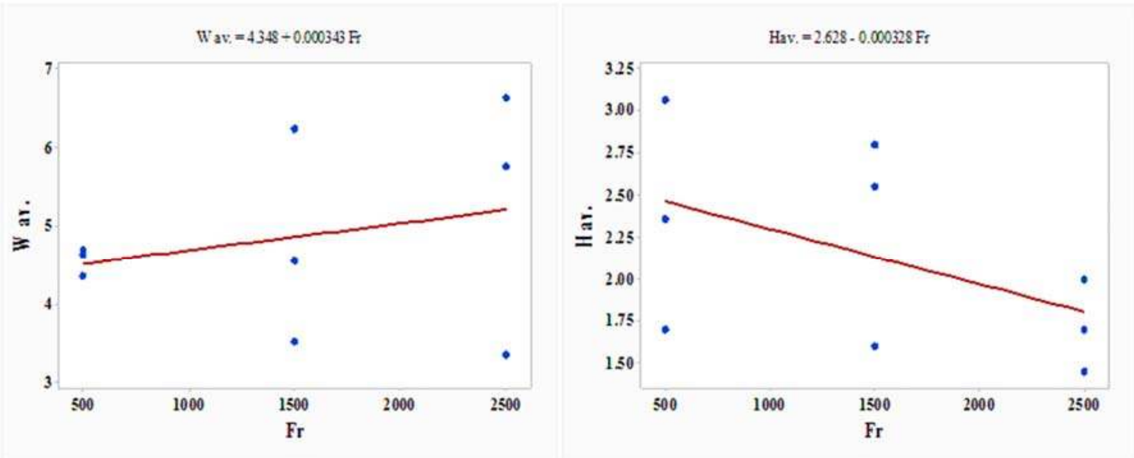

(a) (b)

Figure 5. 3. Effects of high Frequency (HF) on the bead geometry: (a) bead width; (b) bead height.

5.3.1.2 Effects of TS and CR on Bead Characteristics

The results of this study demonstrated that the CR has significant effects on the bead geometry and fusion depth of the substrate plate. From another side, the TS also has an important influence on the bead characteristics as observed in Figure 4.42.

The CR acts in opposite effect to that of TS because of the reduction of heat input which means that the deposited metal does not flow at melting zone and so the bead increases in height instead of widening its bead as shown in Figure 5.4. From the Figure 5.4, it can be discerned that in case of LF deposition processes, the high value of CR makes the bead with relatively high height even at low TS which at the same time significantly affects the process stability since after a few layers the arc length will become very short as well as the bead width become thinner. Therefore, practically the most suitable CR value is 2 since it can use at different TS values and the process is stable.

The effects of CR on the bead geometry and penetration are summarized in the Figure 5.5, where the amounts of penetration are ranged between (0.25 – 1.5) mm in the LF process. Whereas, the CR effects on bead characteristics are summarized in Figure 5.6 in HF process

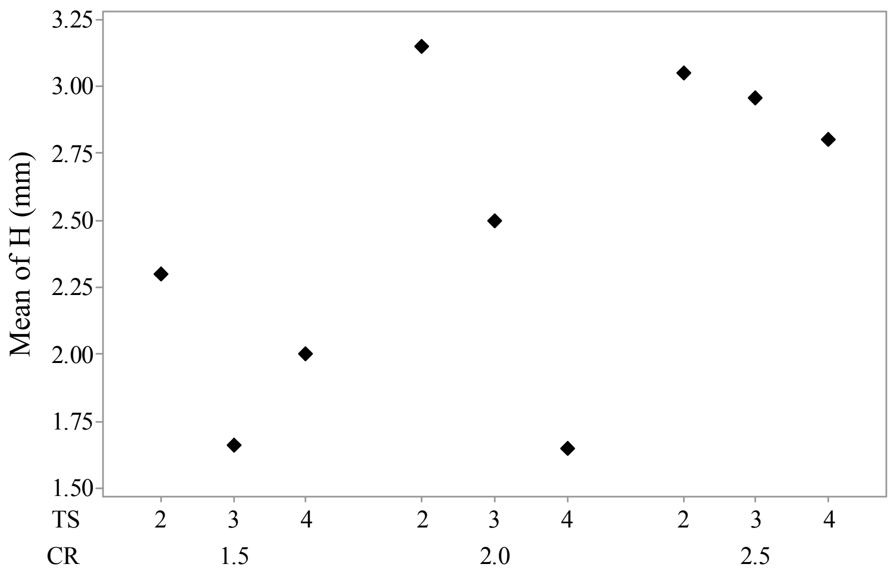

Figure 5. 4. Effects of the CR and TS on the bead height using LF process.

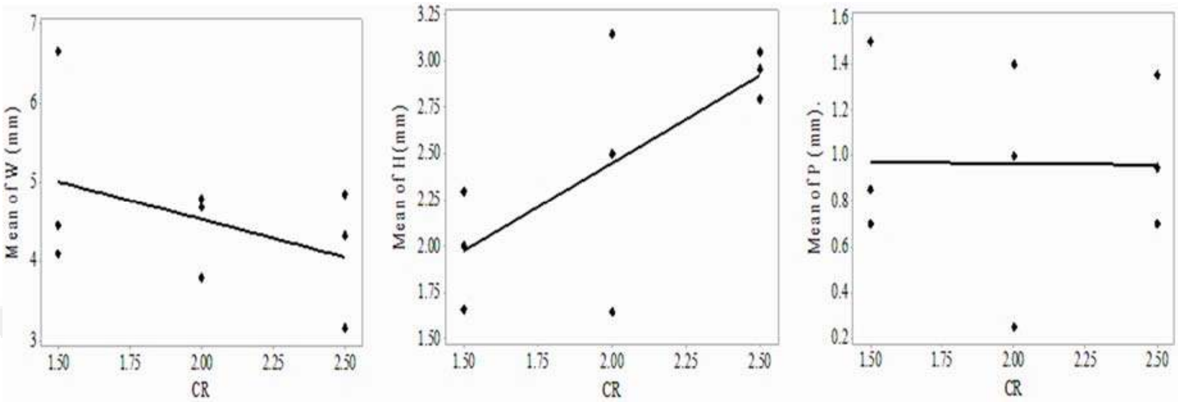

Figure 5. 5. Plots illustrate the effects of CR on the W, H, and P using LF process.

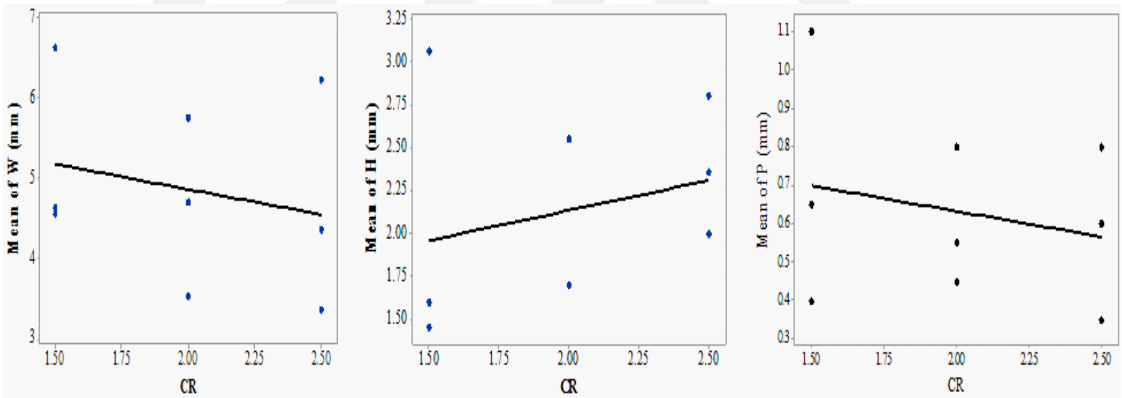

Figure 5. 6. Plots illustrate the effects of CR on the W, H, and P at HF process

5.3.2. Multilayer Wall Features

5.3.2.1. Influence of Main Parameters on Wall Characteristics

The purpose of the present work was to study the influences of primary deposition parameters, such as I_p, Fr, TS, and CR on the evolution of the physical wall geometry i.e. W, H, P in vertical multilayer walls. One of the objectives of this study is to provide additional insight on how multilayers output responses such as wall width, wall height, and hardness of the deposited walls are affected by new processing parameters such as pulse frequency and peak current to base current ratio.

Wall bead characteristics are affected by the process parameters. The most important factor that effects on the wall width and height is the traveling speed (TS) as shown in Figures 4.51 and 4.52. From the Figure 4.51, it is normally the width (W) decreases with increasing the TS. However, the wall height (H) in PCSMD process is not similar to that in CCSMD. This can be attributed to the effect of Fr, which significantly reduces the heat input thereby H becomes higher as TS is low (see Figure 4.51). The effects of Ip on the W and H of the deposited wall are not as that of CR (see Figures 4.50 and 4.51). But at the same time, the peak current (Ip) has the most significant effect on the depth of the fusion of the substrate see Figure 4.53), since it increases the amount of arc power and so the molten metal take more time to solidify and hence the depth of fusion and heat affected zones.

In this study, Fr was found to affect both the H and W, however, too much lesser effects than CR. Another important finding was that CR has an important effect on wall physical geometry as can be discerned from the Figures 5.7 and 5.8.

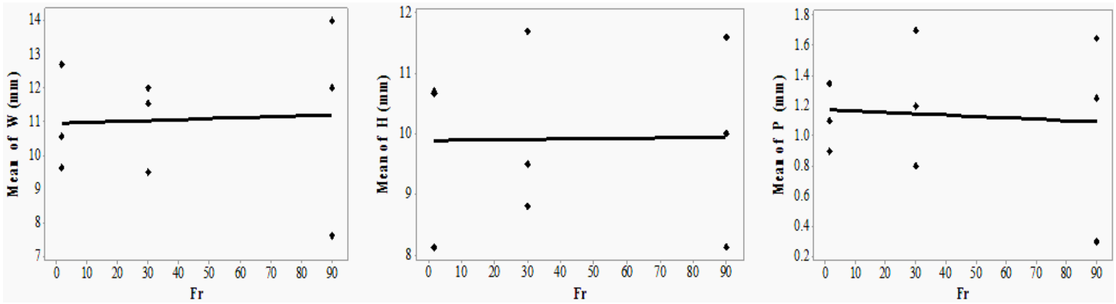

Figure 5. 7. Plots illustrate the effects of Fr on the W, H, and P at multilayer process

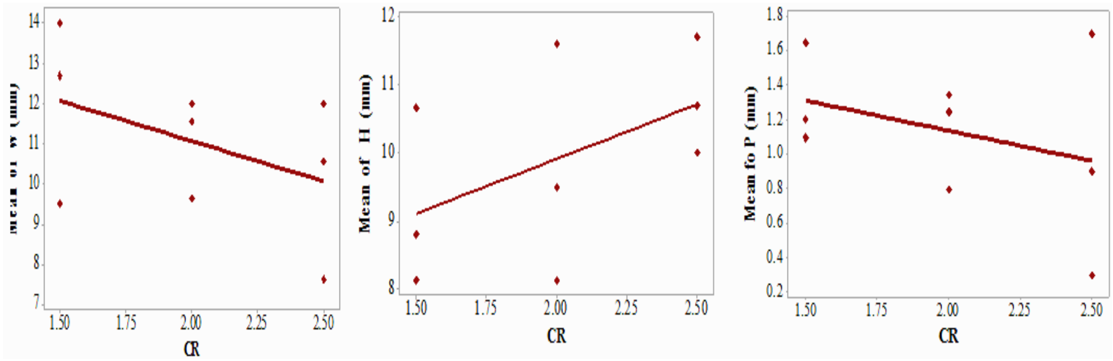

Figure 5. 8. Plots illustrate the effects of CR on the W, H, and P at multilayer process

5.4. Path Planning Strategies

The integrated TW-SMD system was established with a computer aided metal deposition machine having a new interface between the modeling data and the deposition unit. Section 3.6 focused on the planning and implementing the strategies through the experimental study using the integrated TW-SMD system and highlighted the CAMDM capabilities and limitations. The study covers different path patterns, which were planned and implemented for verification of the current system.

Finally, it is important to be mentioned that there are some of the limitations of the SMDM path strategies since not all configurations can be produced by this setup due to the limitations of the process. The present system is unable to produce complex features which contain side holes, and the small features of several millimeters due to the physical nature of this process. Additionally, the wire feeding direction is not flexible with all movement directions during the deposition process, which may result in a significant effect on the deposition possibility and quality.

One of the main challenges in the TW-SMD method is the cumulative heat during the deposition process, which may lead to excessive melting in the deposited part and loss the accuracy in dimensions, especially in the short deposits. In order to overcome such challenges, a proper idle time or inter-pass cooling time must be considered after a few layers to avoid the overheating of the component. But the idle time reduces significantly the productivity since it increases the production time of the part. Therefore, the proper procedure that can be used to avoid the overheating is by well tuning the main process parameters and also using an efficient cooling system to dissipate the heat during the deposition process.

5.5. Metallography Testing

The composition of the Type 308LSi stainless steel filler wire places this alloy well within the primary delta ferrite region (FA). Using the Schaeffler diagram [113, 153] the FN was calculated to be above the 10%. According to the Cr_{eq}:Ni_{eq} ratio (about 1.93), the solidification mode fall into the type shown in Table 5.1 [113, 160, 186]. The unstable delta ferrite (δ-ferrite), which may be formed during solidification will transform into austenite(γ) during further cooling. The austenite phase remains down to room temperature with various ferrite morphologies, which may be identified as residual primary ferrite at a level above 10%. Vermicular ferrite with above 10% FN was observed at the top parts of the CCSMD, which formed due to rapid cooled at these zones and results in incomplete $\delta \rightarrow \gamma$ transformation. The microstructure of the deposited parts depends highly on the process parameters. As the TS increases, which usually leads to rapid solidification. This leads to depressing the ferrite-to-austenite and hence increases the residual ferrite content.

In TIG welding, the fluid flow in the arc is driving by the electromagnetic force or Lorentz force. Whereas the fluid flow in the weld pool is affected by buoyancy force, Lorentz force, and the surface tension force [187]. The arc pressure is another force acting on the pool surface, as was demonstrated by Lin and Eagar [188]. The arc pressure is depending on the pulse frequency and the current ratio as shown in Equation 5.1. Which gives a reasonable explaining for the microstructure changes with change the frequency.

$$\text{Parc} = \frac{\mu_o}{4\pi^2\,R^2}\,\text{Fr}^2\text{Ib}^2(\text{CR tp} + \text{tb})^2 \qquad 5.1$$

where P_{arc} is arc pressure, μ_o is the magnetic permeability of free space, R is the arc radius, Fr is frequency, CR is current ratio, t_p is peak duration, t_b is the base current duration, and Ib is the background current

In the pulsed current process, the grain refinement observed in the pulsed current welds is therefore believed to be a result of other effects of pulsing on the weld pool shape, fluid flow , temperature [120] and the pulse arc pressure. The arc pulsation causes heterogeneous nucleation aided by thermal undercooling resulting from arc pulsation which is responsible for breaking up the dendrite arms and refining the deposited structure [130].

5.6 Mechanical testing

5.6.1 Hardness test

The hardness in both traverse and longitudinal orientations is scattered around the mean value. These scatters may be attributed to the microstructure banding or to the phases formation inside the columnar grains due the inhomogeneous distribution of microstructure across each layer (see Figure 4.87(a-b).

Table 5. 1. Solidification Type and resultant microstructures

Solidification Type	Reaction	Microstructure
FA	L→ L+F → L + F + $(F+A)_{per/eut}$ → F+A→A 1.48<Creq:Nieq ratio<1.95	Skeletal and/or lathy ferrite resulting from ferrite-to-austenite transformation

The results of this study demonstrate that the hardness of CCSMD and PCSMD components varies from a maximum value near the substrate to a minimum value near the top region. This can be attributed to the change in grain sizes along the wall height due to reducing the cooling rate as the wall height increases. The relatively large substrate acts as a heat sink that removes quickly the generated heat from the deposition region and causing a high cooling rate and hence fast solidification rate which leads to finer size of grains, higher residual ferrite content, and a higher hardness as observed in Figure 4.87(c).

Another major finding was that hardness of PCSMD components is significantly higher than that of CCSMD components (see Figure 4.86). This attributes to the existing phases and the grain sizes in PCSMD is different of CCSMD. In PCSMD process, the heat input is significantly less than that of CCSMD and hence the grain structure generally becomes finer. From another side, this leads to making the residual ferrite higher, which appears as lathy or vermicular ferrite embedded in austenite

5.6.2 Tension test

The obtained values from tension test of SS308LSi deposited components were compared with standard tension results of specimens prepared in different states such as reported for the wrought Type 308L stainless steel [112], as-cast austenitic stainless steel [113, 114, 152], and all weld metal SS308LSi by TIG welding [113, 115].

The UTS of CCSMD specimens were 598 MPa and 602 MPa in vertical and horizontal orientation respectively, which are within the range of wrought and cast metals. Whereas the PCSMD revealed some superior mechanical properties in terms of UTS and YS (see Figure 4.96(a)). From another side the ductility of the manufactured components was relatively higher than those can be obtained from wrought, cast, or all weld metal as shown in Figure 4.96(b). Furthermore, the 0.2%YS was higher than the range of cast metal and slightly higher than the all weld metal by TIG welding.

The comparison results are reported in Table 5.2, which also were shown in Figure 4.96. As a comparison to conventional SMD, the increasing in UTS and ductility in PCSMD components attributed mainly to the changes in the microstructure of the deposited materials, since the residual delta ferrite much increased with increasing in pulse frequency and current ratio.

The results of this study demonstrate that the pulse frequency and current ratio play a vital role in breaking the columnar grains and dendrites and affecting the grain refinement due to increasing in the pulse arc pressure. Thus, the mechanical properties of PCSMD components are superior as a comparison to all other methods as shown in Table 5.2. Another major finding in this study was that according to the chemical composition of the selected material as filler metal and the procedure used there was no chromium carbide Type $M_{23}C_6$ can be seen in the grain boundaries of all specimens.

Table 5. 2. **Comparison the UTS and % ductility of the present process and other conventional methods.**

Specimen preparation method	**UTS (MPa)**	**Ductility %**
Wrought Metal (WM) [112]	515 - 620	Min. 40
Casting metal (CM) [113,152]	530 - 621	39-60
All weld by TIG welding (ATW) [113, 115]	510 -628*	30 -59.5
CCSMD (longitudinal direction)	602.2	46.67
PCSMD (longitudinal direction)	729.955	61.67

**UTS depends on the ferrite amount, so it may be about 689 MPa at FN 16[113].*

CHAPTER 6

CONCLUSIONS AND FUTURE WORKS

6.1. Conclusions

This study was conducted to contribute to the knowledge of TW-SMD manufacturing technique. As described in Chapters 1 and 3, the aim of this study is the development of arc metal deposition system with wire feeding and the objectives were focused on investigating the SMD integrated system developing and controlling, process window, and process characterization. The investigations performed in this study are best concluded in (4) Sections. Firstly, the TW-SMD system integrating and developing to study the whole process parameters in SMD technique. Secondly, the influence of the process parameters on the deposition process stability and producing free-defects deposits. Thirdly, the influence of main deposition parameters on the deposit characteristics such as bead/wall geometry and surface quality. Finally, the metallurgical and mechanical properties of the fabricated components and the relation between the properties and the specimen's location and orientation with respect to the deposition height and orientation. Additionally, effects of the pulse frequency and current ratio on the deposited part properties.

6.1.1. System Development and Control

A TIG welding system + metal wire deposition integrating system has been developed successfully. In the present study, a cold wire-feed additive layer manufacturing SMD system was developed to produce fully dense near-net shaped parts. The CAMDM system was constructed in manner reduces the need for slicing strategies for STL files, since the present system directly draws, slices, and simulates the part's drawing at the same CAD module. So that it reduces the efforts and tedious tasks necessary for robots and also shortens the time of teaching the trajectories. The major conclusions are summarized as follows:

- A new type of shaped metal deposition system was designed and constructed in this work. The results showed that the machine has adequate performance during the experiments. This means that the design and construction of CAMDM are feasible and acceptable.
- On-line programming method was used, since it is more suitable for CAMDM and gives the system more flexibility to control the process parameters and it is less complex than off-line programming method.
- The CAMDM software was designed to be applicable for expansion and development since it has an open-source system. Which also allows tuning the main process parameters during the deposition process i.e. reducing the input power or increasing the travel speed, thus the cumulative heat input through the deposited part could be reduced to a limit does not cause the flow of the molten metal. This procedure improves the surface quality of the deposited part and instead of using long idle times between a few layers, so this increases the process productivity.
- The developed CAMDM system is capable of producing various solid filling parts, hollow filling parts and another single stringer whether discrete and polygon features in near net shaped with satisfactory quality components of sizes do not exceed 400 mm in three directions.
- From the comparison results, it was discerned that the current CAMDM system is capable of saving about 66.7% of the raw materials as compared to the conventional machining methods but with longer production time.

6.1.2. Effect of Process Parameters on the Process Condition and Characteristics

The influence of the main parameters on the process stability was investigated using stainless steels 308LSi wire (0.8 mm in diameter). The process window has been established, identifying the set combinations of the parameters, which lead to four deposition states such as dripping state, smooth state, stubbing state and wavy state of deposition. Thus according to the combination of the parameters used, the process falls in one of the aforementioned regions. The high deposition rate may lead to occur the stubbing state, whereas high travel speeds may cause the wavy state. Some of the conclusions can be drawn as;

- Using the suitable deposition variables leads to achieve the stability in deposition process and produce defect free parts with good metallurgical bonding between the successive layers. This can be achieved using the process parameters range within the smooth bead region as aforementioned in Figure 4.7.
- The results show that the most suitable range of travel speed TS is within (0.18-0.30) m/min, whereas WFS/TS ratio is within the range (6 -8), which make the process more stable and fewer defects (as shown in Figure 4.16).
- From the results, it can be discerned that the deposition process may be unstable due to humping defects associated with increasing of TS more than 0.3 m/min at high WFS/TS ratios. So that, selection of TS should be correlated to WFS/TS in order to produce smooth metal deposition and stable process.
- The interpass temperature significantly effects on the roughness of deposited walls. High interpass temperatures lead to lower the MLT and hence increase the productivity, however, the wall width becomes relatively higher.
- For getting stable deposition process in PCSMD process, the CR should be within 1.5-2.5, otherwise, the process becomes unstable. Additionally, the peak current has to be within the working range of (160-210) A. The pulse frequency should be always above the critical value (1.0 Hz).
- The arc length (L) is one of the most important challenges that affect the process stability, which should be maintained less than 6 mm, otherwise, the process becomes unstable and long arc may lead to destroying the deposited walls.

6.1.3 Influence of Parameters on Bead/Wall Geometry

For the TW-SMD technique (CCSMD or PCSMD), the effects of the process variables such as (welding current, travel speed, wire feed speed, arc length, pulse frequency, and current ratio on the bead geometry have been analyzed using DOE. Two types of DOE were used: the full factorial design and Taguchi method. The response variables were the bead/wall width, bead/wall height, bead/wall penetration, thickness of the machined layer, and hardness. The major conclusions that can be drawn from the experiments are:

- The process parameters are the key to controlling the bead/wall characteristics and the response variables.

- TS play a significant effect on the bead/wall geometry. Increasing TS decreased the deposited bead/wall width and decreased the depth of fusion in the substrate plate.
- Increasing the WFS or the WFS/TS increased the bead/wall height.
- Increasing the arc length increased the machining layer thickness so that the arc length should be always less than 5mm. The experimental results showed that the most suitable amount of the arc length is 4 mm for both CCSMD and PCSMD processes.

6.1.4 Mechanical and Metallurgical Properties of the TS-SMD Test Samples

Single-bead walls were used to make samples for mechanical and metallurgical tests using AISI 308LSi stainless steel. The samples were tested according to the aforementioned DOE. The main conclusions from the obtained results can be summarized as follows:

- From the morphology of the deposited parts, it can be seen that the pulse frequency has a significant effect on the columnar grains growth for given process parameters. The microstructure mainly consists of primary ferrite (lathy/ vermicular). However, PCSMD specimens reveal microstructure with relatively fine grains as compared to CCSMD specimens.
- For a given process parameters the pulse frequency has a significant effect on the columnar grains growth. Since the Fr influences the pulsed arc pressure and hence the microstructure of the PCSMD components revealed finer grains and containing higher residual ferrite as compared to the microstructure of CCSMD components.
- The current ratio effects significantly on the morphology and final microstructure of the deposited parts.
- In all specimens, there was no significant inter-granular sensitization M23C6 type chromium carbide or other carbides. As also can be seen in all the tested specimens, mechanical properties of the manufactured components did not suffer from the degeneration or deterioration.

- For both PCSMD and CCSMD processes, the components exhibit a dependence of the mechanical properties to the test orientations. High UTS and YS can be achieved in the longitudinal direction and high ductility in the vertical direction.
- Tension properties are not dependent on the building height of the components. However, ductility slightly lowers near the top of the part. On the other hand, hardness is higher at near the base region and it slightly decreases at the near the top of the part.
- From the results, it was discerned that the hardness is varying with the height of deposited specimens.
- The mechanical properties of the components prepared using PCSMD are generally higher than those prepared by CCSMD for all welded metal, and as-cast metal, and they are comparable to the wrought metal.
- From the metallurgical and mechanical analysis of the deposited samples, the impurity levels of the deposits are considerably low and hence their properties are significantly higher as compared to as cast parts. Therefore, the developed technique may be interesting for fabricating parts that should have low impurity level such as parts used for aerospace applications.

6.2. Future Works

- In order to increase the useful aspects of the current SMD system, another accessories should be added to the system such as milling cutter spindle which can be attached to the same gantry of the SMD machine. This makes the system as universal integrated manufacturing system ready to produce finished parts. Furthermore, in order to increase the flexibility of the present system, it necessary to add another motor to control the feeding direction. This makes the system more flexible.
- The present SMD system can be fully controlled it using feedback system for increasing the accuracy and controlling the precision of the dimensions.
- The present SMD system can be easily modified it for dual-materials deposition processes by adding another wire feeder nozzle to the deposition tool unit. It is very important development in the shaped metal deposition process to produce

parts with different materials or to produce parts with a new combination of mechanical properties.

- Expand the current limited knowledge of the SMD process by applying the thermal modelling in order to predict the size of the melt pool and solidification rates and thermal history of the deposited material. A finite difference (FD) code can be used to estimate the solidification conditions found in the SMD process understudy. The model will be applied in steady state conditions to a solid block austenitic stainless steel Type 308LSi. The FD modelling would be carried out for TW-SMD process using a certain set of process parameters. Outputs obtain from the model consist of temperature control plots, cooling rates, and maximum thermal gradient and growth rate. Further investigation of the thermal stresses and residual stresses and modelling the deposited layers is necessary to understand the effects of these on the surface roughness, microstructure, and the mechanical properties.

SUMMARY OF APPENDED PAPERS

Introduction

In this section, a brief presentation of the appended papers is given. There are 7 included Journal papers and 3 conference proceedings papers, which reflecting the development of the performance research activities.

Paper I

Yilmaz, O., Ugla, AA. (2016) Shaped metal deposition technique in additive manufacturing: A Review. *Proc IMechE Part B: J Engineering Manufacture,* online on 11-April-2016. DOI: 10.1177/0954405416640181.

This paper presents a comprehensive survey on one of the AM methods, namely, shaped metal deposition (SMD). This work offers a survey of various investigations of the SMD process overall: its potential advantages/disadvantages, control structure used SMD techniques, a critical review of the microstructural analysis and effects on mechanical properties, and effects of thermal history on induced residual stresses in SMD parts. In addition, challenges in SMD method such as multi-material use and grain refinement are also discussed. In this survey, a general classification of SMD methods is made on the basis of the used control system, heat source, and material supply techniques for the first time.

Paper II

Yilmaz, O., Ugla, AA. (2016) Microstructure characterization of SS308LSi components manufactured by GTAW-based additive manufacturing: Shaped metal deposition using pulsed current arc, *International Journal of Advanced Manufacturing Technology*, Published online on June-2016. DOI: 10.1007/s00170-016-9053-y.

This paper reports for the first time the using of the pulsed current shaped metal deposition technique for fabricating components using cold wire of AISI 308LSi stainless steel. The aim of the present work was to investigate and compare the effect of pulse frequency and other deposition process parameters on the morphology aspects and microstructure characteristics of the manufactured components using pulsed and continuous current processes.

Paper III

Yilmaz, O., Ugla, AA. (2016). Shaped metal additive layered manufacturing of austenitic stainless steel using DC TIG pulsed arc: Microstructure and mechanical properties, submitted to *Journal of Materials Engineering and Performance.*

This paper presents an investigation on shaped metal deposition method using pulsed current TIG arc for fabricating solid dense parts using externally fed cold wire made of AISI 308LSi austenitic stainless steel. The effect of pulse frequency on the morphology aspects, microstructure characteristics and mechanical properties of the manufactured components are investigated in this research work. Mechanical properties of the samples that are taken from the deposited parts at different locations and orientations are examined for both continuous and pulsed DC current arc heat source in the shaped metal deposition process.

Paper IV

Ugla, AA, Yilmaz, O. (2016) Deposition-paths generation of SS308 components manufactured by TIG welding based shaped metal deposition process, submitted to the *Arabian Journal for Science and Engineering*.

In the present work, a type of shaped metal deposition (SMD) using tungsten inert gas (TIG) welding plus SS308LSi Wire (TW-SMD) technique was developed and integrated it with a new computer aided metal deposition machine (CAMDM). The intent of this paper is to investigate the CAMDM system capabilities about the part modeling and slicing, deposition-path planning, and the part depositing processes. Additionally, this paper highlights the capabilities and limitations of the developed system.

Paper V

Ugla, AA, Yilmaz, O., Jasim AR. (2016) Development and control of shaped metal deposition process using TIG arc heat source in additive layered manufacturing, submitted to *Proc IMechE Part B: J Engineering Manufacture.*

This paper presents the designing, constructing, and controlling of an additive manufacturing (AM) system using TIG plus wire based shaped metal deposition (TW-SMD) method. The aim of the current study is to design and develop an integrated system which is able to reduce the time-consuming and boring task of the deposition process. The developed additive system is capable of producing near net components of sizes not exceed 400 mm in 3-directions directly from CAD drawing.The results showed that the developed system succeeded to produce error-free depositions for various features of SS308LSi components.Additionally, workshop tests have been conducted in order to verify the capability and reliability of the developed AM system.The developed system is also capable of reducing the buy-to-fly ratio from 5 to 2 by reducing waste material from 1717gr to 268 gr for the sample components.

Paper VI

Yilmaz, O., Ugla, AA. (2016). Development of a cold wire-feed additive layer manufacturing system using shaped metal deposition method, submitted to *the Journal of Mechanical Science and Technology.*

The aim of the current study is to design and develop an integrated system which is able to reduce time-consuming and boring task of the deposition process. The developed additive system is capable of producing near net shaped components of sizes not exceed 400 mm in 3 directions directly from CAD drawing.

Paper VII

Ugla, AA, Yilmaz, O. (2016) An Investigation of Shaped Metal Deposition Process Using TIG Arc Heat Source in Additive Layered Manufacturing, submitted to the *Journal of Additive Manufacturing*.

This paper presents an extensive research work aiming to investigate the process capabilities and elaborating the usage of shaped metal deposition method in direct metal part manufacturing and comparing it to traditional methods. To do that, a 3-axis shaped metal deposition system was developed using a tungsten inert gas welding machine and an external cold metal wire feed arrangement. Several workshop experiments were carried out to verify the developed system.

Paper VIII

Yilmaz O, Almosawi ARJ, Ugla AA, Keskin OO. (2015) Design, construction and controlling of a shaped metal deposition machine using arc metal-wire system. In: Proceedings of 8th International Conference and Exhibition on Design and Production of Machine and Dies/MoldsJune18-21, Kusadasi - Aydin, Turkey, pp: 235-244.

This paper aims to study the designing, constructing and controlling a computer controlled the machine with 3-axespositioning, which can be used for SMD process especially for TIG and MIG welding deposition techniques. The SMD machine (SMDM) represents the central part of the SMD hardware system. This study explains the designing, constructing and control programming of the developed SMD system. Additionally, workshop tests have been conducted in order to verify the capability and accuracy of the developed AM system.

Paper IX

Ugla, AA. Yilmaz, O. (2016). Development and application of a cold wire-feed TIG welding based shaped metal deposition method in additive manufacturing technology, In Proceedings of the 4th international conference on welding technology *and exhibitions ICWET'16,* 11-13 May 2016, University of Gaziantep, Gaziantep, Vol. 1: 118-128.

This paper presents the development of a workshop size SMD system. The study covers the designing, constructing and controlling a computer controlled the machine with 3-axis positioning, which can be used for the SMD process especially for TIG and MIG welding deposition techniques. The system developed has been used to study the whole process and to construct and control the TIG + Wire SMD technique. The present work discusses the determination of the weld deposition parameters limits to obtain a stable deposition process and to give an overview of the process window. A comparative experiment between the current system and the conventional machining method was also investigated

Paper X

Yilmaz, O., Ugla, AA. (2016) Development and investigation of shaped metal deposition process using TIG arc heat source in additive layered manufacturing, In *Proceedings of the 17th International Conference on Machine Design and Production*" 12-15th July 2016, Bursa/ Turkey, pp. 28

The control system was designed to have an open-source simple microcontroller board type, which gives the CAMDM system flexibility to develop and edit the operation program as well as allows controlling and tuning of the process parameters during the deposition process. Furthermore, the intent of the present work is to address the reducing or eliminating the time consuming during robot programming with a teach pendant and also all CAD packages and slicing format programs which are used for generating the robot paths and replacing them with a new program suitable for CAMDM system.

REFERENCES

[1] Gebhardt A. (2011). Understanding additive manufacturing, rapid prototyping, rapid tooling, rapid manufacturing, 1st edition, Carl Hasner Verlag, Munich- Germany.

[2] Antonysamy AA. (2012). Microstructure, texture and mechanical properties evolution during additive manufacturing of Ti6Al4V alloy for aerospace applications. University of Manchester, Ph.D. thesis.

[3] Buckner, M.A., Lonnie, J.L. (2012). Automating and accelerating the additive manufacturing design process with multi-objective constrained evolutionary optimization and HPC/Cloud computing. In: *Proceedings of the 2012 IEEE Int Conf on Future of Instrumentation International Workshop (FIIW).* Gatlinburg, NT, USA, 8-9October, pp. 1-4.

[4] Wohlers, T. (2009). Wohlers report 2009, State of the industry, Annual worldwide progress report, *Wohlers.*

[5] Mahmood, R.M., Akinlabi, E.T., Shukla, M., Pityana, S. (2013). Laser Metal Deposition of Ti6Al4V: A Study on the Effect of Laser Power on Microstructure and Microhardness In: *Proceedings of the International MultiConference of Engineers and comp Scientists, IMECS* 2013,March 13-15, Hong Kong,Volume 11.

[6] Klahn, C., Leutenecker, B., Meboldt, M. (2014). Design for Additive Manufacturing- Supporting the Substitution of Components in Series Products, in *Proceedings of the 14th CIRP Design Conference*, 21:138-143. Available online at www.sciencedirect.com.

[7] Shames, H. (2010). Development of a selection program for additive manufacturing system. Stellenbosch University, Master thesis.

[8] ASTM F2792-12 A Standard Terminology for Additive Manufacturing Technologies, doi: 10.1520/F279-12A.

[9] VDI 3404 (2014). Additive Manufacturing: Basics, Definitions, Processes.

[10] Gibson, I., Rosen, D., Stucker, B. (2010). Additive manufacturing technologies, Second Edition, Springer New York Heidelberg Dordrecht London, doi: 10.1007/978-1-4939-2113-3.

[11] Frazier, W.E. (2014). Metal additive manufacturing: A review, *Journal of Materials Engineering and Performance*, 23 (6), 1817-1928

[12] Van Niekerk G.J. (2007). A model for transparent data exchanging in layered manufacturing. Faculty of Science – the University of Johannesburg, Ph.D. thesis.

[13] Griffith, M.L., Ensz, M.T., Puskar, J.D., Robino, C.V. (2000). Brooks, J.A., Philliber, J.A, et al. Understanding the microstructure and properties of components fabricated by laser engineered net shaping (LENS). In: *Proceedings of MRS Spring Meeting Conference*; San Francisco, CA,US, 24-27 April.

[14] Zhang, K., Liu, W., Shang, X. (2009). Study on scanning pattern during laser metal deposition shaping.In: *Proceedings of the 2009 IEEE Second IntConfon Intelligent Computation Techn and Auto*; Changsha, Hunan, 10-11 October, 4, 668-671.

[15] Jardini, A.L., Larosa, M.A., Bernardes, L.F., Zavaglia, C.A.C., Maciel F. R. (2011). Application of direct metal laser sintering in titanium alloy for cranioplasty. *6th BRAZILIAN Conf on Manf Eng*; CaxiasdoSul-RS- Brazil, 11-15 April.

[16] Zhang, K., Liu, W. (2009). Microstructure evolution of stainless steel during laser metal deposition shaping .In: *proceedings of the 2009 IEEE Int Conf on Measuring Techn and Mechatronics Auto*, Zhangjiajie, Hunan, 11-12 April, 2, 93-96.

[17] Kloosterman, A., Wentzel, C., Carton, E. (2006). SLAM, A fast high volume additive manufacturing concept by impact welding; application to Ti6Al4V alloy. *SAE International, Aerospace Man. And Auto. Fast. Conf. & Exhibition*; Toulouse, France, 12-14 September.

[18] Olielodan, J.O. (2010). Fabrication of multi-material structures using ultrasonic consolidation and laser- engineered net shaping. Utah State University, Ph.D. thesis.

[19] Taminger, K.M., Hafley, R.A. (2006). Electron beam freeform fabrication for cost effective near-net shape manufacturing. In *NATO/RTOAVT-139 specialists' meeting on cost effective manufacture via net shape processing* 2006, NATO: Amsterdam (TheNetherlands).

[20] Kobryn, A., Semiatin, S.L. (2001). Mechanical properties of laser-deposited Ti6Al4V. In *Solid Freeform Fabrication Proceedings,* Austin, August 2001, 179-186.

[21] Bourel, D.L., Leu, M.C., Rosen, D.W. (2009). Roadmap for additive manufacturing: Identifying the future of freeform processing, the University of Texas in Ustin, Austin TX.

[22] Sequeira-Almeida, P.M. (2012). Process control, and development in wire and arc additive manufacturing. School of Applied Sciences, Cranfield University, Ph.D. thesis.

[23] Griffith ,M.L., Schlienger, M.E., Harwell, L.D., Ensz, M.T., Greene, D.L., Smugeresky, J.E., et al. (1999). Understanding thermal behavior in LENS Processing of Structural Materials. In: *Proceedings of the annual conference on Surface Engineering: Science and Tech*; San Diego, CA, USA; February 28- March 4.

[24] Adams, R. (2008). Ion fusion formation: An Alternative Additive Manufacturing Approach. *SAE International, Aerospace Manf, and Auto Fastening Conf* ; North Charleston, South Carolina,16-18 September .

[25] Hermans, M.J.M., Ouden, G.D. (1999). Process behavior and stability in short circuit gas metal arc welding. *Welding Journal (Miami, Fla)*, 78(4), 137-141.

[26] Rosenthal, D. (1946). The theory of moving heat and its application to metal treatments. *Transaction of ASME,* 68, 849-866.

[27] Shukla, M., Mahmood, R.M., Akinlabi, E.T., Pityana, S. (2012). Effect of laser power and power flow rate on properties of laser metal deposition Ti6Al4V, *International Scholarly and Science Research & Innovation,* 6(11), 44-48.

[28] Kelly, S., Kampe, S. (2004). Microstructural evolution in laser-deposited multilayer Ti-6Al-4V builds: Part I. Microstructural characterization. *Metallurgical and Materials Transactions A*, 35(6), 1861-1867.

[29] Brandl, E., Baufeld, B., Leyens, C., Gault, R. (2010). Additive manufacturing Ti6Al4V using welding wire: comparison of laser and arc beam deposition and evaluation with respect to aerospace material specifications. In: *Proceedings of 6th International Conference on Laser Assisted Net Shape Engineering (LANE 2010),* 5, 595-606.doi: 10.1016/j.phpro.2010.08.087.

[30] Strano, G., Hao, L., Evans, K.E., Everson, K.M. (2010). Optimization of quality and energy consumption for additive layer manufacturing processes. *ICRM- Green Manufacturing* , Ningbo, China, 364-369.

[31] Zhao, H., Zhang, G., Yin, Z., Wu, L. (2011). A 3D dynamic analysis of thermal behavior during single-pass multi-layer weld-based rapid prototyping. *J Mat Processing Technol,* 488-495.

[32] Online] Available: http://www.dipilab.fr/AxeRecherche/fabricationdirecte/DMD/ENISE_DMD.

[33] Klahn, C., Leutenecker, B., Meboldt, M. (2014). Design for additive manufacturing supporting the substitution of components in series products. In *14th CIRP Design Conference*, 21: 138-143. doi: 10.1016/j.procir.2014.30.145.

[34] Jardini, A.L., Larosa, M.A., Bernardes, L.F., Zavaglia, C.A.C., Maciel Filho, R. (2011). Application of direct metal laser sintering in titanium alloy for cranioplasty. In *6th BRAZILIAN Conf on Manf Eng*; Caxiasdo Sul-RS- Brazil, 11-15 April.

[35] Rieder, H., Dillhofer, A., Spies, M., Bamberg, J., Hess, T. (2014). Online monitoring of additive manufacturing process using ultrasound, In: *11th European Conference on Non-Destructive Testing (ECNDT 2014),* October 6-10, Prague, Czech Republic,

[36] Gardan, J. (2015). Additive manufacturing technologies: state of the art and trends, *International Journal of Production Research*. Doi: 10.1080/00207543.2015.1115909.

[37] Syed, W.U.H., Pinkerton, A.J., Li, L. (2006). Combining wire and coaxial powder feeding in laser direct metal deposition for rapid prototyping, *J. Applied Surface Science,* 252, 4803-4808.

[38] Syed, W.U.H., Pinkerton, A.J., Li, L. (2006). Simulation wire- and powder-feed direct metal deposition: An investigation of the process characteristics and comparison with single-feed methods, *J. Laser Applications*, 18(1), 65-72.

[39] Brandl, E., Layens, C., Palm, F. (2011). Mechanical properties of additive manufactured Ti6Al4V using wire and powder-based processes, *IOP Conf. Series: Materials Science and Engineering,* 26. Doi: 10.1088/1757-899X/26/1/012004.

[40] RAPOLAC Project home page. [online]. Available: http:// www. RAPOLAC.eu.

[41] Bonaccorso, F., Bruno, C., Cantelli, L. (2009). Control of a shaped metal deposition process. In: *Physcon 2009*;Catania, Italy, 1-4 September.

[42] Bonaccorso, F., Cantelli, L., Muscato, G. (2011). An arc welding robot control for a shaped metal deposition plant: modular software interface and sensors. *IEEE Transactions on Industrial Electronics,* 58(8): 3126-3132.

[43] Muscato, G., Spampinato, G., Cantelli, L. (2008). A closed loop welding controller for a rapid manufacturing process.In:*proc.13th IEEE Conf;* EFTA, Hamburg, Germany, 15-18 September2008; 1080-1083.

[44] Merz, R., Prnnz, F.B., Ramaswami, K., Terk, M., Weiss, L.E. (1994). Shape deposition manufacturing. In: *Proceedings of the Solid Freeform Fabrication Symposium*, Texas University in Austin, 8-10 August.

[45] Skiba, T., Baufeld, B.,Vander-Biest, O. (2009). Microstructure and mechanical properties of stainless steel component manufactured by shaped metal deposition, *ISIJ Int,* 49(10), 1588-1591.

[46] Baufeld, B.,Van der Biest, O. (2009). Mechanical properties of Ti-6Al-4V specimens produced by shaped metal deposition. *Sci Tech Adv Mater,* 10(1), 10.

[47] Baufeld, B., Van der Biest, O., Gault, R., Ridgway, K. (2011). Manufacturing Ti6Al4V components by shaped metal deposition: microstructure and mechanical properties. *IOP Conf. Series: Mat. Sci. and Eng,* 26(1).

[48] Baufeld, B., Van der Biest, O., Gault, R. (2010). Additive manufacturing of Ti6Al4V Components by shaped metal deposition: microstructure and mechanical properties. *J Mat and design*, 31, 106-111.

[49] Clark, D., Bache, M.R., Whittaker, M.T. (2008). Shaped metal deposition of A Nickel for aero engine applications. *J Mat Processing Techn,* 203, 439-448.

[50] Baufeld, B. (2012). Mechanical properties on INCONEL 718 parts manufactured by shaped metal deposition (SMD), *J Materials Engineering and Performance.* 21(7), 1416-1421.

[51] Brandl, E., Baufeld, B., Leyens, C., Gault, R. (2010). Additive manufacturing Ti6Al4V using welding wire: comparison of laser and arc beam deposition and evaluation with respect to aerospace material specifications. *J Physical Procedia* 2010; 5: 595-606.

[52] Wang, F., Williams, S., Rush, M. (2011). Morphology investigation on direct current pulsed gas tungsten arc welding additive layer manufacturing Ti6Al4v alloy. *Int J Adva Manf Tech,* 57: 597-603.

[53] Hoye, N.P., Appel, E.C., Cuiuri, D., Li, H. (2013). Characterization of metal deposition during additive manufacturing of Ti-6Al-4V by arc –wire methods. In: *Twenty-Forth Annual International Solid Freeform Fabrication Symposium,* 1015-1023.

[54] Baufeld, B., Gault, R., Van der Biest, O. (2009). Microstructure of Ti-6Al-4V specimens produced by shaped metal deposition. *Int J Mat Res,* 100(11), 1536-1542.

[55] Herallić, A. (2012). Monitoring and control of robotized laser metal-wire deposition. Ph.D. thesis, University West, Trollhattan, Sweden.

[56] Mehnen, J., Ding, J., Lockett, H., Kazanas, P. (2010). Design for wire and arc additive layer manufacturing. In:*Proceedings of the 20th CIRP Design Conference*; Nantes, France, 19-21 April.

[57] Terrazas, C.A., Gaytan, S.M., Rodriguez, E., Espalin, D., Murr, L.E., Medina, F., et al. (2014). Multi-material metallic structure fabrication using electron beam melting. *Int J Adv Manuf Technol*, 71,33-45.

[58] Gong, X., Anderson, T., Chou, K. (2014). Review on powder-based electron beam additive manufacturing technology. *Manufacturing Rev.*, available online at http://mfr.edp-open.org.

[59] Bonaccorso, F., Bruno, C., Cantelli, L., Muscato, G., Longo, D. (2009). A Modular software interface for arc welding robot. In: *Proc HIS,* Catania, Italy, 21-23 May, 450-455.

[60] Zhang, Y.M., Li, P., Chen, Y., Male, A.T. (2002). Automated system for welding –based rapid prototyping. *Mechatronics,* 12, 37-53.

[61] Hartmann, K,, Krishnan, R., Merz, R., Neplotnik, G., Prinz, F., Schultz, L., et al. (1994). Robot-assisted shape deposition manufacturing. In: *Proceedings of the 1994 IEEE IntConf on Rob and Auto*. San Diego, CA: IEEE, May, 2890-2895.

[62] Ding, J. (2012). Thermo-mechanical analysis of wire and arc additive manufacturing process. School of Applied Science, Cranfield University, Ph.D. thesis.

[63] [Online].Available: http://3dprintingindustry.com/wp-content/uploads/2013/05/Atlantis-Report-on-3D-printing.

[64] [online]. Available: http://.www.nasa.gov 2009.

[65] Wanjara, P., Brochu, M., Jahazi, M. (2007). Electron beam freeform of stainless steel using solid wire feed. *J. Maters & Design,* 28, 2278-2286

[66] Sharma, A., Junaidh, M.I., Purushothaman, K.K., Kotwal, C.P., Paul, J., Tripathi, S., et al. (2006). Online monitoring of electron beam welding of Ti6Al4V alloy through

acoustic emission. In: *Proceedings of National Seminar on Non-Destructive Testing ,NDE*; Hyderabad, 7-9 December, 97-107.

[67] Taminger, K.M., Halfey, R.A. (2003). Electron beam freeform fabrication: A rapid metal deposition Process. *Proceedings of the 3rd Annual AutomotiveComposites Conference,* Troy, MI, Society of Plastic Engineering, 9-10 September.

[68] Medina, J. A. I. (2012). Development and application of CFD model of laser metal deposition. Ph.D. thesis, University of Manchester.

[69] Ion, J.C. (2005). Laser processing of engineering materials. Burlington Butterrworth-Heinemann. Oxford.

[70] Hecht, J. (2008). Understanding lasers: an entry level guide. *IEEE Press and Jhn Wi]iley& Sons Inc*., New Jersy, 3 edition.

[71] Brandl, E., Leyens, C., Donne, C.D., Holzinger, V. (2009). Deposition of Ti6Al4V using Nd:YAGlaser &wire: microstructure and mechanical properties. In: *NATO/RTO/MPAVT-163 Specialist Meeting on Additive Technology for Rapid of Military Hardware (NATO unclassified),* Bonn, 1-14.

[72] Kobryn, P.A., Moore, E.H., Semiain, S.L. (2000). The effect of laser power and traverse speed on microstructure, porosity, and build height in laser- deposited Ti6Al4V, *Scripta Mat,* 43(4), 299-305.

[73] Erickson, G., Heeth, M., Woods, B., Dolan, D., Henerson, E., Sears, J. (2004). Design and manufacturing of titanium formula SAE uprights using laser-powder- deposition. *SAE Int, Motorsports Eng Conf and Exh*; Derborn, Michigan, November 30- December 3.

[74] Brandl, E., Michailov, V., Viehweger, B., Leyens, C. (2011). Deposition of Ti-6Al-4V using laser and wire, part II: hardness and dimensions of single beads. *Surface and Coating Technology*, 206, 1130-1141.

[75] Syed, W.U.H., Li, L. (2005). Effects of wire feeding direction and location in multiple layer diode laser direct metal deposition. *Applied Surface Science,* 248(1-4), 518-524.

[76] Gong, H., Rafi, K., Strucker, B. (2012). Effect of defects on fatigue tests of as-built Ti-6Al-4V parts fabricated by selective laser melting. *J Solid Freeform Fabrication Symposium,* 499-506.

[77] Brandl, E., Schoberth, A., Leyens, C. (2012). Morphology, microstructure, and hardness of titanium (Ti-6Al-4V) blocks deposited by wire-feed additive layer manufacturing (ALM), *Materials Science and Engineering A*, 532, 295-307.

[78] Brabdl, E., Palm, F., Michailov, V., Viehweger, B., Lyens, C. (2011). Mechanical properties of additive manufactured titanium (Ti6Al4V) blocks deposited by a solid –state laser and wire, *Materials and Design* 32, 4665-4675. Doi: 10.1016/j.matdes.2011.06.062.

[79] Thivillon, L., Pervushin, D., Bertrand, P.H. Smurov, I. Industrial technology of laser assisted direct metal deposition. Online Available: http://www.dipilab.fr/AxeRecherche/fabricationdirecte/DMD/ENISE_DMD.

[80] Salehi ,D., Brandt, M. (2006). Melt pool temperature control using LabVIEW in Nd:YAG laser blown powder cladding. *Int J Adv Manuf Technol,* 29, 273-278.

[81] Strano, G., Hao, L., Evans, K.E., Everson, K.M. (2010). Optimization of quality and energy consumption for additive layer manufacturing processes. *ICRM- Green Manufacturing* , Ningbo, China, 364-369.

[82] Strano, G., Hao, L., Evans, K.E., Everson, K.M. (2010). Optimization of quality and energy consumption for additive layer manufacturing processes. *ICRM- Green Manufacturing* , Ningbo, China, 364-369.

[83] Jin, G.Q., Li, W.D., Tsai, C.F., Wang, L. (2011). Adaptive tool-path generation of rapid prototype for complex product models. *J Manf Sys,* 30, 154-164.

[84] Hua, T., Jing, C., Xin, L., Fengying, Z., Weidong, H. (2008). Research on molten pool temperature in the process of laser rapid forming. *J Mat Processing Technol,* 2008; 198: 454-462.

[85] Baker, R. (1925). Method of making decorative articles. United States Patent No.1,533,300. Filed Nov. 12 1920, patented 14th April.

[86] Shockey, HK. (1932). Machine for reclaiming worn brake drums, United States Patent No.1, 886, 503.

[87] White, WD. (1964). Pressure roller and method of manufacture. United States Patent No.3, 156, 968.

[88] Grosse-Wördemann J. (1980). The shape welding of heavy semi-finished parts. *Material prüfung,* 22(4), 168-173.

[89] Schmidt, J., Dorner, H., Tenckhoff, F. (1990). Manufacturing of complex parts by shape welding, *Journal of Nuclear Materials*, 171(1), 120-127.

[90] Ribeiro, A.F., Norrish, J., McMaster, R.S. (1994). Practical case of rapid prototyping using gas metal arc welding. In: *Fifth International Conference on "Computer Technology in Welding*", The Welding Institute, printed by Cramptons Printers, 15-16th June, Paris, France, 55, 1-6.

[91] Ribeiro, A.F., Norrish, J. (1996). Rapid prototyping process using metal directly. In: *Proceedings of the 7th Annual Int Solid Freeform Fab Symposium*, 12-14 August, The University of Texas at Austin, Austin, Texas, USA, 249-256.

[92] Spencer, J.D., Dickes, P.M., Wykes, C.M. (1998). Rapid prototyping of metal parts by three-dimensional welding. *Proceedings of the Institution of Mech Engineers, Part B: Journal of Engineering Manufacture*, 212(3), 175-182.

[93] Escobar-Palafox, G., Gault, R., Ridgway, K. (2011). Robotic manufacturing by shaped metal deposition: State of the art. *Industrial Robot*, 38(6), 622-628.

[94] Martina, F., Mehnen, J., Williams, S.W., Colegrove, P., and Wang, F. (2012). Investigation of the benefits of plasma deposition for the additive layer manufacturing of Ti-6Al-4V, *Journal of Materials Processing Technology*, 212(6), 1377-1386.

[95] Arcella, F.G., Froes, F.H. (2000). Producing titanium aerospace components from powder using laser forming. *Journal of Minerals, Metal and Materials Society*, 52 (5), 28-30.

[96] Wang, H., Kovacevic, R. (2001). Rapid prototyping based on variable polarity gas tungsten arc welding for a 5356 aluminum alloy. *Proceedings of the Institution of Mechanical Engineers, Part B: Journal of Engineering Manufacture,* 215(11), 1519-1527.

[97] Zhang, Y.M., Chen, Y., Li, P., Male, A.T. (2003). Weld deposition-based rapid prototyping : A preliminary study. *J Mat Processing Techn,* 135, 347-357.

[98] Ding, J., Colegrove, P., Mehnen, J., Ganguly, S., Sequeiraalmeida, P.M., Wang, F., Williams, S. (2011). Thermo-mechanical analysis of wire and arc additive layer manufacturing process on large multi-layer parts.*Computational Mat Sci,* December, 50 (12), 3315-3322.

[99] Sequeira Almeida, P.M., Williams, S. (2010). Innovative process model of Ti-6Al-4V additive layer manufacturing using cold metal transfer (CMT). In: *Proceeding of Twenty-First Annual Int Sol Freeform Fab Symposium*, the University of Texas at Austin, Austin TX, USA, 9-11 August, 25-36.

[100] Xiong, J., Zhang, G., Hu, J., Wu, L. (2014). Bead geometry prediction for robotic GMAW-based rapid manufacturing through a neural network and a second-order regression analysis. *J Intelligent Manf,* 25(1), 157-163.

[101] Tellez AGM (2010). Fibre Laser metal deposition with parameters study and temperature control. Ph.D. Dissertation, George Green Library of Science and Engineering, Nottingham University.

[102] Adebayo, A. (2013). Characterisation of integrated WAAM and machining processes. Ph.D. Dissertation Cranfield University.

[103] Pan, Z., Polden, J., Larkin, N., Duin, S., Norish, J. (2012). Recent progress on programming methods for industrial robots, *Robotics and Computer Integrated Manufacturing*, 8(2), 87-94.

[104] Topçu, O., Taşcioglu, Y., Ünver, H. Ö. (2011). A method for slicing CAD models in binary STL format. In: *Proceedings of 6th International Advanced Technologies Symposium (IATS'11)*, 16-18 May, Elaziğ, Turkey.

[105] Ibrahim, D., Ding, S., Sun, S. (2014). Roughness prediction for FDM produced surfaces. In: *Proceedings of Int. Conference Recent in Engineering & Technology (ICRET'2014*), Feb 13-14, Batam, Indonesia.
[106] Misra, D., Sundararajan, V., Wright, P.K. (2005). Zig-zag tool path generation for sculpture surface finishing. *Dimacs Series in Direct Mathematics and Theoretical Computer Science*, 67: 265-80.
[107] Dwivedi, R., Kovacevic, R. (2004). Automated torch path planning using polygon subdivision for solid freeform fabrication based on welding. *Journal of Manufacturing system*, 23, 278-291.
[108] Van Niekerk, G.J. (2007). A model for transparent data exchanging in layered manufacturing. Faculty of Science – the University of Johannesburg, Ph.D. thesis.
[109] Ericsson, M., Nylén, P., Danielsson, F., Johansson, H. (2005). Off-line programming or robots for metal deposition. *Proceedings of the 7th International Conference on Trends in Welding Research*, May 16-20, Pine Mountain, Georgia, USA, 149-160.
[110] Huiqiang, W., Jical, F., Jingshan, H. (2004). Microstructure evolution and fracture behaviour for electron beam welding of Ti6Al4V, *Bull Mat Sci,* 27(4), 387-392.
[111] Peters, M., Leyens, C. (2003). Titanium and titanium alloys. Wiley-VCH: Weinheim.
[112] Washko, SD, Agger, G. (1990). Wrought stainless steels. In Properties and selection: irons, steels, and high-performance alloys, vol. 1 of ASM Metal Handbook, 10th ed., Ohio: ASM International Handbook Committee, 841-907.
[113] Lippold, J.C., Kotecki, D.J. (2005). Welding metallurgy, and weldability of stainless steels, 1st ed., Wily, New Jersey.
[114] Parr, JG. (1971). An introduction to stainless steel, 2nd Printing, American Society for Metals, Metals Park, Ohio.
[115] Afrox Product reference Manual (available on): http://www.accrampton.co.za/assets/section-12---stainless-steel.
[116] Amine, T., Newkirk, J.W., Liou, F. (2014). An investigation of effect of direct metal deposition parameters on the characteristics of the deposited layers. *J of Case Studies in Thermal Engineering*, 3, 21-34.
[117] Giridharan, P. K., Murugan, N. (2009). Optimization of pulsed GTA welding process parameters for the welding of AISI 304L stainless steel sheets, *Int J Adv Manuf Technol*, 40: 478-489.
[118] Prasad, K.S., Rao, C.S., Rao, D.N. (2012). An investigation on weld quality characteristics of pulsed current micro plasma arc welded austenitic stainless steels, *Int J of Eng, Sci and Technology,* 4(2), 159-168.
[119] Raveendra, A., Ravi Kumar, B.V.R. (2013). Experimental study on pulsed and non-pulsed current TIG welding of stainless steel sheet (SS304), *Int J of Innovative Research in Science, Engineering and Technology*, 296, 2337-2344.

[120] Karunakaran, N. (2012). Effect of pulsed current on temperature distribution, weld bead profiles and characteristics of GTA welded stainless steel joints, *Int J of Eng and Technology,* 2(12), 1908-1916.

[121] Arivarasu, M., Devendranath Ramkumar, K., Arivazhagan, N. (2014). Comparative studies of High and low-frequency pulsing on the aspect ratio of weld bead in gas tungsten arc welded AISI 304L plates, *Procedia Engineering,* 97, 871-880.

[122] Dinesh, K.R., Elangovan, S., Siva, S.N. (2014). Parametric optimization of pulsed-TIG welding process in butt joining 304Laustenitic stainless steel sheets, *Int J Res in Eng and Technology,* 3(11), 213-219.

[123] Gokul, K., Devendranath Ramkumar, K., Arivazhagan, N. (2015). Characterization of metallurgical and mechanical properties on multi-pass welding of Inconel 625 and AISI 316L, *Journal of Mechanical Science and Technology,* 29(3), 1039-1047.

[124] Kou, S. (2003). Welding Metallugy.2nd Edition, John Wiley &SONS, INC.

[125] Petersen, W.A. (1973). Fine grains weld structure. *Weld. J ,* 53, 74-80.

[126] Yunjia, H., Frost, R.H., Olson, D.L., Edwards, G.R. (1983). Grain refinement of aluminum weld metal. *Weld. J,* 68, 280s.

[127] Matsuda, F., Ushio, M., Nakagawa, H., Nakata, K. (1980). Effect of electromagnetic stirring on the weld solidification structure of aluminum alloys. *In Proceedings of the Conference on Arc Physics and Weld Pool Behavior*, Welding Institute, Cambridge, 1, 337-347.

[128] Pearce, B.P., Kerr, H.W. (1981). Grain refinement in magnetically stirred GTA welds of aluminum alloys. *Metall Trans,* 12B, 479-486.

[129] Obielodan, J.O., Stucker, B.E. (2003). Characterization of LENS-fabrication Ti6Al4V and Ti6Al4V/TiC dual-material transition joins. *Int J Adv Manf Techol*, 66, 2053-2061.

[130] Sharir, Y., Pelleg, J., Grill, A. (Effect of arc vibration and current pulses on microstructure and mechanical properties of TIG tantalum welds. *Metals Technol* 1978; 5: 190-196.

[131] Welsch, G., BoyeR, R.R., Collings, E.W. (1994), Materials properties handbook: titanium alloys. First edition, ASM International, Materials Park, Ohio.

[132] Kou, S., Le, Y. (1988). Welding parameters and the grain structure of weld metal-a thermodynamic consideration. *Metal Trans A*, 19(4), 1075-1082.

[133] David, S.A., Liu, C.T. (1980). Weldability and hot cracking in thorium-doped iridium alloys, *Metals Technol*, 7(1), 102-106.

[134] Balasubramanian, M., Jayabalan, V., Balasubramanian, V. (2008). Effect of microstructure on impact toughness of pulsed current GTA welded α +β titanium alloy. *Mater Lett,* 62, 1102-1106.

[135] Kishore, B.N., Ganesh, S.R.S., Mythili, R., Saroja, S. (2007). Correlation of microstructure with mechanical properties of TIG weldments of Ti6Al4V made with and without current pulsing. *Mater Charact,* 58, 581-587.

[136] Sundaresan, S., Janaki Ram, G.D., Madhusudhan Reddy, G. (1999). Microstructural refinement of weld fusion zones in α-β titanium alloys using pulsed current welding, *Mat Scie Eng A,* 262(1-2), 88-100.

[137] Obielodan, J.O., Stucker, B.E. (2014). A fabrication methodology for dual-material engineering structures using ultrasonic additive manufacturing. *Int J Adv Man Tech*, 70 (1-4), 277-284.

[138] Dickens, P.M., Pridham, M. S., Cobb, R. C., Gibson, I. (1992). 3-D Welding, in: *Proceedings of the First European Conference on Rapid Prototyping*, 6-7th July, University of Nottingham, England, 81 - 93.

[139] Farad, K. and Mehdi, H. (2011), A new approach for predicting and optimizing weld bead geometries in GWAN, *International Journal of Aerospace and Mechanical Engineering*, 5(2), 56 – 62.

[140] Gurev, H. S., Stout, R.D. (1963). Solidification phenomena in inert gas metal arc welding. *Welding Journal*, vol. 42, no. 7, pp. 298s - 310s.

[141] Escobar-Palafox, G., Gault, R., Ridgway, K. (2011). Preliminary empirical model for predicting shrinkage, part geometry and metallurgical aspects of Ti-6Al-4V shaped metal deposition builds, *IOP Conf. Series: Materials Science and Engineering,* 26, doi:10.1088/1757-899X/26/1/012002.

[142] Mendez, P., Eagar, T. (2000). Humping formation in high current GTA welding. *International conference on joining of advanced and specialty materials II. Cincinnati*, OH, USA, pp22 - 30.

[143] Shebecko, L. (1970). Electric arc welding practice, MIR Publishers Moscow.

[144] Nabkarni SV. (1988). Modern arc welding technology, New Delhi, Oerlikon Ltd.

[145] Facchini, L., Magalini, E., Robotti, P., Molinari, A. (2009). Microstructure and mechanical properties of Ti6Al4V produced electron beam melting of pre-alloyed powders. *Rapid prototyping Journal*, 15(3), 171-178.

[146] Wain, NGR, Hao, XJ, Wu, X. (2010). Properties of Ti-5al-Mo-5V-3Cr samples produced via powder hot-isostatic- pressing, in *TMS conference (The Minerals, Metals & Materials Society)*, US.

[147] Bradstreet, B.J. (1968). Effects of surface tension and metal flow on bead formation, *Welding Journal*, 47(7), 314 - 322.

[148] Nguyen, T.C., Weckman, D.C., Johnson, D.A., Kerr, H.W. (2005). The humping phenomenon during high-speed gas metal arc welding, Science and Technology of *Welding and Joining,* 10(4), 447 - 459.

[149] Savage, W.F., Nippes, E.F., Agusa, K. (1979). Effect of arc force on defect formation in GTA welding, *Welding Journal*, 59(7), 212.

[150] Halder, K.S. (2014). TIG welding of AISI 310 stainless steel: experiments, modeling, and process optimization, M.Sc. Thesis, Jadavpur University.

[151] Lima, L.I.L., Schvartzman, M.M.A.M., Quinan, M.A.D., Campos, W.R.C. (2007). Intergranular corrosion evaluation of heat affected zone of ferritic stainless steel, In: *19th International Congress of Mechanical Engineering* November 5-9, Brasilia, DF.

[152] Peckner, D., Bernstein, IM. (1977). Handbook of Stainless Steels, McGraw-Hill Book Company, New York St .Louis San Francisco, USA.

[153] Schaeffler, A. L. (1949). Constitution diagram for stainless steel weld metal, *Metal Progress,* 56(11), 680-680B.

[154] Lippold, J.C., Savage, W.F. (1979). Solidification of austenitic stainless steel weldments: Part I-A proposed a mechanism, *Welding Research Supplement*, 362-374.

[155] Olson, D.L. (1985). Prediction of austenitic weld metal microstructure and properties, *Welding Research Supplement*, 281-295.

[156] Kujanpää ,V., Suutla, N., Takalo, T., Motion, T. (1979). Correlation between solidification cracking and microstructure in austenitic and austenitic-ferritic stainless steel welds, *Welding Research International*, 9(2), 55.

[157] Suutal, N. (1983). Effect of solidification conditions on the solidification mode in austenitic stainless steel. *Met. Trans*. 14A, 191-197.

[158] Raad, D.T., Mchenry, H.I., Steinmeyer, P.A., Thomas, J.R.D. (1980). Metallurgical factors affecting the toughness of 316L SMA weldments at cryogenic temperatures. *Welding Journal* 59(4), 104-112.

[159] Vitek, J. M., David, S.A., Sikka, V. K. (1992). Experimentation of Type 308 and 308CRE stainless steels after interrupted creep testing, *Welding Research Supplement*, 421-435.

[160] Li, J.Y., Sugiyama, S., Yanagimoto, J. (2005). Microstructure evolution and flow stress of semi-solid type 304 stainless steel, *J of Material Processing Technology*, 161, 39-406.

[161] Kotechi, DJ. (1993). Welding of stainless steels, iv welding, brazing, and soldering, vol.6 of ASM Handbook, ASM International, Metals Park, Ohio, 10th edition, 677-705.

[162] Schneider, H. (1960). Investment casting of high hot strength 12% chrome steel, *Foundry Trade Journal*, 108, 562-563.

[163] Kotecki ,D.J., Siewert, T.A. (1992). WRC-1992 constitution diagram for stainless steel weld metals: a modification of the WRC-1988 diagram, *Welding Journal*, 71(5), 171-178.

[164] Nexus 308L/308LSi datasheet, accessed on December 2008,http://www.nexusweld.com,

[165] *Online Available: website :www.leadshine.com.*

[166] Herallić, A. (2009). Towards full Automation of Robotized Laser Metal-Wire deposition. Department of Signals and systems", Chalmers University of Technology, Trollhattan, Sweden, MSc. Thesis.

[167] Nasiruzzaman, ABM. Using MATLAB to develop standalone graphical user interface (GUI) software packages for educational purposes: Available online at http://cdn.intechopen.com/pdfs-wm/11608.pd

[168] DIN Deutsches Institute Fur Normunge.v (1976), Berlin, Steel and Iron Standards on Quality. 24th revised edition. English Translation.

[169] AWS code section II part C, welding Rodes, electrodes, and filler metals, 1989.

[170] Davies, A.C., (1993). The Science and Practice of Welding, Volume 2, the Pitt Building, Trumpington Street, Cambridge, United Kingdom: The Press Syndicate of the University of Cambridge.

[171] Kim, I.S., Son, J.S, Kim, H.J, Chin, B.A. (2006). Development of a mathematical model to study on variation of shielding gas in GTA welding, *Journal of Achievements in Materials and Manufacturing Engineering*, 19(2).

[172] Mok, S.H, Bi, G., Folkes, J., Pashby, I. (2008). Deposition of Ti-6Al-4V using a high power diode laser and wire, Part I: Investigation of the process characteristics, *J. Surface &Coating Technology*, 202, 3933-3939.

[173] Voice, W. (2006). Net-shape processing applied to aero-engine components. In Cost Effective Manufacturing via Net-Shape Processing (PP. 1-1 – 1-12). *Meeting Proceedings RTO-MP-AVT-139,* Paper 1, Neuilly-sur-Siene, France.

[174] ISO/ASTM 52900. (2015). International standard on additive manufacturing –general principles-terminology, First edition.

[175] ASTM International.(2011). Standard test methods for tension testing of metallic materials [metric]. Standard E8/E8M-09, ASTM International, W. Conshohocken, Pa,.

[176] Katherasan, D., Elias, J.V., Sathiya, P., Noorul Haq A. (2012). Flux cored arc welding parameter optimization using particle swarm optimization algorithm**,** *J. Procedia Engineering*, 38, 3913-3926.

[177] Kattamis, T.Z., Coughlin, J.C., Flemings, M.C. (1967). *Trans Metall Soc – ASME*, 239, 1504.

[178] Kannan, T., Murugan, N. (2006). Prediction of ferrite number of duplex stainless steel clad metals using RSM, *Welding J*., 85(5), 91-100.

[179] Kishore Babu, N., Ganesh Sundara Raman, S., Mythili, R., Saroja, S. (2007). Correlation of microstructure with mechanical properties of TIG weldments of Ti-6Al-4V made with and without current pulsing, *Materials Characterization*, 58, 581-587.

[180] Kim, Y.S., Eagar, T.W. (1993). Metal transfer in pulsed current gas metal arc welding, *Welding Research Supplement*, September 27-28, Boulder- Colorado.

[181] Griridharan, P.K., Murugan, N. (2009). Optimization of pulsed GTA welding process parameters for the welding of AISI 304Lstainless steel sheets, *Int J Adv Manu Technol*., 40, 478-489. Doi: 10.1007/s00170-008-1373-0.

[182] Farahani, E., Shamanian, M., Ashrafizadeh, F. (2012). A comparative study on direct and pulsed current gas tungsten arc welding of alloy 617, *Int J on Manuf and Material Science*, 2(1), 6. Doi: 01IJMMMS.0201.41.

[183] Harvey, PD. (1982). *Engineering Properties of Steel*, American Society for Metals.

[184] Luecke, W.E., Slotwinski, J.A. (2014). Mechanical properties of austenitic stainless steel made by additive manufacturing, *Journal of Research of the National Institute of Standards and Technology*, 119, 398-418. http:/dx.doi.org/10.6028/jres.119.015

[185] Arcella, F.G., Froes, F.H. (2000). Producing titanium aerospace components from powder using laser forming. *Journal of Minerals, Metal and Materials Society*, 52(5), 28-30.

[186] Saha, S., Mukherjee, M., Pal, T.K., Microstructure, texture, and mechanical property analysis of gas metal arc welded AISI 304 austenitic stainless steel, *J. Materials Engineering and Performance*, 24(3), 1125-1139.

[187] Lawson, W. H. S., Kerr, H. W. (1976). Fluid Motion in GTA Weld Pools Part I: Flow Patterns and Weld Pool Homogeneity, *Welding Res. Int.,* 6 (5), 63-77.

[188] Lin, M.L., Eagar, T.W. (1986). Pressure produced by gas tungsten arcs, *Metallurgical Transaction*, 178, 601-607

APPENDICES

Appendix A- Composition Analysis Machine

Figure A.1. Chemical composition analysis machine

Appendix B

Welding Machine Technical Specifications

The Invertec V320-T AC/DC (see Figure B.1) are industrial TIG welding machines designed and manufactured using the latest inverter digital technology enabling the machines to perform at high outputs: respectively 320A at 35% duty cycle.

Figure B.1. TIG welding machine

The controller provides all the features you would expect from professional AC/DC TIG inverter welding machines combined with a user-friendly layout. The variable frequency control allows the welder to adjust the arc focus to suit the application.

The machines are equipped with a unique LCD user interface, not only showing welding parameters but also the effect on the arc.

A standard feature is the adjustable cleaning and penetration facility, used togain the ideal balance between cleaningthe aluminum surface of oxide and the penetration of the weld.

The machines operate using a square wave AC form as standard but can be set to an alternative wave form dependent on the welder’s needs.

Appendix B

Adjustable Starting current is also available on these machines. With aluminium, a high starting current will support better wetting and improved weld appearance.

The machines are supplied air-cooled as standard, however they can be easily converted to water-cooled with the addition of the Lincoln COOL ARC 34 water-cooler.

Table B.1. TIG welding machine specification

Primary Voltage	Fuse Size	Weight (kg)	Dimensions HxWxD (mm)	Protection/ Insulation Class	Compliance
230/400V/3/50-60Hz	20A	27.5	432 x 280 x 622	IP23C / H	EN 60974-1 EN 60974-3 EN 60974-10 ROHS
	25A	33			

Appendix C- Data Logger Device

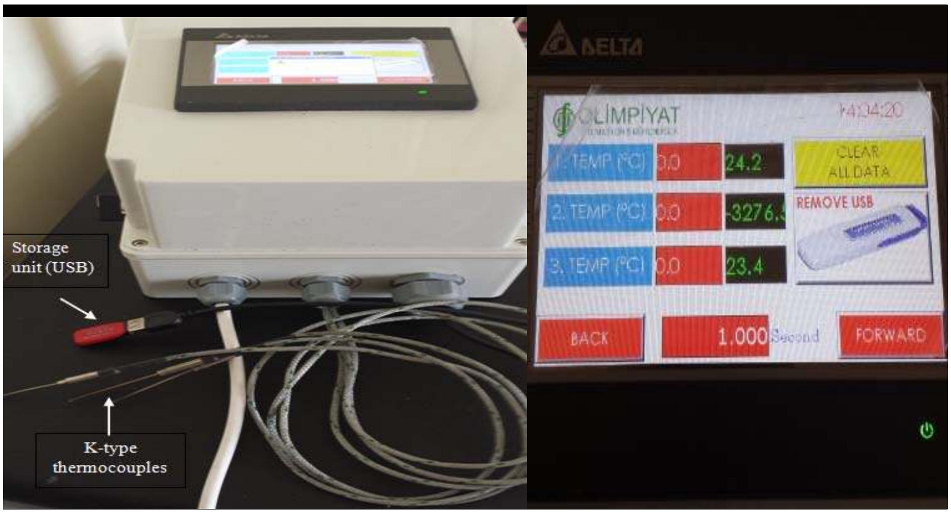

(a) (b)

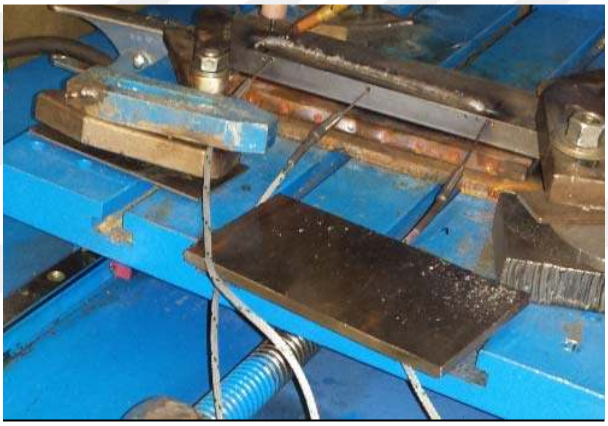

(c)

Figure C.1. (a) general view of the data logger with 3 K-type thermocouples; (b) the details of the screen displays (c) attaching the thermocouples in the located positions

Table C.1. Technical specifications of the data logger

Storage device	External USB of 8 GB
The interval period	One second
Number of measured temperature gates	three
Thermocouple used	K-type
Diameters of thermocouples	1-3 mm
Max. temperature measured	1200 C

Appendix D- Pre-set Parameters of Pulsed Current Mode

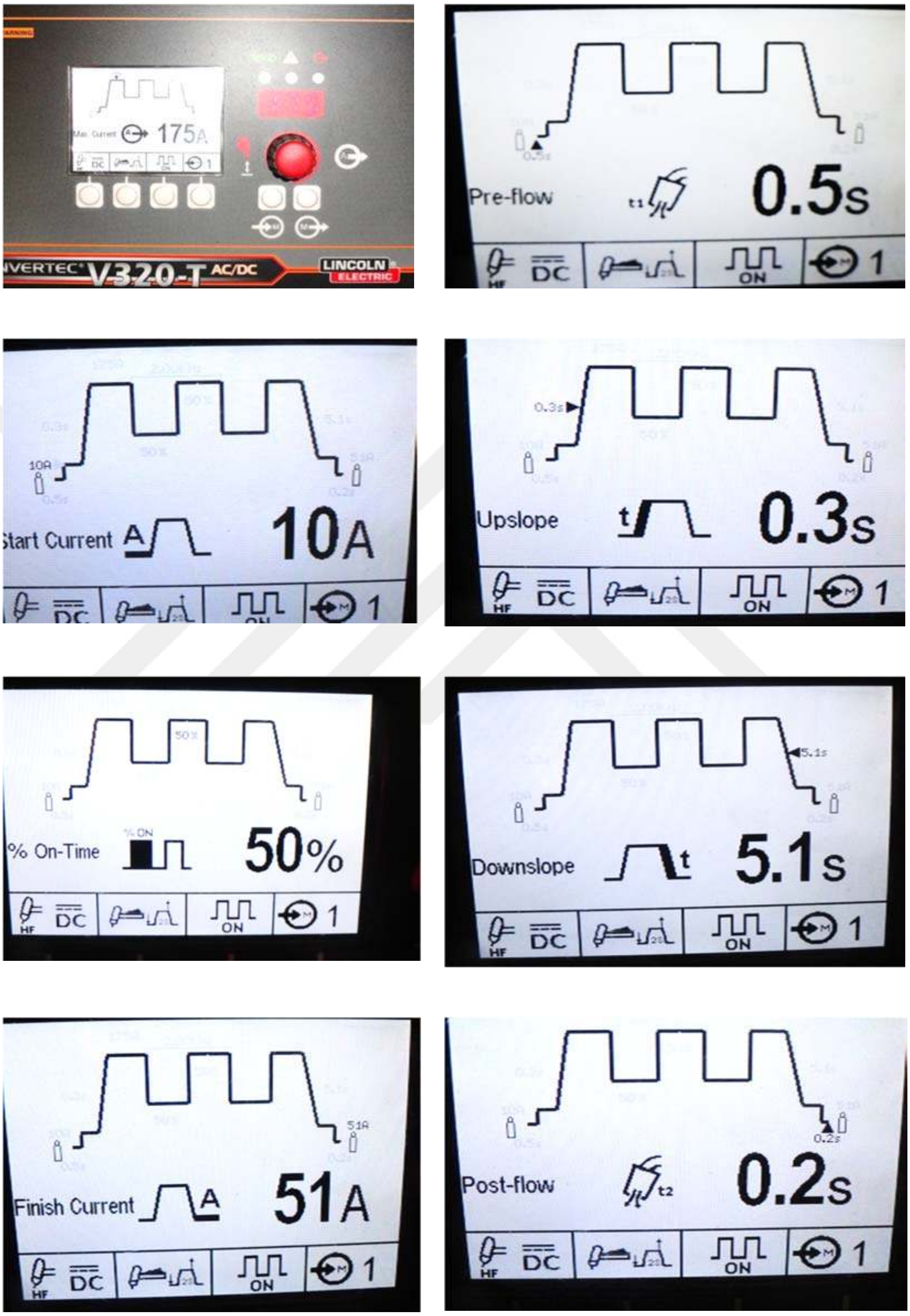

Figure D.1. Photographs illustrate preset parameters, which were kept constant during all experiments

Appendix D- User Interface Overview and Operation

The V320-T AC/DC user interface consists of the following parts as shown in Figure D.2:

(1) Dynamic LCD diplay.

(2) Status LED lights.

(3) 7-segment LED display (H)

(4) Push button / Rotary Encoder

(5) Mode Push buttons (A-D)

A. Weld Mode

B. Trigger Mode

C. TIG Pulse Mode

D. Memory Location Select

(6) Push buttons (E, F)

E. Memory Save

F. Memory Recall

Figure D.2. The V320-T AC/DC user interface.

Appendix E- Mechanical Testing Devices

DIGIROCK hardness tester

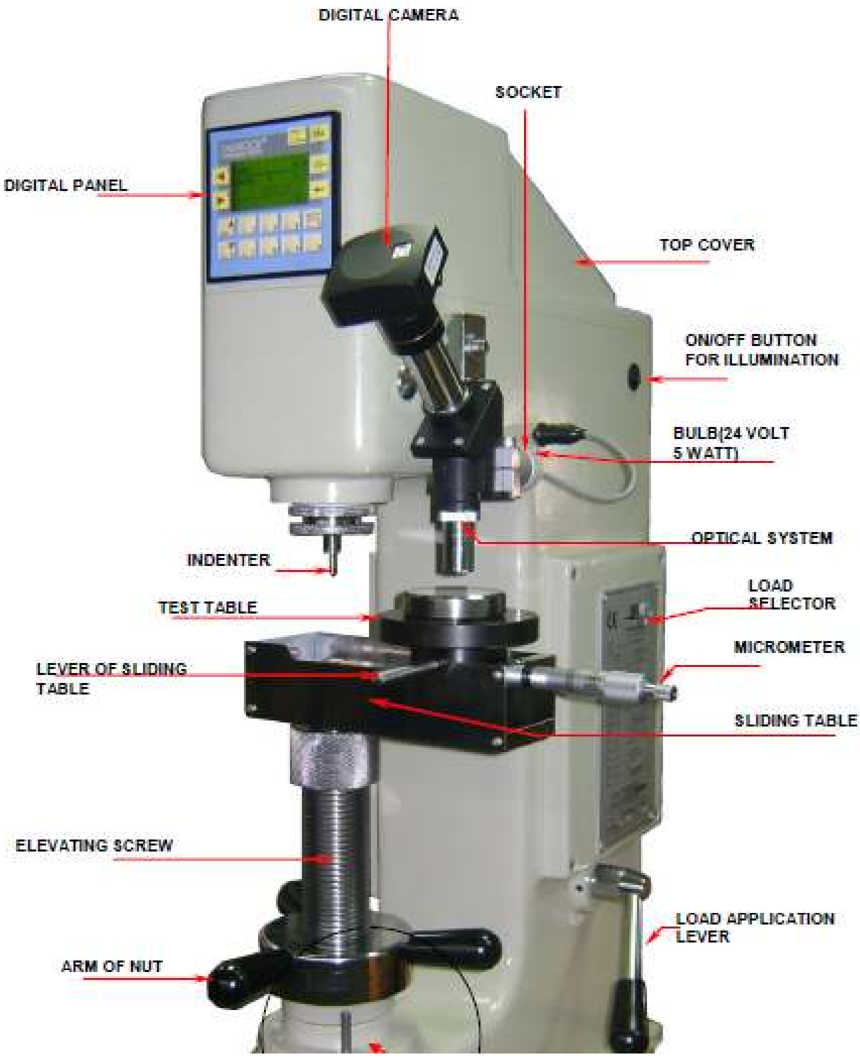

Figure E.1. Shows the DIGIROCK hardness tester

Table E.1. Technical Features of the DIGIROCK hardness tester

Pre-load (kgf)	10
Loads (kgf)	60, 100, 150, kgf Rockwell 62.5, 187.5, kgf Brinell 30 kgf Vickers
Load selection	By load selection disc
Test methods	Rockwell, Brinell, & Vickers
Load application	Hydraulic
Max.testing height	With sliding table 140 mm, without sliding table 240 mm
Throat	145 mm
Machine dimensions	780X550X360 mm
Weight (net/gross)	95/125 kgf
Optical system	75X magnification for Brinell 150 X magnification for Vickers
Power	220 V, 50 Hz

Appendix E- Mechanical Testing Devices

Shimadzu Tension Tester Machine Autograph AG X plus series

It is precision universal tester floor model 300 kN with speed range of 0.0005 to 1000 mm/min. The Shimadzu Autograph AG-X plus series delivers high-level control measurement performance utilizing technologies developed from conventional models. In addition, development focused on intuitive operation and convenient support functions. Furthermore, power savings functionality is provided as standard, as a means of lessening environmental load. As a result, power consumption during standby is 10 to 25% less in comparison to conventional models.

Figure E.2. Tension tester machine type (SHIMADZU)

Appendix E-Photographs of Tensile Testing Specimens

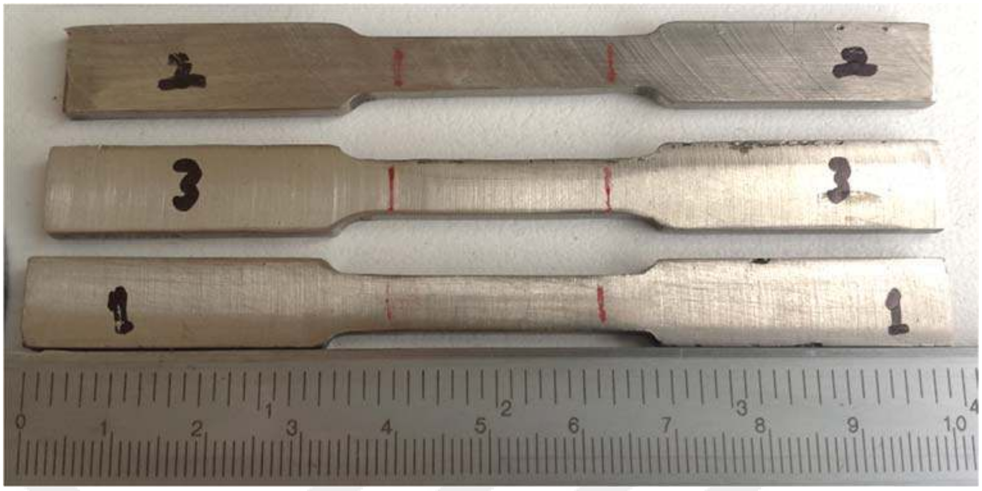

Figure E.3. Photograph illustrates the sub-size tension specimens. Dimensions shown in Figure 3.39(a)

Figure E.4. Photograph illustrates the short tension specimens. Dimensions shown in Figure 3.39(b)

Appendix F- Grinding and Polishing Machine

Grinding and polishing machine with dual 200mm or 250mm wheels, 50 – 600 rpm variable wheel speed, 3/4 HP motor with overload protection, and digital display. FORCIPOL 2V is compatible with the FORCIMAT automatic head which can be ordered at any time.

Figure F.1. Grinding and polishing machine

Figure F.2. Optical Microscopy supplied with Scop photocopy Camera

Appendix G- Optimized ANOVA responses

Analysis of variance and F-Value for bead on plate experiments:

Table G.1. Analysis of Variance for height (main factors)

Source	DF	Adj SS	Adj MS	F-Value	P-Value
WFS/TS	4	11.4108	2.85271	33.49	0.000
TS	3	2.4864	0.82881	9.73	0.001
Error	16	1.3629	0.08518		
Total	23	15.2601			
S =0.291855		R-sq=91.07%	R-sq (pred) = 87.16%		

Table G.2. Analysis of Variance for width w (main factors)

Source	DF	Adj SS	Adj MS	F-Value	P-Value
WFS/TS	1	5.4912	5.4912	97.64	< 0.005
TS	1	30.6636	30.6636	545.22	< 0.005
Error	21	1.1811	0.0562		
Total	23	37.3359			
S = 0.237152	R-sq=96.84%	R-sq (adj) = 96.54%		R-sq (pred)= 95.70%	

Table G.3. Analysis of Variance results for penetration p (main factors)

Source	DF	Adj SS	Adj MS	F-Value	P-Value
WFS/TS	1	0.04370	0.04370	0.74	0.399
TS	1	4.85214	4.85214	82.28	< 0.005
Error	21	1.23845	0.05897		
Total	23	6.13430			
S = 0.399	R-sq =79.81%	R-sq (adj) = 77.89%		R-sq (pred)= 72.46%	

Appendix H- Optimized ANOVA responses

Analysis of variance and F-Value for multi-layers walls:

Table H.1. Analysis of Variance for wall height h_{av} (main factors)

Source	DF	Adj SS	Adj MS	F-Value	P-Value
I	1	4.395	4.395	1.05	0.327
TS	1	12.317	12.317	2.94	0.114
WFS	1	50.007	50.007	11.95	0.005
L	1	3.507	3.507	0.84	0.380
Error	11	46.015	3.507		
Total	15	116.240			
S = 2.04529 R-sq =60.41% R-sq (adj) = 46.02% R-sq (pred)= 25.44%					

Table H.2. Analysis of Variance for wall width w (main factors)

Source	DF	Adj SS	Adj MS	F-Value	P-Value
I	1	10.534	10.534	8.72	0.013
TS	1	30.631	30.631	25.35	<0.005
WFS	1	12.113	12.113	10.02	0.009
L	1	4.311	4.311	10.02	0.086
Error	11	13.294	1.209		
Total	15	70.883			
S = 1.09933 R-sq =81.25% R-sq (adj) = 74.43% R-sq (pred)= 61.91%					

Table H.3. Analysis of Variance for MLT (main factors)

Source	DF	Adj SS	Adj MS	F-Value	P-Value
I	1	0.00011	0.000113	0.00	0.969
TS	1	0.08863	0.088629	1.23	0.290
WFS	1	0.02831	0.028313	0.39	0.543
L	1	0.35578	0.355778	4.95	0.048
Error	11	0.79007	0.071824		
Total	15	1.26290			
S 0.268000 R-sq =37.44% R-sq (adj) = 14.69% R-sq (pred)= 0.00%					

Table H.4. Analysis of Variance for DV (main factors)

Source	DF	Adj SS	Adj MS	F-Value	P-Value
I	1	0.9710	0.9710	4.48	0.058
TS	1	29.3345	29.3345	135.35	<0.05
WFS	1	15.5759	15.5759	71.87	<0.05
L	1	0.0420	0.0420	0.19	0.668
Error	11	2.3841	0.2167		
Total	15	48.3075			
S = 0.465551 R-sq = 95.06% R-sq (adj) = 93.27% R-sq (pred)= 88.69%					

Table H.5. Analysis of Variance for HRA (main and interaction factors)

Source	DF	Adj SS	Adj MS	F-Value	P-Value
I	1	1.7009	1.7009	0.47	0.532
TS	1	0.2048	0.2048	0.06	0.824
WFS	1	1.1796	1.1796	0.32	0.600
L	1	3.6863	3.6863	1.01	0.372
I*TS	1	3.1087	3.1087	0.85	0.408
I*WFS	1	3.3413	3.3413	0.92	0.393
I*L	1	3.0129	3.0129	0.83	0.415
TS*WFS	1	0.3805	0.3805	0.10	0.763
TS*L	1	1.2666	1.2666	0.35	0.587
WFS*L	1	1.0568	1.0568	0.29	0.619
TS*WFS*L	1	1.5348	1.5348	0.42	0.552
Error	4	14.6019	3.6505		
Total	15	76.6044			
S = 1.91062 R-sq 80.94%		R-sq (adj) = 28.52%		R-sq (pred)= 0.00%	

Table H.6. Analysis of variance for MLT (factors and interactions)

Source	DF	Adj SS	Adj MS	F-Value	P-Value
TS	1	0.01980	0.019799	0.81	0.463
WFS/TS	1	0.00773	0.007729	0.32	0.631
T_{sub}	1	0.00258	0.002578	0.11	0.776
TS*WFS/TS	1	0.01072	0.010720	0.44	0.576
TS*Tsub	1	0.01577	0.01577 4	0.65	0.506
WFS/TS*Tsub	1	0.00510	0.005096	0.21	0.693
TS*WFS/TS*Tsub	1	0.01954	0.019541	0.80	0.466
Error	2	0.04889	0.024444		
Total	9	1.01112			
S =0.156345	R-sq =95.17%	R-sq(adj)= 78.24%		R-sq(pred)= 0.00%	

Appendix I- Optimized ANOVA responses

Analysis of variance and F-Value for single bead of pulsed current process:

Table I.1. Analysis of Variance for wall width W (main factors)

Source	DF	Adj SS	Adj MS	F-Value	P-Value
Ip	1	3.8240	3.8240	14.28	0.019
Fr	1	0.3314	0.3314	1.24	0.328
TS	1	0.7704	0.7704	2.88	0.165
CR	1	1.3824	1.3824	5.16 25.73	0.086
Error	4	1.0715	0.2679		
Total	8	7.3798			

S = 0.517573 R-sq =85.48% R-sq (adj) = 70.96% R-sq (pred)= 25.73%

Table I.2. Analysis of Variance for bead height H (main factors)

Source	DF	Adj SS	Adj MS	F-Value	P-Value
Ip	1	0.25627	0.25627	2.93	0.162
Fr	1	0.06371	0.06371	0.73	0.442
TS	1	0.70042	0.70042	8.00	0.047
CR		1.35375	1.35375	15.47	0.017
Error	4	0.35001	0.08750		
Total	8	2.72416			

S = 0.295810 R-sq =87.15% R-sq (adj) = 74.30% R-sq (pred)= 29.59%

Table I.3. Analysis of Variance for depth of penetration P (main factors)

Source	DF	Adj SS	Adj MS	F-Value	P-Value
Ip	1	0.09375	0.093750	0.61	0.478
Fr	1	0.01312	0.013121	0.09	0.784
TS	1	0.57042	0.570417	3.73	0.126
CR	1	0.00042	0.000417	0.00	0.961
Error	4	0.61230	0.15307		
Total	8	1.2900			

S = 0.391247 R-sq = 52.54% R-sq (adj) = 5.07% R-sq (pred)= 0.00%

Table I.4. Analysis of Variance for the bead width (main factors)

Source	DF	Adj SS	Adj MS	F-Value	P-Value
Ip	1	6.0742	6.07423	109.95	0.000
Fr	1	0.7052	0.70521	12.77	0.023
TS	1	2.6707	2.67067	48.34	0.002
CR	1	0.5847	0.58469	10.58	0.031
Error	4	0.2210	0.05524		
Total	8	10.2558			

S = 0.235041 R-sq = 97.85% R-sq (adj) 95.69% R-sq (pred)= 86.68%

Table I.5. Analysis of Variance for the bead height (main factors)

Source	DF	Adj SS	Adj MS	F-Value	P-Value
Ip	1	0.4593	0.4593	3.45	0.137
Fr	1	0.6468	0.6468	4.87	0.092
TS	1	0.8513	0.8513	6.40	0.065
CR	1	0.1837	0.1837	1.38	0.305
Error	4	0.5317	0.1329		
Total	8	2.6728			

S = 0.364596 R-sq = 80.11% R-sq (adj) 60.21% R-sq (pred)= 0.00%

Table I.6. Analysis of Variance for the bead height (main factors)

Source	DF	Adj SS	Adj MS	F-Value	P-Value
Ip	1	0.43870	0.43870	9.74	0.026
Fr	1	0.19901	0.19901	4.42	0.09
TS	1	0.12661	0.12661	2.81	0.154
CR	1	0.09018	0.09018	02.00	0.216
Error	5	0.22519	0.04504		
Total	9	1.07969			

S = 0.212223 R-sq = 94.87% R-sq (adj) 90.77% R-sq (pred)= 76.68%

Appendix J- Optimized ANOVA responses

Analysis of variance and F-Value for multi-layer wall of pulsed current process:

Table J.1. Analysis of Variance for wall width W (main factors)

Source	DF	Adj SS	Adj MS	F-Value	P-Value
I_p	1	2.3563	2.3563	1.92	0.238
Fr	1	0.0975	0.0975	0.08	0.792
TS	1	16.4341	16.4341	13.42	0.022
CR	1	6.0200	6.0200	4.92	0.091
Error	4	4.8972	1.2243		
Total	8	29.8052			
S = 1.10649 R-sq = 83.57% R-sq (adj) = 67.14% R-sq (pred)= 18.31%					

Table J.2. Analysis of Variance for wall Height H (main factors)

Source	DF	Adj SS	Adj MS	F-Value	P-Value
I_p	1	0.8214	0.8214	1.57	0.279
Fr	1	0.0030	0.0030	0.01	0.943
TS	1	8.2720	8.2720	15.77	0.017
CR	1	3.8480	3.8480	7.34	0.054
Error	4	2.0981	0.52453		
Total	8	15.0425			
S = 0.724244 R-sq = 86.05% R-sq (adj) = 72.10% R-sq (pred)= 43.55%					

Table J.3. Analysis of Variance for penetration depth P (main factors)

Source	DF	Adj SS	Adj MS	F-Value	P-Value
I_p	1	1.04167	1.04167	108.48	0.000
Fr	1	0.01006	0.01006	1.05	0.364
TS	1	0.24000	0.24000	24.99	0.007
CR	1	0.18375	0.18375	19.14	0.012
Error	4	0.03841	0.00960		
Total	8	1.51389			
S = 0.097992 R-sq = 97.46% R-sq (adj) = 94.93% R-sq (pred)=88.01%					

Table J.4. Analysis of Variance for wall cross-section hardness HRA (main factors)

Source	DF	Adj SS	Adj MS	F-Value	P-Value
I_p	1	15.8763	15.8763	10.45	0.032
Fr	1	1.1242	1.1242	0.74	0.438
TS	1	6.3161	6.3161	4.16	0.111
CR	1	0.1190	0.1190	0.08	0.793
Error	4	6.0760	1.5190		
Total	8	29.5116			
S = 1.23248 R-sq = 79.41% R-sq (adj) = 58.82% R-sq (pred)= 0.00%					

Appendix K- Tensile test results

Table K.1. Tension results for specimens tested in horizontal direction in three positions

No.	Ultimate strength (MPa)			0.2 yield strength (Mpa)			Elongation %		
	Bottom	Middle	Top	Bottom	Middle	Top	Bottom	Middle	Top
				CCSMD (0 HZ)					
Average	616.7	595.51	604.42	457.74	452.52	457	50	45	45
				PCSMD (5 HZ)					
1	696.2	694.73	634.5	449.59	471.98	423.65	55	45	58
2	685.6	664.05	676.83	442.7	420.74	468.5	53	60	50
Average	690.9	679.39	667.66	446.14	446.36	446.	54	52.5	54
				PCSMD (500 HZ)					
1	712.4	744.47	761.26	442.6	408	468.4	60	60	53
2	746.7	719.03	695.82	462.15	490.8	486.6	65	60	56
Average	729.5	731.75	728.54	452.37	449.4	477.5	62.5	60	54.
				PCSMD (2000 HZ)					
1	670.18	737.22	719.75	449.23	449.96	455.07	60	60	5
2	697.21	648.84	643.36	455.81	422.68	441.92	57	60	60
Average	683.7	693.03	681.55	452.52	446.32	448.49	58.5	60	57.5

Appendix K- Tensile test results

Table K.2. Tension results for specimens tested in the vertical direction with and without stress relief H.T.

No.	**Without Heat Treatment**			**With Heat Treatment**		
	σ_u MPa	**σ_y MPa**	**El %**	**σ_u MPa**	**σ_y MPa**	**El %**
			PCSMD (5 HZ)			
1	638.08	431.38	60	617.9	428.486	60
2	677.109	443.34	56	----	-----	
3	719.575	475.61	57	714	464.84	65
Average	678.254	450.11	57.67	665.95	446.663	62.5
			PCSMD (500 HZ)			
1	647.254	460.97	60	661.52	442.24	67
2	-----	-----	-----	633.4	434.14	61
3	698.84	441.93	65	634.35	435	60
Average	673.375	451.45	62.5	643.1	437.127	62.66
			PCSMD (2000 HZ)			
1	685.83	444.45	60	677.7	425.6	65
2	645.85	423.15	60	702.36	457.31	60
3	665.26	469.65	55	------	-----	---
Average	665.647	445.75	58.334	690.03	441.455	62.5
			CCSMD (0 HZ)			
1	580.4		52			
2	602.77		50			
3	610.07		51			
Average	597.766		51			

CURRICULUM VITAE (CV)

PERSONAL INFORMATION

Full Name and Surname: Adnan A. Ugla AL-OMAR

Nationality: Iraq

Email: adnan.alomar@ymail.com

Education	Graduate School	Year
Master	University of Baghdad	2003
M.Sc. Thesis: *Improvement of welding quality by using robotic welding.*		
Bachelor	University of Baghdad	2001

Work Experience	Place	Enrollment
2011- Present	University of Thi-Qar	Assist. Prof.
2008-2011	University of Thi-Qar	Lecturer
2004-2008	University of Thi-Qar	Assist. Lecturer

Language: Arabic native language, English, Turkish

Some of the old publications:

[1]. Ugla, A. A. 2011 "Experimental investigation of variation in mechanical and microstructural properties along the length of similar AA6063 FSW". *Thi-Qar University Journal for Engineering Sciences* V.2 N.3.

[2]. Ugla, A. A.,Hashim, F. A. , 2011, "Microstructural investigation on severe cold work and treated drawn wires" *Thi-Qar University Journal for Engineering Sciences* V.2 N.1

[3]. Ugla, A. A. 2011,"Use of statistical charts and process capability for improving quality control techniques, an experimental study in Ur company", *Thi-Qar University Journal for Engineering Sciences* V.2 N.2.

[4]. Ugla, A. A., Hanoon R. M., 2011," Prediction of power chimney parameters influence the operation at Nassiriya City" , *Thi-Qar University Journal for Engineering Sciences* V.2 N.2.

[**5**]. Ugla, A. A., Salman M. D.,2011 "Recovery of Cu(II) from model water using Emulsion Liquid Membrane (ELM) Technique", *Thi-Qar University Journal for Engineering Sciences* V.2 N.4.

[**6**]. Ugla, A. A., 2008, "Study the process capability for mass production by designed tolerances" *Journal of Thi-qar University*